Unravelling conformational flexibility and chirality in molecules using microwave spectroscopy

DISSERTATION

zur Erlangung des Doktorgrades
der Mathematisch-Naturwissenschaftlichen Fakultät
der Christian-Albrechts-Universität zu Kiel

Angefertigt am
Deutschen Elektronen-Synchrotron,
ein Forschungszentrum der Helmholtz-Gemeinschaft

Himanshi Singh

Hamburg, Dezember 2023

Erste Gutachterin: Prof. Dr. Melanie Schnell
Zweiter Gutachter: Prof. Dr. Friedrich Temps

Tag der mündlichen Prüfung: 28.02.2024

In loving memory of my nana, Ram Sanehi

List of Publications

- H. Singh , P. Pinacho, D. A. Obenchain, M. M. Quesada-Moreno, and M. Schnell "The many forms of alpha-methoxy phenylacetic acid in the gas phase: flexibility, internal dynamics, and their intramolecular interactions", Physical Chemistry Chemical Physics **24**, 27312-27320 (2022).
- H. Singh$^+$, F. E. L. Berggötz$^+$, W. Sun, and M. Schnell, "Chiral control of gas-phase molecules using microwave pulses", Angewandte Chemie International Edition **62**, e202219045 (2023).
- W. Sun, D. S. Tikhonov, H. Singh, A. L. Steber, C. Pérez, and M. Schnell, "Inducing transient enantiomeric excess in a molecular quantum racemic mixture with microwave fields", Nature Communications **14**, 934 (2023).

Abstract

Aspects such as conformational flexibility and chirality play a critical role in biochemical and pharmacological processes. Therefore, a comprehensive understanding of molecular structure, intra- and intermolecular forces, and chirality is required to comprehend the interplay between the three-dimensional structure of a biomolecule and its functionality. Molecular rotational spectroscopy is well suited for the investigation of the conformational flexibility and chirality of small and medium-sized molecules and clusters. The high resolution and sensitivity of rotational spectroscopy provide highly accurate structure determination and manipulation of chiral molecules in the gas phase. In this thesis, the analysis of chiral molecules using the chirped-pulse Fourier transform microwave spectrometer is demonstrated. Part I of the thesis focuses on the conformational analysis of flexible molecules with broadband rotational spectroscopy, while the second part showcases the applicability of its chirality-sensitive extension, microwave three-wave mixing, to manipulate and control gas-phase chiral molecules.

In part I, the conformational landscape and internal rotation of six molecules with increasing structural complexity and flexibility were analyzed based on the recorded rotational spectra. Starting with the relatively rigid [2,2]-paracyclophane family, the isolated gas-phase structures of overall four mono-substituted [2,2]-paracyclophanes were investigated. Thereafter, the rotational spectrum of α-methoxy phenylacetic acid was used to determine the barrier of methyl internal rotation and to reveal the influence of intramolecular interactions in determining its conformational space. Due to the amyl chain, 6-amyl-α-pyrone has a large conformational ensemble compared to the other two molecular systems. The high sensitivity of the microwave spectroscopy technique facilitated the determination of the gas-phase structures of aldehyde-substituted [2,2]-paracyclophane, α-methoxy phenylacetic acid, and 6-amyl-α-pyrone. The conformational analysis of α-methoxy phenylacetic acid and 6-amyl-α-pyrone serves as the basis for future microsolvation studies.

Minor modifications to the COMPACT spectrometer setup enable us to perform microwave three-wave mixing experiments and its extension to create enantioselective population transfer. In part II, a general approach demonstrating the enhancement of enantiomer-selective population transfer by addressing the thermal population and spatial degeneracy of the rotational levels is presented. The experimental results illustrate an achieved enantiomeric excess of about 40% in a rotational level of interest using tailored microwave pulses. The subsequent chapter introduces a non-linear and resonant microwave six-wave mixing approach for the manipulation of flexible chiral molecules, whose enantiomers are inseparable using conventional methods, not even in the cold conditions of the supersonic jet, due to their short racemization times. The experiments were performed with the transiently chiral ben-

zyl alcohol and successfully demonstrated a transient enantiomeric excess induced in a particular rotational state. This presented technique could be further extended to reveal information on the tunnelling rates of such transiently chiral molecules. These experimental results showcase the high level of chiral control that can be achieved in gas phase samples using microwave spectroscopy and establish the foundation for future experiments aiming for chiral purification and high-precision measurements.

Rotational spectroscopy and microwave three-wave mixing offer a promising toolkit for chemical, structural, and chiral analysis. Broadband rotational spectroscopy allows us to extract significant structural and chemical information, including details about flexibility and internal dynamics. Microwave three-wave mixing techniques enable us to study, control, and manipulate chirality at the molecular level in the gas phase. Developing an understanding of these phenomena at the molecular level brings us closer to unraveling the functionality of molecules in nature.

Kurzzusammenfassung

Aspekte wie die konformative Flexibilität und Chiralität spielen eine fundamentale Rolle in biochemischen und pharmakologischen Prozessen. Deshalb ist ein umfassendes Wissen über die molekulare Struktur, inter- und intramolekulare Kräfte sowie Chiralität notwendig, um das Zusammenspiel des dreidimensionalen Aufbaus eines Moleküls und seiner Funktion zu verstehen. Rotationsspektroskopie ist bestens geeignet, um die konformative Flexibilität und Chiralität von kleinen bis mittelgroßen Molekülen und Clustern zu erforschen. Das hohe Auflösungsvermögen und die Empfindlichkeit dieser Technik ermöglichen eine genaue Strukturbestimmung und die Manipulation chiraler Moleküle in der Gasphase. In dieser Arbeit wird die Untersuchung chiraler Moleküle mittels breitbandiger Fourier-Transform-Mikrowellenspektroskopie dargelegt. Dabei konzentriert sich der erste Teil der Arbeit auf die konformative Analyse flexibler Moleküle mithilfe der Breitband-Rotationsspektroskopie, während im zweiten Teil die Anwendung der chiralitätssensitiven Erweiterung, das Mikrowellen-drei-Wellen-Mischen, zur Manipulation und Kontrolle chiraler Moleküle in der Gasphase vorgestellt wird.

In Teil I werden die Konformerenlandschaft und die interne Rotation von sechs verschiedenen Molekülen mit steigender struktureller Komplexität und Beweglichkeit auf Grundlage ihrer gemessenen Rotationsspektren analysiert. Zu Beginn werden insgesamt vier monosubstituierte Strukturen aus der Familie der vergleichsweise starren [2,2]-Paracyclophane isoliert in der Gasphase betrachtet. Danach wird über die Analyse des Rotationsspektrums von α-Methoxyphenylessigsäure die Barriere der internen Rotation der Methylgruppe des Moleküls bestimmt und der Einfluss intramolekularer Wechselwirkungen auf die Konformationsanalyse gezeigt. Aufgrund der Amylkette hat das Molekül 6-Amyl-α-pyron verglichen mit den anderen beiden molekularen Systemen eine große Anzahl an Konformeren. Die hohe Empfindlichkeit der Mikrowellenspektroskopie ermöglicht die Bestimmung der Gasphasenstruktur von Aldehyd-substituiertem [2,2]-Paracyclophan, α-Methoxyphenylessigsäure und 6-Amyl-α-pyron über Isotopensubstitution in natürlicher Häufigheit. Die Konformerenanalyse letzterer beider Molekülsysteme bildet die Grundlage für zukünftige Untersuchungen zur Mikrosolvatation.

Kleine Änderungen am COMPACT Spektrometer ermöglichen uns die chiralitäts-empfindliche Messung von Mikrowellen-drei-Wellen-Mischen und seine Erweiterung, dem enantioselektivem Populationstransfer. Im zweiten Teil wird ein allgemeiner Ansatz zur Steigerung des enantioselektiven Populationstransfers vorgestellt, der sich mit der thermischen Besetzung und der räumlichen Entartung der Rotationsniveaus befasst. Die experimentellen Ergebnisse zeigen einen erreichten Enantiomerenüberschuss von ca. 40% in einem Rotationsniveau unter Benutzung maßgeschneiderter Mikrowellenpulse. Das darauffolgende Kapitel stellt den nichtli-

nearen und resonanten Ansatz des Mikrowellen-sechs-Wellen-Mischens für die Manipulation flexibler chiraler Moleküle vor, deren Enantiomere sich wegen ihrer kurzen Razemisierungszeiten durch konventionelle Methoden-sogar unter den kalten Bedingungen einer Überschallexpansion-nicht trennen lassen. Die Experimente wurde mit dem transient-chiralen Benzylalkohol durchgeführt und zeigen die erfolgreiche Erzeugung eines transienten Enantiomerenüberschusses in einem gewählten Rotationszustand. Eine Erweiterung der vorgestellten Technik kann Aufschluss über die Tunnelraten in derartigen transient-chiralen Molekülen geben. Die experimentellen Ergebnisse lassen ein hohes Maß an chiraler Kontrolle erkennen, die durch Mikrowellenspektroskopie über Proben in der Gasphase erlangt werden kann. Dies bildet eine Grundlage für zukünftige Experimente, die Enantiomerenreinheit und Hochpräzisionsmessungen zum Ziel haben.

Rotationsspektroskopie und Mikrowellen-drei-Wellen-Mischen bieten vielversprechende Mittel und Wege für chemische, strukturelle und chirale Untersuchungen. Breitband-Rotationsspektroskopie erlaubt uns, wichtige strukturelle und chemische Informationen einschließlich Kenntnis zu Beweglichkeit und interner Dynamik zu gewinnen. Durch Mikrowellen-drei-Wellen-Mischen können wir Chiralität in der Gasphase untersuchen, kontrollieren sowie manipulieren. Indem wir unser Verständnis solcher Phänomene auf molekularer Ebene vertiefen, können wir die Funktionalität von Molekülen in der Natur weiter entschlüsseln.

Contents

Chapter 1

Introduction

Conformational flexibility is innately related to the functionality of biomolecules.[1] Biomolecular functioning is deeply rooted in the events occurring at the molecular level and is often governed by their smaller structural units. Proteins, for instance, are made of linear chains of amino acids-only 20 distinct types of which are commonly found in proteins. These amino acids exhibit significant conformational flexibility owing to multiple torsional degrees of freedom, enabling the folding and functionality of proteins.[2] Therefore, an in-depth knowledge of the structure and internal dynamics of these molecules is important in understanding their physical and chemical properties, which can facilitate a better comprehension of the mechanisms behind their biological activity.

The activities and functions of biomolecules in biochemical and pharmacological processes are intimately related to their three-dimensional structures. For example, the three-dimensional structure of hemoglobin, the protein responsible for oxygen transport in our bloodstream, has helped biologists understand how a large number of human mutant hemoglobins relate to particular symptoms of diseases.[2] Hence, the characterisation of biomolecular structures is essential for understanding biological processes and developing targeted drugs on that basis.

Various techniques, including X-ray crystallography, electron diffraction, and nuclear magnetic resonance (NMR), are employed for studying molecular structures. X-ray crystallography is widely used for structural studies of large biomolecules like proteins and viruses.[3–6] It deduces the corresponding structure from patterns of diffracted X-ray radiation scattered by the electron cloud of molecules in the crystal. Despite the high resolution of the data obtained from X-ray diffraction experiments (below 1 Å in some cases) the resolution of the technique is limited by the feasibility of sample crystallisation and the quality of the crystal. Furthermore, X-ray crystallography is performed in a solid state, which prevents the observation of multiple conformations due to crystal packing.

NMR spectroscopy performed in both the solid and liquid phases, is extensively used for conformational studies. However, its drawback is mainly related to the timescale of the experiment with respect to the interconversion time between conformers. Conformations with low barriers are usually observed as broad peaks, hindering the distinction of their spectroscopic signatures.[7] Although comparatively high-resolution information about biomolecular structures can be obtained through these techniques, they are limited by the factor that target biomolecules need to be purified to a certain homogeneity.[8] A further disadvantage of these techniques is that a solid or liquid environment significantly influences the intrinsic conformational properties of molecules under investigation, whose effects are difficult to disentangle. To address this, conformational studies are conducted in the gas phase, enabling examinations of molecules in isolated, collision-free environments. The isolated gas phase investigation of molecules allows us to understand the inherent properties of molecules that are otherwise inaccessible.

Supersonic jets, combined with other spectroscopic techniques, offer an ideal collision-free environment for structural and conformational studies. Gas phase laser spectroscopic techniques, such as laser-induced fluorescence and double resonance techniques like UV-UV hole-burning spectroscopy, ion dip infrared and ultraviolet spectroscopy (IR-UV), are widely used for the investigation of biomolecules.[9] These techniques provide precise electronic and vibrational information, and can discriminate between conformers when used in conjunction with high-level ab initio calculations.[9] However, these gas phase laser spectroscopic techniques are applicable only to molecules containing a UV-chromophore in their structure.

Rotational spectroscopy, with its high resolution and sensitivity, is well suited for the characterisation of the three-dimensional structures of molecules in the gas phase. The molecular rotational spectroscopy technique is one of the most direct methods for determining the gas-phase structure of molecules due to its relationship with the molecular moments of inertia. The only requirement of the technique is that molecules must possess a permanent dipole moment.

The combination of rotational spectroscopy with different vaporisation techniques, including laser ablation, and breakthroughs such as the development of chirped pulse Fourier transform microwave (CP-FTMW) spectroscopy have made it possible to investigate a wide range of molecules. The investigation of biologically relevant molecules with microwave (MW) spectroscopy includes amino acids,[10–13] sugars,[14–16] and neurotransmitters.[17–19] The high sensitivity of the technique allows us to observe the isotopically substituted species of molecules in their natural abundance, enabling precise determination of molecular structures in the gas phase.[20–23] For example, an accurate gas-phase structure of a steroid hormone, estradiol (shown in Fig. 1.1 chemical analysis), could be determined from its ^{13}C isotopologues rotational spectra observed in natural abundance in the rotational spectroscopy experiments.[24]

Rotational spectroscopy, sensitive to minor structural changes, serves as a key experimental technique for discriminating among several conformers and isotopologues within a molecular system. One of the early milestones in conformational studies using MW spectroscopy dates back to 1962 when Hirota presented a potential energy surface featuring two isomers of propyl fluoride (C_3H_7F).[25] Real-time spectral analysis, on-the-fly graphical assignment, as well as automatic assignment and fittings in the present day have significantly accelerated the identification of numerous molecular species in multi-conformer spectra. The number of conformers that can be identified in the rotational spectra of complex, flexible molecules has significantly increased from three[26] or seven[27] to up to thirty[28]. The unambiguous identification of signatures of molecular components with high-resolution spectroscopy offers its utility as a chemical analysis tool, capable of identifying the chemical components of complex mixtures like essential oils, as illustrated in the chemical analysis part of Fig. 1.1.

MW spectroscopic studies provide valuable chemical insights into molecules, uncovering not just their conformational and tautomeric preferences, but also the intricacies of their intra- and intermolecular interactions. The conformational landscapes and structural configurations are influenced by a delicate balance of non-covalent intramolecular interactions occurring in the spatial vicinity of neighbouring atoms within the molecule. These interactions include various types such as hydrogen bonds, halogen bonds, $\pi \cdots \pi$ stacking, van der Waals interactions, etc. The spectroscopic investigations of serotonin[29] and strawberry aldehyde[21] serve as examples of how the interplay among intramolecular non-covalent interactions shape the conformational space of molecules. These non-covalent interactions not only characterise the structural preferences of small structural units but are also critical in maintaining the three-dimensional structure of large molecules, such as proteins, nucleic acids, and molecular complexes.

Biomolecular activities predominantly occur in aqueous environments, where water acts not just as a solvent but as an active participant, significantly influencing molecular structure and functionality. Understanding the role of the subtle non-covalent interaction forces responsible for solvation requires isolating molecules from the condensed phase environment (due to solvent effects), allowing for a gas-phase study with controlled hydration degrees. Such an environment, involving a limited number of water molecules interacting with another molecule (the solute) in isolation, is called microsolvation. MW spectroscopy employing a supersonic jet as a molecular source provides a valuable approach to investigate the initial steps of the hydration process, bridging the gap between the gas-phase and solution-phase behavior in microsolvated clusters. The complexes of different kinds of biologically important molecules with water have already been studied, contributing relevant information about solute-solvent interactions in those systems.[30, 31] Furthermore, it has also been shown that microsolvation may affect not only the structure of the solute[32] but also its conformational preferences, as observed for the 12-crown-4 ether.[33] Microsolvation studies of molecules help gain insights into the fundamental nature of intermolecular interactions and their influence on intramolecular interactions and conformational landscapes of structurally flexible molecules.

The information obtained from microwave spectra is multifaceted. The high resolution of rotational spectroscopy has been utilised to resolve tunneling splittings in the spectra resulting from large-amplitude internal motions, such as methyl and hydroxyl group internal rotation,[34–37] ammonia inversion,[38] and ring-puckering[39]. In the presence of solvent molecules, the line splittings of molecules are also influenced. Over the years, the scope of rotational spectroscopy has expanded from fundamental observations, such as structure determination and internal dynamics, to encompass intermolecular interactions within molecular aggregates, chiral recognition, and applications in astrochemistry, as shown in Fig. 1.1.[Chap 15, [40]] [41]

In the domain of radioastronomy, this technique plays a pivotal role in exploring the chemical composition of the interstellar medium. More than 300 different molecular species, including chiral molecules, free radicals, and polycyclic aromatic hydrocarbons (PAHs) (illustrated in the astrochemistry part of Fig. 1.1), have been identified in the interstellar medium (ISM) via radioastronomy through the observation and assignment of their rotational spectra.[42] The molecular detection in the data collected from radio observatories like the Atacama Large Millimeter/submillimeter Array (ALMA) and the Herschel space telescope relies on the analysed rotational spectra obtained in laboratories.[43–46] However, a limitation of rotational spectroscopy is the size of the molecule. Recent studies on larger molecules (including thioether ($C_{20}H_{30}S$) and androsterone ($C_{19}H_{30}O_2$)) highlight the challenges for the measurement and analysis of such large-size compounds and their complexes using this technique (shown in chemical analysis part of Fig. 1.1).[23, 47]

Most biomolecules are chiral, a characteristic that significantly impacts their structure and functionalities. The phenomenon of chirality is ubiquitous in nature and has intrigued chemists for over a century. The first significant step in comprehending chirality dates back to the 19th century when J. B. Biot discovered that organic substances in solution, like tartaric acid, could rotate the plane of linearly polarised light.[52] In 1848, Louis Pasteur successfully separated enantiomers by hand-picking individual crystals, conclusively illustrating the distinct properties of enantiomers.[53, 54] Since Pasteur's pioneering work, chirality has evolved into a crucial concept in stereochemistry and biochemistry.

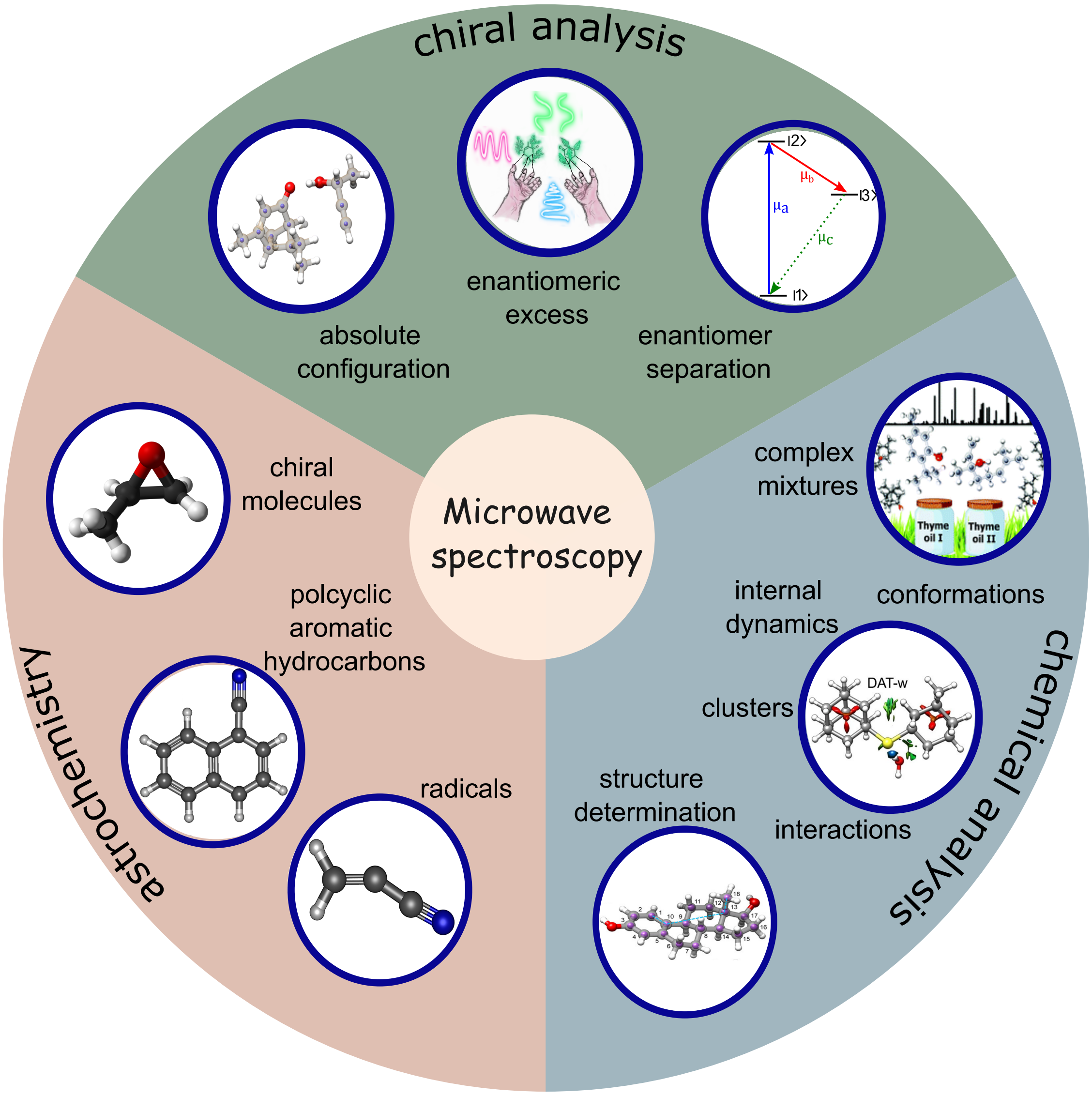

Figure 1.1: A glimpse of different applications of microwave spectroscopy. The pictures in this figure were used from the following references: [23, 24, 48–51].

The vast majority of organic, biological, and pharmacological compounds are chiral; they are encoded with a preferred handedness and thus have a stereoselective bias for specific chemical interactions. For instance, the left-handed enantiomer of the molecule carvone has the aroma of spearmint, while its right-handed counterpart emits the fragrance of caraway seeds (depicted in chiral analysis part of Fig. 1.1,). All living systems are selectively made of left-handed amino acids and right-handed sugars; this preference is called homochirality of life. Homochirality is considered to be a signature of life, and unravelling the mystery behind its origins is crucial for gaining insight into the origin of life. However, the origin of biological homochirality is a debated topic.[55, 56]

Enantiomers are energetically equivalent, except for a small difference due to the parity-violating character of the weak force. These enantiomers share almost identical physical properties, but they often exhibit different chemical and biochemical behaviours due to stereoselective biases. Thus, beyond the structural analysis, enantiomer differentiation and separation become key steps in understanding these enantiomer-based functionalities. In recent years, two distinct approaches, namely microwave three-wave mixing (M3WM) and chiral tagging (shown in the chiral analysis part of Fig. 1.1), have been developed for analysing chiral samples using rotational signatures. Chiral tagging capitalises on the well-established concept of non-covalently bound diastereomer formation, which is also the basis for chirality recognition. In chiral tag rotational spectroscopy, the sample of interest interacts with well-characterised chiral tag molecules to form weakly bound complexes, resulting in diastereomers that can be differentiated via their structure (chiral analysis part of Fig. 1.1).[57, 58]

M3WM relies on the mirror-image character of the electric dipole moment components of enantiomers. The difference in the sign of the triple product of the transition dipole moments of enantiomers ($\boldsymbol{\mu}_a[\boldsymbol{\mu}_b \times \boldsymbol{\mu}_c]$) results in a π radian phase difference between enantiomers in the free-induction decay.[59, 60] Both chiral tagging and M3WM techniques can be employed to determine the enantiomeric excess and absolute configuration of enantiomers in complex chiral mixtures.[58] In 2017, the M3WM technique was extended to achieve enantiomer-selective population transfer in gas-phase chiral samples.[61–63] The π phase difference between two enantiomers can be used to selectively enhance the population of one enantiomer in a particular rotational state while the population of the opposite enantiomer is depleted in this state but enhanced in the connecting state of the corresponding transition. The enantiomer shuffling with the tailored microwave pulses has allowed us to manipulate and control chirality in various types of chiral molecules.[50, 64, 65] The energetic separation of enantiomers that can be achieved with enantio-sensitive microwave spectroscopy is an important step towards spatial separation of enantiomers. On-the-fly generation of enantiomer separation demonstrated in recent M3WM-based experiments can facilitate advanced precision spectroscopy measurement, for example, aimed at detecting the frequency difference between the two enantiomers arising from the parity-violation effects.[66]

Historical highlights in the progress of microwave spectroscopy

The use of MW spectroscopy to investigate molecular properties has been an active area of research for more than seven decades. The emergence of MW spectroscopy followed World War II, fueled by the advancements in radar technology. Ammonia was the first molecule to be extensively studied with microwave spectroscopy.[67–69] The focused research on ammonia led to the development of the MASER (microwave amplification by stimulated emission of radiation), marking the first experimental demonstration of stimulated emission.[70, 71] During the 1940s, the widespread availability of oscillators and detectors led to the development of Stark[72] and Zeeman-modulators.[73] These instruments were based on the absorption signal, which is typically less sensitive, leading to the investigation of emission signals.[74] One of the drawbacks of both types of instruments was their operation at room temperature, resulting in the distribution of the molecular population over many rotational and vibrational states, which further results in less intense and more complex spectra.[75, 76]

A significant milestone in the field of MW spectroscopy occurred when W. H. Flygare combined Balle-Flygare time-domain spectroscopy with a Fabry-Perot cavity resonator and a supersonic jet.[77] In this setup, similar to the Fourier-transform nuclear magnetic resonance spectroscopy technique,[78] a pulse of radiation was used to excite the molecular transition, and the resulting molecular emission was collected as free-induction decay (FID). The time-domain FID signal was then Fourier transformed to produce the frequency spectrum. The high sensitivity and resolution from the Fabry-Perot cavity and low rotational temperatures due to the supersonic expansion populating mostly lower rotational states resulted in intense and simplified rotational spectra. The combination of these two techniques enabled the study of isolated weakly bound clusters in the microwave regime.[79, 80] The resolution of the instrument was further enhanced by J. U. Grabow and his colleagues through modifications to the Fourier transform microwave (FTMW) spectrometer's design, involving the coaxial arrangement of the molecular beam and the microwave field. These enhancements significantly improved the utility of the FTMW technique.[81] Two-dimensional MW spectroscopy was employed in conjunction with various spectrometer designs to elucidate coherence pathways, population transfer, and the interconnections between rotational energy levels.[82–85] The major constraint with the Balle-Flygare FTMW instrument was its operation in small bandwidths (1 MHz) per acquisition, requiring longer times to acquire a spectrum spanning over several GHz.

The advancement in digital electronics, particularly waveform generators and broadband signal digitisers, led to the development of CP-FTMW spectroscopy, adding a new dimension to the realm of rotational spectroscopy.[86] This technique enabled the collection of a rotational spectrum with a bandwidth of more than 10 GHz and with high resolution in a single microwave pulse of the spectrometer. The method facilitated the measurement of rotational spectra of large molecules and clusters[87, 88] with several gigahertz bandwidths within tens of microseconds. The data acquisition time and sample consumption were decreased by a factor of 100 and 30, respectively, compared to a cavity-based spectrometer.[86] Since then, several CP-FTMW spectrometers have been constructed in different frequency ranges with different applications.[89–96] The research article by Park *et al.* in 2016 highlighted the achievement of the CP-FTMW technique in its first decade.[97]

Outline of the thesis

The work described herein comprises the analysis of the rotational spectra of different organic molecules with increasing structural complexity using CP-FTMW spectroscopy and its extension to analyse chiral molecules. The chirped-pulse microwave spectrometer used for measurements is described in Chapter 3. Using the chirped-pulse microwave spectrometer, different organic molecules with increasing structural intricacy and flexibility are investigated. The exploration begins with the examination of the relatively rigid compounds from the [2,2]-paracyclophane ($C_{16}H_{16}$) family substituted with the following functional groups: hydroxy-, aldehyde-, ketone-, and carboxylic acid in Chapter 4. The intramolecular interactions within these derivatives of [2,2]-paracyclophane are then presented and extensively compared with similar molecules. Subsequently, in Chapter 5, a flexible chiral carboxylic acid α-methoxy phenylacetic acid ($C_9H_{10}O_3$) is explored. The influence of intramolecular interactions on the conformational space and methyl internal rotation barriers is discussed. Chapter 6 delves into the rotational spectrum of 6-amyl-α-pyrone ($C_{10}H_{14}O_2$), which, due to the presence of the amyl chain, exhibits greater flexibility compared to the α-methoxy phenylacetic acid and monosubstituted [2,2]-paracyclophanes. The conformational landscape of 6-amyl-α-pyrone features a more diverse array of minimum structures compared to the other two molecular systems. The rotational constants of the assigned calculated minimum structures are provided in the respective chapter.

In addition to the conformational analysis and the gas phase structure determination of flexible molecules using broadband MW spectroscopy, the extension of the M3WM approach was employed for enantio-sensitive manipulation of chiral molecules. Chapter 7 presents a general approach for the enhancement of enantioselective population transfer using solely microwave pulses. The high level of chiral control that could be achieved in the gas phase with this technique is demonstrated with trifluoromethyl oxirane ($C_3H_3F_3O$).

In chapter 8, a new non-linear and coherent microwave six-wave mixing approach is proposed for structurally flexible chiral molecules. The experimental demonstration showcases that the microwave six-wave mixing technique can be used to manipulate the handedness in a quantum racemic mixture of benzyl alcohol (C_7H_8O). The subsequent chapter provides an overview of the theoretical methods utilised in this study, including an explanation of the rotational Hamiltonian, the principle of the microwave three- and six-wave mixing approach and a brief introduction to quantum chemical methods.

Chapter 2

Theoretical background

Spectroscopy is the study of the interaction of light with matter.[98] Molecular spectroscopy is defined as the analysis of the interaction of molecules with electromagnetic radiation. The absorption, emission, or scattering of photons from different regions of the electromagnetic spectrum prompts different types of responses in molecules. For example, infrared radiation has photons with sufficient energy to induce vibrational motion in molecules, whereas microwave radiation induces molecular rotations.[98] Microwave radiation spans the 1 to 300 GHz frequency range of electromagnetic radiation and is invisible to the human eye. The interaction of the molecule with the microwave region causes the molecule's rotational energy to change, according to Planck's relation ($E = h\nu$, where h is Planck's constant and ν is the frequency). When the molecule interacts with radiation of the correct frequency, a quantum-mechanically allowed transition occurs, giving rise to a line-shaped absorption/emission signal corresponding to that frequency in the spectrum. These lines, or transitions, and their intensities are related to the structural properties of the molecule that can be calculated.

The interaction of electromagnetic radiation with matter can be understood using quantum mechanics. According to quantum mechanics, the energy levels of a system can be obtained by solving the time-independent Schrödinger equation:[98]

$$\hat{H}\psi = E\psi \tag{2.1}$$

where ψ is the wavefunction of the energy Hamiltonian operator $\hat{H}$, and E is its corresponding eigenvalue. For a molecule of N atoms and M electrons, the time-independent Schrödinger equation is:

$$\begin{aligned}&\hat{H}\psi_n(\mathbf{Q_1}, ..., \mathbf{Q_i}, ..., \mathbf{Q_N}, \mathbf{q_1}, ..., \mathbf{q_j}, ..., \mathbf{q_M})\\ &\qquad = E_n\psi_n(\mathbf{Q_1}, ..., \mathbf{Q_i}, ..., \mathbf{Q_N}, \mathbf{q_1}, ..., \mathbf{q_j}, ..., \mathbf{q_M}).\end{aligned} \tag{2.2}$$

Here, $\mathbf{Q_i}$ and $\mathbf{q_j}$ are vectors describing the position of the i-th nucleus and the j-th electron, respectively, while ψ_n and E_n represent the eigenfunctions and eigenvalues of the Hamiltonian operator $\hat{H}$, respectively. The Hamiltonian operator $\hat{H}$ denotes the energy operator, which is the sum of the kinetic energy ($\hat{T}$) and potential energy ($\hat{V}$) terms:[99]

$$\hat{H} = \hat{T} + \hat{V} = \hat{T}_{\text{nuc}} + \hat{T}_{\text{elec}} + \hat{V}_{\text{elec-elec}} + \hat{V}_{\text{elec-nuc}} + \hat{V}_{\text{nuc-nuc}}. \tag{2.3}$$

where $\hat{T}_{\text{nuc}}$, $\hat{T}_{\text{elec}}$ are the kinetic energy operators of nuclei and electrons, respectively. The potential energy part consists of Coulomb's repulsion term for electrons and nuclei ($\hat{V}_{\text{elec-elec}}, \hat{V}_{\text{nuc-nuc}}$), respectively, and Coulomb's attraction term between the positive and negative charges of nuclei and electrons ($\hat{V}_{\text{elec-nuc}}$).

Electronic motions in molecules takes place on time scales of 1 femtosecond which is faster than the vibrational motions occurring on timescales of 100 femstosecond.[99] Molecular rotations, on the other hand, take place on picosecond timescales.[99] These differences in the timescales of various electronic, vibrational, and rotational motions enable the separation of the distinct motions.

The Born-Oppenheimer approximation separates the electronic and nuclear motion by exploiting the fact that the nuclei are practically immobile during the fast electronic movement due to the larger mass of the nuclei compared to that of the electrons.[100] Within the Born-Oppenheimer approximation, the Hamiltonian can be evaluated for the electronic part with the nuclei at fixed positions, and the nuclear motion can be evaluated by using the averaged electronic potential obtained from the solution of the electronic part. The electronic structure is then solved as:

$$\hat{H}_{\text{elec}}\psi_{\text{elec}}(\mathbf{Q}, \mathbf{q}) = E_{\text{elec}}\psi_{\text{elec}}(\mathbf{Q}, \mathbf{q}) = (\hat{T}_{\text{elec}} + \hat{V}_{\text{elec-elec}} + \hat{V}_{\text{elec-nuc}})\psi_{\text{elec}}(\mathbf{Q}, \mathbf{q}) \tag{2.4}$$

where ψ_{elec} is the electronic wavefunction, which depends on the position of atoms and electrons.

The separation of electronic and nuclear motions within the Born-Oppenheimer approximation leads to the factorisation of the electronic and nuclear wave functions. The total wavefunction and molecular energy levels are expressed as follows:[99]

$$\psi = \psi_{\text{elec}}(\mathbf{Q}, \mathbf{q})\psi_{\text{nuc}}(\mathbf{Q}) \tag{2.5}$$

$$E = E_{\text{elec}} + E_{\text{nuc}} \tag{2.6}$$

Since the nuclei's movement during fast electronic motion is assumed to be negligible and they experience hardly any rotational motion during a vibrational period, the vibrational motion can be seen as occurring within an average electronic cloud.

Similarly, the rotational motion occurs at nuclear configurations corresponding to an average over the vibrational motion. Thus, the average contribution of the fast vibrational motions is included parametrically in the rotational part of the Hamiltonian. Therefore, the nuclear wavefunction can be further separated into the vibrational and the rotational motions. The total wavefunction then is:

$$\psi = \psi_{\text{elec}}(\mathbf{Q}, \mathbf{q})\psi_{\text{vib}}(\mathbf{Q})\psi_{\text{rot}}(\mathbf{q}) \tag{2.7}$$

and the overall energy of the molecular system can be written as:

$$E = E_{\text{elec}} + E_{\text{rot}} + E_{\text{vib}} \tag{2.8}$$

In this work, the focus is on the rotational energy of a system in the electronic and vibrational ground states. Thus, the rotational Hamiltonian and the corresponding time-independent Schrödinger equation in focus is:

$$\hat{H}_{\text{rot}}\psi_{\text{rot}} = E_{\text{rot}}\psi_{\text{rot}} \tag{2.9}$$

The subsequent section describes the theoretical aspects of rotational spectroscopy, discussing solutions for the time-independent Schrödinger equation for different classes of molecules and their selection rules. Following this discussion, the section explores centrifugal distortion effects, internal rotation in molecules, and use of rotational spectroscopy for determining molecular structures.

2.1 Rotational Spectroscopy

The rotational energy of a molecule, E_{rot}, can be evaluated using quantum mechanics by using the rigid rotor approximation in a similar way to classical mechanics.[101] In this approximation, the rotational energy of a molecule can be calculated using the following equation:[98]

$$E_{\text{rot}} = \frac{1}{2}\boldsymbol{\omega}^t\mathbf{I}\boldsymbol{\omega} = \mathbf{L}^t\mathbf{I}^{-1}\mathbf{L} \tag{2.10}$$

where $\boldsymbol{\omega}$ is the angular velocity, $\mathbf{I}$ is the moment of inertia tensor and $\mathbf{L}$ is the angular momentum. The inertia tensor of a rigid molecule has a significant contribution only from the nuclei due to their larger masses compared to the electrons. These nuclei can then be treated as point particles, each with mass m_i at coordinate $\mathbf{Q_i} = (x_i, y_i, z_i)$ in a molecular frame using Cartesian coordinates. The inertia tensor in this coordinate system can be represented as:

$$\mathbf{I} = \sum_{n=0}^{N} m_i \begin{pmatrix} y_i^2 + z_i^2 & -x_i y_i & -x_i z_i \\ -y_i x_i & x_i^2 + z_i^2 & -y_i z_i \\ -z_i x_i & -z_i y_i & x_i^2 + y_i^2 \end{pmatrix} = \begin{pmatrix} I_{xx} & I_{xy} & I_{xz} \\ I_{yx} & I_{yy} & I_{yz} \\ I_{zx} & I_{zy} & I_{zz} \end{pmatrix} \tag{2.11}$$

The inertia tensor **I** can be simplified by placing the origin of the axis system at the center of mass of the rotating body in such a way that the tensor becomes diagonal. This new molecular axis system is called the principal axis system, where the axes are denoted as a, b, and c, and it is unique for each rotating system.

In addition to the center of mass condition, the axis system is selected so that the diagonal elements of **I**, referred to as principal moments of inertia (I_a, I_b, I_c), are defined in increasing size as $I_a \leqslant I_b \leqslant I_c$. The Cartesian axis system (x, y, z) can be mapped to the principal axis system (a, b, c) in six possible ways, as tabulated in Table 2.1.

Table 2.1: Possible identification of principal axis system a, b, c with the Cartesian axes x, y, z resulting in six different representations. A prolate symmetric top or a slightly asymmetric prolate top is best described by the I^r representation, while the III^r representation is suitable to describe oblate symmetric top or slightly asymmetric oblate tops.

	I^r	I^l	II^r	II^l	III^r	III^l
x	b	c	c	a	a	b
y	c	b	a	c	b	a
z	a	a	b	b	c	c

The symmetry of a molecule can lead to the vanishing of one of its three moments of inertia or the equality of some of the three moments of inertia. Consequently, four distinct classifications need to be established to categorise molecules in rotational spectroscopy. Fig. 2.1 shows examples of four classes of molecules.

- **Linear top molecules** ($I_a = 0$ and $I_b = I_c$): These molecules belong to the $C_{\infty v}$ or $D_{\infty h}$ point groups. For example, carbon dioxide (CO_2) and carbonyl sulphide (OCS).

- **Spherical top molecules** ($I_a = I_b = I_c$): With all three moments of inertia equal to each other they belong to the cubic (O_h, T_d) or icosahedral (I_h) point group. Examples are methane (CH_4) and sulphur hexafluoride (SF_6).

- **Symmetric top molecules**: In this category, two moments of inertia are equal, and they possess either a $C_n (n > 2)$- or S_4-axis of symmetry. They can either be prolate or oblate tops.

  - Prolate tops ($I_a < I_b = I_c$): These molecules are cigar-shaped, with the symmetry axis of the molecule along the a-axis. Examples include chloromethane (CH_3Cl) and propyne (C_3H_4).
  - Oblate tops ($I_a = I_b < I_c$): They have a disc shape, and examples include ammonia (NH_3) and benzene (C_6H_6).

- **Asymmetric top molecules** ($I_a \neq I_b \neq I_c$): These molecules have all moments of inertia different and cover a wide range of molecules. Examples of these are water (H_2O) and phenol (C_6H_5OH).

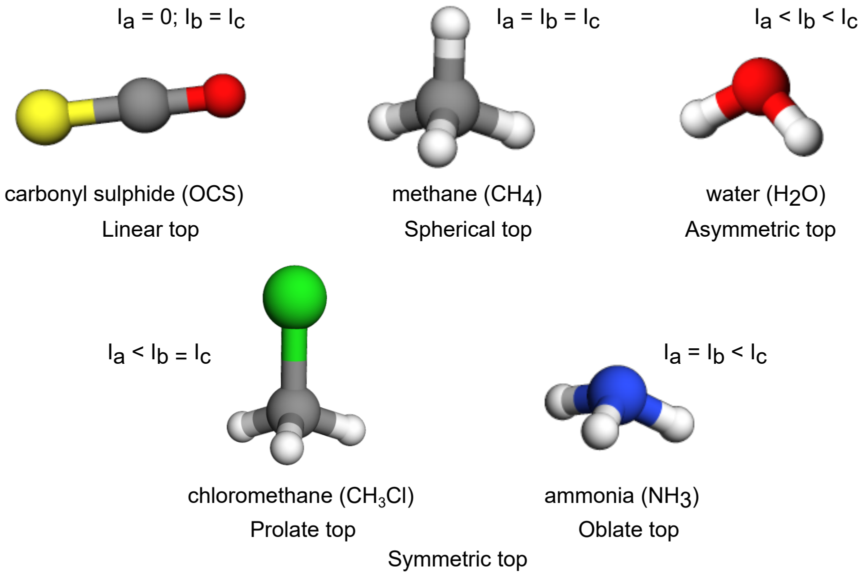

Figure 2.1: Examples of the four different classes of molecules depending on their symmetry.

This categorisation leads to different ways of calculating the energies of rotational levels and to varying patterns of transitions in the rotational spectra. In the principal axis system, the rotational energy assumes the form:

$$E_{\text{rot}} = \frac{1}{2}(I_a\omega_a^2 + I_b\omega_b^2 + I_c\omega_c^2) = \frac{L_a^2}{2I_a} + \frac{L_b^2}{2I_b} + \frac{L_c^2}{2I_c} \tag{2.12}$$

where L_a, L_b, and L_c are the components of the angular momentum along the respective principal axis and I_a, I_b, and I_c are the principal moments of inertia. The quantum mechanical energy can be derived from the classical mechanical version by introducing the angular momentum operator $\hat{\mathbf{J}}$. Eq. 2.13 presents the rigid-rotor Hamiltonian, where $\hbar$ represents the reduced Planck's constant ($\hbar = h/2\pi$):

$$\hat{H}_{\text{rig}} = \frac{\hat{\mathbf{J}}^2}{2\mathbf{I}} = \frac{1}{2}\left(\frac{\hat{J}_a^2}{I_a} + \frac{\hat{J}_b^2}{I_b} + \frac{\hat{J}_c^2}{I_c}\right) \tag{2.13}$$

with

$$\hat{\mathbf{J}} = \hat{\mathbf{r}} \times \hat{\mathbf{p}} = -i\hbar(\hat{\mathbf{r}} \times \nabla) \tag{2.14}$$

Here, $\hat{\mathbf{r}}$ and $\hat{\mathbf{p}}$ represent the position and momentum operators, respectively, and ∇ is the vector differential operator.

While a molecular axis system (x, y, z) effectively describes the internal movements of the electrons and the nucleus, it must be related to the laboratory frame (X, Y, Z) to determine the rotational energy of the molecule. Considering only the rotational motion, both coordinate systems coincide at the center of mass of the molecule. The relative orientation of these two coordinate systems is described by the three Euler angles θ, ϕ, and χ (see Fig. 2.2). The first two angles θ and ϕ are the polar and the azimuthal angles of the molecular z-axis in the laboratory frame (X, Y, Z), while χ describes the internal orientation of the molecule relative to the molecular z-axis. Both coordinate systems can be transformed by a direction cosine matrix described in reference [98]. The direction cosine matrix can be derived using the description of Euler angles as rotations along these axes:[[98], Chap. 6]

- rotation of X and Y by an angle of ϕ about Z.
- rotation of X' and Z by an angle of θ about Y'.
- rotation of X'' and Y' by an angle of χ about z.

The three components of the angular momentum operator $\hat{\mathbf{J}}$ in eq. 2.13 can be expressed in terms of the euler angles in the molecular axis system (x, y, z):[[98], Chap. 6]

$$\hat{J}_x = -i\hbar\left[\frac{-\cos\chi}{\sin\theta}\frac{\partial}{\partial\phi} + \frac{\cos\chi\cos\theta}{\sin\theta}\frac{\partial}{\partial\chi} + \sin\chi\frac{\partial}{\partial\theta}\right] \tag{2.15a}$$

$$\hat{J}_y = -i\hbar\left[\frac{\sin\chi}{\sin\theta}\frac{\partial}{\partial\phi} - \frac{\sin\chi\cos\theta}{\sin\theta}\frac{\partial}{\partial\chi} + \cos\chi\frac{\partial}{\partial\theta}\right] \tag{2.15b}$$

$$\hat{J}_z = -i\hbar\frac{\partial}{\partial\chi}. \tag{2.15c}$$

The corresponding expressions in the laboratory axis system (X, Y, Z) will be as follows:[[98], Chap. 6]

$$\hat{J}_X = -i\hbar\left[\frac{-\cos\phi\cos\theta}{\sin\theta}\frac{\partial}{\partial\phi} + \frac{\cos\phi}{\sin\theta}\frac{\partial}{\partial\chi} - \sin\phi\frac{\partial}{\partial\theta}\right] \tag{2.16a}$$

$$\hat{J}_Y = -i\hbar\left[\frac{-\sin\phi\cos\theta}{\sin\theta}\frac{\partial}{\partial\phi} + \frac{\sin\phi}{\sin\theta}\frac{\partial}{\partial\chi} + \cos\phi\frac{\partial}{\partial\theta}\right] \tag{2.16b}$$

$$\hat{J}_Z = -i\hbar\frac{\partial}{\partial\phi}. \tag{2.16c}$$

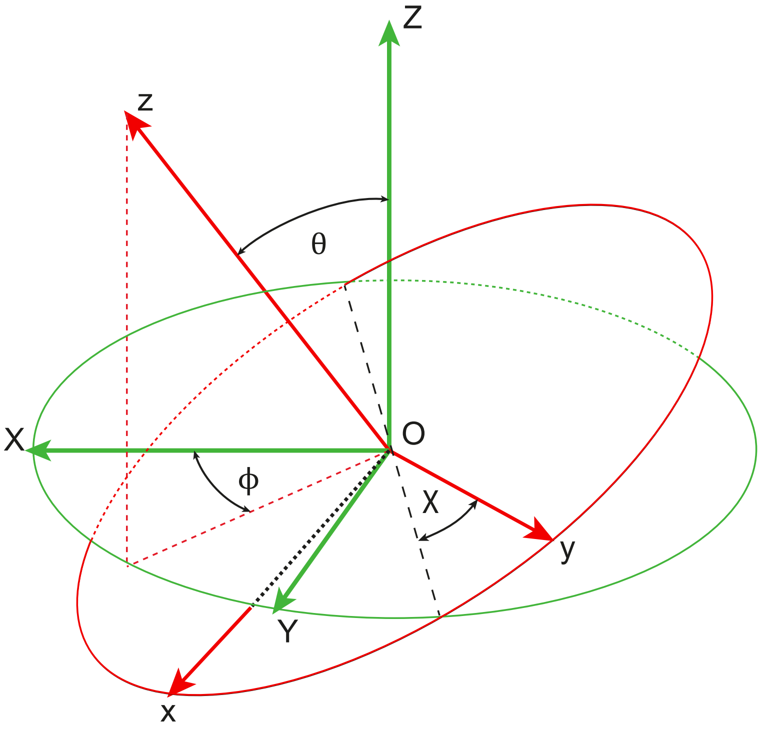

Figure 2.2: Illustration of Euler angles θ, ϕ, and χ that relate the orientation of laboratory frame coordinate system (X, Y, Z) to the molecular axis system (x, y, z). The figure is adapted from reference [98].

These angular momentum operators satisfy the following commutation relationships. Their components do not commute with each other but commute with the $\hat{\mathbf{J}}^2$ operator:[[98], Chap. 6]

$$[\hat{J}_x, \hat{J}_y] = -i\hbar\hat{J}_z, \tag{2.17a}$$

$$[\hat{J}_X, \hat{J}_Y] = i\hbar\hat{J}_Z, \tag{2.17b}$$

$$[\hat{\mathbf{J}}^2, \hat{J}_g] = 0, \quad g = x, y, z, \tag{2.17c}$$

$$[\hat{\mathbf{J}}^2, \hat{J}_G] = 0, \quad G = X, Y, Z, \tag{2.17d}$$

$$[\hat{J}_g, \hat{J}_G] = 0, \quad g = x, y, z \quad G = X, Y, Z, \tag{2.17e}$$

with

$$\hat{\mathbf{J}}^2 = \hat{J}_x^2 + \hat{J}_y^2 + \hat{J}_z^2. \tag{2.18}$$

According to the Heisenberg uncertainty principle, any two variables that do not commute cannot be measured simultaneously. Thus, only the operator $\hat{\mathbf{J}}^2$, one of the operators $\hat{J}_g$ and one of the operators $\hat{J}_G$ can be measured simultaneously. The projections of the total angular momentum on the z- and Z-axes, i.e., $\hat{J}_z$, $\hat{J}_Z$ operators are chosen in accordance with the spectroscopic literature. The z-axis is assigned to the principal axis with the highest symmetry using the appropriate representation in Table 2.1.

From quantum mechanics, commuting operators share a common set of eigenfunctions. Thus, a complete set of eigenfunctions denoted as $|JKM\rangle$ can be found for the operators $\hat{\mathbf{J}}^2$, $\hat{J}_z$, and $\hat{J}_Z$. The derivation of the wavefunction $|JKM\rangle$ is lengthy, but can be expressed in a closed form, as provided in references [98, 99]. The eigenvalues for the $\hat{\mathbf{J}}^2$, $\hat{J}_z$, $\hat{J}_Z$ operators can then be derived with the help of the commutation relation and the ladder operator $\hat{J}_\pm = \hat{J}_x \pm i\hat{J}_y$:[98, 102]

$$\hat{\mathbf{J}}^2|JKM\rangle = J(J+1)\hbar|JKM\rangle, \tag{2.19a}$$

$$\hat{J}_Z|JKM\rangle = M_J\hbar|JKM\rangle, \tag{2.19b}$$

$$\hat{J}_z|JKM\rangle = K\hbar|JKM\rangle, \tag{2.19c}$$

with quantum numbers:

$$\begin{gathered} J = 0, 1, 2, ... \\ K = -J, -J+1, ..., J-1, J \\ M_J = -J, -J+1, ..., J-1, J, \end{gathered}$$

where the quantum number J is a measure of the total angular momentum, and the quantum numbers K and M_J describe the projections of the total angular momentum operator onto the z- and Z-axis, respectively. This knowledge of the angular momentum operators and their corresponding eigenvalues can then be used to solve the rotational Hamiltonian for different classes of molecules. Because rotational transitions and the corresponding energy levels are mostly in the frequency ranges of MHz and GHz, the rotational Hamiltonian is usually expressed in units of frequency rather than units of energy in rotational spectroscopy. The rotational constants A, B, and C, in units of frequency and with $A \geqslant B \geqslant C$, are:

$$A = \frac{\hbar}{2I_a}, \quad B = \frac{\hbar}{2I_b} \quad C = \frac{\hbar}{2I_c} \tag{2.20}$$

The rotational Hamiltonian $\hat{H}_{\text{rig}}$ can be redefined in units of frequency:

$$\hat{\mathcal{H}}_{\text{rig}} = A\hat{\mathcal{J}}_a^2 + B\hat{\mathcal{J}}_b^2 + C\hat{\mathcal{J}}_c^2 \tag{2.21}$$

where the angular momentum operators are now unitless quantities with $\hat{\mathcal{J}}_g = \hat{J}_g/\hbar(g = (x, y, z, X, Y, Z))$ and $\hat{\mathcal{J}} = \mathbf{J}/\hbar$.

Linear top molecules are considered a special case of symmetric-top molecules with $A = 0$ and $B = C$. Thus, the rotational Hamiltonian in I^r representation gets reduced from eq. 2.21 to:

$$\hat{\mathcal{H}}_{rig} = B\hat{\mathcal{J}}^2 \text{ (Linear)} \tag{2.22a}$$

$$\mathcal{E}_{rig} = BJ(J+1) \tag{2.22b}$$

as $\hat{\mathcal{J}}_a = 0$ for a linear molecule.

The rotational Hamiltonian of a prolate symmetric-top molecule employing the I^r representation (for $B = C$ and with the principal axis a as the highest symmetry axis) is given as:

$$\hat{\mathcal{H}}_{\text{rig}} = A\hat{\mathcal{J}}_a^2 + B(\hat{\mathcal{J}}_b^2 + \hat{\mathcal{J}}_c^2) = B\hat{\mathcal{J}}^2 + (A - B)\hat{\mathcal{J}}_a^2 \quad \text{(prolate)}, \tag{2.23}$$

while for an oblate symmetric top we use the III^r representation (where $A = B$), then the rotational Hamiltonian takes the form:

$$\hat{\mathcal{H}}_{\text{rig}} = B\hat{\mathcal{J}}^2 + (C - B)\hat{\mathcal{J}}_c^2 \quad \text{(oblate)}. \tag{2.24}$$

It is important to note that the choice of representation does not impact the eigenstates and eigenfunctions. However, assigning the z-axis to the principal axis with the highest symmetry greatly simplifies the computation of the Hamiltonian.

In the case of a symmetric top, the Hamiltonian is a function of the $\hat{\mathcal{J}}^2$ and $\hat{\mathcal{J}}_z^2$ operators. Consequently, the eigenfunctions of the angular momentum, represented as $|JKM\rangle$, also serve as eigenfunctions of the symmetric-top Hamiltonian, and the eigenvalues are given as $\mathcal{E}_{\text{rig}}$. These corresponding energy levels are $(2J+1)$ degenerate in M_J and twofold degenerate in K in the absence of any external field. The energy eigenvalues for symmetric-top molecules are independent of the M_J quantum number as given below:[98]

$$\mathcal{E}_{\text{rig}} = BJ(J+1) + (A-B)K_a^2 \qquad \text{(prolate)} \tag{2.25a}$$

$$\mathcal{E}_{\text{rig}} = BJ(J+1) + (C-B)K_c^2 \qquad \text{(oblate)}, \tag{2.25b}$$

where K_a^2 and K_c^2 are described in the next paragraph. The rigid-rotor Hamiltonian for an asymmetric top cannot be solved analytically since $\hat{\mathcal{J}}_z$ does not commute with $\hat{\mathcal{H}}_{rig}$. But it can be solved numerically by choosing the appropriate representation such as I^r and III^r representations for near-prolate $(A \gg B > C)$ and near-oblate $(A > B \gg C)$ asymmetric tops, respectively. The rotational Hamiltonian for asymmetric top is determined by knowing their asymmetry, which is measured by Ray's asymmetry parameter, κ, and depends on the rotational constants of the molecules.[98]

$$\kappa = \frac{2B - A - C}{A - C} \tag{2.26}$$

A molecule is considered as fully asymmetric when $\kappa = 0$. As the value of κ approaches -1 or +1, the molecules are identified as prolate $(B = C)$ or oblate symmetric $(A = B)$ top respectively (depicted in Fig. 2.3). The asymmetric top Hamiltonian employing the I^r representation gives the following non-vanishing elements for the energy matrix:[99]

$$\langle JKM|\hat{\mathcal{H}}_{\text{rig}}|JKM\rangle = \frac{1}{2}(B+C)(J(J+1) - K^2) + AK^2 \tag{2.27}$$

$$\begin{aligned}\langle JKM|\hat{\mathcal{H}}_{\text{rig}}|JK \pm 2M\rangle &= \\ &\frac{1}{2}(B-C)\sqrt{(J(J+1) - K(K \pm 1))(J(J+1) - (K \pm 1)(K \pm 2))}\end{aligned} \tag{2.28}$$

Here, K is not a suitable quantum number anymore for labelling the energy levels for an asymmetric top. Thus, two pseudo-quantum numbers K_a and K_c using the King-Hainer-Cross notation $(J_{K_aK_c})$ are introduced.[103] They denote the limiting cases of prolate and oblate symmetric-top molecules, respectively (shown in Fig. 2.3). The energy-level ordering can also be extracted from the K_a and K_c values: $K_a - K_c$ difference gives the position in the energy-level ordering ranging from $-J$ to $+J$. This energy level scheme for an asymmetric top molecule is illustrated in Fig. 2.3.

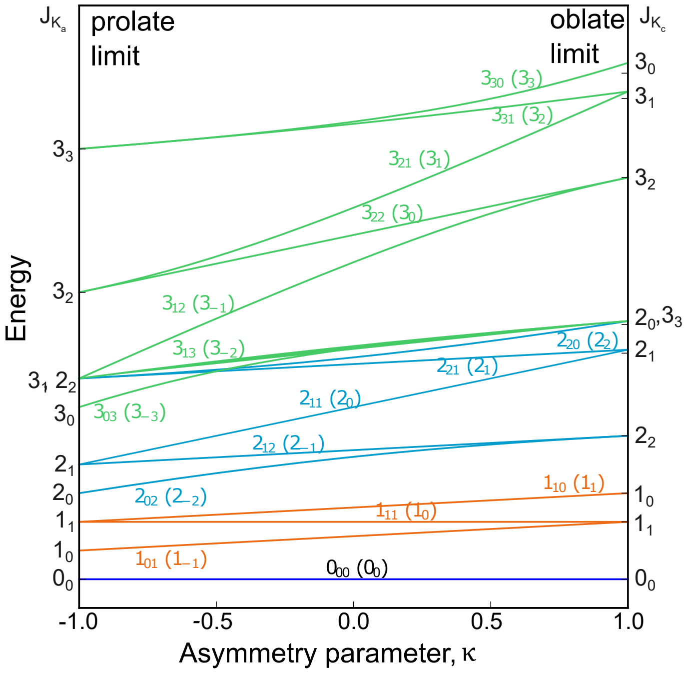

Figure 2.3: Rotational energy levels of an asymmetric-top molecule. On the left, the quantum numbers for the prolate symmetric top are given and the right y-axis shows the quantum numbers for the oblate top limit case. The asymmetric-top energy levels are labelled using two different schemes: the King-Hainer-Cross notation $J_{K_aK_c}$ and labelling J_τ, where $\tau = K_a - K_c$ ranges between $-J$ and J and represents the energy ordering of a certain energy level within a J-stack. The energy levels are not to scale. The figure is adapted from reference [101, 104].

2.1.1 Selection rules

The rotational Hamiltonian discussed above gives us information on the energy for the rotational levels, but it does not provide information on whether a transition is allowed or forbidden. A rotational transition is permitted if the transition dipole moment integral is non-vanishing.

$$\langle J'K'M'|\hat{\mu}_\alpha|J"K"M"\rangle \neq 0. \tag{2.29}$$

Here $\hat{\mu}_\alpha(\alpha = a, b$, or $c)$ is the projection of the electric dipole moment on the principal axes. The integral is non-vanishing when $J" = \pm 1$. Therefore rotational transitions are only allowed for $\Delta J = 0, \pm 1$. The transitions with $\Delta J = -1$, and $+1$ constitute the P- and R-branch, while $\Delta J = 0$ forms the Q-branch transitions.

Due to the high degree of symmetry, spherical tops cannot be studied by MW spectroscopy as they lack an overall permanent electric dipole moment. Taking the transition dipole moments into account, the selection rules for pure rotational spectra are:[98]

- Linear tops:

$$\Delta J = \pm 1 \qquad \Delta M_J = 0, \pm 1$$

- Symmetric tops:

$$\Delta J = \pm 1 \qquad \Delta M_J = 0, \pm 1 \qquad \Delta K = 0$$

- Asymmetric tops:

$$\Delta J = 0, \pm 1 \qquad \Delta M_J = 0, \pm 1.$$

In asymmetric tops, $\Delta M_J = 0$ is forbidden for Q-branch (i.e., $\Delta J = 0$) transitions.[105] The non-vanishing dipole moment components along the principal axes in the case of asymmetric tops give rise to an additional set of selection rules for the pseudo-quantum number K_a and K_c. These rotational transitions can be classified into three different types based on which principal axis induces the rotation and which dipole moment component $\boldsymbol{\mu} = (\mu_a, \mu_b, \mu_c)$ is responsible for the rotation as summarised in Table 2.2.

Table 2.2: Different types of rotational transitions in an asymmetric top molecule and their selection rules for the pseudo quantum numbers K_a and K_c.

rotational transition type	dipole	ΔK_a	ΔK_c
a-type	μ_a	0, ±2, ...	±1, ±3, ...
b-type	μ_b	±1, ±3, ...	±1, ±3, ...
c-type	μ_c	±1, ±3, ...	0, ±2, ...

2.1.2 Centrifugal distortion effects

In the previous section, rigid rotor approximation was used to calculate the rotational energy of molecules. However, in reality, real molecules are not rigid and undergo distortions due to various factors such as molecular vibrations, internal rotations, and centrifugal forces which distort their equilibrium geometry. Since vibrations occur on a much faster timescale than the rotation of a molecule, they can be parametrically included in the Hamiltonian. Thus, in practice, a different set of rotational constants is used for each normal vibrational mode. On the other hand, internal rotation and centrifugal distortion alter the angular momentum of the molecule, and they cannot be treated as effectively as vibrational motions. The theory for internal rotation is covered in the next section, while the effects of centrifugal distortion are discussed here.

The energy attributed to centrifugal distortion constitutes only a minor portion of the overall rotational energy. Therefore, these effects can be adequately addressed by including higher-order terms of the angular momenta in the rigid rotor Hamiltonian.[106][[101], Chap. 8]

$$\hat{\mathcal{H}}_{\mathrm{cd}} = \hat{\mathcal{H}}_{\mathrm{rig}} + \frac{\hbar^4}{4} \sum_{\alpha\beta\gamma\delta} \tau_{\alpha\beta\gamma\delta} \hat{\mathcal{J}}_\alpha \hat{\mathcal{J}}_\beta \hat{\mathcal{J}}_\gamma \hat{\mathcal{J}}_\delta + O(6) + \cdots , \tag{2.30}$$

where α, β, γ and δ can take any value of x, y, and z in the molecular-axis system. The parameters $\tau_{\alpha\beta\gamma\delta}$ are related to the force constants within a molecule. This means that weak bonds will have smaller force constants and the bonds will exhibit more deviation from their equilibrium values compared to the stronger bonds.[107] The sum in eq. 2.30 will have 81 components (3^4), but Watson demonstrated that due to symmetry properties and commutation relations, these 81 components can be reduced to five determinable linear combinations of fourth-order corrections.[101, 108] Watson proposed two possible combinations of the terms giving rise to A (asymmetric) and S (symmetric) reduced Hamiltonian. The A-reduction scheme is best suited for most of the asymmetric-top molecules, while the S-reduced Hamiltonian is most suited for symmetric and slightly asymmetric-top molecules.

In Watson's A reduction scheme, the rotational Hamiltonian includes the five quartic centrifugal distortion coefficients Δ_J, Δ_{JK}, Δ_K, δ_J, and δ_K:[[101], Chap. 8]

$$\begin{aligned}\hat{\mathcal{H}}^{(A)}_{\text{cd}} =& \frac{1}{2}(B^{(A)}+C^{(A)})\hat{\mathcal{J}}^2 + \left[A^{(A)} - \frac{1}{2}(B^{(A)}+C^{(A)})\right]\hat{\mathcal{J}}_z^2 + \frac{1}{2}(B^{(A)}-C^{(A)})(\mathcal{J}_x^2-\mathcal{J}_y^2) - \\ & \Delta_J\mathcal{J}^4 - \Delta_{JK}\mathcal{J}^2\mathcal{J}_z^2 - \Delta_K\mathcal{J}_z^4 - 2\delta_J\mathcal{J}^2(\mathcal{J}_x^2-\mathcal{J}_y^2) + \delta_K\left[\mathcal{J}_z^2(\mathcal{J}_x^2-\mathcal{J}_y^2) + (\mathcal{J}_x^2-\mathcal{J}_y^2)\mathcal{J}_z^2\right] \\ & + O(6) + \cdots ,\end{aligned} \tag{2.31}$$

where Δ_J is always positive since it already has a negative sign included in the rotational Hamiltonian (eq. 2.31). The quartic distortion constants have typically much smaller values than the rotational constants (A, B, C) by three to six orders of magnitude, but they become crucial for high-resolution measurements and rotational spectra with high J and K states. The rotational constants are influenced by the order of the correction and the type of reduction employed, denoted by the superscript in the Hamiltonian (eq. 2.31). The complete S-reduction Hamiltonian with the corresponding energy matrix elements is provided in reference [[101], Chap. 8].

The effect of centrifugal distortion on the observed spectra is to shift the rotational transitions to a lower frequency from the values predicted for a rigid rotor. The effects are usually within a few kHz for transitions with $J \leqslant 10$, but are more significant (in order of MHz or more) for higher J transitions.[109] The main advantage of centrifugal distortion terms lies in their ability to provide a more accurate description of the rotational Hamiltonian. It is also possible to estimate the dissociation energies of complexes from the centrifugal distortion effects as reported by Gou *et al.*[110, 111]

2.1.3 Internal rotation

Some flexible molecules exhibit line splittings in their rotational spectrum as a result of large amplitude motion (LAM). These LAMs encompass internal rotation (like methyl group internal rotation in α-methoxy phenylacetic acid);[34] inversion;[38] ring-puckering;[39] proton tunneling[112]. LAMs with an amplitude on the order of a bond length convert the molecule from one equivalent configuration to another configuration via tunneling. Typically, these motions arise from shallow double or multi-well potentials and result from coupling between conventionally well-isolated vibration and rotational degrees of freedom in molecules. Such motions connect several equivalent structures in the potential energy well, which results in interaction between localised states and the formation of a new set of eigenstates, lifting the energy degeneracy.

The present work explores the LAM arising from the internal rotation of a methyl group (CH_3), which has a C_3-symmetry. Due to this symmetry, the rotation of the methyl top results in three equivalent minima and another three equivalent transition states in the potential energy surface along the internal rotation coordinate of the methyl top (Fig. 2.4). The internal rotation Hamiltonian for a methyl group rotation with potential barrier V(α) is given as:[[101], Chap. 12]

$$\hat{H}\psi(\alpha) = \left[-F\frac{\partial^2}{\partial\alpha^2} + V(\alpha)\right]\psi(\alpha) = E\psi(\alpha), \tag{2.32}$$

where α is the angle of the internal rotation and F is the reduced rotational constant for the methyl top. Due to the symmetry properties of the methyl top, the methyl internal rotation is $2\pi/3$ periodic. Thus, the potential $V(\alpha)$ can be expanded in the following way:

$$V(\alpha) = \frac{V_3}{2}(1 - \cos 3\alpha) + \frac{V_6}{2}(1 - \cos 6\alpha) + \cdots \tag{2.33}$$

The V_3 and V_6 terms represent the three-fold and six-fold barriers, respectively. Usually, in the first approximation to solve the problem, only the first term is considered, as V_3 term is dominating ($V_3 \gg V_6$), and higher-order terms are neglected. In the scope of this thesis, only three-fold barriers are considered. The shape of such potential is illustrated in Fig. 2.4. The internal rotation Hamiltonian (eq. 2.32) for only a three-fold barrier gets reduced to:

$$\hat{H}\psi(\alpha) = \left[-F\frac{\partial^2}{\partial\alpha^2} + \frac{V_3}{2}(1 - \cos 3\alpha)\right]\psi(\alpha) = E\psi(\alpha). \tag{2.34}$$

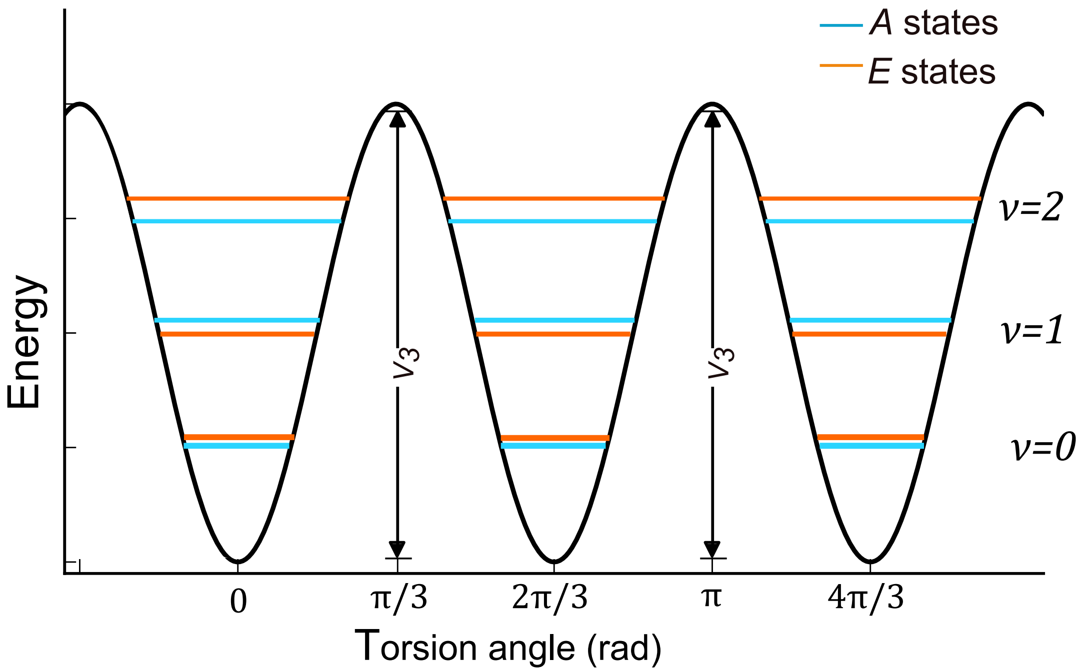

Figure 2.4: Schematic representation of the potential energy function of an internal rotor with C_{3v}-symmetry. The levels are labelled according to their torsional quantum number v. The torsional sublevels are denoted as A and E in blue and orange, respectively.

The above rotational Hamiltonian can be solved analytically for two limiting cases:

- Very low barriers : $V_3 \rightarrow 0$ (free rotation, Fig. 2.5)
  The eigenfunctions (${\psi_m}^{(0)}(\alpha)$) and energy eigenvalues (${E_m}^{(0)}$) for this case have the following form: [[101], Chap. 12]

$$ {\psi_m}^{(0)}(\alpha) = A_m e^{im\alpha} \tag{2.35} $$

$$ {E_m}^{(0)} = Fm^2, \tag{2.36} $$

  where the quantum number m can be 0, ±1, ±2, $\cdots$ due to the ${\psi_m}^{(0)}(\alpha) = {\psi_m}^{(0)}(\alpha + 2\pi)$ boundary conditions. The free rotor states given by quantum number m, are doubly degenerate except for the state m=0.

- Very high barriers: $V_3 \rightarrow \infty$ (infinite barrier, Fig. 2.5)
  In this case, the internal rotation involves only small oscillations within the potential well so the potential can be expanded in $\cos 3\alpha$ around small values of α in a Taylor series:[[101], Chap. 12]

$$ \cos 3\alpha = 1 - \frac{9}{2}\alpha^2 + \frac{27}{8}\alpha^4 + ... \tag{2.37} $$

> If the expansion is truncated after the quadratic term (α^2), the well-known harmonic oscillator wavefunctions serve as a solution for the rotational Hamiltonian, which gives the following energy eigenvalues:[[101], Chap. 12]
>
> $$E_v{}^{(\infty)} = \sqrt{3V_3F}\left(v + \frac{1}{2}\right) \tag{2.38}$$
>
> where v can take integer values 0, 1, 2,... And the energy depends on the v quantum number. Each of the vibrational sublevels is now triply degenerate, which corresponds to independent vibrations in each well of the potential.

For an intermediate barrier, tunnelling through the barrier becomes possible, causing the triply degenerate vibrational sublevels to split into a non-degenerate level labelled A (with the quantum number $\sigma = 0$) and doubly degenerate levels denoted with the symmetry label E (with the quantum number $\sigma = \pm 1$). The new quantum number σ defines the symmetry of the corresponding torsional wavefunction. The Schrödinger equation for such a barrier is solved by using the Mathieu equation,[113] for which the solutions are given by the Fourier series:[[101], Chap. 12]

$$\varphi_{v\sigma}(\alpha) = |v\sigma\rangle = \sum_{k=-\infty}^{\infty} A_k^{(v)} e^{i(3k+\sigma)\alpha}. \tag{2.39}$$

The calculated eigenvalues and the coefficients $A_k^{(v)}$ are described in reference [[101], Chap. 12]. Fig. 2.5 shows the energies of the internal rotor as a function of the barrier height V_3. As V_3 approaches 0, the energies are doubly degenerate and match the energy of the free rotor. Conversely, for $V_3 \to \infty$, the energies become threefold degenerate and converge with the energies of a harmonic oscillator.

The splitting of energy levels into A and E components causes each transition to appear as a doublet (or A-E splittings) in the spectrum. The spacing between the two components in the spectrum depends on the V_3 barrier height and on the mass of the rotating group. An additional selection rule arises for the methyl group internal rotation, where only transitions between states of the same symmetry are permitted: $A \leftarrow A$, $E \leftarrow E$.

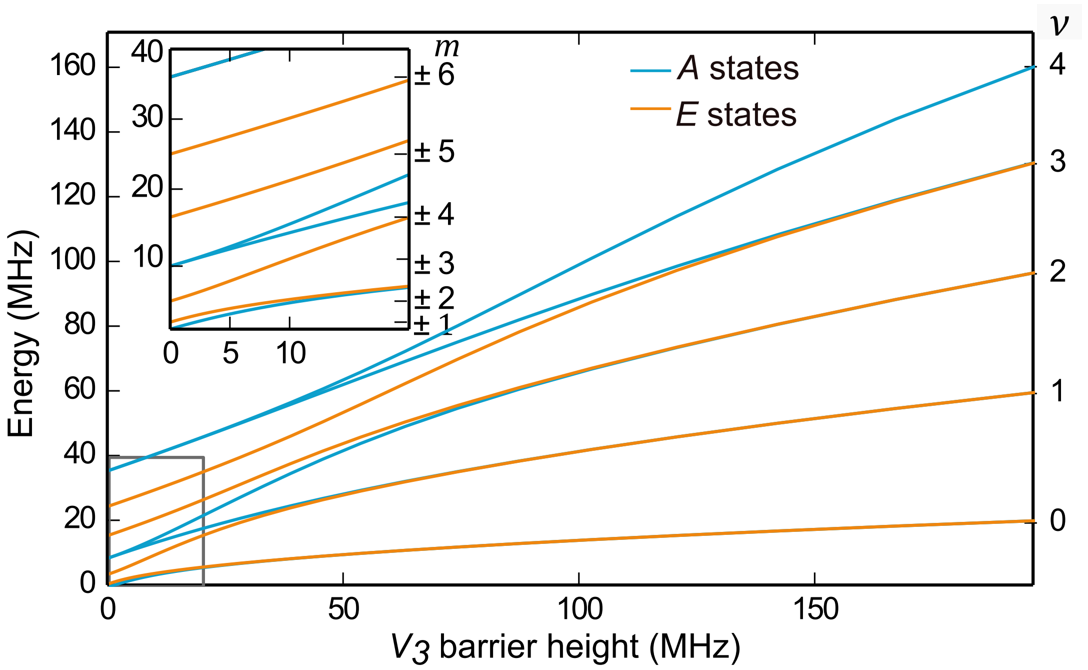

Figure 2.5: The energy levels of a methyl rotor as a function of the barrier height of V_3, with the reduced rotation constant $F = 160$ GHz. The energies are twofold degenerate in the limit $V_3 \rightarrow 0$, coinciding with the energies of a free rotor (quantum number m, eq. 2.36), as seen in the inset. Conversely, as $V_3 \rightarrow \infty$, the energies become threefold degenerate, converging to the energies of a harmonic oscillator (quantum number v, eq. 2.38). The figure is adapted from reference [104].

2.1.4 Molecular structure

MW spectroscopy is one of the most widely applicable and accurate methods for structure determination. The structure information is encoded in the principal moments of inertia I_a, I_b, and I_c, which are derived from the rotational constants A, B, and C. It is not possible to determine a complete molecular structure just from the rotational constants of the parent molecule: additional information from isotopologues is necessary. The high sensitivity of MW spectroscopy allows for the observation of rare isotopic species in their natural abundances. The most commonly observed isotopes are ^{13}C (1.1% relative to the ^{12}C), ^{15}N (0.4% of ^{14}N), ^{18}O (0.2% of ^{16}O) with sufficient signal-to-noise ratio (SNR). In some cases, if SNR is not enough, isotopically enriched samples can be used. Each isotopologue has a unique set of rotational constants as a result of the change in moment of inertia on the isotopic substitution of the nuclei in the molecule. There are two methods of constructing structures using the isotopic data: the effective structure and the substitution structure.[114, 115]

2.1.4.1 Equilibrium structure

The equilibrium structure, r_e, represents the distance between the nuclei with hypothetical vibrationless effects and corresponds to a minimum energy structure in the potential energy surface. The equilibrium rotational constants and the rotational constants in different vibrational states are correlated by:

$$A_e = A_\nu + \sum_i^{3N-6} \alpha_i(\nu_i + \frac{d_i}{2}), \quad B_e = B_\nu + \sum_i^{3N-6} \alpha_i(\nu_i + \frac{d_i}{2}) \quad C_e = C_\nu + \sum_i^{3N-6} \alpha_i(\nu_i + \frac{d_i}{2}) \tag{2.40}$$

where α_i are the rotation-vibration interaction constants and d_i accounts for the vibrational degeneracy.[[101], Chap. 13] The r_e structure is hard to obtain directly from experiments but can be obtained for diatomics, triatomics, and a few symmetric molecules.

2.1.4.2 Effective structure

The effective structure of a molecule represents the structure in a certain vibrational state.[116] In the majority of MW spectroscopy structures, the effective structure is determined for the ground vibrational state, and thus, is called r_0 structure. In this method, the structural parameters such as bond lengths, bond angles, and dihedral angles are fit in a least-squares manner to get a good agreement with the experimentally obtained rotational constants for all the available isotopic species. During the fitting procedure, certain structural parameters can be kept fixed at constant values if their coordinates are already known or fixed to calculated values. In this thesis, the STRFIT program was used to determine the effective structure of the molecule.[117]

2.1.4.3 Substitution structure

The substitution structure, r_s, is based on the changes in the moments of inertia upon isotopic substitution assuming that the internuclear distances are unchanged upon substitution. This structure determination method is based on the application of Kraitchman equations.[118] The moments of inertia of the parent molecule (I_a, I_b, I_c) and the isotopologue (I'_a, I'_b, I'_c) in the principal axis system can then reveal the coordinates of the substituted atom. The Kraitchman equations for determining the coordinates of the atom in asymmetric top molecules are:[[101], Chap. 13]

$$|a| = \left[\frac{\Delta P_a}{\mu}\left(1+\frac{\Delta P_b}{I_a - I_b}\right)\left(1+\frac{\Delta P_c}{I_a - I_c}\right)\right]^{1/2} \tag{2.41}$$

$$|b| = \left[\frac{\Delta P_b}{\mu}\left(1+\frac{\Delta P_c}{I_b - I_c}\right)\left(1+\frac{\Delta P_a}{I_b - I_a}\right)\right]^{1/2} \tag{2.42}$$

$$|c| = \left[\frac{\Delta P_c}{\mu}\left(1+\frac{\Delta P_a}{I_c - I_a}\right)\left(1+\frac{\Delta P_b}{I_c - I_b}\right)\right]^{1/2} \tag{2.43}$$

where P_i are the planar moments of inertia, which can be defined for each i as:

$$P_a = \frac{1}{2}(I_b + I_c - I_a), \quad P_b = \frac{1}{2}(I_c + I_a - I_b), \quad P_c = \frac{1}{2}(I_a + I_b - I_c). \tag{2.44}$$

The reduced mass for the isotopic substitution, μ is given by:

$$\mu = \frac{M\Delta m}{M + \Delta m} \tag{2.45}$$

where M is the total mass of the molecule and Δm is the change in mass as a result of isotopic substitution. The change of the moments of inertia upon isotopic substitution leads to a partial cancellation of the rovibrational contribution. The r_s structure gives an intermediate structure between the effective structure, r_0 and the equilibrium structure, r_e. The r_s method gives only the absolute values for each atomic coordinate as shown in eq. 2.41-2.43. Thus, further information on signs for the coordinates of each atom is obtained from a priori assumptions on the molecular structure, for instance from quantum-chemical calculations. The method can yield imaginary coordinates when the substituted atom is close to or on an inertial axis. In those cases, coordinates are assigned to be zero with respect to the relevant axes. The coordinates of the isotopically substituted atoms are calculated in this way with the KRA programme in this thesis.[117] The experimental gas-phase structure can then be built atom by atom.

2.2 Quantum-chemical calculations

The advancements in computational capabilities coupled with the development of efficient numerical methods and approximations have made it possible to perform increasingly accurate quantum-chemical calculations on increasingly large molecules. Spectroscopic parameters such as rotational constants and dipole moment components, obtained through quantum-chemical calculations, are used to assist in the assignment of rotational spectra. The following section gives a brief description of the quantum-chemical methods used to optimise structures and to obtain their energy and rotational parameters, in this work. All the calculations were performed with the ORCA 4.2 program suite.[119, 120]

Most of the molecules presented in this work are flexible and offer a rich conformational space. The presence of multiple functional groups in flexible molecules results in a non-trivial landscape of possible conformations. To efficiently navigate and explore this conformational space, CREST (Conformer-Rotamer Ensemble Sampling Tool) program was used.[121] CREST utilises metadynamics simulations in conjunction with the semiempirical tight-binding quantum mechanical method GFN-xTB (short for Geometries, vibrational Frequencies, and Noncovalent interactions-eXtended Tight Binding).[121–123]. In this work, CREST was used as an automated conformational search tool to explore and screen the low-energy chemical structures by generating a conformational ensemble with significant computational efficiency. The screened structures in an energy window of 6 kcal/mol were further refined by optimising their geometries using density functional theory (DFT), as shown in Fig. 2.6.

Structural optimisations were performed with the B3LYP functional within the DFT functional. The B3LYP (Becke's three-parameter, Lee-Yang-Parr) functional is a hybrid functional, which uses a linear combination of the exact Hartree-Fock functional with the electron-electron and exchange-correlation to describe the system.[124, 125]
A further correction was made for dispersion correction (D3) along with Becke-Johnson (BJ) damping to better account for intramolecular dispersion interactions.[126, 127] Additional single-point energy calculations were also performed with the wavefunction based coupled cluster singles doubles perturbative triple (CCSD(T)) method coupled with the domain-based local pair natural orbital (DLPNO) method.[128–132] Coupled-cluster-based methods like DLPNO-CCSD(T) are known for high accuracy and reasonable computational cost in computing the reliable energies of molecules.[133]

Two different basis sets, def2-TZVP and aug-cc-pVTZ, were employed to model the orbitals of the molecules. The def2-TZVP basis set represents a polarized triple zeta basis set, where def stands for default in TURBOMOLE 2.0[134, 135] and TZVP stands for valence triple-ζ polarization. On the other hand, augmented-cc-pVTZ (augmented-correlation-consistent polarized valence-only Triple-ζ) is a Dunning-type basis set that includes correlation correction polarized valence triple ζ functions and is augmented by diffuse functions[136]. The Dunning-type basis set was used with the DLPNO-CCSD(T) method, while def2-TZVP was employed with the B3LYP-D3(BJ) method.

The optimised structures were then checked for real minima structures and accounted for zero-point corrected energies through harmonic frequency calculations. Systematic dihedral scans were performed to explore the interconversion pathways of conformers and determine methyl internal rotation barriers. To understand the intramolecular interactions stabilising the conformers and characterise different forces in the molecular systems, wavefunction files were generated by Atoms In Molecules (AIM)[137] calculations in ORCA. These files were used for making non-covalent interaction (NCI) plots[138] to visualise the attractive and repulsive type interactions present in the molecular systems.

The optimised structures were visualised and analysed using UCSF Chimera[139] and MOLDEN[140] graphical programs, allowing for the examination of molecular structures and related data such as bond distances, bond angles, and dihedral angles as well as NCI plots.

2.3 Spectral analysis

The optimised geometries of conformers and the subsequent comparison of their predicted rotational parameters such as rotational constants and electric dipole moment components with the experimental ones is a good guide to conformation assignment. The PGOPHER program was used for simulating and fitting molecular spectra.[141] The initial assignments of structures were performed in PGOPHER using a recurrent fit based on Watson's A reduction Hamiltonian (as mentioned in eq. 2.31 in section 2.1) in I^r representation. These initially fitted rotational parameters were refined using the SPFIT/SPCAT suite of programs developed by Pickett.[142]

The CORSCL program was used to obtain the rotational constants of monosubstituted isotopologues of the molecule. Isotopic data were subsequently used for experimental structure determination by using the KRA program (KRAitchman structure, r_s substitution structure) and STRFIT (STRucture FITing, r_0 structure) program.[117] Line splittings due to methyl internal rotational were fitted using the XIAM program as developed by Hartwig and Dreizler.[143, 144] All of these spectral fitting programs except PGOPHER are listed and available on the Programs for ROtational SPEctroscopy (PROSPE) website, providing a comprehensive toolkit for spectral analysis and structure determination.[117] The conformational analysis was supported with self- and group-written Python scripts that were also written for sorting conformations based on their relative energies and rotational parameters. Fig. 2.6 provides a workflow for the conformational and experimental analysis performed in part I of the thesis.

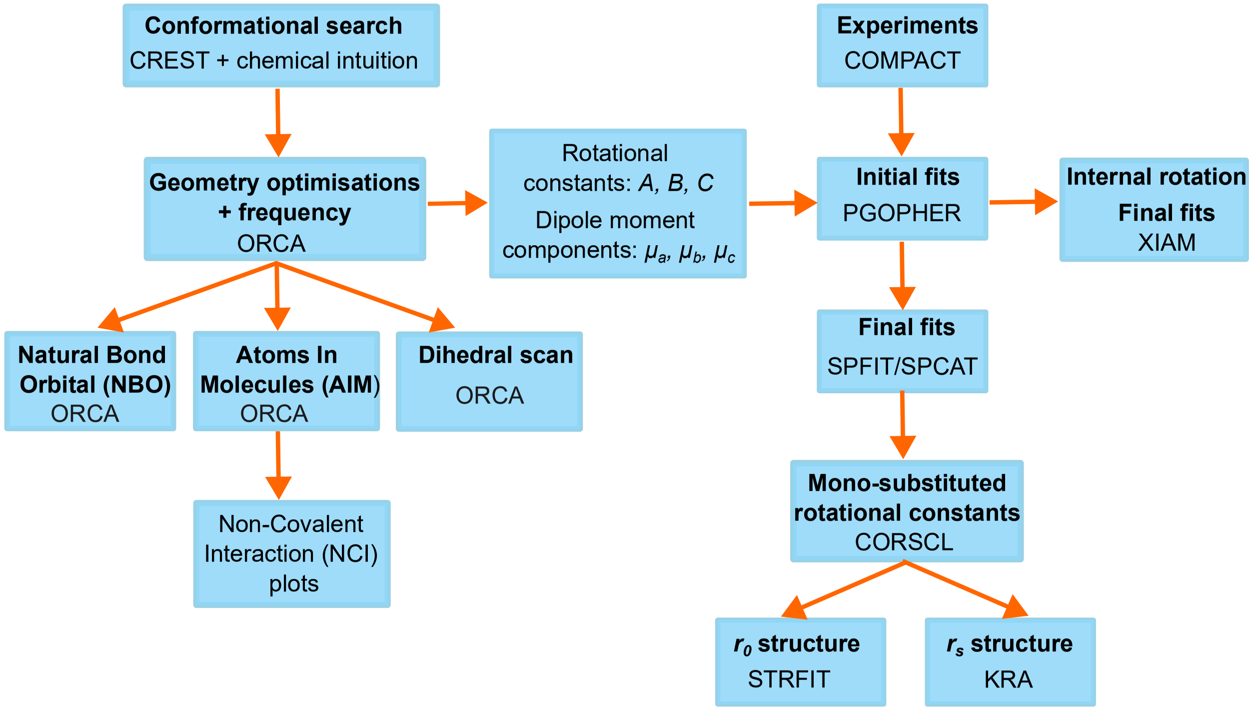

Figure 2.6: Workflow of quantum-chemical calculations and experimental analysis. Rotational spectra were recorded with the CP-FTMW spectrometer detailed in Chapter 3. In parallel, rotational parameters were obtained from quantum-chemical calculations performed at the B3LYP-D3(BJ)/def2-TZVP level of theory using the ORCA program package. These parameters were then used to find the molecular species in the rotational spectrum. Some additional calculations are performed to calculate the interconversion barriers or wavefunction files to make the non-covalent interaction plots.

2.4 Microwave three-wave mixing

The subsequent section discusses how rotational spectroscopy can be extended for chiral analysis. Broadband rotational spectroscopy cannot differentiate between the mirror images, i.e., enantiomers of chiral molecules, due to their nearly identical rotational constants and magnitudes of electric dipole moment components. However, recent advancements in the field of rotational spectroscopy have enabled us to differentiate enantiomers and study various types of chiral molecules. Two different approaches have been developed for analysing chiral molecules using rotational spectroscopy: M3WM and microwave chiral tagging (Fig. 1.1).[57, 60]

In the microwave chiral tagging method, the sample of interest interacts with a known enantiomer of a chiral tag molecule, forming weakly bound complexes that result in diastereomers with distinguishable structures and thus different rotational constants.[57, 145] By conducting two different types of measurements, one with a racemic sample of the chiral tag molecule and another one with an enantio-enriched sample of known handedness for the tag, the excess enantiomer of the unknown sample, as well as its corresponding enantiomeric excess, can be determined with impressive statistical accuracy.[51, 58, 146]

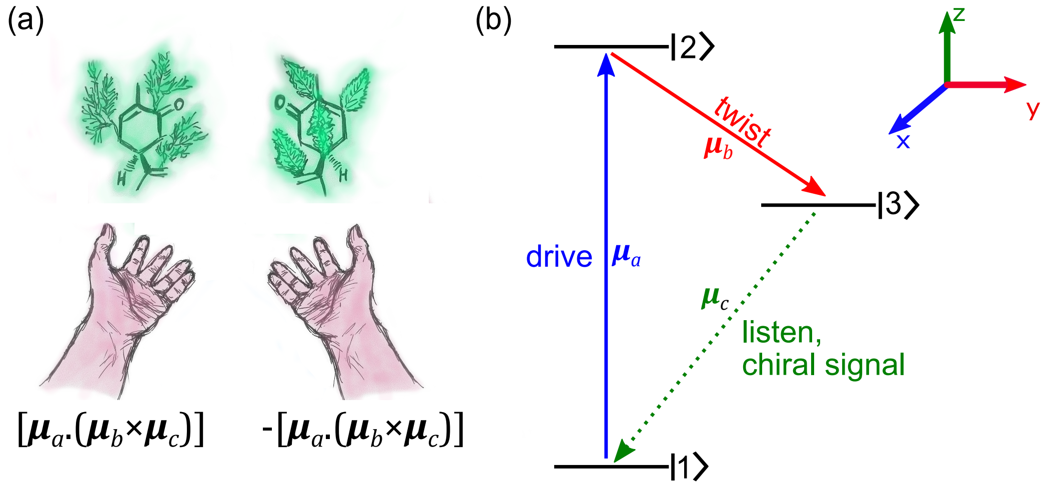

Figure 2.7: (a) The signs of the triple product of transition dipole moments of enantiomers are opposite. (b). A generalised microwave three-wave mixing scheme consisting of drive transition, twist transition, and listen signal. Three states $|1\rangle$, $|2\rangle$, and $|3\rangle$ are connected by, e.g., a-type (blue), b-type (red) and c-type (green) transitions. M_J sublevels are omitted here for clarity.

M3WM on the other side is a coherent, non-linear, resonant approach to differentiate enantiomers and can additionally be applied to control and manipulate chiral molecules.[60–62, 65] This work focuses on the application of M3WM in manipulating chiral molecules.

Even though the enantiomeric pair has the same rotational constants and dipole moment component magnitudes, the scalar triple product of the transition dipole moments $\boldsymbol{\mu}_a$, $\boldsymbol{\mu}_b$, and $\boldsymbol{\mu}_c$ flips signs between enantiomers since the dipole moments are mirrored, as depicted in Fig. 2.7(a).[147]

$$[\boldsymbol{\mu}_a \cdot \big(\boldsymbol{\mu}_b \times \boldsymbol{\mu}_c\big)]_R = -[\boldsymbol{\mu}_a \cdot \big(\boldsymbol{\mu}_b \times \boldsymbol{\mu}_c\big)]_S \tag{2.46}$$

This fact is exploited to differentiate enantiomers by a combined resonant excitation of rotational energy levels that are connected by a-, b-, and c-type dipole-allowed transitions in a M3WM approach.[59, 60] The scheme consists of a closed loop of three rotational transitions involving all three transition dipole moments ($\boldsymbol{\mu}_a$, $\boldsymbol{\mu}_b$, and $\boldsymbol{\mu}_c$) as shown in Fig. 2.7(b). In an excitation and detection scheme, the two transitions of a closed loop are excited simultaneously or sequentially (Fig. 2.10(a)), and the signal of the third transition (called as listen transition) is recorded, where the molecule itself is acting as a sum or difference frequency generator. The FID of the recorded signal at the frequency of the listen transition has a phase difference of π radians between opposite enantiomers and allows for their differentiation.

For any chiral molecule to be investigated with M3WM, it needs to satisfy the following condition:

- The molecule should be an asymmetric rotor, as this type of molecule has the components of the electric dipole moment along all the three principal axes of inertia: a, b, and c. All three dipole moment components of the molecule should be non-zero, i.e., $\mu_a \neq 0$, $\mu_b \neq 0$, $\mu_c \neq 0$).

In the subsequent section, a two-level system coupled by an external resonant electromagnetic field is described as the main model for the interaction of molecules with external radiation. This model will then be used to elucidate the concept of M3WM as detailed in section 2.4.2.[*]

---

[*] The theory in the upcoming sections is based on the work done by Dr. Denis Tikhonov, which is yet to be published.

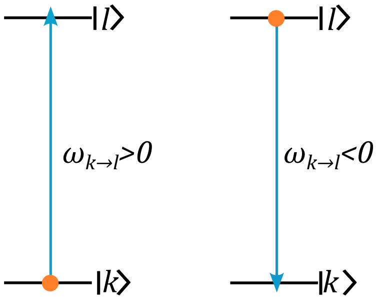

Figure 2.8: Two-level system with $|k\rangle$ and $|l\rangle$ transition. $|k\rangle$ is the initial state of the system.

2.4.1 Two-level system

The discussion in this section is focused on the interaction of molecules with electromagnetic fields by considering the two-level system. The unperturbed molecular Hamiltonian $\hat{\mathcal{H}}_0$ has two stationary states $|n\rangle$, for which the solutions of the Schrödinger equation are:

$$\hat{\mathcal{H}}_0|n\rangle = \hbar\omega_n|n\rangle \tag{2.47}$$

where $\hbar\omega_n$ is the energy of the state $\Big|n\rangle$. To account for interaction, the unperturbed rotational Hamiltonian is extended by the time-dependent interaction term $\hat{V}(t)$, which is defined as:

$$\hat{V}(t) = -\boldsymbol{\mu}\cdot\mathbf{E}_0\cos(\omega t+\varphi). \tag{2.48}$$

Here $\hat{V}(t)$ is the operator for interaction energy with $\omega = 2\pi\nu$ as the angular frequency of the pulse and phase φ. Any arbitrary time-dependent wavefunction for two states $|m\rangle$ and $|n\rangle$ can be written as:[148]

$$|\psi(t)\rangle = \sum_n c_n\cdot\exp(-i\omega_n t)|n\rangle \tag{2.49}$$

where c_n is the time-dependent coefficient of the expansion. The initial state of the system before the interaction is provided by the coefficient ${c_n}^{(0)} = c_n(0)$ at $t = 0$ and the time evolution of the state after the interaction for time duration τ ($t = \tau + t' \geqslant \tau$) is described as:

$$|\psi(t)\rangle = \sum_n c_n(\tau)\cdot\exp(-i\omega_n\tau)\cdot\exp(-i\omega_n t')|n\rangle. \tag{2.50}$$

After the electromagnetic wave passes, there will be a new set of initial condition coefficients $\Big\{c_n(\tau)\cdot\exp(-i\omega_n\tau)\Big\}_n$. The time-dependent Schrödinger equation has the form:

$$-i\hbar\frac{\partial}{\partial t}|\psi\rangle = \hat{\mathcal{H}(t)}|\psi\rangle = \hat{\mathcal{H}}_0|\psi\rangle + \hat{V}(t)|\psi\rangle \tag{2.51}$$

On substituting the wavefunction $|\psi(t)\rangle$, defined in eq. 2.49, into the previous equation, it simplifies to:

$$\begin{aligned} i\hbar \sum_n \dot{c_n} \exp(-i\omega_n t)\langle m|n\rangle &= \sum_n c_n \cdot \exp(-i\omega_n t)\langle m|\hat{V}(t)|n\rangle \\ &= -\sum_n c_n \cdot \mathbf{E}_0 \cdot \exp(-i\omega_n t)\cdot\cos(\omega t + \varphi) \cdot \langle m|\hat{\boldsymbol{\mu}}|n\rangle \end{aligned} \tag{2.52}$$

here $\langle m|\hat{\boldsymbol{\mu}}|n\rangle = \boldsymbol{\mu}_{mn}$ are the transition dipole moments, which is assumed to be real ($\boldsymbol{\mu}_{mn} = \boldsymbol{\mu}_{nm}$). The transition dipoles to the same states are zero, i.e., $\boldsymbol{\mu}_{mm} = 0$ this simplifies the eq. 2.52 to:

$$i\dot{c_n} = -\sum_n \Omega_{|n\rangle\to|m\rangle} \cdot \exp(i\omega_{|m\rangle\to|n\rangle} t) \cdot \cos(\omega t + \varphi) \cdot c_n \tag{2.53}$$

where $\Omega_{|m\rangle\to|n\rangle}$ is defined as the Rabi frequency, ($\Omega_{|m\rangle\to|n\rangle} = \Omega_{|n\rangle\to|m\rangle}$):

$$\Omega_{|m\rangle\to|n\rangle} = \frac{\boldsymbol{\mu}_{mn} \cdot \mathbf{E}_0}{\hbar}, \tag{2.54}$$

with the transition angular frequencies as

$$\omega_{|m\rangle\to|n\rangle} = \omega_m - \omega_n = \frac{E_m - E_n}{\hbar} = 2\pi\nu_{|m\rangle\to|n\rangle}, \tag{2.55}$$

that are related to the normal transition frequencies $\nu_{|k\rangle\to|l\rangle}$. The eq. 2.53 can be used to model the interaction of the molecule with a single frequency pulse in time $0 \leqslant t \leqslant \tau$.

When the pulse is resonant with one of the transitions, the angular frequency of the pulse is equal to the transition frequency. $\omega = |\omega_{|k\rangle\to|l\rangle}| = |\omega_{|l\rangle\to|k\rangle}|$, as shown in the two-level system in Fig. 2.8. In the rotating-wave approximation (RWA), the non-resonant terms that give rise to fast oscillations can be neglected. On applying the RWA, the two cases of $\omega_{|k\rangle\to|l\rangle} > 0$ ($E_k < E_l$) and $\omega_{|k\rangle\to|l\rangle} < 0$ ($E_k > E_l$) (illustrated in Fig. 2.8) will then be described by:

$$i\dot{c_k} \approx -\frac{\Omega_{|l\rangle\to|k\rangle}}{2} \exp\left(+is_{k\to l}\varphi\right) \cdot c_l \tag{2.56a}$$

$$i\dot{c_l} \approx -\frac{\Omega_{|l\rangle\to|k\rangle}}{2} \exp\left(-is_{k\to l}\varphi\right) \cdot c_k \tag{2.56b}$$

where $s_{k\to l} = \operatorname{sign}\left(\omega_{|k\rangle\to|l\rangle}\right)$, meaning $s_{|k\rangle\to|l\rangle} = 1$ if $\omega_{|k\rangle\to|l\rangle} > 0$ and $s_{|k\rangle\to|l\rangle} = -1$ if $\omega_{|k\rangle\to|l\rangle} < 0$.

The eqs. 2.56a and 2.56b of the two-level system are exactly solvable, and the complete solution for them is:

$$c_k(t) = \cos\left(\frac{\Omega_{|l\rangle\to|k\rangle}}{2}t\right) \cdot {c_k}^{(0)} - i\exp(+is_{k\to l}\varphi)\sin\left(\frac{\Omega_{|l\rangle\to|k\rangle}}{2}t\right) \cdot {c_l}^{(0)} \tag{2.57a}$$

$$c_l(t) = \cos\left(\frac{\Omega_{|l\rangle\to|k\rangle}}{2}t\right) \cdot {c_l}^{(0)} - i\exp(+is_{k\to l}\varphi)\sin\left(\frac{\Omega_{|l\rangle\to|k\rangle}}{2}t\right) \cdot {c_k}^{(0)}. \tag{2.57b}$$

This two-level model can describe the evolution of the multistate system driven by the resonant pulses and will be used in the next sections on three-level system and enantiomer-selective population transfer.

The resonant excitation of a system induces a macrosopcic dipole moment, this observable is given by the polarisation operator, $\hat{\mathbf{P}}$. For the two-level system ($|k\rangle - |l\rangle$), the polarisation operator $\hat{\mathbf{P}}_{kl}$ depends on the dipole moment operator and the coherence between the two states $|k\rangle$ and $|l\rangle$. The induced polarisation from initial states $|k\rangle$ and $|l\rangle$ at time $t+\tau$, will be the same but opposite in phase.

$$\langle\psi_k|\hat{\mathbf{P}}_{kl}|\psi_k(t+\tau)\rangle = -\boldsymbol{\mu}_{kl} \cdot \sin\left(\Omega_{|k\rangle\to|l\rangle}\tau\right) \cdot \sin\left(\omega_{|k\rangle\to|l\rangle}t + \omega_{|k\rangle\to|l\rangle}\tau + \varphi\right) \tag{2.58a}$$

$$\langle\psi_l|\hat{\mathbf{P}}_{kl}|\psi_l(t+\tau)\rangle = \boldsymbol{\mu}_{kl} \cdot \sin\left(\Omega_{|k\rangle\to|l\rangle}\tau\right) \cdot \sin\left(\omega_{|k\rangle\to|l\rangle}t + \omega_{|k\rangle\to|l\rangle}\tau + \varphi\right) \tag{2.58b}$$

where $|\psi_k\rangle$ and $|\psi_l\rangle$ are the solution for states $|k\rangle$ and $|l\rangle$ with initial conditions ($c_k^{(0)} = 1$ and $c_l^{(0)} = 0$) and ($c_l^{(0)} = 1$ and $c_k^{(0)} = 0$), respectively. The induced macroscopic dipole moment is directly proportional to the population difference between the two states:

$$\begin{aligned}\langle\mathbf{P}_{kl}\rangle &= N_l\langle\psi_l|\hat{\mathbf{P}}_{kl}|\psi_l\rangle + N_k\langle\psi_k|\hat{\mathbf{P}}_{kl}|\psi_k\rangle \\ &= -(N_k - N_l)\boldsymbol{\mu}_{kl} \cdot \sin(\Omega_{|l\rangle\to|k\rangle}\tau) \cdot \sin(\omega_{|k\rangle\to|l\rangle}t + \omega_{|k\rangle\to|l\rangle}\tau + \varphi).\end{aligned} \tag{2.59}$$

where N_k and N_l are the number of molecules in state $|k\rangle$ and $|l\rangle$, respectively.

In experiments, the resulting macroscopic dipole moment is measured in a specific direction, say $\mathbf{n}_1$, then the measured signal intensity is given as:

$$\begin{aligned}I_{\text{obs}} \propto \Big(\mathbf{n}_1 \cdot \langle\mathbf{P}_{kl}\rangle\Big) = -(N_k - N_l) \cdot (\mathbf{n}_1 \cdot \boldsymbol{\mu}_{kl}) \cdot \sin(\Omega^{\max}_{|l\rangle\to|k\rangle}\cos(\theta)\tau) \cdot \\ \sin(\omega_{|k\rangle\to|l\rangle}t + \omega_{|k\rangle\to|l\rangle}\tau + \tilde{\varphi}),\end{aligned} \tag{2.60}$$

where $\tilde{\varphi}$ denotes the phase of the pulse and $\Omega^{max}_{|l\rangle\to|k\rangle}$ is the condition of maximum Rabi frequency. The Rabi frequency (eq. 2.54) depends not only on the electric field but also on the orientation of molecules in space. The orientational dependence of the Rabi frequency is because the electric field inducing the transition must have a well-oriented dipole moment.

$$\Omega_{|k\rangle\to|l\rangle} = \frac{\boldsymbol{\mu}_{kl}\cdot\mathbf{E}_0}{\hbar} = \frac{\overbrace{\mu_{kl}\cdot E_0}^{\Omega^{\max}_{|k\rangle\to|l\rangle}}}{\hbar}\cdot(\overbrace{\mathbf{n}_{|k\rangle\to|l\rangle}\cdot\mathbf{n}_0}^{\cos\theta}), \tag{2.61}$$

Here $E_0 = (\mathbf{E}_0 \cdot \mathbf{n}_0)$ and $\mu_{kl} = (\boldsymbol{\mu}_{kl} \cdot \mathbf{n}_{|l\rangle\to|k\rangle})$ are the electric field polarisation and transition dipole moment with $\mathbf{n}_0$ and $\mathbf{n}_{|k\rangle\to|l\rangle}$ directions, respectively, in the laboratory frame. At $\theta = 0°$, the condition for maximum Rabi frequency given as $\Omega^{\max}_{|l\rangle\to|k\rangle}$ is satisfied.

In experiments, the rotational transition for a two-level system is optimised by measuring its so-called nutation curve. The nutation curve represents the signal intensity of the rotational transition monitored as a function of different pulse durations. Each of the rotational transitions can be optimised for a maximum signal either by varying the electric field strength or the pulse duration. Varying electric field strength can be more complicated than optimising the pulse duration, so the pulse duration of each transition of the pulse sequence is optimised in the experiments. Each rotational transition can be optimised for either a $\pi/2$ or π condition.

$$\Omega_{|k\rangle\to|l\rangle}\cdot\tau = \frac{\boldsymbol{\mu}_{kl}\cdot\mathbf{E}_0}{\hbar}\tau = \frac{\pi}{2} \text{ or } \pi \tag{2.62}$$

Density-matrix formalism

Another approach to describe the interaction of a two-level system with the resonant radiation is using the density-matrix formalism introduced by von Neumann. The mixed quantum states can be described best with the density-matrix formalism. A thorough treatment of this formalism is detailed in reference [149] and only the main results and properties are stated here. The diagonalised density operator is defined as:

$$\hat{\rho} = \sum_n p_n |\psi_n\rangle\langle\psi_n|, \tag{2.63}$$

where p_n is the probability of encountering a single quantum system of the mixture in the state $|\psi_n\rangle$. This operator can also be expressed in a matrix representation using a convenient set of n basis sets.[149] This density matrix is a $n \times n$ Hermitian matrix with a $tr(\rho)$ =1, i.e., the sum of all the diagonal elements is one. The diagonal elements of the matrix indicate the probability of finding the system in the respective state, while the off-diagonal elements describe the coherences between the two states. The density matrix encapsulates all information about the statistical ensemble, including the expectation values of observables, which are given by the trace of the product of the observable operator with the density matrix ($\langle\hat{O}\rangle = \mathrm{Tr}(\hat{\rho}\hat{O})$). The density matrix operator for states $|k\rangle$ and $|l\rangle$ mentioned in Fig. 2.8 is denoted as:

$$\hat{\rho} = \begin{pmatrix} \rho_{kk} & \rho_{kl} \\ \rho_{lk} & \rho_{ll} \end{pmatrix} \tag{2.64}$$

and the Hamiltonian operator describing the unperturbed system is given by:

$$\hat{\mathcal{H}}_0 = \begin{pmatrix} E_k & 0 \\ 0 & E_l \end{pmatrix} \tag{2.65}$$

The time evolution of the density matrix $\hat{\rho}$ is governed by the Neumann equation:

$$i\hbar\frac{\partial\hat{\rho}(t)}{\partial t} = \left[\hat{\mathcal{H}}(t), \hat{\rho}(t)\right] \tag{2.66}$$

with $\hat{\mathcal{H}(t)} = \hat{\mathcal{H}}_0 + \hat{V}(t)$ (eqs. 2.48, 2.51) The time evolution of the Neumann equation yields:

$$\begin{aligned} \dot{\rho}_{kk} &= i\Omega\cos\omega t(\rho_{lk} - \rho_{kl}) && \text{(2.67a)} \\ \dot{\rho}_{ll} &= -i\Omega\cos\omega t(\rho_{lk} - \rho_{kl}) && \text{(2.67b)} \\ \dot{\rho}_{kl} &= i\omega_0\rho_{kl} - i\Omega\cos\omega t(\rho_{ll} - \rho_{kk}) && \text{(2.67c)} \\ \dot{\rho}_{lk} &= -i\omega_0\rho_{kl} + i\Omega\cos\omega t(\rho_{ll} - \rho_{kk}) && \text{(2.67d)} \end{aligned}$$

with the Rabi frequency Ω (eq. 2.61). The frequency ω_0 is the resonant frequency of the two-level system. Before the time evolution of the density matrix is derived, the Hamiltonian can be simplified by applying the RWA, that is, nonresonant terms are eliminated. The resulting simplified equations are called optical Bloch equations and are given as:

$$\begin{aligned} \dot{\rho}_{kk} &= i\frac{\Omega}{2}(\rho_{lk}e^{i\omega t} - \rho_{kl}e^{-i\omega t}) && \text{(2.68a)} \\ \dot{\rho}_{ll} &= -i\frac{\Omega}{2}(\rho_{lk}e^{i\omega t} - \rho_{kl}e^{-i\omega t}) && \text{(2.68b)} \\ \dot{\rho}_{kl} &= -i\delta\rho_{kl} - i\frac{\Omega}{2}e^{i\omega t}(\rho_{ll} - \rho_{kk}) && \text{(2.68c)} \\ \dot{\rho}_{lk} &= i\delta\rho_{kl} + i\frac{\Omega}{2}e^{-i\omega t}(\rho_{ll} - \rho_{kk}), && \text{(2.68d)} \end{aligned}$$

with the detuning $\delta = \omega - \omega_0$. The time dependence of these density matrix elements of a two-level system can be visualised using Bloch vector $\mathbf{R} = (u, v, w)$:[150]

$$\mathbf{R} = \begin{pmatrix} u \\ v \\ w \end{pmatrix} = \begin{pmatrix} \rho_{kl} e^{i\omega t} + \rho_{lk} e^{-i\omega t} \\ i(\rho_{kl} e^{i\omega t} - \rho_{lk} e^{-i\omega t}) \\ \rho_{kk} - \rho_{ll} \end{pmatrix} \tag{2.69}$$

which lies inside the Bloch sphere depicted in Fig. 2.9. The north and south poles of the Bloch sphere represent the two states $|k\rangle$, $|l\rangle$, respectively. The vertical component w corresponds to the population difference of the two-level system.

The temporal evolution of the vector $\mathbf{R}$ is then given by:

$$\frac{\partial \mathbf{R}}{\partial t} = \mathbf{\Lambda} \times \mathbf{R} \tag{2.70}$$

with the driving vector $\mathbf{\Lambda}$

$$\mathbf{\Lambda} = \begin{pmatrix} \Omega \\ 0 \\ \delta \end{pmatrix} \tag{2.71}$$

Thus, the Bloch vector $\mathbf{R}$ processes around the driving vector, $\mathbf{\Lambda}$. For a pure state two-level system, it is assumed that all the population is initially in the ground state. In the case of a π-pulse, the Bloch vector $\mathbf{R}$ is rotated by 180°, and the population gets transferred to the upper state $|l\rangle$, while a $\pi/2$-pulse rotates the vector $\mathbf{R}$ by 90° into the uv-plane and generates a maximum coherence.

Molecular transitions can be probed with various experimental techniques, such as transient emission and fast passage excitation. In transient emission, molecules are excited by a short pulse, and a damped emission signal, known as FID, is measured in the time domain. A maximum coherence results in a maximum emission signal, achieved by applying a $\pi/2$ pulse, where the length of the pulse is chosen such that $\Omega \cdot \tau = \pi/2$. In contrast, a π-pulse leads to population inversion and a vanishing emission signal.

A π-pulse leads to incomplete population transfer due to the velocity distribution of the molecules in the experiments, as Doppler shifts decrease the excitation probability. In contrast to the constant frequency in π- or $\pi/2$-pulses, the fast passage excitation can more robustly transfer population, as in this case, the frequency of the excitation radiation is swept over the molecular resonance in a short time. An

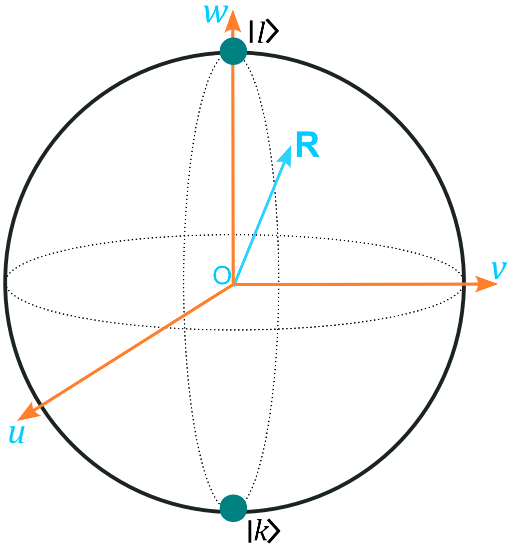

Figure 2.9: Schematic representation of the Bloch sphere with a Bloch vector $\mathbf{R}$, which describes the two-level system with states $|k\rangle$ and $|l\rangle$ denoted at the north and south poles of the Bloch sphere. The projection of $\mathbf{R}$ on the w-axis gives the population difference.

example of fast passage excitation is a rapid adiabatic passage (RAP) pulse, where the term rapid in RAP refers to a pulse duration shorter than the lifetime of the excited state. The RAP pulse has a strong coupling effect due to a large Rabi frequency (Ω), and the Bloch vector $\mathbf{R}$ can smoothly follow the driving vector $\mathbf{\Lambda}$, leading to complete population inversion.

These different excitation schemes can be employed to prepare the system in particular ways. For example, M3WM makes use of a $\pi/2$-pulse to first create a maximum coherence in a set of rotational states, which is then transferred using a π-pulse to the second set of rotational states of the M3WM scheme. This results in a chiral signal at the frequency of the third transition closing the M3WM triad. These pulse schemes are also applied to create coherent enantiomer-selective population transfer, explained in the section 2.5. The Bloch equations, originally derived for a two-level system, can be extended to three-level or more complex energy-level systems.

2.4.2 Three-level system

The two-level system detailed above will now be employed to understand the three-level system. For the three-level system, $|1\rangle \rightarrow |2\rangle \rightarrow |3\rangle$ (shown in Fig. 2.7(b)), the transitions $|1\rangle \leftrightarrow |2\rangle$ and then $|2\rangle \leftrightarrow |3\rangle$ are excited sequentially (Fig. 2.10(a)), as mentioned in section 2.4. The initial state of the system at time $t = 0$ is:

$$|\psi_1(0)\rangle = \exp\left(-i\phi_1\right) \cdot |1\rangle, \tag{2.72}$$

with ϕ_1 as the initial phase. Each microwave pulse of the three-level scheme is optimised prior to performing M3WM experiments for following conditions:

- The first resonant pulse called drive pulse (Fig. 2.7(b)) is optimised for the $\pi/2$-condition for the rotational transition $|1\rangle \rightarrow |2\rangle$ to create the maximum coherence between the two initial rotational states (condition: $\frac{\pi}{2} = \Omega_1 \cdot \tau_1$, Fig. 2.10(b)). Ω_1, τ_1 is the Rabi-frequency and pulse duration of the drive pulse.
- The second pulse, the so-called twist pulse (Fig. 2.7(b)), is optimised for π condition to transfer the coherence from states $|2\rangle$ and $|1\rangle$ to states $|1\rangle$ and $|3\rangle$ (condition: $\pi = \Omega_2 \cdot \tau_2$, Fig. 2.10(b)). Ω_2, τ_2 is the Rabi-frequency and pulse duration of the twist pulse.

The resonant excitation of the drive pulse with frequency ω_1 ($\omega_{|1\rangle\rightarrow|2\rangle}$) and phase φ_1 for a duration τ_1, yields a new state after time t ($t = \tau_1$):

$$|\psi_1(t = \tau_1)\rangle = \cos\left(\frac{\Omega_1\tau_1}{2}\right)|1\rangle - i\exp(-is_1\varphi_1 - i\omega_{|1\rangle\rightarrow|2\rangle}\tau_1) \cdot \sin\left(\frac{\Omega_1\tau_1}{2}\right) \cdot |2\rangle, \tag{2.73}$$

where $\Omega_1 = \frac{E_1 \cdot (\mathbf{n_1} \cdot \boldsymbol{\mu}_{12})}{\hbar}$, with E_1 and $\mathbf{n_1}$ as the intensity and the polarisation of the first pulse, and $s_1 = \mathrm{sgn}(\omega_{|1\rangle\rightarrow|2\rangle})$. On applying the twist pulse to resonantly excite the $|2\rangle \rightarrow |3\rangle$ transition with frequency $\omega_{|2\rangle\rightarrow|3\rangle}$ and φ_2 for a time τ_2, a new state is yielded at time $t = \tau_1 + \tau_2 + \tau_{\text{free}}$ where, τ_{free} is the time for which the FID is collected:

$$\begin{aligned}|\psi_1(t = \tau_1 + \tau_2 + \tau_{\text{free}})\rangle = &\cos\left(\frac{\Omega_1\tau_1}{2}\right)|1\rangle - i\exp(-is_1\varphi_1 - i\omega_{|1\rangle\rightarrow|2\rangle}\tau_1) \cdot \\ &\sin\left(\frac{\Omega_1\tau_1}{2}\right) \cdot \cos\left(\frac{\Omega_2\tau_2}{2}\right)|2\rangle \\ &+ \exp(-is_1\varphi_1 - i\omega_{|1\rangle\rightarrow|2\rangle}\tau_1 - is_2\varphi_2 - i\omega_{|2\rangle\rightarrow|3\rangle}(\tau_2 + \tau_{\text{free}})) \\ &\cdot \sin\left(\frac{\Omega_1\tau_1}{2}\right)\sin\left(\frac{\Omega_2\tau_2}{2}\right)|2\rangle\end{aligned} \tag{2.74}$$

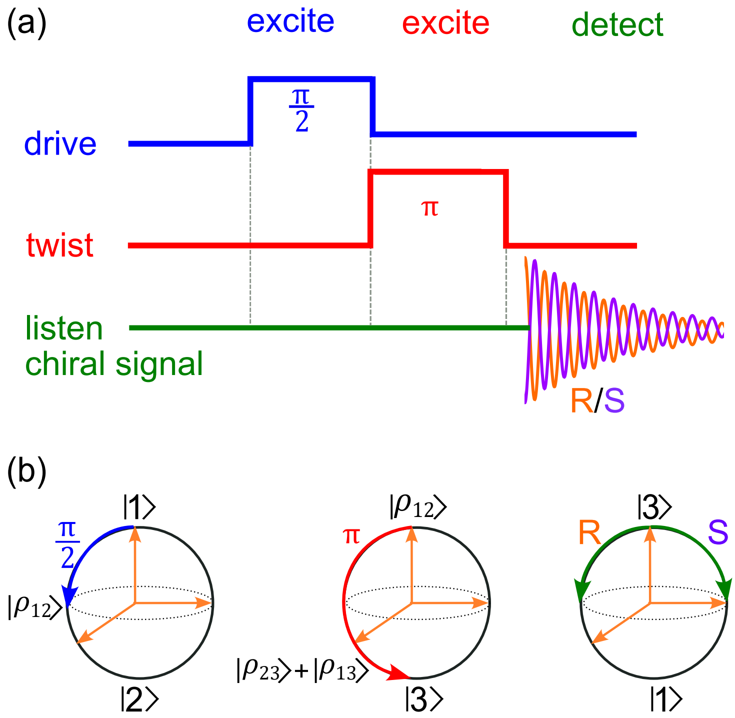

Figure 2.10: (a) Pulse sequence of the excitation-detection scheme of microwave three-wave mixing along with the FID that has a phase difference of π between the two enantiomers. (b) The coherence created with different pulses is shown via the Bloch sphere. The first sphere depicts the rotational states connected via the drive transition. Upon excitation with a $\pi/2$ pulse, coherence is created between the rotational states $|1\rangle$ and $|2\rangle$. The second sphere depicts the coherence transfer ($\rho_{12} \rightarrow \rho_{13}$) achieved when the twist pulse is employed with π conditions between the rotational states $|2\rangle$ and $|3\rangle$. The listen signal collected at the third transition is depicted by the third sphere on the most right, which shows the π-shifted phase between the enantiomers.

Here, $\Omega_2 = \frac{E_2\cdot(\mathbf{n}_2\cdot\boldsymbol{\mu}_{23})}{\hbar}$ is the Rabi fequency of the twist pulse with E_2, $\mathbf{n_2}$ as the intensity and the polarisation of the twist pulse, and s_2 is $\mathrm{sgn}(\omega_{|2\rangle\rightarrow|3\rangle})$. The pulse sequence ($|1\rangle \rightarrow |2\rangle \rightarrow |3\rangle$) induces a macroscopic dipole moment at the frequency of the so-called listen transition (connecting the rotational levels $|3\rangle$ and $|1\rangle$) and is given by the polarisation operator, $\hat{\mathbf{P}}_{|1\rangle\rightarrow|3\rangle}$. The induced polarisation is:

$$\begin{aligned}\langle\psi_1(\tau_{\text{free}})|\hat{\mathbf{P}}_{13}|\psi_1(\tau_{\text{free}})\rangle = -\boldsymbol{\mu}_{|1\rangle\rightarrow|3\rangle}\sin\left(\Omega_1\tau_1\right)\cdot\sin\left(\frac{\Omega_2\tau_2}{2}\right)\\ \cdot\cos\left(\omega_{|1\rangle\rightarrow|3\rangle}\tau_{\text{free}}+s_1\varphi_1+s_2\varphi_2+\Phi\right),\end{aligned} \tag{2.75}$$

where Φ is the total phase accumulated during the excitation cycle. The induced polarisation (eq. 2.75) has a sign change for the two enantiomers as the sign of the electric dipole moment flips between them.

While the cycle $|1\rangle \rightarrow |2\rangle \rightarrow |3\rangle$ is excited, at the same time, an alternative excitation cycle ($|1\rangle \leftarrow |2\rangle \rightarrow |3\rangle$) can start with state $|2\rangle$ instead of $|1\rangle$. The polarisation for the alternate cycle will be same in magnitude but opposite in phase to the signal from the cycle $|1\rangle \rightarrow |2\rangle \rightarrow |3\rangle$. So, the total resulting signal depends on the population difference between the two initial states ($|1\rangle$ and $|2\rangle$ with N_1 and N_2 numbers of molecules, respectively) as in the case of two-level system (eq. 2.59).

$$\langle \hat{\mathbf{P}}_{|1\rangle\rightarrow|3\rangle} \rangle = (N_1 - N_2) \cdot \langle \psi_1 | \hat{\mathbf{P}}_{|1\rangle\rightarrow|3\rangle} | \psi_1 \rangle \tag{2.76}$$

The resulting signal intensity depends on the population difference between the initial states of the M3WM cycle. Thus, a larger listen signal in experiments can be achieved with a large population difference between the initial states of the M3WM experiments. The intensity of the chiral signal recorded at the listen signal, I_{M3WM} is the projection of total induced polarisation, $\mathbf{P}_{|1\rangle\rightarrow|3\rangle}$ onto the polarisation direction $\mathbf{n_3}$, in which the listen signal is recorded ($I_{\mathrm{M3WM}} = \mathbf{n_3} \cdot \langle \hat{\mathbf{P}}_{|1\rangle\rightarrow|3\rangle} \rangle$). In experiments, the polarisation directions of drive ($\mathbf{n_1}$), twist ($\mathbf{n_2}$), and induced polarisation ($\mathbf{n_3}$) are orthogonal to each other in order to have a maximum signal intensity for the listen signal.

Density matrix formalism for a three-level system

The density matrix formalism, as explained in section 2.4.1, can also be further extended for the three-level system to understand M3WM theory.

$$\hat{\rho} = \begin{pmatrix} \rho_{11} & \rho_{12} & \rho_{13} \\ \rho_{21} & \rho_{22} & \rho_{23} \\ \rho_{31} & \rho_{32} & \rho_{33} \end{pmatrix} \tag{2.77}$$

The time evolution of the density matrix elements can be obtained by using Neumann equations as were used for the two-level system in eq. 2.67a-2.67d:

$$i\hbar \frac{\partial \hat{\rho}(t)}{\partial t} = \left[\hat{\mathcal{H}}(t), \hat{\rho}(t) \right] \tag{2.78}$$

to give the chiral signal as:

$$\mathbf{P}_{|1\rangle\rightarrow|3\rangle}(\tau_{\mathrm{free}}) \propto ee \cdot |\mu_{12}\mu_{23}\mu_{13}| \cdot \cos\left(\omega_{|1\rangle\rightarrow|3\rangle}\tau_{\mathrm{free}} + \frac{\pi}{2} \frac{\mu_{12}\mu_{23}\mu_{13}}{|\mu_{12}\mu_{23}\mu_{13}|} \right). \tag{2.79}$$

where *ee* is the enantiomeric excess described in the next paragraph. A detailed derivation for this expression can be found in reference [151].

Enantiomers are identical in nature except for the change in the sign of their triple product of dipole moment components. Due to which everything in eq. 2.75 is same except of sign of the term $[\boldsymbol{\mu}_a \cdot (\boldsymbol{\mu}_b \times \boldsymbol{\mu}_c)]$ for R- and S-forms of enantiomers. This leads to an equivalent intensity for the chiral signal for the two enantiomers, but with opposite phase signals observed in FID. The total signal intensity is then given as:

$$I_{\text{tot}}(\tau_{\text{free}}) = \frac{\overbrace{(N_R - N_S)}^{ee}}{N_R + N_S} \cdot \langle I_{\text{M3WM}}(\tau_{\text{free}}) \rangle \tag{2.80}$$

with N_R and N_S being the amounts of the R and S enantiomers in the experiment, respectively. The difference between the amounts of the two enantiomers is referred to as enantiomeric excess (*ee*). Since the overall signal intensity in M3WM is directly proportional to the *ee*, the technique can be employed to determine the *ee* in any chiral mixture. For a racemic sample, no net M3WM signal is obtained, and a nonzero net signal arises only if one of the enantiomers is in excess. Normalising the signal amplitude of the target chiral sample with that of a sample with known *ee* gives us the *ee* of the target sample.

Due to the different arrival times of the incoming fields (drive and twist) at the interaction region, the phase relationships and timings between drive, twist, and listen fields must be carefully taken into account for a precise determination of the absolute configuration. These aspects are explored and discussed in reference [152]. An alternative approach for determining the absolute configuration involves comparing the phases of a sample with a known absolute configuration to the sample where the handedness needs to be determined.

The M3WM technique has been applied to different chiral molecules since its first demonstration on 1,2-propanediol ($C_3H_8O_2$).[153, 154] In this work, this was applied to differentiate the two enantiomeric forms of 2-trifluoromethyl oxirane by comparing them with an enantiopure measurement of the same sample (Chapter 7). Further details on experimentally implementing the M3WM technique are provided in section 3.2.2 of Chapter 3.

2.5 Enantiomer-selective population transfer

In addition to enantiomer differentiation, an extension of M3WM has showcased its capabilities to manipulate and control chiral molecules to achieve energetic enantioseparation at the molecular level. The cyclic population transfer (PT) process based on the sign difference of the triple product of the enantiomers has been proposed as a way to isolate particular enantiomers in a chosen quantum state by optical means.[147, 155, 156] The same idea could be exploited to achieve enantiomeric enrichment by performing PT processes with three rotational energy levels of M3WM. The phase difference of the two enantiomers generated for the FID at the chiral listen signal on excitation of the drive and twist pulse (depicted in Fig. 2.10(a)) of the M3WM cycle can be used to selectively enhance the population of one enantiomer in a particular rotational state while depleting the population of the second enantiomer in this state, which is consequently enhanced in the other connecting state of the corresponding transition. This enantio-selective population transfer is achieved by introducing a third pulse to the M3WM scheme, the so-called transfer pulse, which is resonant to the frequency of the listen transition, i.e., involving states $|1\rangle$ and $|3\rangle$ as shown in Fig. 2.11, which results in direct excitation of this transition. This direct excitation interferes with the phase-dependent listen signal induced by the M3WM scheme and converts the coherence into a longer-lived population in the states $|1\rangle$ and $|3\rangle$.[61, 62, 65, 155–157] Depending on the phase of the transfer pulse with respect to the M3WM scheme or the time delay in between, constructive or destructive interference between the two paths can be achieved.

Thus, the evolution of the population in the connected rotational states varies according to the relative phase of the transfer pulse. The interference between the chiral signal generated on excitation of the drive and twist pulses with the transfer pulse transfers populations into the rotational state $|1\rangle$ and $|3\rangle$ in an enantio-selective manner. The induced enantiomeric enrichment in these two rotational states can be probed with different readout schemes:

- probe transition for enantio-enriched samples (Fig. 2.11(a))[61, 62] or
- chiral signal intensity of the listen transition in additional M3WM cycle[65] (Fig. 2.11(b)).

The read-out method (Fig. 2.11(a)) using the probe transition was utilised to measure the coherent enantiomer-selective population transfer created in carvone ($C_{10}H_{14}O$), for example, by Pérez *et al.*[62]. A M3WM probe cycle was employed to measure the state-specific enantiomeric enrichment created in a transiently chiral molecule, cyclohexyl methanol ($C_7H_{14}O$).[65] The discussion in this section will be focused on using the M3WM cycle as a probe to determine the induced enantiomeric

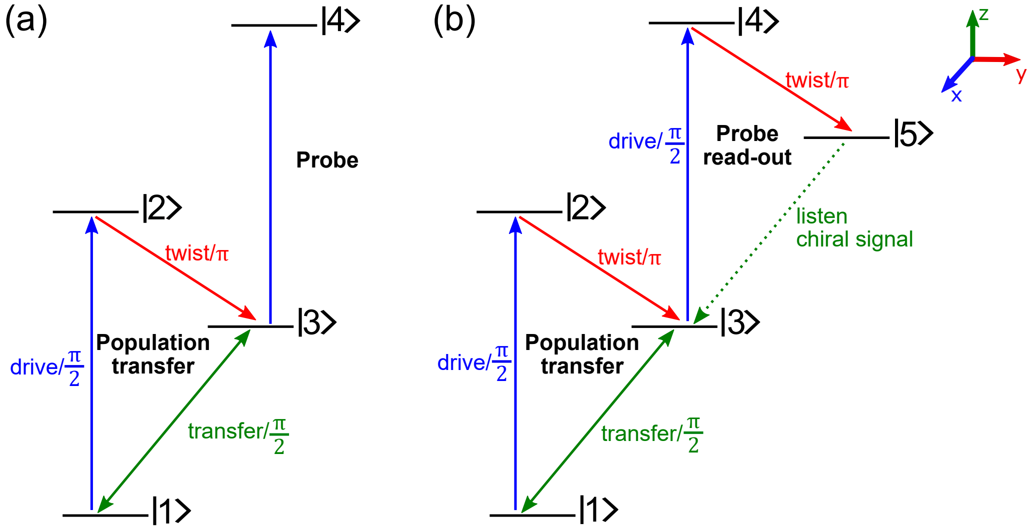

Figure 2.11: Rotational energy diagram for creating enantiomer-selective population transfer generated in rotational states $|1\rangle$ and $|3\rangle$ (lower left energy level cycle in (a) and (b)). (a) and (b) represent two different energy level schemes for probing the generated enantio-selective population transfer as described in the text. The M_J sublevels of the rotational states are omitted here for clarity.

enrichment in the rotational states $|1\rangle$ and $|3\rangle$.

The derivation for the two- and three-level systems discussed in the previous sections 2.4.1, 2.4.2 can then be applied to understand the cyclic PT process.[†] For $|\psi_0\rangle$ as the initial state of the system at time $t = 0$, the initial wavefunction of the system can be defined as:

$$|\psi_0(t=0)\rangle = |\psi(0)\rangle = \sum_{k=1}^{5} c_k^{(0)} |k\rangle. \tag{2.81}$$

Here, $k = 1, 2, 3, 4, 5$ denotes the rotational states. The pulse conditions of the PT process and of the M3WM probe sequence have the same pulse conditions as in the M3WM experiment.

- Pulse #1 is the drive transition connecting the rotational states $|1\rangle$ and $|2\rangle$ and is optimised for the $\pi/2$-pulse condition to create a maximum coherence. $\Omega_1, \omega_{|1\rangle\rightarrow|2\rangle}, \tau_1$, and ϕ_1 are the Rabi-frequency, angular frequency, time duration, and phase of the pulse #1, respectively.

[†] The theory in the upcoming sections is based on the work done by Dr. Denis Tikhonov that is yet to be published.

- Pulse #2 is the twist transition connecting the rotational states $|2\rangle$ and $|3\rangle$. The twist pulse is optimised for π-conditions to transfer the initial coherence into coherence between rotational levels $|1\rangle$ and $|3\rangle$. $\Omega_2, \omega_{|2\rangle\rightarrow|3\rangle}, \tau_2$, and ϕ_2 are the Rabi-frequency, angular frequency, time duration, and phase of the pulse #2, respectively.

- Pulse #3 is the direct excitation applied at the frequency of the chiral signal generated on the excitation of pulses #1 and #2, and is optimised for a $\pi/2$ condition. This so-called transfer pulse converts the coherence of rotational states $|1\rangle$ and $|3\rangle$ into a population difference between these states. The interferance of the chiral signal and direct excitation can be maximised using the $\pi/2$ condition for the transfer pulse #3. $\Omega_3, \omega_{|1\rangle\rightarrow|3\rangle}, \tau_3$, and ϕ_3 are the Rabi-frequency, angular frequency, time duration, and phase of the transfer pulse, respectively.

- Pulse #4 is the drive transition of the M3WM probe cycle, which connects the rotational states $|3\rangle$ and $|4\rangle$. This pulse is called the second drive and is optimised for the $\pi/2$-pulse condition as in the PT cycle. The second drive pulse creates a coherence of enantiomer population between rotational states $|3\rangle$ and $|4\rangle$ generated in rotational level $|3\rangle$ from the PT cycle. $\Omega_4, \omega_{|3\rangle\rightarrow|3\rangle}, \tau_4$, and ϕ_4 are the Rabi-frequency, angular frequency, time duration, and phase of the pulse #4, respectively.

- Pulse #5 is the twist transition of the M3WM probe cycle and connects the rotational states $|4\rangle$ and $|5\rangle$. This pulse is called the second twist and is optimised for the π-pulse condition to transfer the coherence between $|3\rangle$ and $|4\rangle$ to rotational levels $|4\rangle$ and $|5\rangle$. $\Omega_5, \omega_{|4\rangle\rightarrow|5\rangle}, \tau_5$, and ϕ_5 are the Rabi-frequency, angular frequency, time duration, and phase of the pulse #5, respectively.

- The resulting chiral signal is collected at the frequency of the listen transition $|3\rangle$ to $|5\rangle$ for time τ_{free}. The measured signal has a phase difference of π between enantiomers in their FID.

The system evolves in the same manner as in the case of a three-level system on applying the drive and twist pulse and prepares the population of enantiomers in the rotational state $|3\rangle$. When the transfer pulse (pulse #3) is applied, it transfers some of the population from the state $|1\rangle$ to state $|3\rangle$, and some of the population from the state $|3\rangle$ to $|1\rangle$. The time evolution of the wavefunction at time τ_3, i.e., after the transfer pulse (pulse #3) is applied, is given as:

$$|\psi_3(\tau_3)\rangle = \sum_{k=1}^{3} \overbrace{c_{(k)}^{(3)}(\tau_5)\exp\left(-i\omega_{|1\rangle\rightarrow|k\rangle}\tau_5\right)}^{C_k^{(3)}} |k\rangle + 0\cdot|4\rangle + 0\cdot|5\rangle \tag{2.82}$$

The enantiomeric population created in the rotational state $|3\rangle$ is then probed with the additional M3WM sequence by sequentially applying the second drive (pulse #4) and twist (pulse #5) (Fig. 2.11(b)). The coefficients of pulses #1 and #2 can be omitted since they do not contribute to the M3WM probe sequence. The resulting wavefunction of sequential excitation of all the five pulses (pulses #1–#5) will have relevant contributions only from the states $|3\rangle$ and $|5\rangle$:

$$|\psi(\tau_{\text{free}})\rangle = \exp\left(-i\omega_{|1\rangle\to|3\rangle}\tau_{\text{free}}\right)\cdot\left(C_3^{(5)}|3\rangle + C_5^{(5)}\exp\left(-i\omega_{|3\rangle\to|5\rangle}\tau_{\text{free}}\right)|5\rangle + \cdots\right) \tag{2.83}$$

where $C_3^{(5)}$ and $C_5^{(5)}$ are the coefficients for the state $|3\rangle$ and $|5\rangle$ after applying pulse #5. The five-pulse sequence ($|1\rangle \to |2\rangle \to |3\rangle \to |4\rangle \to |5\rangle$) induces a macroscopic oscillating dipole moment; this observable is given by the polarisation operator, $\hat{\mathbf{P}}_{35}$:

$$\hat{\mathbf{P}}_{35} = \hat{\boldsymbol{\mu}}_{35}\cdot\left(|3\rangle\langle 5| + |5\rangle\langle 3|\right) \tag{2.84}$$

where $|3\rangle\langle 5| + |5\rangle\langle 3|$ is the off-diagonal element of the density matrix operator that shows the coherence between these two states. The created macroscopic dipole will be proportional to the amplitude of the M3WM:

$$\mathbf{P}_{35} \propto \overbrace{\boldsymbol{\mu}_{35}\sin\left(\Omega_4\tau_4\right)\sin\left(\frac{\Omega_5\tau_5}{2}\right)}^{A_{\text{M3WM}}}\cdot\cos(\omega_{|3\rangle\to|5\rangle}\tau_{\text{free}} + \varphi_4 - \varphi_5 + \phi_{\text{M3WM}}) \tag{2.85}$$

Here, A_{M3WM} and ϕ_{M3WM} is the amplitude and the phase of the signal accumulated during the M3WM sequence. At optimal conditions the terms from pulse#1-pulse#3 are 1. The chiral M3WM signal from the probe cycle can be maximised ($|A_{\text{M3WM}}| \to$max) by using the optimised pulse conditions for the second drive (pulse #4, $\pi/2$ condition) and second twist (pulse #5, π condition) transition. The resulting signal in the time domain has an amplitude part and a phase part, where the phases of the PT sequence (i.e., pulse #1-#3) control the amplitude of the signal while the phases of the M3WM probe sequence (i.e., pulse #4 and #5) control the total phase of the signal. The resulting signal is as well influenced by the population difference between the initial rotational states, as for the M3WM cycle (eq. 2.76).

The enantiomer population in the state $|3\rangle$ varies with the phase of the transfer pulse and can be tracked with the parameter $\Delta w^{(PT)}_{|1\rangle\to|3\rangle}$. The parameter $\Delta w^{(PT)}_{|1\rangle\to|3\rangle}$ shows the increase in number of molecules in the rotational states $|3\rangle$ due to the PT sequence and is at the optimal pulse conditions of pulses #1-#3:

$$\Delta w^{(PT)}_{|1\rangle\to|3\rangle} = \frac{1}{2}\left(1 + \sin\left(\varphi_3 - \varphi_1 + \varphi_2 - \omega_{|1\rangle\to|2\rangle}\tau_1\right)\right). \tag{2.86}$$

Eq. 2.86 implies that the additional population in the state $|3\rangle$ will oscillate between 1 and 0 due to the PT process. The value 1 implies that all the molecules from state $|1\rangle$ are transferred to state $|3\rangle$, and 0 means there are no new molecules in state $|3\rangle$. By scanning the phase of the transfer pulse (pulse #3) of the PT sequence, a sinusoidal oscillation of the enantiomers is observed for the rotational states $|1\rangle$ and $|3\rangle$ (Fig. 2.12).

Assuming that only the rotational state $|1\rangle$ was initially populated. The change in population of the two enantiomers for rotational state $|3\rangle$ after the PT process is:

$$\begin{aligned} \Delta w^{(PT)}_{R,|3\rangle} &= \frac{1}{2}\Big[1+\sin\left(\varphi_3-\varphi_1+\varphi_2+\phi_{\mathrm{PT}}\right)\Big], \\ \Delta w^{(PT)}_{S,|3\rangle} &= \frac{1}{2}\Big[1-\sin\left(\varphi_3-\varphi_1+\varphi_2+\phi_{\mathrm{PT}}\right)\Big]. \end{aligned} \tag{2.87}$$

The enantiomeric population is transferred oppositely in phase in the rotational states $|1\rangle$ and $|3\rangle$. By scanning the phase of the transfer pulse (pulse #3), while assuming that $\varphi_1+\varphi_2+\phi_{\mathrm{PT}}=0$, the populations of the two enantiomers are oppositely transferred to the rotational states $|1\rangle$ and $|3\rangle$, and the chiral separation is achieved. A visualisation of the variation of the enantiomer population as a function of the phase of the transfer pulse (φ_3) is depicted in Fig. 2.12.

In experiments, the two factors that affect the efficiency of the PT process are the thermal population and the spatial degeneracy of the rotational states involved. The spatial degeneracy is described by the quantum number M_J, representing the projection of the total angular momentum onto the laboratory frame. In the absence of the external field, each rotational level is $(2J+1)$-fold degenerate in M_J (section 2.1). Due to this, a simple three-level system of a M3WM scheme involving $J>0$ will have several open M3WM cycles, which curbs the efficiency of the process. For example, a M3WM cycle involving the three lowest rotational states $|0_{00}\rangle$, $|1_{01}\rangle$ and $|1_{11}\rangle$ will have seven rotational states in total and three active M3WM cycles.

This spatial degeneracy was omitted in the previous section for the simplification of the three-level system problem. There have been theoretical proposals on how to account for this spatial degeneracy, but so far, most of the experiments on M3WM and enantiomer-selective population transfer have not accounted the effects of this spatial degeneracy.[105, 158] Recently, a control theory has been formulated by Leibscher *et al.* to predict pulse sequences for complete control over these M_J-substates.[105] Their simulations imply the existence of M3WM protocols that enable complete enantiomer-selective population transfer, even in the presence of M_J-degeneracy. They demonstrate that using circularly polarised microwave radiation, the enantiomer-selective enrichment can be enhanced from 6% to 8% in carvone by

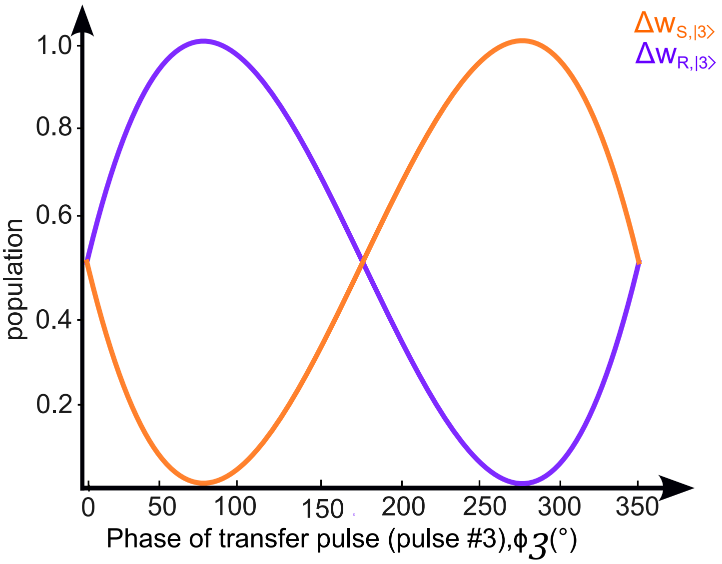

Figure 2.12: A visualisation of enantiomer population variation in rotational state $|3\rangle$ as a function of the phase of the transfer pulse. When enantiomer R is increasingly populated in the state $|3\rangle$, the S-enantiomer is depopulated in that state.

involving all the M_J substates. The reported increase from 6% to 8% is still limited by the thermal population.

The overall M3WM signal, and consequently the achieved population transfer, depends on the population difference between the initial rotational states (eq. 2.76), which is influenced by the rotational temperature of around 1-2 K achieved in the experiments. Enantiomer-selective population transfer was experimentally demonstrated for the first time with a buffer-gas cooled (T_{rot}=7-10 K) sample of 1,2-propanediol, where an enantiomeric enrichment of 0.6% could be achieved.[153] Soon after, the efficiency of population transfer was enhanced by an order of magnitude in carvone with the use of molecular jets (T_{rot}=1-2 K).[62] However, the achieved enantiomeric enrichment in these experiments is still limited by the initial thermal population of the rotational states.

This limitation can be tackled by using controlled schemes to deplete the initial thermal population and increase the population differences between the initial states. Different approaches have been proposed to enhance this population contrast, such as using a vibrationally excited state or depleting the population of a rotational level involved in the M3WM scheme via electronic excitation.[157, 159] One suggested method is using a three-level scheme involving two infrared pulses and one microwave pulse and addresses the thermally unoccupied rotational level in the excited vibrational state, thus enabling coupling between fully coherent states.[160–162] Another method suggests depleting the thermal population of the initial rotational state by using a UV excitation.[157] This was demonstrated recently with 1-indanol ($C_9H_{10}O$), in which the population of a rotational level involved in the PT scheme was depleted through electronic excitation S_0 to S_1.[157] This resulted in a significant enhancement of the PT efficiency, with the enantiomeric enrichment measured using laser-induced fluorescence. It is important to note that the demonstrated approach can be applied only to a subset of chiral molecules containing a UV chromophore.

In an alternative approach, the undesired thermal population can be exchanged to a higher rotational state prior to the population transfer process by using controlled microwave pulses. This can be realised by applying a π-pulse or a RAP-pulse as discussed at the end of section 2.4.1. These pulses can create a larger population contrast in the initial rotational states of the PT cycle either through population inversion or via complete population transfer between the two states.[50, 163] Chapter 7 presents the results on the effect of depleting thermal population with a preceding RAP- or a π-pulse before the PT cycle.

2.6 Microwave six-wave mixing

Chiral molecules are often considered that at least one chemical bond should break within the molecule to convert one enantiomer into its mirror image. However, there are many aspects of molecular chirality that go beyond this consideration. Another form of chirality can be, for example, atropisomerism, where the two mirror images can convert to each other without breaking chemical bonds but just by hindered internal rotation around single bonds. This kind of chirality arising from the spatial arrangement of a conformer with a low barrier between the two enantiomers is called transient chirality.[164, 165] These transiently chiral molecules can periodically interconvert between two enantiomeric forms via tunneling motions depending on the racemisation barrier. If the barrier height is low then the energy levels may split into two vibrational components (symmetric and antisymmetric) and lead to the observation of doublets in the rotational spectrum.[166] These kinds of internal dynamics provide us with information about the tunneling rates and potential energy surface of the molecular systems as mentioned in section 2.1.3. These permanently and transiently chiral molecules can be classified into four cases according to their racemisation barrier, as shown in Fig. 2.13.

- **Case 1**: Chiral molecules with an infinitely high barrier between enantiomeric pairs are referred to as permanently chiral molecules. Most of the chiral molecules such as carvone, 1,2-propanediol, and styrene oxide (C_8H_8O) have a stereogenic center and are permanently chiral on the timescales of our experiments. Their enantiomers can be separated by conventional separation techniques and enantiopure samples can be produced. M3WM, along with the chiral tag rotational spectroscopy, can be employed on such chiral molecular systems to sense their chirality and determine *ee* in complex chiral mixtures.[49, 57, 58, 60, 167]

- **Case 2**: When the torsional stereomutation barrier connecting the two mirror images is low enough, enantiomers periodically interconvert between one another at room temperature (RT=298 K) through rotation of some torsional angle (first case of transient chirality in Fig. 2.13). The racemisation barrier for such a class of molecules is typically around 5-15 kJ/mol or even less. These chiral molecules exist in racemate form and cannot be separated at room temperature. With the cold conditions of a supersonic expansion, enantiomers can be isolated in their potential wells. Cyclohexyl methanol, and propofol ($C_{12}H_{18}O$) with a racemisation barrier of 15 kJ/mol and 10 kJ/mol, respectively are examples of this class of transiently chiral molecule. The two enantiomers of cyclohexyl methanol have an opposite dipole moment component sign along the *b*-axis of molecular rotation, while the sign of the *a*- and *c*-axis dipole moment components remains unchanged between enantiomers. Due to racemisation at room temperature, M3WM cannot be directly used to sense chirality on this class of molecules. But the chiral conformers could be kinetically stabilised in their potential wells in supersonic expansion upon cooling to T_{rot}=1-2 K. This way, they can be treated as case 1, and the PT process can be employed to first create state-selective enrichment of chiral conformers in a particular rotational state, which can be then measured with another M3WM cycle.[65] The theory for this kind of PT process was demonstrated in the previous section 2.5.

- **Case 3**: When the racemisation barrier decreases further such that the enantiomeric pairs tunnel from one enantiomeric form to another and cannot be separated even at the experimental timescales, they are also referred to as transiently chiral molecules (second case of transient chirality in Fig. 2.13). Examples of such class of transiently chiral molecules are benzyl alcohol ($C_6H_5CH_2OH$) and benzyl mercaptan ($C_6H_5CH_2SH$), which have barriers of about 3.3 and 3.1 kJ/mol, for the enantiomeric forms arising due to concerted rotation of the CH_2OH or CH_2SH and OH or SH groups in the plane above the phenyl ring.[36, 168] These molecules can have two minima on the potential energy surface with each minimum corresponding to a certain enantiomer, separated by an achiral transition state, as shown in Fig. 2.13.[36] Each stationary state of such molecules is of a specific parity with respect to the inversion operation denoted as ($|\pm\rangle$). These stationary states are the positive and negative combinations of the non-stationary localised wavepackets of the R- and S-enantiomers with a chosen parity ($|\pm\rangle = \frac{1}{\sqrt{2}}(|R\rangle \pm |S\rangle)$). For such transiently chiral molecules, a specific enantiomeric state can be achieved by generating a coherent superposition of the states ($|\pm\rangle$) with opposite parity.[169, 170] Such an approach to create a coherent superposition state for rotational states of an asymmetric rotor has been proposed by Hirota.[59, 171] Chapter 8 presents an experimental demonstration of an approach to induce transient *ee* in a transiently chiral molecule, benzyl alcohol, with the theoretical framework of the approach discussed below.[64]

- **Case 4**: Another group of chiral molecules are those with state-dependent chirality, for example, molecules that have achiral electronically excited states or those that are achiral in their vibronic ground state but become chiral when excited to vibrational modes. An example of this class of chiral molecules is carbonyl chlorofluoride (COFCl), which is planar in the vibronic ground state. In the first vibrational mode, however, the molecule performs an umbrella-type motion, changing its handedness on the timescale of the motion. Tikhonov *et al.* recently suggested how the chiral vibrational dynamics of an achiral

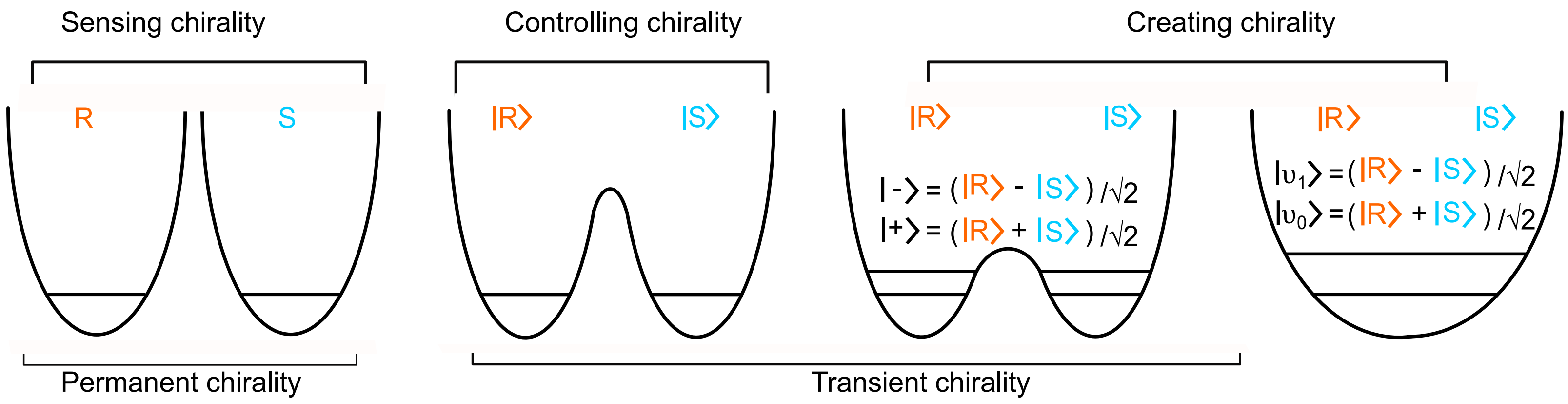

Figure 2.13: Potential energy surface for four cases of permanent and transiently chiral molecules. The figure is adapted from the theory work done by Dr. Denis Tikhonov that is yet to be published.

molecule such as carbonyl chlorofluoride can be investigated in the gas phase. [172]

The work presented in this thesis focuses on structurally flexible molecules such as benzyl alcohol, which exhibit transient chirality (case 3) and have low racemisation barriers. Two enantiomers of benzyl alcohol can interconvert into each other even at cryogenic temperatures due to quantum tunnelling. These kinds of transiently chiral molecules have each rotational energy level split into two tunneling states, $|+\rangle$ and $|-\rangle$, which correspond to the linear combinations of the two enantiomer forms, R and S, as illustrated in Fig. 2.14. Each tunnelling state carries the signature of both enantiomers. As shown in Fig. 2.14(a) the two enantiomers of benzyl alcohol differ in the orientation of the CH_2OH group, arising from the concerted rotation of this group in the plane above the phenyl ring.[36]

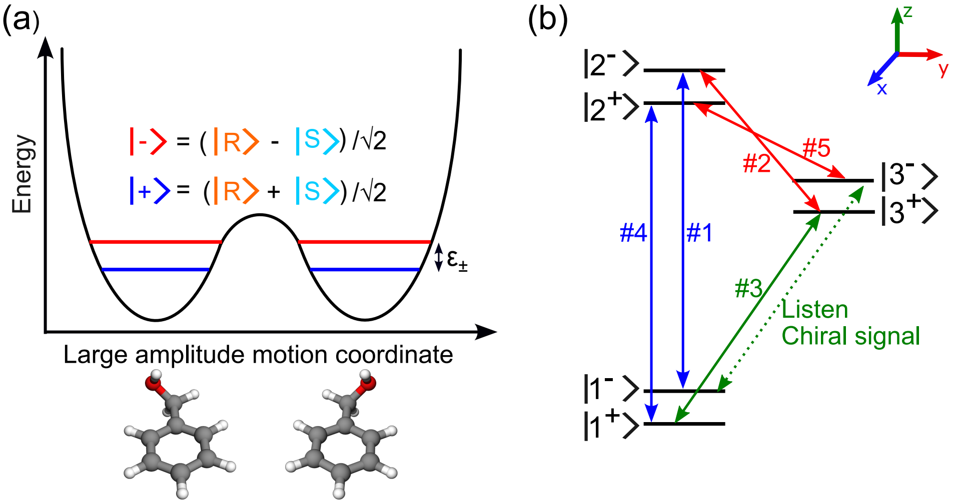

Figure 2.14: (a) The schematic of the potential energy surface of benzyl alcohol is shown with energy on the y-axis as a function of large amplitude motion coordinates. The two enantiomeric forms of benzyl alcohol are depicted with vibronic ground states with opposite parity denoted as $|\pm\rangle$. $|R\rangle$ and $|S\rangle$ states represent the localised wavepackets of particular chirality. $\epsilon_\pm$ represents the energy difference between the two tunneling states, which is experimentally determined to be 492.816(2) MHz in benzyl alcohol arising from a barrier with a height of about 280 cm^{-1}.[36] (b) Microwave six-wave mixing approach to induce transient enantiomeric excess. Each rotational level is marked as $|J^\pm\rangle$ (for example, $J = 1, 2$) with J as the total angular momentum and ± indicates the parity of the torsional state. Each microwave transition is labelled #1-#5 according to the order of the pulse sequence and color indicates the polarisation direction of the excitation pulse. A chiral signal is coherently induced by the excitation of five microwave pulses. M_J sublevels of rotational states are omitted here for clarity.

The concerted rotation of CH_2OH and OH groups changes the sign of the electric dipole-moment component along the b-axis in the principal axis system. The corresponding b-type rotational transitions occur between the two tunneling states of opposite symmetry (interstate transitions). Due to these interstate transitions a closed M3WM loop cannot be formed, as it does not satisfy symmetry conditions. Thus, both M3WM and the related microwave population transfer schemes become impossible to be applied to such transiently chiral molecules.

Instead, five resonant excitation pulses are needed, where the first three pulses create a chiral wavepacket and the second two probe it, similar to the PT scheme probed with the M3WM cycle. The five-pulse sequence induces a chiral response in the form of a listen transition at the sixth rotational transition, which closes the loop. Such an energy scheme is presented in Fig. 2.14(b), and the theoretical details for this are discussed in the section below. This microwave six-wave mixing (M6WM) approach consists of a closed cycle of six rotational transitions $|1^-\rangle \rightarrow |2^-\rangle \rightarrow |3^+\rangle \rightarrow |1^+\rangle \rightarrow |2^+\rangle \rightarrow |3^-\rangle$ as illustrated in Fig. 2.14(b). ± superscript to the $|k^\pm\rangle$ rotational state denotes the parity of the torsional state of the molecule.

The following section is based on the supplementary information provided in reference [64]. As described in the section 2.4.1, the wavefunction for any two-level system at time $t = 0$ is given as:

$$|\psi(t)\rangle = \exp\left(-iE_k t/\hbar\right) c_k(t)|k\rangle + \exp\left(-iE_l t/\hbar\right) c_l(t)|l\rangle. \tag{2.88}$$

The simplified Schrödinger equations after applying RWA will be similar to eqs. 2.56a, 2.56b. The solutions for equations eqs. 2.56a, 2.56b with initial conditions $|c_k(t=0)|^2 = 1$ and $|c_l(t=0)| = 0$ will be:

$$c_k(t) = \exp\left(i\phi_k^{(0)}\right) \cdot \cos\left(\frac{\Omega_{kl} t}{2}\right) \tag{2.89a}$$

$$c_l(t) = -i \exp\left(i\phi_k^{(0)} - i s_{k\rightarrow l}\varphi\right) \cdot \sin\left(\frac{\Omega_{kl} t}{2}\right) \tag{2.89b}$$

where $\phi_k^{(0)}$ is the initial phase of the state $|k\rangle$ at $(t = 0)$. The final state after the interaction with an external resonant field for time $(t = \tau)$ is:

$$|\psi(t)\rangle = \exp i\phi_k^{(0)} \cdot \left[\exp\Big(-\frac{iE_k t}{\hbar}\Big) \cdot \cos\Big(\frac{\Omega_{kl}\tau}{2}\Big)|l\rangle - i\exp\Big(-is_{k\rightarrow l}\varphi - \frac{iE_k t}{\hbar}\Big) \cdot \sin\Big(\frac{\Omega_{kl}\tau}{2}\Big)|k\rangle\right] \tag{2.90}$$

with the condition $s_{k\to l} = \text{sign}\,(\omega_{k\to l})$ (going down in energy), meaning $s_{k\to l} = 1$ if $\omega_{k\to l} > 0$ and $s_{k\to l} = -1$ if $\omega_{k\to l} < 0$ (going up in energy).

By applying this wavefunction form to the sequence of the pulses in the M6WM scheme, one can follow the evolution of the system, starting with the initial state, $|1^-\rangle$. The five subsequent microwave pulses that transfer the population between rotational states labelled $|k^\pm\rangle$ are:

- Pulse #1 ($|1^-\rangle \to |2^-\rangle$) is an intrastate transition with Rabi frequency Ω_1 and duration τ_1, $\omega_1 = \omega_{|1^-\rangle\to|2^-\rangle}$ and phase of the pulse as φ_1 with $s_1 = s_{1^-\to2^-} = +1$ (as it goes from a lower state to higher state).
- Pulse #2 ($|2^-\rangle \to |3^+\rangle$) is an interstate transition with Rabi frequency Ω_2 and duration τ_2, $\omega_2 = \omega_{|2^-\rangle\to|3^+\rangle}$ and phase of the pulse as φ_2 with $s_2 = s_{2^-\to3^+} = -1$ (as it goes from a higher state to a lower state).
- Pulse #3 ($|3^+\rangle \to |1^+\rangle$) is an intrastate transition with Rabi frequency Ω_3 and duration τ_3, $\omega_3 = \omega_{|3^+\rangle\to|1^+\rangle}$ and phase of the pulse as φ_3 with $s_3 = s_{3^+\to1^+} = -1$.
- Pulse #4 ($|1^+\rangle \to |2^+\rangle$) is an intrastate transition with Rabi frequency Ω_4 and duration τ_4, $\omega_4 = \omega_{|1^+\rangle\to|2^+\rangle}$ and phase of the pulse as φ_4 with $s_4 = s_{1^+\to2^+} = +1$.
- Pulse #5 ($|2^+\rangle \to |3^-\rangle$) is an interstate transition with Rabi frequency Ω_5 and duration τ_5, $\omega_5 = \omega_{|2^+\rangle\to|3^-\rangle}$ and phase of the pulse as φ_5 with $s_5 = s_{2^+\to3^-} = -1$.

The condition of orthogonal polarisations and different dipole-type rotational transitions of all three microwave pulses in the case of M3WM also has to be satisfied for the M6WM process. The excitation of this energy scheme as described above and represented in Fig. 2.14(b) induces a macroscopic polarisation for the $|3^-\rangle \to |1^-\rangle$ listen transition with the frequency $\omega = \omega_{|3^-\rangle\to|1^-\rangle}$. Similarly, on evaluating the wavefunctions sequentially using eq. 2.88, the final state we obtain after applying the five microwave pulse sequence is:

$$\begin{aligned}|\psi\rangle =& \exp\left(i\phi^{(0)}_{|1^-\rangle} - \frac{iE_{|1^-\rangle}t}{\hbar}\right)\cdot\Bigg[\overbrace{\cos\left(\frac{\Omega_1\tau_1}{2}\right)}^{c_{|1^-\rangle}}|1^-\rangle \\ & \overbrace{-i\exp\left(-i\omega t + i\Phi\right)\prod_{k=1}^{5}\exp\left(-is_k\varphi_k\right)\sin\left(\frac{\Omega_k\tau_k}{2}\right)}^{c_{|3^-\rangle}}|3^-\rangle + \cdots\end{aligned} \tag{2.91}$$

with Φ as the total phase accumulated during the cycle. The polarisation operator for the observable in this M6WM for the macroscopic dipole moment created at the listen transition ($|3^-\rangle \rightarrow |1^-\rangle$) will be:

$$\hat{\mathbf{P}}_{3^-1^-} = \boldsymbol{\mu}_{1^-3^-} \cdot (|1^-\rangle\langle 3^-| + |3^-\rangle\langle 1^-|). \tag{2.92}$$

The macrosopcic polarisation created by the excitation five-pulse sequence oscillates with amplitude A at the frequency of the listen transition (ω).

$$\langle \hat{\mathbf{P}}_{3^-1^-} \rangle \propto \overbrace{-\boldsymbol{\mu}_{3^-1^-} \cdot \sin(\Omega_1\tau_1) \cdot \left(\prod_{k=2}^{5} \sin\left(\frac{\Omega_k\tau_k}{2}\right)\right)}^{\propto A} \cdot \sin\left(\omega t + \sum_{k=1}^{5} s_k\varphi_k - \Phi\right) \tag{2.93}$$

The five resonant microwave pulses are optimised for the following conditions to obtain the maximum listen signal :

- Pulse #1 ($\Omega_1\tau_1 = \pi/2$) as it will maximise $\sin(\Omega_1\tau_1)$.
- Pulse #2 and all the other pulses #3-#5 are π-pulses to maximise the $\sin(\Omega_k\tau_k/2)$ terms.

The $\pi/2$-condition for pulse #1 splits the population in state $|1^-\rangle$ into two equal parts, one part of the population is left in $|1^-\rangle$ till the end of the experiment, and the other half is transferred from $|2^-\rangle$ to $|3^-\rangle$ using the pulses #2-#5.

The two enantiomeric forms are interchangeable due to quantum tunnelling in our experimental timescale, so the molecule will exist in the $|\pm\rangle$ state. On applying the first three pulses of the sequence, it creates a 50/50 superposition of $|+\rangle$ and $|-\rangle$ states. This result can be illustrated by the *ee* observable, which is the difference between the amounts of R and S enantiomers. The $\hat{ee}$ observable is given by the operator:[173–175]

$$\hat{ee} = |R\rangle\langle R| - |S\rangle\langle S| = |+\rangle\langle -| + |-\rangle\langle +| \tag{2.94}$$

which is the coherence between the $|\pm\rangle$ states. The *ee* for the rotational state $|1\rangle$ in M6WM experiments will be:

$$\langle ee \rangle = \langle \psi_3|\hat{ee}|\psi_3\rangle = -\overbrace{\sin(\Omega_1\tau_1)\left(\prod_{k=2}^{3} \sin\left(\frac{\Omega_k\tau_k}{2}\right)\right)}^{\propto|ee|} \cdot \sin\left(\omega_{|1^+\rangle\rightarrow|1^-\rangle}t + \Phi' - \sum_{k=1}^{3} s_k\varphi_k\right) \tag{2.95}$$

where the $|\psi_3\rangle$ is the wavefunction after the excitation of the first three pulses

(pulses #1-#3). After the first three pulses, the resulting state is an oscillating chiral wavepacket, which oscillates at the tunneling frequency $\omega_{|1^+\rangle \rightarrow |1^-\rangle}$ between the tunneling state $|1^+\rangle \rightarrow |1^-\rangle$ with the amplitude $|ee|$.

Due to quantum tunneling the created chiral wavepacket does not have persistent chirality and keeps interconverting between the two enantiomers. The amount of enantiomeric excess created with the pulses #1-#3 then can be measured by exciting pulses #4 and #5 that in turn create a coherent signal at the listen transition ($|3^-\rangle \rightarrow |1^-\rangle$), which allows us to probe the magnitude of the *ee* created using the polarisation operator, $\hat{\mathbf{P}}_{3^-1^-}$(eq. 2.93). Thus, a quantum racemate of two interconvertible enantiomers can be steered to create a transient enantiomeric enrichment at a rotational level of interest by using the M6WM approach. An experimental demonstration of this approach is presented in Chapter 8.

Chapter 3

Experimental details

With a background in the theory of rotational spectroscopy and its application in investigating flexible and chiral molecules, the following chapter provides a detailed description of the experimental setup and operating principles of the CP-FTMW spectrometer used in this thesis. This spectrometer was employed to investigate the conformational flexibility of molecules and perform chiral analysis. The spectrometer covers a frequency range of 2-18 GHz. The instrument employs supersonic expansion as a molecular source to efficiently cool down the rotational and other degrees of freedom, facilitating the investigation of molecules with complex conformational landscapes. The chapter is organised as follows: Section 3.1 discusses the supersonic expansion and its advantages for studying weakly bound clusters and conformational cooling, section 3.2 lays out the basic framework of CP-FTMW spectroscopy, and in section 3.2.1 the setup of the CP-FTMW spectrometer is described. The modifications to the spectrometer to perform chirality-sensitive M3WM experiments are detailed in section 3.2.2.

3.1 Supersonic expansion

Supersonic expansion is used to study molecules in the gas phase.[176–179] A supersonic jet is formed when a gas expands from a high-pressure region, P_0, to a low-pressure region, P_B, through an orifice (often mm or sub-mm diameter) or nozzle. In the first stage of the supersonic expansion, atoms and molecules are cooled adiabatically to convert the random thermal motion of the static gas into a directed mass flow in the expanding gas. This conversion of internal energy into directed motion cools the translational motion, resulting in very low translational temperatures. These translational temperatures are determined by the width of the velocity distribution; the narrower the velocity distribution, the colder the translational temperature. Therefore, the molecules are translationally cold, but still moving at supersonic speeds. The number of collisions decreases dramatically due to the reduction in molecular density with an increase in the distance x from the nozzle exit. As a result, at some point after the first stage of expansion, no interactions occur between atoms and molecules. This allows us to investigate isolated molecules and obtain their spectra in a collision-free environment. Two-body collisions between carrier gas atoms and the molecules under study in the early stage of expansion also cool down their vibrational and rotational temperatures, populating the lower energy levels. Higher population in low-energy states increases the intensity of observed transitions relative to a high-temperature experiment, which in turn simplifies the spectrum. Moreover, the three-body collisions that occur very close to the nozzle result in the formation of weakly bound complexes, which can be investigated in experiments. The parameters that govern the collision rate and the formation of complexes are the stagnation pressure, temperature, and nozzle diameter. These advantages of supersonic expansion have led to the combination of the supersonic jet with various spectroscopic techniques, such as laser and MW spectroscopy, enabling the study of complex molecules, weakly bound complexes, and molecular interactions.[176–180]

Properties of supersonic expansion

The primary characteristics of supersonic jets, focusing on the properties of atomic beams, are outlined below. The expansion is treated as an atomic beam due to the low concentration of the sample in comparison to the seeded carrier gas, which is usually an inert atomic gas.[181] The most common carrier gases used for such techniques are helium (He), neon (Ne), and argon (Ar). For ideal monoatomic gases, the velocity distribution inside the high-pressure reservoir follows the Maxwell-Boltzmann distribution and is given as:

$$P(v) = 4\pi\left(\frac{m}{2\pi k_B T_0}\right)^{3/2} v^2 \exp\left[-\frac{mv^2}{2k_B T_0}\right] \tag{3.1}$$

where m, k_B and T_0 represent the atomic mass, the Boltzmann constant and the temperature of the nozzle, respectively. Fig. 3.1 shows the velocity distribution of Ne at different temperatures using eq. 3.1. Depending on the relationship between the mean free path length of the atoms, λ (which is the distance travelled before encountering collision), and the diameter of the orifice, D, two different types of beams can be distinguished: effusive and supersonic beams.

The effusive beam is formed when the mean free path length λ is larger than the diameter of the orifice, ($\lambda \gg D$). In this case, atoms do not encounter any collisions with other atoms during the expansion through the pinhole; as a result, no energy

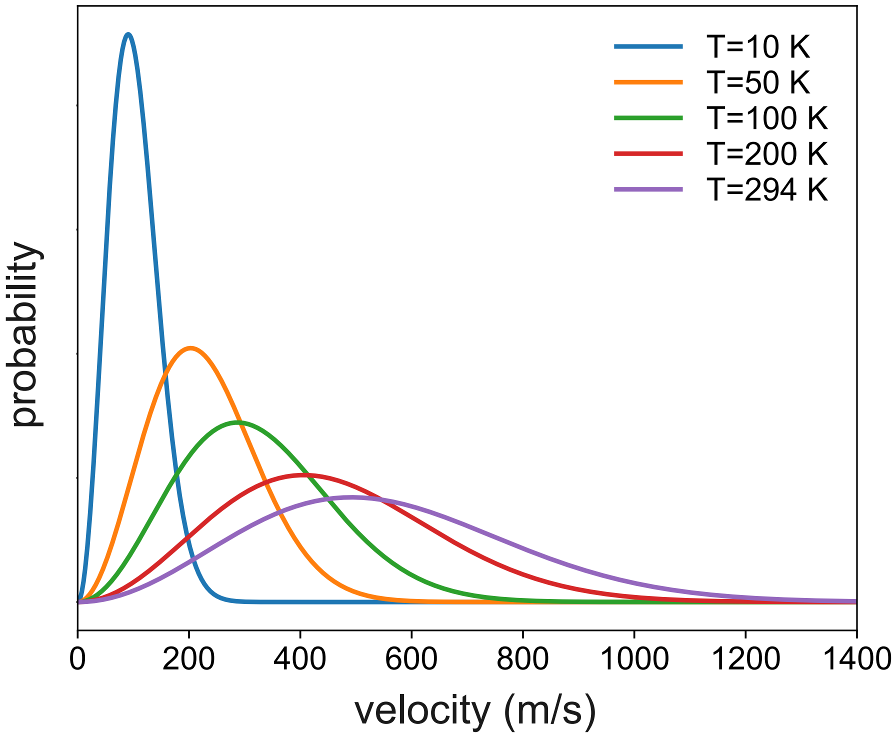

Figure 3.1: The Maxwell-Boltzmann velocity distribution of neon atoms calculated at different temperatures. This figure is taken from reference [182].

is transferred, and there is no cooling. The velocity distribution of an effusive beam follows the Maxwell-Boltzmann distribution. While these beams are not cold, they do provide a non-interacting environment to probe the conditions inside the reservoir. They are utilised to obtain equilibrium constants and thermodynamic data for gas-phase reactions even at elevated temperatures.[183]

In contrast, supersonic beams are formed when the orifice diameter is much larger than the mean free path length ($D \gg \lambda$). In this limiting case, the internal and external degrees of freedom of atoms and molecules undergo efficient cooling due to several collisions between the atoms. Due to the collision energy transfer that takes place in the first stage of the expansion, the atomic beam is more confined and the velocity distribution is much narrower compared to the Maxwell-Boltzmann velocity distribution at the reservoir temperature, even though the mean velocity is higher.

The terminal velocity of the beam can be estimated by assuming the expansion to be isentropic and adiabatic. For such an expansion, the sum of the enthalpy H

and the kinetic energy of the directed mass flow is conserved and both the enthalpy and the directed mass flow are dependent on the distance x from the expansion.

$$H(x) + \frac{1}{2}mv^2(x) = const. \tag{3.2}$$

If the enthalpy is converted into a directed mass flow, then the terminal velocity of the atoms for an ideal monoatomic gas depends only on the temperature of the reservoir T_0 and the mass of the atoms (m) as follows:

$$v = \sqrt{\frac{5k_BT_0}{m}} \tag{3.3}$$

However, in reality, the expansion is not completely isentropic or adiabatic, and the mean velocities of the ensemble of atoms do not always reach the terminal velocity. This can be estimated by making approximations for a real system. As gas mixtures in the supersonic expansion contain only a small percentage of the molecule, the carrier gas can be used to calculate the terminal velocity of the gas mixture in the expansion. For He, Ne, and Ar, terminal velocities of about 1760 m/s, 790 m/s, and 560 m/s, respectively, are achieved during the expansion at $T_0 = 300$ K.

The different stages of the supersonic expansion have varying velocities, pressures, and temperatures, which depend on the ratio of the specific heat and the local Mach number. The most common way to describe the different areas of the expansion process is by using the Mach number, M, which is defined as:

$$M = \frac{v}{c} \tag{3.4}$$

where v is the velocity of the atomic beam at a specific position, and c is the local speed of sound. The supersonic expansion can be described in terms of the speed of the sound because the propagation of sound in a gas can also be treated as an adiabatic and nearly isentropic process. Fig. 3.2 highlights the different expansion zones according to the Mach number value. In the nozzle, which is the pre-expansion area, the gas is in a stagnation state, and this state is defined in terms of the temperature T_0 and the pressure P_0. In this pre-expansion area, the collision frequency is higher, and therefore the speed of sound is much faster than the velocity of the atomic beam, leading to a small Mach number value ($M \ll 1$). As the atomic beam proceeds towards expansion, the pressure difference between the high-pressure and the low-pressure regions accelerates the gas. With the decreasing volume of the reservoir, the random motion converges to a directed motion, and a Mach number of 1 ($M = 1$) is achieved at the orifice. The decrease in particle density and collision frequency, coupled with an increase in the flow area, leads to an increase in the mean velocity. At this point, the Mach number M increases beyond unity, and the expansion is then referred to as a supersonic expansion. The expansion has a barrel shape and shock wave formed at the boundaries due to collision with the warmer background gases as the atomic gas expands through a point source (Fig. 3.2). The barrel shock wave has a parabolic shape centred on the jet axis, opening from the expansion orifice. The second shock zone begins where the barrel shock zone ends. This central shock wave is the Mach disk and appears in supersonic processes occurring in supersonic aircraft or bullets. The shock waves are defined as thin, non-isentropic regions that modify the direction of the supersonic flow and reduce the Mach number values to less than 1. The volume of the limiting zone is further subdivided into regions with collisions that maintain equilibrium, followed by a collision-less flow region. The collision-less zone, where the density is so low that no more interactions take place, is called the zone of silence, as marked in Fig. 3.2. In this region, the speed of sound in the expanding gas drops down to nearly zero. The zone ends when the expanding molecules reach the Mach disk, and their velocities are randomised again by collisions. The length of the silence zone depends on D and on the difference in pressure between the two areas, inside the reservoir or nozzle and the vacuum chamber, and is given by:

$$x_M = 0.67D\sqrt{\frac{P_0}{P_B}} \tag{3.5}$$

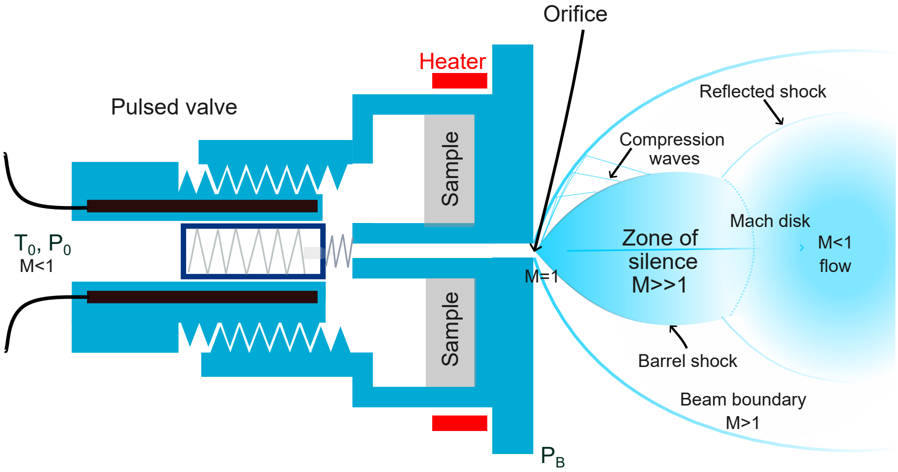

Figure 3.2: Schematic drawing of the pulsed valve with the supersonic expansion propagating through the nozzle. The different areas of the supersonic expansion are labelled on the basis of their Mach number M.

The experimental performance is affected by the pumping speed, which defines the ultimate pressure P_B in the vacuum chamber. In the experimental setup presented in this thesis, a pressure of approximately 10^{-6} mbar is reached, and low rotational temperatures of 1-4 K are attained using Ne as carrier gas. These low rotational temperatures populate only low-energy rotational states, leading to simplified molecular spectra with more intense rotational transitions when compared to conditions at room temperature.

As a result of the collisions happening during the first stages of the supersonic expansion, it is possible to observe different conformational cooling effects in experiments with different carrier gases. Conformational relaxation in the supersonic expansion is a result of the binary collisions of the molecules with the carrier gas. The choice of carrier gas influences the vibrational temperature due to different cooling behaviours, which in turn affects conformational relaxation. Heavier carrier gases, such as Ar (and Kr), provide more efficient cooling compared to lighter carrier gases (such as Ne and He), because they have more effective binary collisions with high-energy conformers. If the conformers are connected by energy barriers lower than the energy transferred by the binary collisions, then the higher energy conformer relaxes into the lower energy conformer. Thus, the rotational spectra obtained with Ar could exhibit less complexity (due to fewer numbers of conformers) than the same experiment repeated with He or Ne carrier gas due to conformational relaxation. However, if the barrier to the interconversion of the conformers or isomers exceeds about 4-5 kJ/mol, conformational relaxation becomes less likely, at least not in expansions with any of these four gases as carriers.[184]

As already mentioned in this section, the binary collisions cool down the vibrational and rotational degrees of freedom, reaching low temperatures, simplifying the spectrum and contributing to the conformational relaxation. Meanwhile, three-body collisions are responsible for the formation of weakly bound complexes and clusters. Weakly bound clusters can also be formed and stabilised because of the translational temperature or the low velocity spread. The weak molecular clusters can be destroyed through additional two-body collisions, but they can be investigated in the isolated environment if they reach this area. The ratio of three-body collisions to binary collisions is proportional to the number density of atoms, n_0, and the diameter of the orifice, D. The total number of two-body and three-body collisions occurring during the expansion varies according to $n_0 D$ and $n_0^2 D$, respectively.[181] The experimental conditions are optimised according to the motivation of the study; for example, higher backing pressure is used to investigate clusters or complexes. Consequently, low-pressure and large-diameter orifices are preferred to observe fewer clusters in the experiment.

For the experiments presented in this work, generally, the supersonic expansion is created using Ne as a carrier gas at stagnation pressures of 1-5 bar, resulting in rotational temperatures of 1-3 K. Considering the possibilities of inter-conversion of conformers in cases of rich conformational landscapes of molecules, additional experiments can be performed with He or Ar to observe different cooling effects from the carrier gases (Chapter 5).

3.2 Chirped-pulse Fourier transform microwave (CP-FTMW) spectroscopy

CP-FTMW spectroscopy is based on an efficient linear fast-passage excitation to excite the molecular sample. This is achieved through a linear frequency sweep, as such frequency sweeps are efficient in polarising molecular samples, as demonstrated by McGurk *et al.*[185] The frequency sweeping has to be faster than the relaxation time of the excited states, and this is typically 1-4 µs long. This allows us to detect the molecular signal in the absence of the polarising radiations. The electric field waveform for a linear chirp is:[86]

$$E(t) = E_0 \exp(i(\omega_0 t + \alpha t^2/2)). \tag{3.6}$$

where E_0 is the amplitude of the electric field and remains constant across the chirp, and α is the chirp rate defined as:

$$\alpha = \frac{\omega_f - \omega_0}{t_{pulse}} \tag{3.7}$$

with ω_0, ω_f as the initial and final frequency of the chirped pulse, respectively, and t_{pulse} as the pulse length. The intensity of the emitted molecular signal is proportional to the transition frequency ω, the square of the transition dipole moment μ^2, the amplitude of the exciting electric field E_0, the population difference of the two states involved in the transition ΔN_0, and the inverse square root of the chirp rate α:

$$S \propto \omega \cdot \mu^2 \cdot E_0 \cdot \Delta N_0 \cdot \sqrt{\frac{\pi}{\alpha}} \tag{3.8}$$

These are the factors that govern the design, construction, and operation of any CP-FTMW spectrometer. The home-built 2-18 GHz COMpact-Passage Acquired Coherence Technique (COMPACT) spectrometer[94] as shown in Fig. 3.3 is based on the design proposed by Grabow.[150]

The linear frequency sweep chirps of 2-8 GHz are well-suited to investigate larger molecules with large moments of inertia, leading to small rotational constants and transitions lying in the lower frequency region of the spectrum. The spectrometer is also extendable to a higher frequency range (up to 18 GHz) and a longer bandwidth (2–12 GHz) by making small changes in the electronic equipment. Further, the spectrometer could be modified to perform microwave experiments for chirality detection using a three-wave mixing approach, as proposed by Hirota.[59] The next sections provide detailed information on the 2-8 GHz COMPACT spectrometer (shown in Fig. 3.3) and its modification to perform chirality detection experiments.

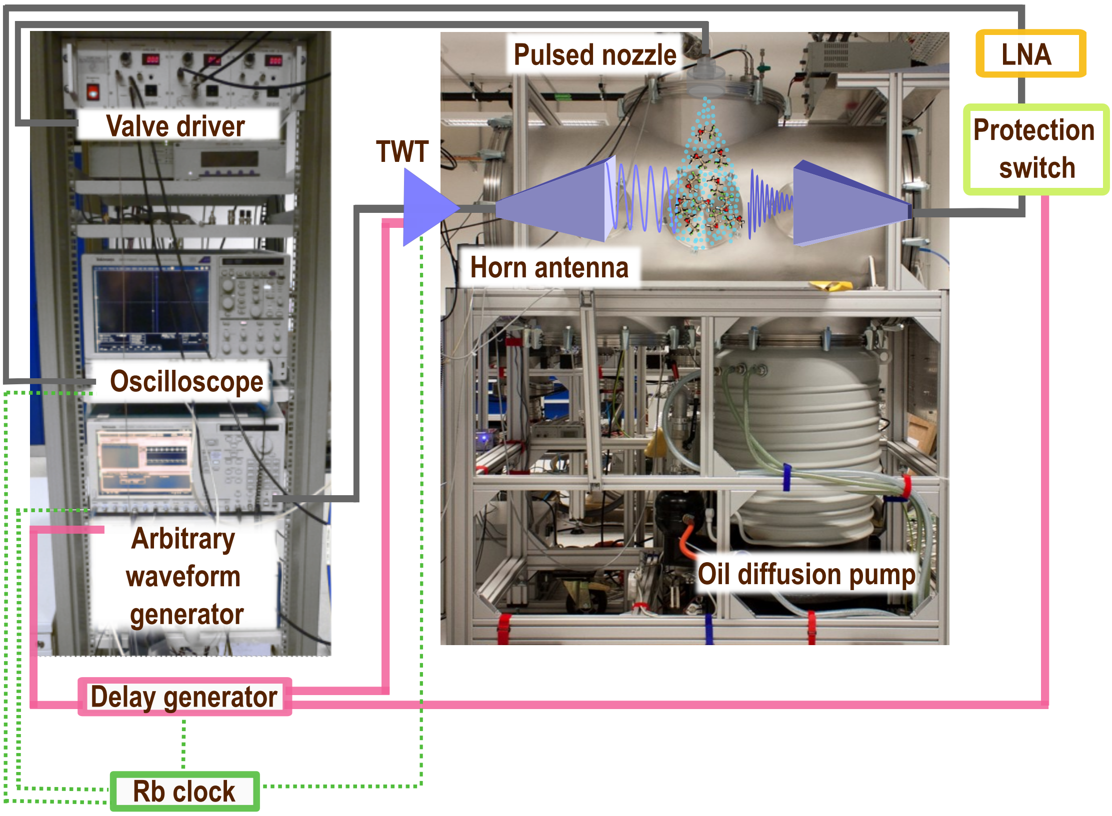

Figure 3.3: The Hamburg COMPACT spectrometer, which operates in the 2-18 GHz frequency region. The main components of the setup are labelled here.

3.2.1 The COMPACT (2-8 GHz) spectrometer

The COMPACT spectrometer covers a frequency range of 2–8 GHz. The heart of the spectrometer is a Tektronix 7122A arbitrary waveform generator (AWG), which is used to create the microwave chirps. The AWG can be operated in either interleave or dual-channel mode with 24 GS/s and 12 GS/s sampling rates, respectively. For broadband measurements, the AWG is operated in interleave mode (24 GS/s) with a Nyquist frequency up to 12 GHz. A 4 µs short sweep chirp is created using the AWG and amplified with an adjustable travelling wave tube amplifier (Amplifier Research 300T2G8, (TWT)) with an output power of 300 W to polarise the molecular ensemble on a time scale faster than the dephasing of the rotational signal which is typically around 10 µs. Two digital data channels (Marker1 and Marker2) of the AWG are used as separate marker channels to control the trigger and timings in the experiment. One marker (Marker1) triggers the digital delay generator (DDG, Stanford Research Systems Model DG645) that controls the timings of the amplifiers and the protection switches. The second marker (Marker2) of the AWG provides the trigger pulse to the digital oscilloscope to initiate the data collection. Another digital pulse generator, referred to as the master delay generator, triggers the AWG and valve driver.

After excitation and amplification, the chirped pulse is transmitted into a 163 cm long cylindrical vacuum chamber operating at a pressure of 10^{-6} mbar (while pulsing) using a high-gain dual-polarised horn antenna (Q-Par Angus WBHDP2-17# HGDual Polarised). The molecules of interest seeded either in a rare gas or its mixture are supersonically expanded into the vacuum chamber using the pulsed valve (Parker General Valve, Series 9) with a diameter of around 1 mm. The valve is mounted on the top of the vacuum chamber and is perpendicular to the horn antennas. Generally, Ne is used as a backing gas at a stagnation pressure of 1–5 bar. Depending on the vapor pressure, melting point, and boiling point of the molecule either a gas mixture (typically 0.1–0.5% of molecule in the inert gas) can be prepared or the sample can be heated to bring the molecules into the gas phase. Solid or liquid samples are usually transferred to the gas phase by placing the samples in the reservoir equipped with a heating system. The heater is positioned close to the reservoir to heat the sample directly, as marked in Fig. 3.2. The maximum temperature for heating the sample is limited to 180 °C, in the present setup.

The supersonically expanded molecular jet interacts with the perpendicular microwave chirped pulse broadcast via an excitation horn antenna with linear polarisation to polarise the molecular ensemble. The polarised molecular ensemble starts to decay when the chirped pulse is stopped. The decay of the macroscopic dipole moment is collected in the form of FID by a receiving horn antenna (QWH-DL-

2-18-N-SG-R) mounted on the opposite side with respect to the excitation horn antenna. The signal is then amplified via a low-noise amplifier (Miteq Amplifier AMF-5F-0200080-15-10P) and digitised using the 100 GS/s oscilloscope adjusted to a 25 GS/s digitisation rate for the broadband measurement of 2-8 GHz frequency range. The high-power excitation pulses during the molecular excitation are blocked by a PIN diode limiter (Aeroflex ACLM-4535) and a solid-state single pole single throw switch (SPST, Advanced Technical Materials S1517D) to protect the low-noise amplifier (LNA) and the oscilloscope. The FID can be collected typically for 10-50 µs, and in our experiment it is recorded for 40 µs. After collecting the FID, a fast Fourier transformation is performed using a Kaiser-Bessel window to obtain the spectrum in the frequency domain. Since the resolution is mainly determined by the length of the FID, a resolution of 25 kHz and an accuracy in frequency measurement better than 10 kHz are obtained in experiments with the collection of 40 µs of the FID. Other time-domain filters, such as rectangular and Gaussian windowing functions are also available to improve the baseline resolution of the spectrum. For example, the Gaussian function was employed in experiments with the M6WM technique applied to transiently chiral benzyl alcohol, as described in Chapter 8.

The most crucial devices of the experimental setup, i.e., microwave and trigger sources, as well as detectors for molecular emission signals, are phase-locked using a 10 MHz Rb quartz oscillator (Stanford Research FS 725) to ensure phase stability while averaging the FIDs of many acquisitions. This ensures all the electromagnetic waves travelling through AWG, amplifier, oscilloscope, and delay generator in the experiment are synchronised in each measurement.

The experiment begins with the start of the master delay generator, which is triggered internally and controls the valve driver and AWG (Fig. 3.4). The valve operation starts at time t_0 and remains open for t_{valve} as the molecules expand for t_{exp}. Typically, in an experiment using Ne carrier gas, t_{exp} is about 1.1–1.2 ms, and it varies when different carrier gases are used. After the expansion time, the molecules reach the interaction region, and the chirped-pulse excitation sequence is initiated with the AWG trigger from the master delay generator. Marker1 of AWG then provides the external trigger to the second delay generator (second DDG, Stanford Research Systems Model DG645), which controls the timings of the TWT and the protection switch involved in the excitation sequence. The chirped-pulse excitation begins with the opening of the protection switch for time t_{prot} followed by a short delay. After this short delay, the TWT amplifier is turned on for a time period of t_{amp} and amplifies only for the time the chirped pulse (t_{pulse}) is emitted, usually with some pre-buffer time to account for the ramp-up time of the TWT. The protection switch remains open all the time the TWT amplifier amplifies so

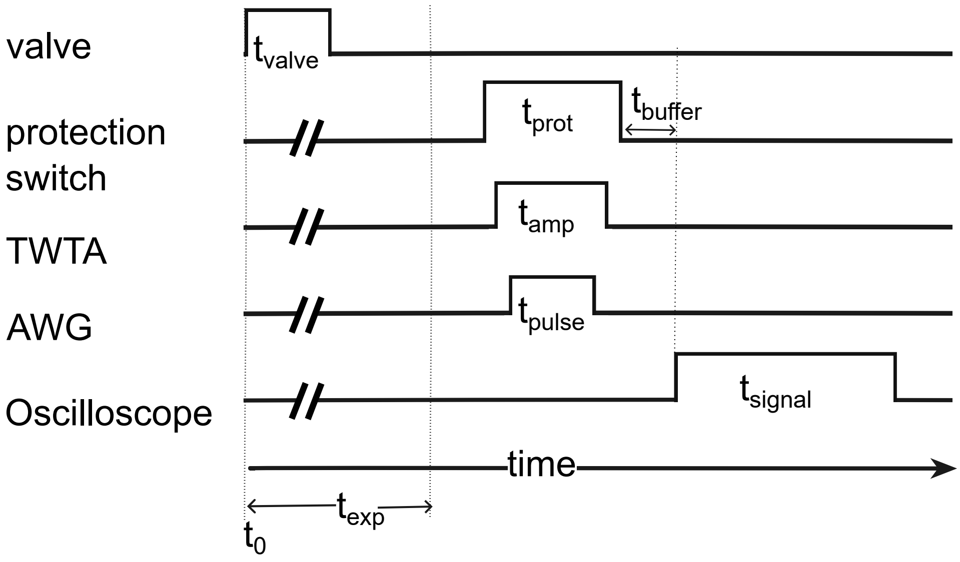

Figure 3.4: The scheme illustrates the timings of the devices and their triggers for the COMPACT spectrometer. The timings presented here are not to scale. The experiment begins with the start of the valve operation at time t_0 and is opened for t_{valve} time. The next step of the experiment continues with the start of the chirped-pulse excitation sequence when the expanded jet reaches the interaction zone after time t_{exp}. The excitation sequence begins with the start of the protection switch and travelling wave tube amplifier after a short delay. This is followed by the emission of a 4 µs long microwave chirp. The free-induction decay is then collected for 40 µs after a buffer time of about 0.5 µs to prevent the detection of any spurious signals from the excitation pulse.

that $t_{prot} > t_{amp} > t_{pulse}$. Finally, the AWG is triggered to fire the microwave pulse, which triggers the oscilloscope via its second marker channel to record the FID for a time, t_{signal}. A 0.5 µs buffer time is kept between the excitation pulse and the signal recording on the oscilloscope so that the excitation signal does not interfere with the recorded signal. Each experiment together with all the buffer timings takes about 52 µs.

The experiment uses the fast-frame approach, which reduces sample consumption and measurement time significantly, as several excitation-FID cycles can be recorded for each gas pulse. In this approach, for each gas pulse of about 600 µs, eight microwave chirped pulses (also called frames) of 4 µs length can be broadcast for excitation in a series with a 45 µs time gap between two consecutive chirps for collecting 40 µs of FID and 1 µs buffer time for the electronics. The acquired FID acquisitions are co-added and then subsequently averaged in the time domain. With the COMPACT spectrometer, the fast-frame setup can be performed together with a repetition rate of 9 Hz for the operation of the valve (meaning eight gas pulses). This, in combination with eight excitation chirps (or eight frames) per pulse train, results in an effective repetition rate of 72 Hz in experiments. This allows us to acquire approximately 4-6 million acquisitions in 24 hours of measurement and is often enough to give a signal-to-noise ratio (SNR) sufficient to observe rare isotopologues such as ^{13}C and ^{18}O in their natural abundances. One of the limitations to achieve the repetition rate is the pumping speed of the pumping system. The oil diffusion pump (Leybold DIP12000, pumping speed 12 000 1/s) is connected to one of two ISO-K 500 flanges from the bottom of the vacuum chamber. The diffusion pump is backed by a booster (Leybold Trivac D40B ATEX vacuum pump), and a mechanical pump (Leybold WAU251 RUVAC pump).

The spectrometer can also be extended to perform measurements in the 8-18 GHz frequency range by using a 40 W solid-state amplifier (SSA, Mercury Systems, L0618-46-T680) that operates in the 8-18 GHz frequency range along with a frequency doubler. Further details on the extended frequency range of the COMPACT spectrometer can be found in reference [89].

3.2.2 Modifications of the general setup for microwave three-wave mixing experiments

The experimental setup described in the previous section is employed to perform broadband measurement to record the rotational spectra of different molecular systems and to also perform chiral tag rotational spectroscopy experiments for chiral analysis, as outlined in the section 2.4 of Chapter 2. The general setup of the 2–8 GHz COMPACT spectrometer can also be used for performing M3WM experiments (described in section 2.4.2 of chapter 2) with minor modifications to the experimental setup.

M3WM is based on high-resolution rotational spectroscopy in the gas phase. It makes use of the geometrical orientation of the three dipole moment components within a chiral molecule as shown in Fig. 2.7(a). In an excitation and detection scheme consisting of a triad of three rotational transitions (as depicted in inset of Fig. 3.5), two transitions are excited simultaneously or sequentially, and the signal of the third transition, termed listen transition is recorded. The excitation of the first pulse of the triad known as the drive pulse transfers the population difference between the two rotational levels into a coherence. The resonant excitation of drive pulse creates a superposition state of the two rotational states. The second microwave pulse, called as twist pulse, is broadcast orthogonally to the drive pulse. This transfers existing coherence between the rotational states of the drive transition into coherence between the rotational states of the third transition that closes the M3WM triad. On applying this pulse sequence to a molecular ensemble, it generates a molecular response at the frequency of the third transition in a polarisation direction mutually orthogonal to the drive and twist pulses. The FID recorded at the listen transition has a phase difference of π radians between opposite enantiomers and allows for their differentiation (Fig. 3.5).

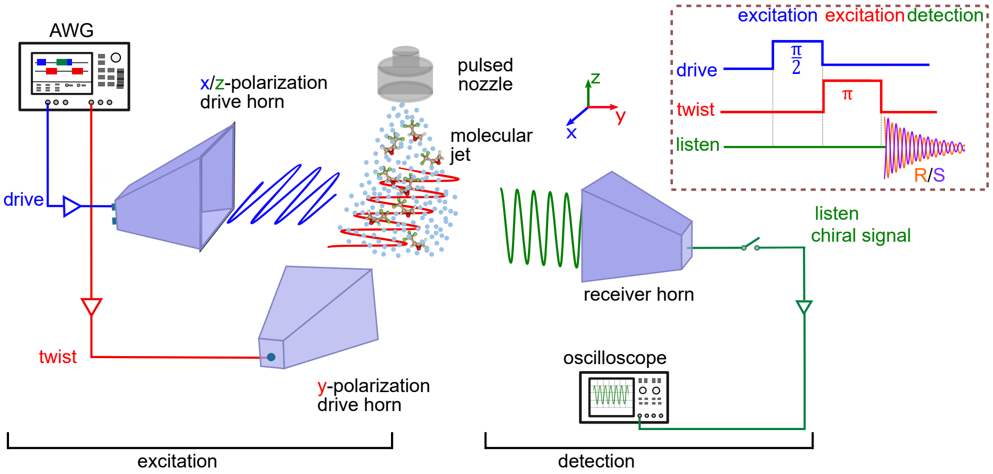

Figure 3.5: Scheme of the modified COMPACT setup used for the microwave three-wave mixing experiment. Drive and twist pulses are both generated by the AWG and amplified with different amplifiers and broadcast by a dual-polarised horn antenna; the chiral signal is collected by the receiving horn antenna and digitised using the oscilloscope. The excitation and detection scheme of microwave three-wave mixing with the free-induction decay that has a phase difference of π between the two enantiomers is shown in the inset box. Red, blue, and green colors represent the polarisation directions of microwave fields in the laboratory frame.

The preparation of M3WM experiments involves identifying a set of three rotational transitions forming a closed loop within the frequency range of the chirality-sensitive spectrometer. This requires information on the rotational energy levels and transition intensities obtained from their respective rotational spectrum. M3WM cycles is typically arranged so that the strongest transition is chosen for the listen transition.

For M3WM experiments, the AWG is used in dual-channel mode to generate the drive and twist excitation pulses of the M3WM scheme from separate channels of the AWG and then amplified using different amplifiers depending on the frequency of the two exciting transitions. The rotational transitions in the frequency range of 2-8 GHz can be amplified with a TWT amplifier or with a 3 W SSA (2-8 GHz, Mini-Circuits AMPLIFIER ZVE-3W-83+). The rotational transitions in the 2-6 GHz frequency range can also be amplified with a 50 W SSA (2-6 GHz, AAMCS-AMP-2000M-6000M-50dB-47dBm-01). The transitions covering the 8-12 GHz frequency range can be pre-amplified, doubled, and then amplified further with a 40 W SSA. Each of the exciting microwave pulses of the M3WM scheme is optimised in a single-photon excitation experiment before the three-wave mixing experiments to achieve the optimal conditions for the maximum M3WM signal. Nutation curves are performed, where each exciting pulse is investigated for the signal intensity as a function of pulse duration, and they are optimised for either a $\pi/2$ or a π pulse condition (eq. 2.62) as mentioned in section 2.4.2 of Chapter 2.

In the M3WM experiment, the drive transition is optimised for $\pi/2$-condition, while the twist transition is optimised for a π-condition. The optimised pulse durations determine the pulse sequence which can have drive and twist microwave pulses applied either simultaneously or sequentially. This subsequently dictates the timings of the amplifiers and the protection switch on the second delay generator.

In the modified COMPACT setup for M3WM experiments, the drive pulse is applied in the z-polarisation (or x-polarisation) direction using the same excitation horn antenna used in broadband experiments. The twist pulse is broadcast orthogonally to the drive pulse in the y-polarisation direction using a second horn antenna (1-10 GHz) fixed on the side flange and positioned perpendicular to the excitation (polarised in the x- or z-direction) and emitter horn antenna. The aligned electric dipole polarisation induced by the interaction of the molecular jet with the drive and twist pulses of the three-wave mixing scheme starts to oscillate at the frequency of the listen transition in the third mutually orthogonal polarisation direction. The listen signal is collected via the receiver horn antenna and then amplified and digitised using a fast oscilloscope, like in broadband experiments. The FID collected with the digital oscilloscope has a phase difference of π for two enantiomers at the listen frequency. These modifications to the experimental setup of the COMPACT spectrometer enabled the identification of enantiomers in chiral mixtures, such as thyme oil and peppermint oil, using rotational spectroscopy.[49, 186]

3.2.3 Additional modifications for enantiomer-selective population transfer experiments

The technique of M3WM has been extended further to perform enantiomer-selective population transfer experiments, as explained in section 2.5 of Chapter 2. The phase difference of π in the FID of the listen transition can be utilised to selectively populate one enantiomer in a particular rotational state while depleting the population of the other enantiomer in that state but enhancing it in the connecting state of the corresponding rotational transition. By applying a direct excitation at the frequency of the listen transition, which interferes with the phase-dependent listen signal generated from the M3WM cycle, the coherence difference between enantiomers is transferred into a population difference and enantiomer-selective population transfer is achieved.

The experimental approach for the enantio-selective population transfer experiments has already been demonstrated by Pérez *et al.*[62, 65] using the modified COMPACT setup. In this work, the COMPACT setup was modified to create enantio-selective population transfer in trifluoromethyl oxirane.[50] The experiment is set up according to the frequencies involved in the energy scheme and the pulse sequence. Fig. 5(b) of the manuscript attached in Chapter 7 shows the energy scheme used to achieve and enhance enantiomer-selective population transfer in the trifluoromethyl oxirane molecular system. The schematic of the experimental setup used for this experiment is depicted in Fig. 3.6(c).

The AWG is used in dual-channel mode to generate five different microwave excitation pulses with optimised durations, which are then amplified using three different amplifiers. According to energy scheme in Fig. 5(b) of the manuscript in Chapter 7[50], the two drive pulses #1, #4 and the preceding pulse #6 are in the 6-9 GHz range and thus have to be amplified and doubled before being amplified with the 40 W SSA. The twist pulses #2 and #5 are low-frequency rotational transitions and are amplified using a 300 W TWT amplifier. The transfer pulse #4 was amplified with a 3 W SSA. Each of these microwave excitation pulses are initially optimised with the corresponding amplifiers by measuring the nutation curves. This optimisation can be done either via direct excitation of that pulse or via a M3WM experiment. In this energy scheme, pulses #1, #3, #4 were optimised by a single-photon experiment, while pulse #2 was optimised via a M3WM experiment. The nutation curve plots for all five pulse involved in the enantiomer-selective population transfer of trifluoromethyl oxirane are provided in the supplementary information of the article attached in Chapter 7. The optimised pulse durations are then used to determine the optimal pulse sequence, which dictates the timings of amplifiers, switches connected to amplifiers, and the protection switch on the second delay generator.

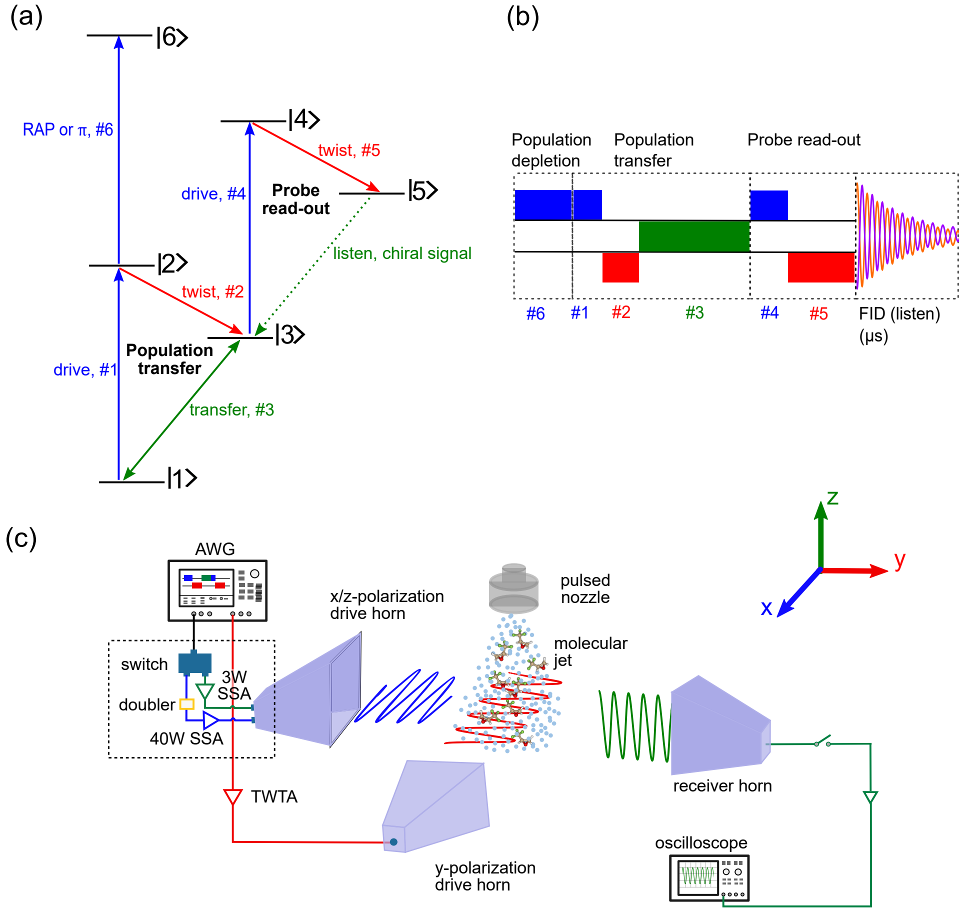

Figure 3.6: (a) Energy scheme for creating enantiomer-selective population transfer as demonstrated for trifluoromethyl oxirane in Chapter 7. (b) Pulse scheme for the corresponding energy scheme depicted in (a). Pulse durations are not scaled. (c) Schematic of the experimental setup to perform enantiomer-selective population transfer experiments discussed in section 2.5 of Chapter 2. Here, both channels of the AWG are used to create a five-pulse sequence that is broadcast in three different polarisations using dual-polarised horn antennas. The pulse sequence from channel 1 of the AWG is fed through the single pole double throw switch, to amplify with different amplifiers and broadcast them in orthogonal polarisations (e.g. x, or z). Red, blue, and green colors represent the polarisation directions of microwave fields in the laboratory frame. The free induction decay is collected in the orthogonal direction of excitation.

As the polarisation direction of pulse #3 must be orthogonal to the pulses #1 and #4, a single pole double throw switch (SPDT) with a switching speed of up to 25 ns was used to feed the signals into the respective amplifiers. The switch receives a single input from the AWG, and its two outputs are subsequently connected to a 40 W amplifier (for pulses #1, #4) and a 3 W amplifier (for pulse #3). Two marker channels (Marker1 and Marker2) of channel 2 of the AWG are then used to trigger the output of the switch through TTL pulses. In this way, two sets of pulses, pulses #1 and #4, and pulse #3, are amplified with two different amplifiers and broadcast orthogonally into a vacuum chamber using a single channel of the AWG. Pulses #1, #4, and #6 are applied in x-polarisation, pulses #2, #5 in y-polarisation, and #3 in the z-polarisation direction same as in which FID is collected. Thus, a five-microwave pulse sequence could be excited to create and enhance the efficiency enantiomer-selective population transfer in trifluoromethyl oxirane using the COMPACT spectrometer. The results for these experiments are provided in Chapter 7. A similar experimental setup could be employed to induce chirality in a transiently chiral molecule, benzyl alcohol, using a M6WM approach described in section 2.6 of Chapter 2. The details on the experimental setup for performing M6WM experiments on benzyl alcohol is provided in reference [64].

Part I: Conformational flexibility in molecules investigated with broadband rotational spectroscopy

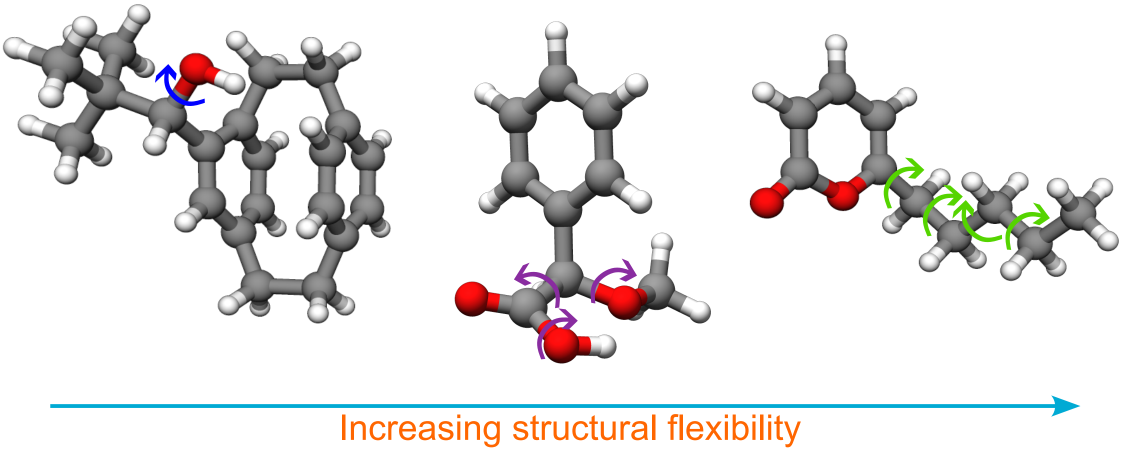

Chapter 4

[2,2]-Paracyclophane: A bridged benzene dimer

Cyclophanes are strained organic molecules that contain aromatic ring(s) as well as aliphatic unit(s) that bridge the aromatic unit(s).[187] The aromatic rings provide rigidity to their structure while the aliphatic units give flexibility.[187] Cyclophanes play an important role as hosts in host-guest chemistry, being able to encapsulate the guest between the two aromatic rings and assembly.[188–190] Due to their peculiar structural properties, they also have wide applications in material science with interesting photophysical and optoelectronic properties.[191–194]

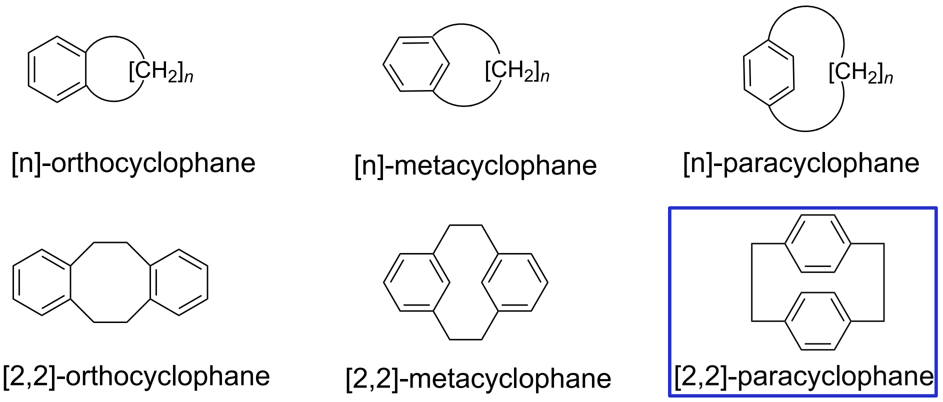

Figure 4.1: Different types of cyclophane molecules are categorised based on the relative position of the aliphatic units, as adapted from reference [187]. Here, [n] represents the number of methylene groups in the aliphatic bridge. The lower row illustrates the three different possible configurations of cyclophane with two benzene rings bridged via an ethylene group.

Cyclophanes can be classified into three classes according to the relative position of the aliphatic units. The prefixes ortho, meta, or para represent the relative position of the attachment to the aromatic systems, while [n] indicates the number of methylene groups in the aliphatic bridge. For example, cyclophanes with two benzene rings can be connected by an ethylene bridge at three different positions giving rise to three cyclophane configurations: [2,2]-orthocyclophane, [2,2]-metacyclophane, and [2,2]-paracyclophane, as shown in Fig. 4.1.[187] Several classes of cyclophanes consisting of two or more aromatic systems and aliphatic bridges have been reported in the literature.[187] Out of this, [2,2]-paracyclophanes have particularly gained a lot of attention from researchers ever since their discovery by Brown and Farthing[195] followed by its first synthesis by Cram and Steinberg.[196] [2,2]-Paracyclophanes and their derivatives gained popularity among chemists due to their unusual photophysical and optoelectronic properties arising from their unique three-dimensional structure.[197]

[2,2]-Paracyclophanes consist of two co-facially stacked benzene units, the "decks", connected by the ethylene chains, the "bridges". The ethylene bridge causes the aromatic carbons to bend out of the benzene plane, giving rise to a unique "bent and battered" planar chiral structure of [2,2]-paracyclophanes, as shown in Fig. 4.2(a). The two stacked benzene rings have a maximum distance of 3.09 Å between them, which is even shorter than the distance of 3.4 Å between the graphite planes.[198] The co-facial stacking of aromatic rings at such close proximity leads to transannular π-π strain in the rings with a strain energy of about 31 kcal/mol.[199] This strain forces the two benzene rings to bend out of their inherent planarity and also leads to the lengthening of the C-C ethylene bond to 1.63 Å compared to 1.54 Å in ethane.

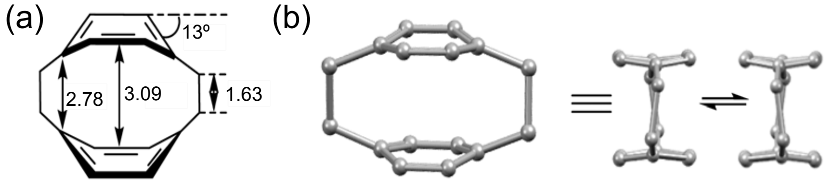

Figure 4.2: (a) [2,2]-Paracyclophane illustrating the strain and structural parameters (Å) obtained from X-ray diffraction analysis. This figure also displays transannular distances (in Å) and benzene ring deformations. The aromatic ring distance is 3.09Å. (b) Two different side views of [2,2]-paracyclophane are presented to illustrate the structural distortions. Figure is adapted from reference [198].

The distortion abnormalities in [2,2]-paracyclophanes, deviating from normal aromatic planarity due to transannular strain, correlate with their properties and unusual reactivity behaviour. Thus, it becomes important to investigate the connectivity and the relative position of the aromatic units in [2,2]-paracyclophanes. Most of the recent work on [2,2]-paracyclophanes so far has been focused on the synthesis of functionalised [2,2]-paracyclophanes and its derivatives to find their applications in asymmetric synthesis, energy materials, and polymer coatings.[197]. The substitution of a functional group on one or both of the benzene rings results in a planar chirality, while substitution on the ethylene bridge results in central chirality in [2,2]-paracyclophanes. These planar chiral paracyclophanes have been utilised in preparing chiral auxiliaries or chiral ligands for regioselective synthesis in synthetic organic chemistry and organometallic chemistry.[200] [2,2]-Paracyclophane has demonstrated its versatility as tectons for structured polymers and supramolecular chemistry.[197] The progress in the area of [2,2]-paracyclophane chemistry have revolved around synthesising functional materials for diverse applications, emphasising the understanding of their structure-reactivity relationships and decoding their physical-chemical properties.[201] Therefore, it is essential to discern their accurate structures and gain information on their intramolecular interactions and internal dynamics.

In this study, the conformations of a series of substituted [2,2]-paracyclophanes are examined in the gas phase while also analysing their intramolecular interactions. CP-FTMW spectroscopy (as described in section 3.2 of Chapter 3) was used to determine the accurate gas-phase structure of monosubstituted [2,2]-paracyclophane. The main molecule from this family of compounds, [2,2]-paracyclophane, cannot be investigated by rotational spectroscopy due to its lack of a permanent electric dipole moment. However, through the substitution of different functional groups on the aromatic rings or the introduction of heteroatoms such as oxygen, nitrogen, or halogens, a strong dipole moment can be induced, which makes the [2,2]-paracyclophane molecules observable by MW spectroscopy. Monosubstituted [2,2]-paracyclophanes, investigated here, can be synthesised through electrophilic aromatic substitution that inserts functional groups either in a single step (e.g. CHO, COR) or by quenching their lithium derivative prepared from bromide with various electrophiles, thereby leading to the incorporation of other chemical groups such as OH, COOH.[197] The distorted structure and steric effects within the electronic rings increase the basicity or nucleophilicity of the [2,2]-paracyclophanes, thus facilitating the electrophilic substitutions and making [2,2]-paracyclophanes an attractive synthon.

The rotational spectra and quantum-chemical calculations of four structural homologues of [2,2]-paracyclophanes with different electrophilic substituents: hydroxy (OH), aldehyde (CHO), ketone (RCO), and carboxylic acid (COOH) groups are presented here. This investigation sheds light on the conformational arrangement of these mono-substituted [2,2]-paracyclophanes. The subsequent section briefly outlines the experimental and computational methodologies used in this study. This is followed by the spectroscopic assignments of different conformers of [2,2]-paracyclophane derivatives and a discussion of the overall findings in a comparative manner.

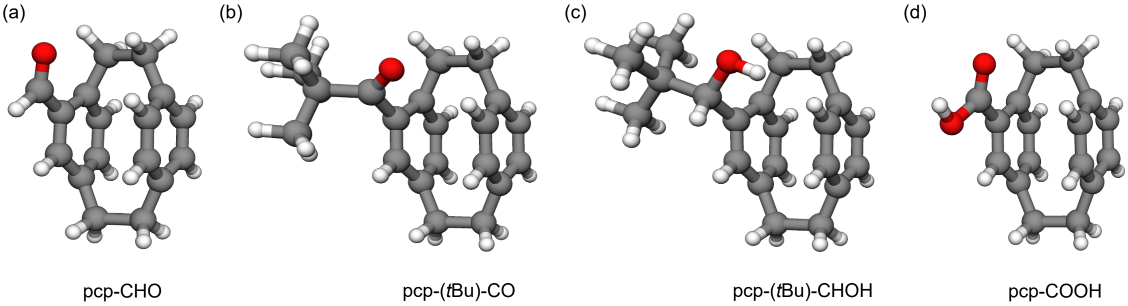

Figure 4.3: The four derivatives of [2,2]-paracyclophane investigated in this work: pcp-CHO, pcp-(*t*Bu)-CO, pcp-(*t*Bu)-CHOH, and pcp-COOH.

4.1 Experimental and computational details

The four derivatives of [2,2]-paracyclophanes, pcp-CHO ($C_{17}H_{16}O$), pcp-(*t*Bu)-CO ($C_{21}H_{24}O$), pcp-(*t*Bu)-CHOH ($C_{21}H_{26}O$), and pcp-COOH ($C_{17}H_{16}O_2$) (Fig. 4.3), synthesised by the research group of Prof. Stefan Bräse, were used without any further purification for measuring their rotational spectra. All the samples are white solid powders, with melting points ranging from 70°C to 180°C. The structures of these derivatives are shown in Fig. 4.3.

All measurements were performed with the COMPACT spectrometer, which is detailed in Chapter 3 and special aspects of these particular measurements are described in the following. The molecules were seeded into a carrier gas to generate a supersonic expansion using a pulsed nozzle (Parker General valve) operated at a repetition rate of 6 GHz. The substituted aldehyde and ketone species were heated up to 75°C and 80°C, respectively, while the hydroxy and carboxylic acid derivatives were heated to about 180°C. Ne was used as a carrier gas at a stagnation pressure of 2 bar to generate the supersonic expansion with the sample molecules diluted in it.

After the supersonic expansion into the vacuum chamber, the molecular ensemble was polarised with a 4 µs amplified chirped pulse spanning 2-8 GHz of the frequency range. Following excitation, 40 µs of the FID of the macroscopic ensemble of the polarised molecules were recorded using a oscilloscope. This yielded a frequency resolution of 25 kHz in the rotational spectra obtained by Fourier transformation using a Kaiser-Bessel window function. For pcp-CHO, pcp-(*t*Bu)-CO, and pcp-(*t*Bu)-CHOH, 2.1, 1.2, and 1.4 million FIDs, respectively, were coadded and averaged to obtain the final rotational spectrum. Only 700 thousand acquisitions could be acquired for pcp-COOH after several tries, due to difficulties in getting it into the gas phase.

The analysis of the experimental spectra was supported by quantum-chemical calculations performed with ORCA.[119, 120] Fig. 2.6 illustrates the workflow employed for this and subsequent conformational analysis work presented in this thesis. The minimum energy structures were predicted by employing the GFNn-xTB method CREST[121] and were then optimised using ORCA[120] at the B3LYP-D3(BJ)/def2-TZVP level of theory.[124–127, 134, 202] All the structures were confirmed to be real minima by harmonic frequency calculations and were sorted by their relative energy including zero-point energy corrections. The different interactions in the paracyclophane moiety and its derivatives were explored by performing non-covalent interactions (NCI) analysis calculations.[138, 203] Potential energy scans varying some dihedral angles were also performed to explore the conformational relaxation possibilities for the hydroxy-substituted paracyclophane. The interconversion barriers were calculated at the same level of theory, i.e., B3LYP-D3(BJ)/def2-TZVP.

The assignment of the species in a rotational spectrum is guided by the rotational constants and dipole moments obtained from quantum-chemical structures. This method of guided assignment of molecular species has given good results for large molecules[47] and clusters, such as studies on the sevoflurane trimer.[204] The experimental spectra were initially assigned using a recurrent fit based on Watson's A-reduction Hamiltonian in the I^r representation as implemented in PGOPHER.[141, 205] These initial rotational parameters were refined with Pickett's SPFIT/SPCAT program suite.[142]

4.2 Results

The subsequent section presents a conformational analysis of each monosubstituted [2,2]-paracyclophane and the gas-phase structures identified in experiments, this is followed by an investigation into intramolecular interactions.

4.2.1 Aldehyde-substituted [2,2]-paracyclophane, pcp-CHO

Two conformers with different arrangements for the aldehyde group were predicted from quantum-chemical calculations (Fig. 4.4(a)), with one of them being significantly more stable and populated than the second conformer (Table 4.1). The experimental spectrum of pcp-CHO is presented in the positive trace (black) of Fig. 4.4(b). Table 4.1 lists the computed and experimentally determined rotational constants of both of these conformers.

The rotational spectrum for the most stable conformer, pcp-CHO-1, shows predominantly a-type transitions, as μ_a is the largest dipole-moment component as provided in Table 4.1. In the final fit, a-, b- and c-type rotational transitions were assigned and fitted. The observed rotational lines range from $J = 2$ to $J = 10$, with a maximum K_a of 8 in the experimental spectrum of the pcp-CHO-1 conformer. The second lowest conformer, with a predicted relative energy of 4.5 kJ/mol (pcp-CHO-2), was also observed. The rotational spectrum for this conformer is rich with plenty of characteristic patterns, although with overall weak intensity. These patterns consist of four rotational transitions, out of which the two lines in the middle are either a-type or c-type transitions, while the outside lines are b-type transitions (*baab* or *bccb*).[109]

The sufficient SNR of the rotational spectrum of the dominant conformer, pcp-CHO-1, allowed the observation of the rotational spectra of all of its singly-substituted ^{13}C isotopologues in natural abundance (1.1%) for the most intense rotational transition (i.e., $6_{1,5} - 5_{1,4}$ with a SNR of 900:1) and many other transitions. Table 1 in the appendix summarises the experimentally determined rotational parameters of the seventeen singly substituted ^{13}C isotopologues and their comparison with the parent species. The atom positions of these carbon atoms with respect to the center of mass of the molecule were derived using the Kraitchman equations described in section 2.1.4.3. This facilitated the construction of the so-called substitution structure, r_s, of the [2,2]-paracyclophane moiety displayed in Fig. 4.5, compared with the equilibrium structure, r_e, obtained from the quantum-chemical calculations at the B3LYP-D3(BJ)/def2-TZVP level of theory.

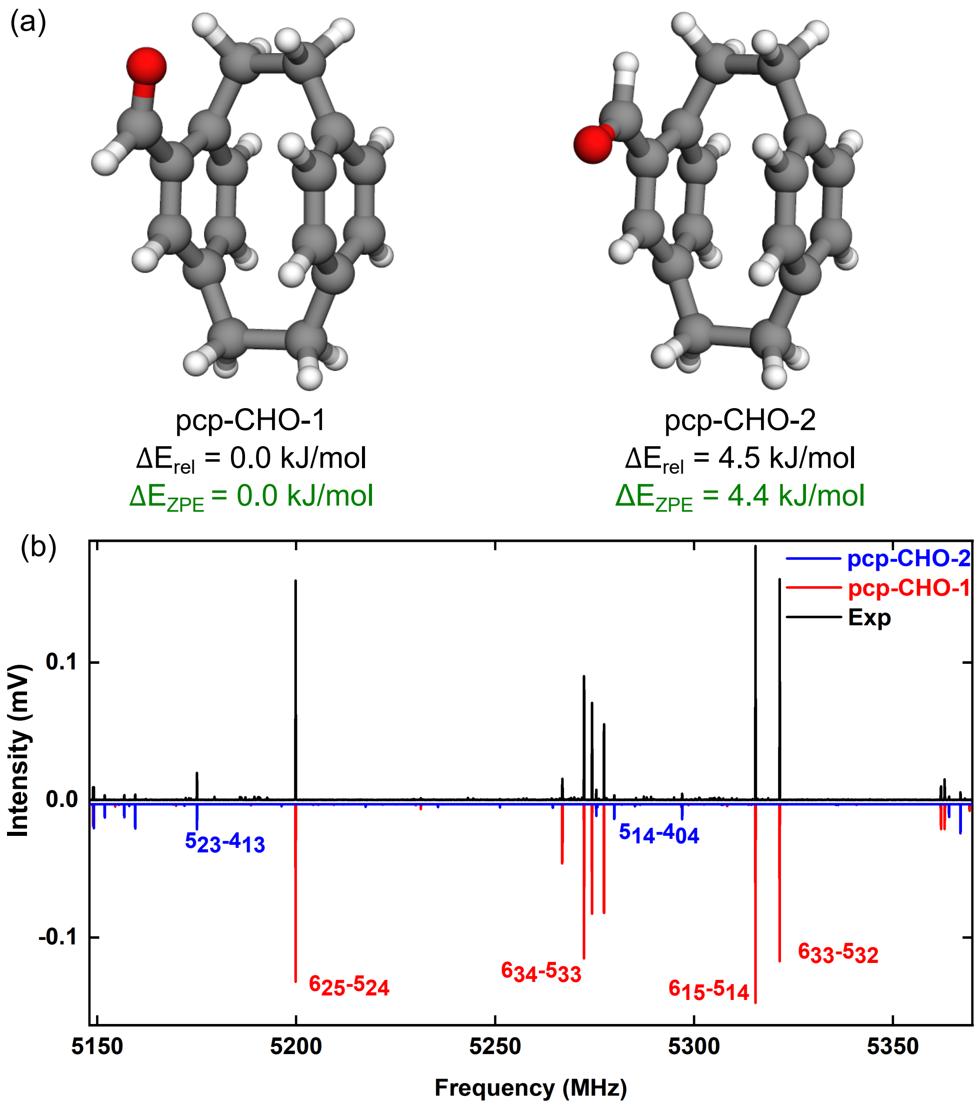

Figure 4.4: (a) Molecular structures of both conformers of pcp-CHO optimised at the B3LYP-D3(BJ)/def2-TZVP level of theory, along with their relative energies without (black) and with zero-point energy correction (red) in kJ/mol. (b) The upper trace is the experimental rotational spectrum of pcp-CHO in the 5150-5355 MHz region, while the lower traces are the simulations based on the experimentally fitted rotational parameters presented in Table 4.1. The most stable conformer, pcp-CHO-1, is represented in red and pcp-CHO-2 in blue. For the simulations, a rotational temperature of 3 K gave the best match between the simulated and experimental intensities for both conformers.

Table 4.1: Relative energies and experimental rotational parameters of pcp-CHO conformers are tabulated. Relative energies and predicted parameters reported here are obtained at the B3LYP-D3(BJ)/def2-TZVP level of theory. The experimental parameters are obtained by fitting in Watson's A-reduction scheme using the SPFIT program.

Parameters	pcp-CHO-1		pcp-CHO-2	
	calc.	expt.	calc.	expt.
A/MHz[1]	702.4	703.45372(19)	627.1	628.42855(21)
B/MHz	468.4	466.28972(11)	491.1	488.907724(89)
C/MHz	408.8	407.45446(12)	419.9	419.43526(14)
Δ_J/kHz	-	0.0119(10)	-	0.02158(70)
Δ_{JK}/kHz	-	0.0215(31)	-	-
Δ_K/kHz	-	-	-	0.0387(37)
δ_J/kHz	-	-	-	-0.00808(57)
δ_K/kHz	-	0.0762(48)	-	0.0887(50)
μ_a/D[2]	-3.0	Y	-1.5	Y
μ_b/D	-0.5	Y	2.0	Y
μ_c/D	1.2	Y	2.4	Y
N[3]	-	196	-	184
σ/kHz	-	6.8	-	6.4
ΔE_{rel}(kJ/mol) [4]	0.0	-	4.5	-
ΔE_{ZPE}(kJ/mol)	0.0	-	4.4	-

[1] A, B, and C are the rotational constants, and Δ_J, Δ_{JK}, Δ_K, δ_J, and δ_K are the quartic centrifugal constants in Watson's A-reduction scheme. [2] Y and N indicate whether the respective type of rotational transition was observed or not. [3] N denotes the number of fitted transitions, and σ is the root-mean-square deviation of the fit. [4] ΔE_{rel}, ΔE_{ZPE} are the calculated (B3LYP-D3(BJ)/def2-TZVP) relative energies without and with zero-point energy (ZPE) correction, respectively.

This structural information was then corroborated by fitting the effective ground state structure, r_0 using STRFIT program available at PROSPE (as mentioned in section 2.1.4.2 of Chapter 2).[117] The r_0 parameters are indicated in blue in Fig. 4.5. Table 2 summarises the r_s and r_0 parameters such as bond lengths and angles, compared with the r_e. The SNR was not sufficient to observe the rotational spectra of the ^{18}O isotopologues (0.2%) in natural abundance or any other rare isotopologue for the conformer pcp-CHO-2.

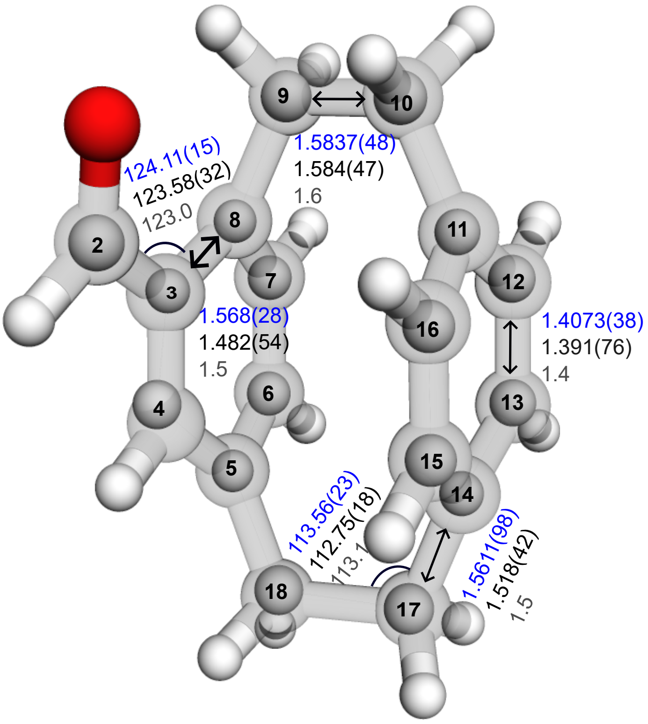

Figure 4.5: An overlay of the experimentally determined r_s (inner spheres) structure with respect to calculated r_e equilibrium geometry is displayed. The bond lengths and bond angles for the r_s structure are shown in blue, for the r_0 in black and for r_e in grey.

4.2.2 Ketone-substituted [2,2]-paracyclophane, pcp-(*t*Bu)-CO

It was then interesting to explore how the structural arrangement of the carbonyl group changes on substituting an alkyl group in place of a hydrogen atom. A ketone-substituted [2,2]-paracyclophane with a *tert*-butyl group on the carbonyl carbon (Fig. 4.3) was measured with the COMPACT spectrometer. Only one conformer was predicted from quantum-chemical calculations within the threshold of 10 kJ/mol, while the next two conformers were found to be 20 kJ/mol higher in energy. The most stable conformer pcp-(tBu)-CO-1 is expected to be more stable than the other two conformers due to the stabilising interaction of the carbonyl group with the ethylene hydrogen atoms.

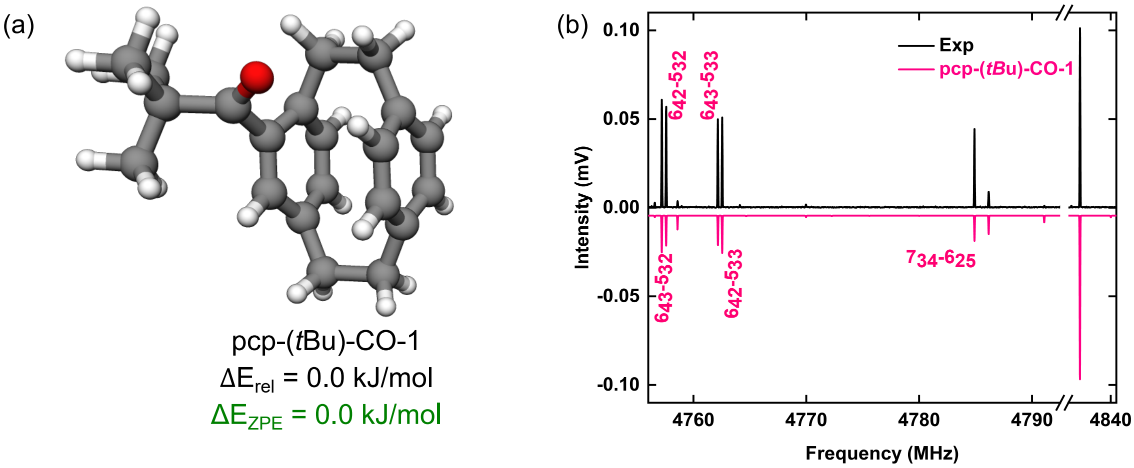

Figure 4.6: (a) Optimised geometry of the experimentally observed conformer of pcp-(tBu)-CO obtained at the B3LYP-D3(BJ)/def2-TZVP level of theory along with its relative energy without (black) and with zero-point energy correction (green) in kJ/mol. (b) An excerpt of the rotational spectrum of pcp-(tBu)-CO is displayed. The top trace is the experimental spectrum while the bottom trace represents the simulation based on fitted rotational parameters at a temperature of 3 K.

Some spectral patterns compatible with pcp-(tBu)-CO-1 conformer were observed in the experiment. A section of the experimental rotational spectrum of pcp-(tBu)-CO is presented in Fig. 4.6(b) in black. Plenty of characteristic *bccb* patterns were observed and guided the initial assignment for the ketone derivative. These patterns consist of two *c*-type lines in the middle, while the outside lines are *b*-type transitions. The rotational transitions ranging from J=3 to J=23 with a maximum K_a of 13 are fitted. The experimentally determined rotational constants from SPFIT/SPCAT are tabulated in Table 4.2 along with the computed parameters obtained at the B3LYP-D3(BJ)/def2-TZVP level of theory.

Table 4.2: Experimental rotational parameters of the pcp-(tBu)-CO-1 conformer along with the predicted parameters and relative energy obtained at the B3LYP-D3(BJ)/def2-TZVP level of theory are listed. The experimental parameters are obtained in Watson's A-reduction scheme using the SPFIT fitting program.

Parameters	pcp-(tBu)-CO-1	
	calc.	exp.
A/MHz[1]	506.5	511.186015(60)
B/MHz	255.7	253.035291(38)
C/MHz	221.1	219.190469(34)
Δ_J/kHz	-	0.003823(88)
Δ_{JK}/kHz	-	-0.00769(25)
Δ_K/kHz	-	0.03018(29)
δ_J/kHz	-	0.000307(27)
δ_K/kHz	-	-
μ_a/D[2]	0.3	Y
μ_b/D	2.0	Y
μ_c/D	1.7	Y
N[3]	-	792
σ/kHz	-	5.9
ΔE_{rel}(kJ/mol) [4]	0.0	-
ΔE_{ZPE}(kJ/mol)	0.0	-

[1] A, B, and C are the rotational constants, and Δ_J, Δ_{JK}, Δ_K, δ_J, and δ_K are the quartic centrifugal constants. [2] Y and N denote whether the respective type of rotational transition was observed or not. [3] N signifies the number of fitted transitions while σ is the root-mean-square deviation of the fit. [4] ΔE_{rel}, ΔE_{ZPE} are the relative energies without and with zero-point correction, respectively.

4.2.3 Hydroxy-substituted [2,2]-paracyclophane, pcp-(*t*Bu)-CHOH

The conformational landscape and structure of a hydroxy analogue, pcp-(*t*Bu)-CHOH, was also explored with rotational spectroscopy. The group provides some flexibility to the molecules, and in this case, three different rotamers, (*anti* (a), *gauche*(+) (gp), *gauche*(-) (gm)) are identified within a threshold of 10 kJ/mol from quantum-chemical calculations, which are shown in Fig 4.7.

The pcp skeleton is the same for the three rotamers, which differ only in the orientation of the hydroxy group. The pcp-(*t*Bu)-CHOH-gm conformer is the global minimum; pcp-(*t*Bu)-CHOH-a is calculated to be essentially isoenergetic; and on the basis of its relative energy, the other rotamer pcp-(*t*Bu)-CHOH-gp could also be populated in our experiments.

Out of these three low-energy isomers, only the most stable conformer, pcp-(*t*Bu)-CHOH-gm rotamer with a hydroxy group in gauche(-) orientation have been identified in the experiment, as shown in Fig. 4.8. The observation of only the pcp-(*t*Bu)-CHOH-gm conformation can be explained by conformational relaxation processes between the conformers.

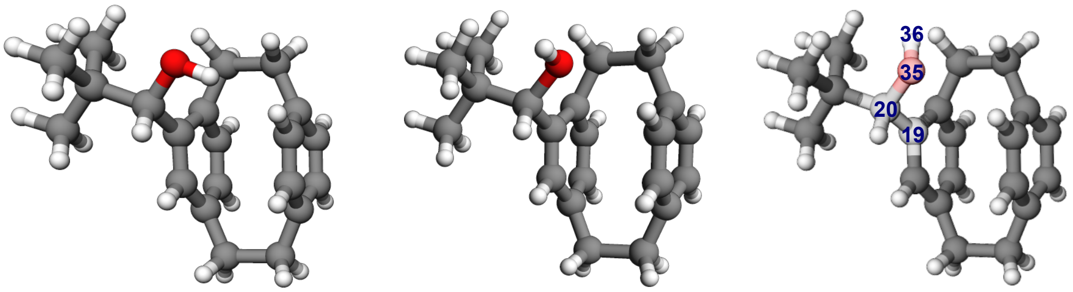

pcp-(*t*Bu)-CHOH-gm
ΔE_{rel} = 0.0 kJ/mol
ΔE_{ZPE} = 0.0 kJ/mol

pcp-(*t*Bu)-CHOH-a
ΔE_{rel} = 0.7 kJ/mol
ΔE_{ZPE} = 0.6 kJ/mol

pcp-(*t*Bu)-CHOH-gp
ΔE_{rel} = 4.2 kJ/mol
ΔE_{ZPE} = 4.2 kJ/mol

Figure 4.7: Optimised structures of the three conformers of pcp-(*t*Bu)-CHOH obtained at the B3LYP-D3(BJ)/def2-TZVP level of theory along with their relative energies without (black) and with zero-point energy correction (green) in kJ/mol. The group dihedral angle $\angle\theta$ (H36-O35-C20-C19) that gives rise to the three different rotamers of pcp-(*t*Bu)-CHOH is labelled on the pcp-(*t*Bu)-CHOH-gp conformation.

Table 4.3: Experimental and calculated rotational parameters of pcp-(tBu)-CHOH rotamers along with their relative energies predicted at the B3LYP-D3(BJ)/def2-TZVP level of theory.

Parameters	pcp-(tBu)-CHOH-gm		pcp-(tBu)-CHOH-a	pcp-(tBu)-CHOH-gp
	calc.	exp.	calc.	calc.
A/MHz[1]	512.7	518.28485(30)	517.0	515.2
B/MHz	249.7	248.176996(80)	249.8	249.5
C/MHz	217.2	214.382062(73)	216.4	216.8
Δ_J/kHz	-	0.00441(27)	-	-
Δ_{JK}/kHz	-	-0.0160(14)	-	-
Δ_K/kHz	-	0.5583(13)	-	-
δ_J/kHz	-	-	-	-
δ_K/kHz	-	0.0487(60)	-	-
μ_a/D[2]	1.2	Y	-1.6	-0.6
μ_b/D	-0.8	Y	- 1.0	-0.6
μ_c/D	0.1	N	-0.4	1.4
N[3]	-	169	-	-
σ/kHz	-	6.4	-	-
ΔE_{rel}/(kJ/mol)[4]	0.0	-	0.7	4.2
ΔE_{ZPE}/(kJ/mol)	0.0	-	0.6	4.2

[1] A, B, and C are the rotational constants and Δ_J, Δ_{JK}, Δ_K, δ_J, and δ_K are the quartic centrifugal constants. The errors given here for the measured values are the standard errors. [2] Y and N indicate if the respective types of rotational transitions were observed or not. [3] N is the number of lines included in the fit and σ is the standard deviation of the fit. [4] ΔE_{rel}, ΔE_{ZPE} are the relative energies without and with zero-point correction, respectively.

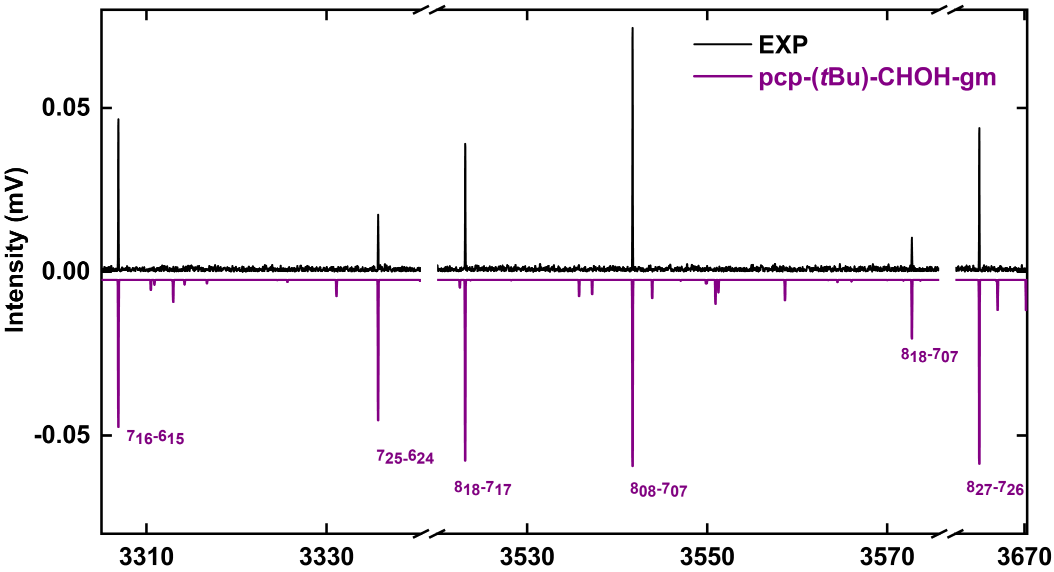

Figure 4.8: A portion of the experimental rotational spectrum of pcp-(*t*Bu)-CHOH is shown. The upper experimental trace in black is compared with a simulated spectrum of the most stable conformer pcp-(*t*Bu)-CHOH-gm based on fitted rotational parameters. A rotational temperature of 3 K gives the best match between the simulated and the experimental intensities.

The possible relaxation pathways can be understood from the potential energy curve for the dihedral angle $\angle\theta$(H36-O35-C20-C19) (marked in Fig. 4.7), as the rotation of the hydroxy group connects the three rotamers. The potential energy barriers predicted at B3LYP-D3(BJ)/def2-TZVP level of theory range from 3 to 4.8 kJ/mol (Fig. 4.9). The collisions of the Ne carrier gas atoms with the higher-energy conformers can transfer enough energy to overcome the conversion barrier and induce relaxation into the most stable structure, pcp-(*t*Bu)-CHOH-gm.[184] The SNR of approximately 50:1 for the most intense rotational transitions did not permit the observation of transitions originating from ^{13}C (1.1%)- or ^{18}O (0.2%)-isotopologues of pcp-(*t*Bu)-CHOH-gm to enable its structure determination.

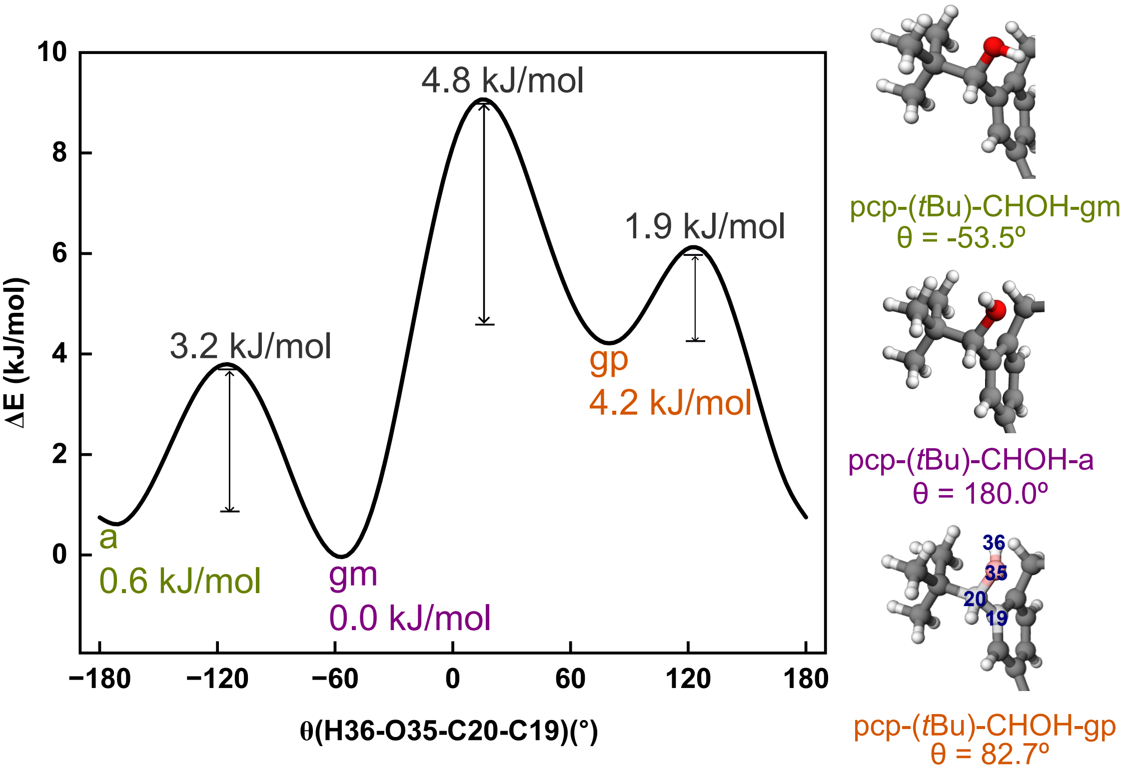

Figure 4.9: Potential energy scan for the dihedral angle ∠θ(H36-O35-C20-C19) to investigate the relaxation pathways between the three conformers. The curve was computed at the B3LYP-D3(BJ)/def2-TZVP level of theory. The arrows indicate the energy barrier between the conformers. The relative zero-point corrected energy determined at the B3LYP-D3(BJ)/def2-TZVP level of theory is given for all three conformers. The three different orientations, a, gp, and gm, of the hydroxy group are depicted with their respective dihedral angles.

4.2.4 Carboxylic acid substituted [2,2]-paracyclophane, pcp-COOH

Two conformers were identified for the COOH functionalised [2,2]-paracyclophane, pcp-COOH, from calculations (Fig. 4.10). The rotational spectrum for pcp-COOH had an overall weak signal, and it was difficult to recognise any kind of characteristic transition patterns unlike in other substituted [2,2]-paracyclophane molecules. After meticulous investigation, a few rotational transitions belonging to pcp-COOH-1 conformer could be recognised. The experimental rotational parameters of the lowest energy isomer, pcp-COOH-1, obtained by fitting some of these rotational lines, are presented in Table 4.4. Many weak rotational transitions remain in the spectrum, which may come from fragmentation of the sample or impurities from the synthesis process. Due to experimental challenges, only 700k acquisitions could be collected.

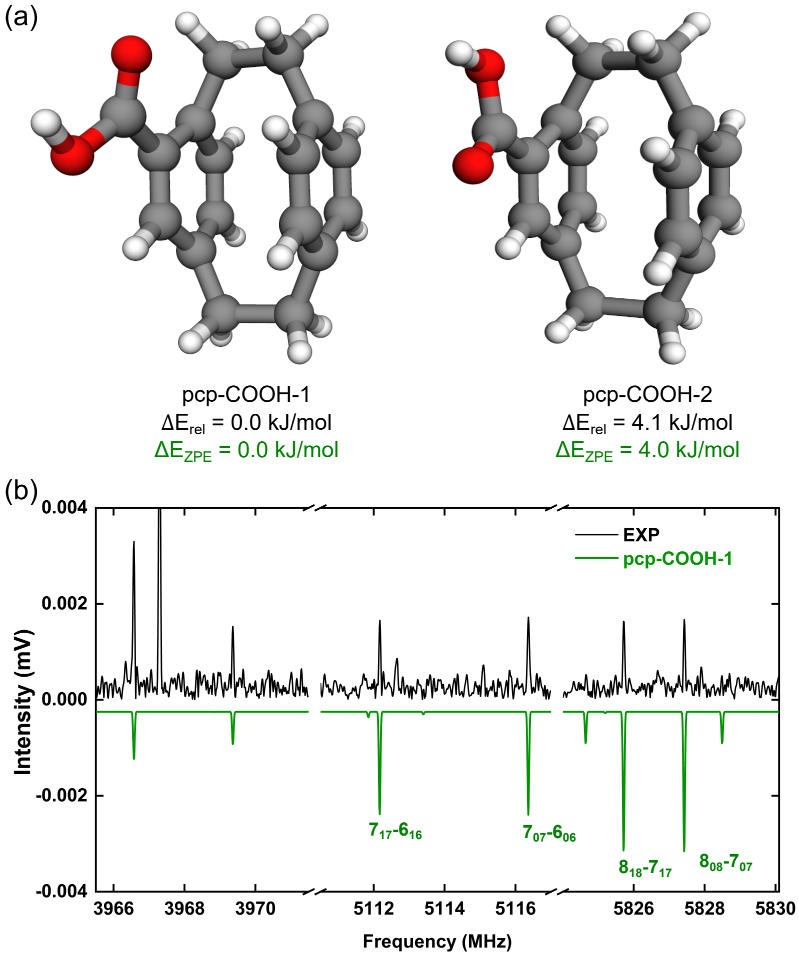

Figure 4.10: (a) Molecular structures of two different conformers of pcp-COOH optimised at the B3LYP-D3(BJ)/def2-TZVP level of theory along with their relative energies without (black) and with zero-point energy correction (green) in kJ/mol. (b) The upper trace is the experimental spectrum of pcp-COOH in the 3966-5830 MHz region, while the lower trace is the simulation based on the fitted rotational parameters obtained at a rotational temperature of 3 K. The most stable conformer pcp-COOH-1 is represented in green.

Table 4.4: Relative energies and rotational parameters of pcp-COOH predicted at the B3LYP-D3(BJ)/def2-TZVP level of theory are given here. The experimental and calculated rotational parameters were obtained with the SPFIT fitting program.

Parameters	pcp-COOH-1		pcp-COOH-2
	calc.	exp.	calc.
A/MHz[1]	596.6	597.31366(47)	613.8
B/MHz	423.9	422.31638(30)	412.2
C/MHz	358.0	356.24851(34)	361.8
Δ_J/kHz	-	0.01323(10)	
Δ_{JK}/kHz	-	-	-
Δ_K/kHz	-	-	-
δ_J/kHz	-	-	-
δ_K/kHz	-	-	-
μ_a/D[2]	-1.6	Y	-0.6
μ_b/D	-0.8	N	1.1
μ_c/D	0.5	Y	1.4
N[3]	-	20	-
σ/kHz	-	4.0	-
ΔE_{rel}/kJ/mol[4]	0.0	-	4.1
ΔE_{ZPE}/kJ/mol	0.0	-	4.0

[1] A, B, and C are the rotational constants and Δ_J, Δ_{JK}, Δ_K, δ_J, and δ_K are the quartic centrifugal constants in Watson's A-reduction scheme. [2] Y and N mean if the respective type of rotational transitions were observed or not. [3]σ is the standard deviation of the fit and N indicates the number of lines included in the fit. [4] ΔE_{rel}, ΔE_{ZPE} are the relative energies without and with zero-point correction, respectively at the B3LYP-D3(BJ)/def2-TZVP level of theory.

4.2.5 Intramolecular interactions

The exploration of intramolecular interactions within [2,2]-paracyclophane and its derivatives involved NCI analysis. The NCI analysis gives information about attractive and repulsive interactions present in the [2,2]-paracyclophane molecules. The sign of the Laplacian of the electron density ($\nabla^2\rho$), provides information on the different types of interactions.[138, 203] This Laplacian has contributions from all the three principal axes of maximal variation, which have three eigenvalues λ_i of the electron density of the Hessian matrix. The second eigenvalue λ_2 then helps to discern between different types of non-covalent interactions such as hydrogen bonding, dispersion and steric interactions. When λ_2 is negative, it indicates the presence of strong attractions, while values around 0 reveal weak attractions, respectively. A positive value of λ_2 implies repulsive interactions.

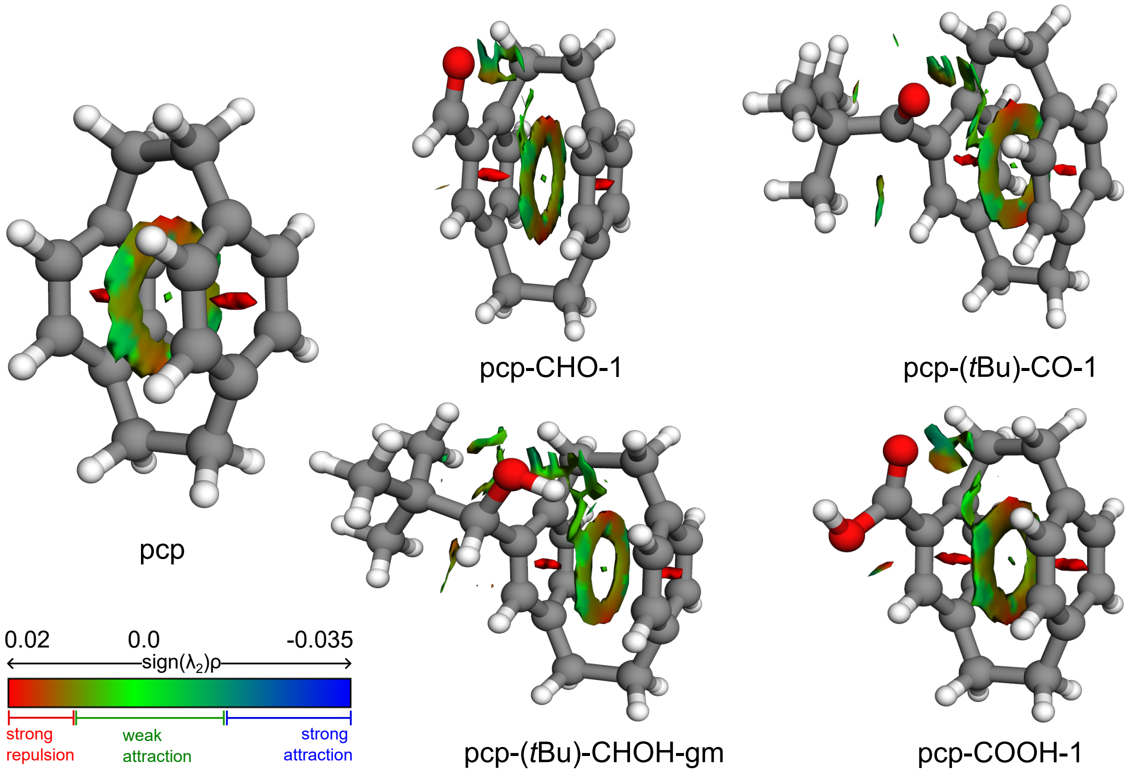

Figure 4.11: NCI analysis of the [2,2]-paracyclophane and its four derivatives investigated in this work. Optimised structures of the most stable conformations of the monosubstituted [2,2]-paracyclophanes were used as inputs for the NCI analysis; the sign of λ_2 distinguishes the different types of interactions. A doughnut-shape weak attractive interaction is observed between stacked benzene rings in [2,2]-paracyclophanes and its substituted species.

The NCI plots of [2,2]-paracyclophanes and its four substituted forms showcase a doughnut-shaped $\pi \cdots \pi$ interaction surface between the two co-facially stacked benzene rings, as shown in Fig. 4.11. The transannular strain in these substituted and non-substituted pcp lengthens the CH_2-CH_2 bond distances and bends the benzene units out of the plane, making them non-planar. The doughnut-shaped inter-ring interactions are affected only slightly by different substitutions on the [2,2]-paracyclophane and have a common repulsive interaction near the ethylene bridge. An additional $CH \cdots O$ interaction is present in all the derivatives, of similar length and strength. Some secondary interactions, such as $CH \cdots \pi$, are also present in the ketone- and hydroxy-substituted paracyclophane due to the presence of the *tert*-butyl group. The presence of intramolecular $OH \cdots \pi$ interaction between the hydroxy group and the $\pi \cdots \pi$ interaction surface of paracyclophane moiety could be a possible reason for the higher stability of the pcp-(tBu)-CHOH-gm conformer compared to its isoenergetic pcp-(tBu)-CHOH-a conformer.

4.3 Discussion

The intramolecular interactions of the aldehyde-substituted [2,2]-paracyclophane can be compared with a structurally similar benzaldehyde-benzene complex as presented in Fig. 4.12. The complex of benzene with benzaldehyde has a parallel-displaced structure, similar to the benzene dimer.[206] The structure of the benzaldehyde-benzene complex resembles the second most stable conformer of pcp-CHO with respect to the aldehyde functional group. In both of these species, the carbonyl oxygen points toward the hydrogen atom of the benzene at the meta-position. Due to this, a very weak intramolecular $CH \cdots O$ interaction is present between the CH and the carbonyl oxygen in both structures. A similar $CH \cdots O$ interaction between the carbonyl oxygen and ethylene hydrogen is present in the most stable conformer of aldehyde substituted [2,2]-paracyclophane, i.e., pcp-CHO-1 conformer (Fig. 4.12). The $CH \cdots O$ interaction in the pcp-CHO-1 conformer is stronger than the $CH \cdots O$ interaction in the pcp-CHO-2 conformer and benzaldehyde-benzene complex, due to the short distance of 2.4 Å between the ethylene hydrogen and oxygen atom in the pcp-CHO-1 compared to the other species. Both the benzaldehyde-benzene complex and the pcp conformers have weak $\pi \cdots \pi$ attractions between the benzene rings, with some additional repulsive interactions near the ethylene bridge unit in [2,2]-paracyclophanes.

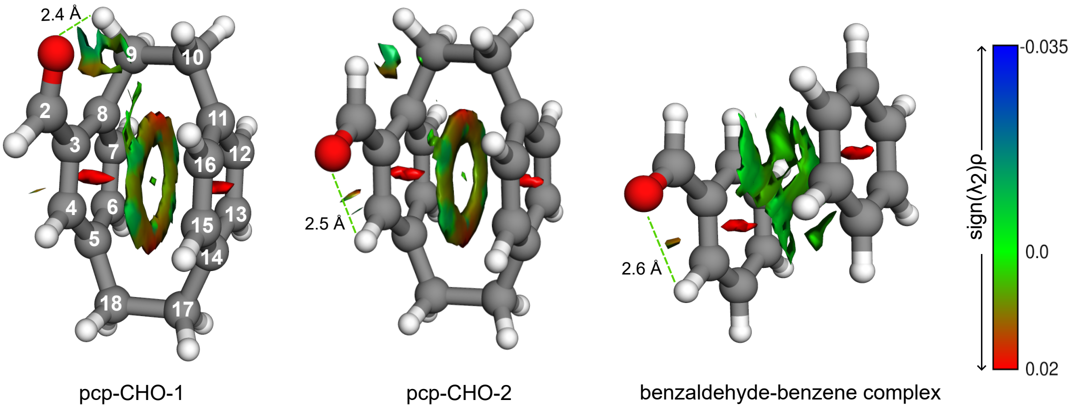

Figure 4.12: Comparison of NCI plots of aldehyde-substituted [2,2]-paracyclophane with a structurally similar benzaldehyde-benzene complex obtained at the B3LYP-D3(BJ)/def2-TZVP level of theory. The transannular $\pi \cdots \pi$ interactions in pcp-CHO are weak attractions between the stacked benzene rings and repulsive near the ethylene bridge connecting the two aromatic rings. The benzaldehyde-benzene complex has a parallel-displaced structure with weak $\pi \cdots \pi$ interactions between the benzene rings.

To understand the effect of the ethylene bridge on benzene rings in the series of substituted paracyclophanes, NCI analysis of [2,2]-paracyclophane can be compared with similar molecular systems, such as the benzene dimer and pyrene dimer (Fig. 4.13). The benzene dimer resembles the [2,2]-paracyclophanes without the bridge that maintains the co-facial stacking, while the benzene-benzaldehyde can be compared directly to pcp-CHO (Fig. 4.12). The pyrene dimer was chosen since it can model larger systems, such as graphite and graphene bilayers. Graphite is a layered material composed of sheets of hexagonally arranged sp^2-hybridised carbon atoms, forming a planar network. These layers are not co-facially stacked; instead, they have a slight displacement from one another, which gives graphite its slippery texture. Graphene layers are held together by weak van der Waals forces.

For the benzene dimer, several isomers are possible. It has been demonstrated that the conformation with both rings exactly overlapping, as in paracyclophanes, is a saddle-point structure.[207] A minimum structure arises from a shift of the upper benzene with respect to the center of the bottom one, i.e., a parallel-displaced structure as reported by Podeszwa *et al.*[207] However, this minimum structure of the benzene dimer is not observed in MW spectroscopy experiments due to its nonpolar nature.[206, 208] Instead, the tilted T-shaped structure is observed.[206, 208] The discussion here is focused on the parallel-displaced geometry due to its structural similarity with [2,2]-paracyclophanes. Similarly, the pyrene dimer also has a parallel-displaced structure with aromatic rings not exactly facing each other. The NCI analysis of benzene and pyrene dimers (Fig. 4.13) reveals pure $\pi \cdots \pi$ interactions between the two planes with a similar nature as depicted in the benzene-benzaldehyde complex (Fig. 4.12).

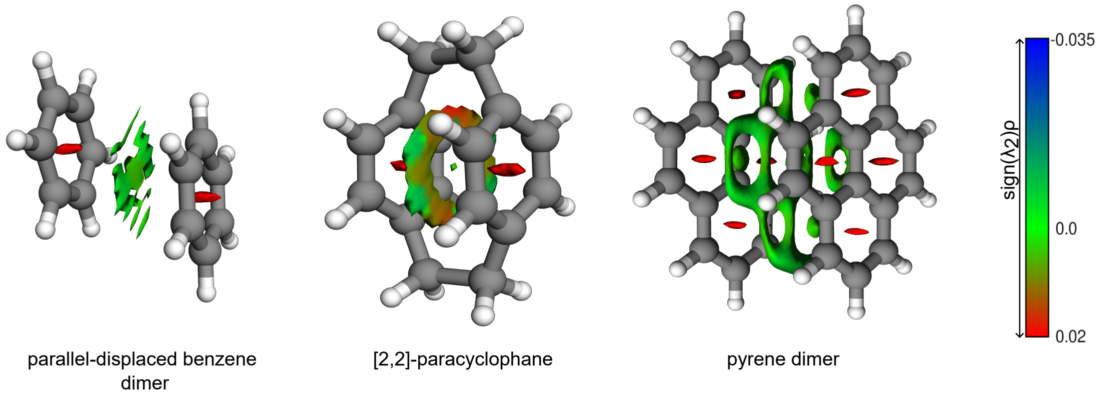

Figure 4.13: NCI plots for the parallel-displaced isomer of the benzene dimer, [2,2]-paracyclophane, and the displaced pyrene dimer obtained at the B3LYP-D3(BJ)/def2-TZVP level of theory.

A remarkable property of [2,2]-paracyclophanes is the proximity between the two aromatic rings. The experimental inter-annular distance between the benzene units in the case of the aldehyde-substituted [2,2]-paracyclophane (3.118(58) Å, Fig. 4.5) is 0.31 Å shorter than the standard van der Waal distance between the graphite layers.[197] It is also shorter than the computed distances between the two aromatic rings in the benzene dimer and benzene-benzaldehyde complex, with distances of 3.5 Å and 3.6 Å, respectively. Due to the short distance in [2,2]-paracyclophane derivatives, in principle, a large repulsion force between the two aromatic rings arising from the overlap between the two π clouds could be expected. However, attractive forces between the two rings can be identified in the four derivatives studied, with just a small repulsive area in the region close to the ethylene chains due to the steric hindrance. The mix of attractive and repulsive forces with the transannular strain due to the ethylene groups in [2,2]-paracyclophanes can provide a basis for the correlation between their properties.

However, the presence of transannular strains in paracyclophanes is still an ongoing discussion. Some theoretical or in-silico studies report the lack of this strain and conclude its absence due to the influence of both ethylene bridges and the distortion of the benzene rings to quasi-boat conformation.[209] Recent articles report its presence and explain the co-facial stacking of the benzene rings in close proximity as a reason for it.[197] The accurate experimental structure determined in this work, supported by the NCI computations, suggests the presence of such transannular strains.

It is also interesting to observe the possible changes in the Mulliken atomic charges of the carbon atoms in both the benzene dimer and [2,2]-paracyclophanes, to get insights into their electronic structure arrangement. To gain insights, natural bond orbital computations were carried out at the same level of theory, i.e., B3LYP-D3(BJ)/def2-TZVP, focusing on the carbon atoms situated at the edges of the benzene ring (C5, C8, C11, and C14 as marked in Fig. 4.12). These four carbon atoms have an atomic charge of about +0.17 in [2,2]-paracyclophane, while all the other carbon atoms in the [2,2]-paracyclophane have negative charges, as could be expected. In the benzene dimer, all the carbon atoms have a negative charge of about -0.12. This effect represents an electron deficit in the C5, C8, C11, and C14 carbon atoms of the [2,2]-paracyclophane. Due to the ethylene bridge that holds both aromatic rings, those four carbon atoms are pushed away from the plane of the aromatic ring affecting the resonance of the electrons in the ring. The determined experimental structure of the aldehyde-substituted [2,2]-paracyclophane in this investigation allowed us to calculate the deviation of these edge carbon atoms (C5, C8, C11, and C14) from the benzene plane. These carbon atoms have a deviation from planarity by an angle between 4° (C8 and C11) and 8° (C5 and C14), as mentioned in Table 5 in appendix.

The experimentally determined C-C bond lengths of the aldehyde-substituted [2,2]-paracyclophane determined in the gas phase are compared with the X-ray structure of [2,2]-paracyclophane in Table 4.5. Interestingly, the experimental data from both X-ray crystallography and microwave investigation agree well, which points to small crystal packing effects in the solid phase.[209] Additionally, the ground-state structure determined from MW spectroscopy provided information on the interannular distance, for example C7-C12 bond distance is determined to be 3.118(58) Å (according to the labelling in Fig. 4.12).

Table 4.5: Comparison of bond lengths obtained from X-ray diffraction studies on [2,2]-paracyclophane and r_0, r_s structure determination method employed on pcp-CHO-1 conformer. The carbon atom numbers are according to the labelled pcp-CHO-1 conformer in Fig. 4.12.

Bond distances	X-ray data (in Å)	r_0 structure (in Å)	r_s structure (in Å)
C9-C10	1.580(1)	1.584(47)	1.5837(48)
C10-C11	1.508(1)	1.516(69)	1.5112(68)
C11-C12	1.400(1)	1.400(85)	1.365(11)
C12-C13	1.392(1)	1.391(76)	1.4073(38)
C7-C12	3.09	3.118(58)	3.1100(39)

4.4 Summary

CP-FTMW spectroscopy was employed to investigate the MW spectra of four structural homologues of monosubstituted [2,2]-paracyclophanes. The good agreement between quantum-chemically predicted and experimentally determined rotational parameters led to the identification of the observed species as the low-energy forms of respective substituted [2,2]-paracyclophanes. These low-energy forms are stabilised by the CH$\cdots$O interaction formed between the carbonyl/hydroxy oxygen of these derivatives and the hydrogen atom of the [2,2]-paracyclophane ethylene bridge. The hydroxy substituted [2,2]-paracyclophane exhibits more flexibility compared to the rigid aldehyde, ketone, and carboxylic acid substituted [2,2]-paracyclophanes. To explore the conformational landscape of pcp-(*t*Bu)-CHOH, a dihedral scan for the rotation of the hydroxy group was performed, revealing the barriers for the interconversion of the three rotamers of pcp-(*t*Bu)-CHOH and suggesting that relaxation processes can be expected in experiments. Further, the presence of intramolecular OH$\cdots\pi$ interaction in the pcp-(*t*Bu)-CHOH-gm conformer also suggests its higher stability than its isoenergetic conformer, pcp-(*t*Bu)-CHOH-a, pointing to gm as a preferred arrangement for the hydroxy group in the gas phase.

In experiments, both predicted isomers of pcp-CHO were detected, showing strong rotational transitions for the lowest energy conformer, pcp-CHO-1. The observation of carbon-13 isotopic species of pcp-CHO-1 facilitated its accurate structure determination in the gas phase. The r_0 structure of pcp-CHO-1 revealed a proximity of 3.118(58) Å between the stacked benzene rings, akin to the 3.09 Å distance obtained from the solid-state structure of [2,2]-paracyclophane. The comparison of the gas-phase structure of paracyclophane moiety determined from this study on pcp-CHO-1 and the solid-state structure of [2,2]-paracyclophane, indicates that the presence of a functional group, such as aldehyde does not substantially alter the paracyclophane moiety. Additionally, the r_0 structure of pcp-CHO-1 indicates a 4°and 8° deviation of edge carbon atoms (C5, C8, C11, and C14, as marked in Fig. 4.12) from the benzene ring plane.

NCI analysis of [2,2]-paracyclophane and all of its four monosubstituted species reveals a doughnut-shaped transannular interaction between co-facially stacked benzene rings, along with an additional $\mathrm{CH}\cdots\mathrm{O}$ interaction present only in the derivatives. Notably, derivatives with a *tert*-butyl group, like pcp-(*t*Bu)-CHO and pcp-(*t*Bu)-CHOH-gm, exhibit an additional $\mathrm{CH}\cdots\pi$ interaction between the methyl group of *tert*-butyl and the aromatic ring backbone.

The investigation of structural similarities between [2,2]-paracyclophane and parallel-displaced benzene dimer led to an observation regarding the influence of ethylene bridges, compelling the decks to stack over each other. NCI analysis comparing benzene (parallel-displaced) and pyrene dimers with [2,2]-paracyclophane revealed a mix of attractive and repulsive interactions in the latter, whereas weakly attractive $\pi\cdots\pi$ interactions were present in the former dimers. Mulliken atomic charge analysis on [2,2]-paracyclophane predicted a positive atomic charge on the four edge carbon atoms (C5, C8, C11, and C14) held by the ethylene bridge, suggesting that the resonance of the electrons in the benzene ring is affected by the presence of the ethylene bridge.

The large size and structural complexity of [2,2]-paracyclophane and its structural homologues once more tested the limits of rotational spectroscopy. The characterisation of conformations and interannular interactions of substituted [2,2]-paracyclophane can aid in understanding the chemical properties of the paracyclophane derivatives, which can be valuable for fine-tuning them for specific applications for example in asymmetric synthesis and material science.

Chapter 5

The many forms of α-methoxy phenylacetic acid in the gas phase: flexibility, internal dynamics, and their intramolecular interactions

The conformational flexibility in chiral molecules is particularly interesting, as most of the biomolecules are chiral in nature. An example of such a molecule is α-methoxy phenylacetic acid (AMPA), a methoxy-derivative of mandelic acid ($C_8H_8O_3$). Mandelic acid is one of the simplest aromatic chiral molecule. It is an important molecule with wide applications in the cosmetic industry.[210] The conformational landscape of mandelic acid has been investigated before, and four isomers were described.[211] Exploring the conformational landscape of AMPA extends this prior work, given AMPA's additional degree of molecular flexibility compared to mandelic acid, offering insight into how functional groups sequentially contribute to molecular flexibility. AMPA plays a significant role in the stereochemical analysis of sulfoxides due to its ability to form strong adducts with sulfoxide functional groups.[212] Another interesting property of AMPA is that it finds applications in organic chemistry and pharmaceutical industry as a starting material for the synthesis of organic compounds with different biological activities like neuroprotective anticonvulsants.[213, 214]

It is intriguing to explore how the relative orientation of the functional groups contribute to the formation of intramolecular interactions and their importance for the stabilisation of conformers. The first aim of this study was to investigate the conformational landscape of AMPA, paving the pathway for future investigations involving its complexes with different solvent molecules, such as dimethyl sulfoxide.

This chiral carboxylic acid comprises two functional groups at the chiral center, offering distinct binding sites for intra- and intermolecular interactions. Due to the structural flexibility introduced by the methoxy and carboxylic acid groups, it is expected to observe several structural forms of AMPA in both monomer and microsolvation experiments stabilised by intramolecular interactions. The second objective of this investigation was to understand the role of intramolecular interactions in shaping AMPA's conformational space. Broadband rotational spectroscopy, as described in Chapter 3 was used to explore the conformational space of AMPA, as this is a powerful technique for acquiring precise and high-resolution structural details of gas-phase molecules. The specific experimental and computational details of the study are provided in experimental and computational methods section of the manuscript. The findings of the investigation are presented in the results and discussion section of the manuscript. The effect of the carrier gas on the relative population of conformers during experiments was also explored, along with calculations on conformational relaxation trajectories to interpret observations, which are discussed in the conformational relaxation part of results and discussion section. The internal dynamics of the molecule, primarily arising from the methyl rotor, were also explored.

Title	The many forms of alpha-methoxy phenylacetic acid in the gas phase: flexibility, internal dynamics, and their intramolecular interactions
Authors	Himanshi Singh, Pablo Pinacho, Daniel A. Obenchain, Mariá Mar Quesada-Moreno, and Melanie Schnell
Journal	*Phys. Chem. Chem. Phys.*
Volume	24
Year	2022
Pages	27312-27320
DOI	https://doi.org/10.1039/D2CP03962A
Pages	9 pages of the article and 40 pages of supplementary information
My contributions	Experiment Analysis Manuscript preparation

PCCP

ROYAL SOCIETY
OF CHEMISTRY

PAPER

View Article Online
View Journal | View Issue

Check for updates

Cite this: *Phys. Chem. Chem. Phys.*, 2022, **24**, 27312

The many forms of alpha-methoxy phenylacetic acid in the gas phase: flexibility, internal dynamics, and their intramolecular interactions†

Himanshi Singh,[ab] Pablo Pinacho,*[a] Daniel A. Obenchain,[c]
María Mar Quesada-Moreno[d] and Melanie Schnell*[ab]

Received 26th August 2022,
Accepted 17th October 2022

DOI: 10.1039/d2cp03962a

rsc.li/pccp

We present a rotational spectroscopy study of alpha-methoxy phenylacetic acid in the gas phase. This acid is a derivative of mandelic acid and is used in various organic reactions. The conformational landscape of alpha-methoxy phenylacetic acid was explored to gain insight into its intramolecular dynamics. A rich rotational spectrum was obtained using chirped-pulse Fourier transform microwave spectroscopy in the 2–8 GHz range. Five conformers out of six calculated low-energy forms were identified in the spectrum, and the assignment of the ^{13}C singly substituted isotopologues for the lowest-energy conformer led to its accurate structure determination. Splitting patterns were analyzed and attributed to the internal rotation of a methyl top. The analysis of the non-covalent interactions within the molecule highlights the subtle balance in the stabilization of the different conformers. We thus provide high-level structural and intramolecular dynamics information that is also used to benchmark the performance of quantum-chemical calculations.

Introduction

Carboxylic acids are an important group of molecules in organic chemistry. Within this family of molecules, chiral carboxylic acids can be found in a myriad of molecules involved in biological processes.[1] Mandelic acid (Fig. 1a) is an example of a chiral carboxylic acid used in the cosmetic industry, among other applications, to cure skin problems such as acne and pimples.[2] The presence of a phenyl ring, a hydroxy group, and a carboxylic acid group attached to the chiral center provides different possibilities for intra- and intermolecular interactions. These functional groups offer great binding sites for solute and solvent interactions, which are also of crucial importance to understand their biological activities. Furthermore, the relative orientation of these groups also gives rise to a rich conformational landscape. It becomes important to study such molecules to identify the conformations that they can present, characterize their structures, analyze the interconversion pathways between the possible conformers, and evaluate their intra- and intermolecular interactions. Among different structurally sensitive experimental approaches, rotational spectroscopy is a valuable technique to address these challenges and perform the structural analysis of molecules. The study of such molecules in the gas phase provides detailed information about each conformation and allows us to characterize intramolecular interactions that stabilize the conformers.[3–7] The accurate spectroscopic information on the structures and their

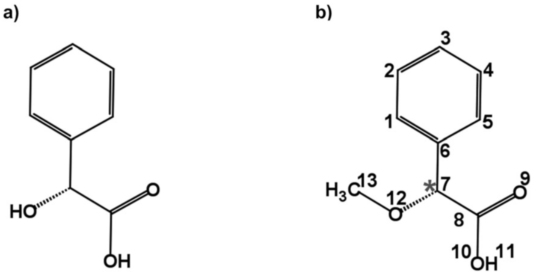

Fig. 1 Schematic structures of (a) mandelic acid ($C_8H_8O_3$) and (b) alpha-methoxy phenylacetic acid (AMPA; $C_9H_{10}O_3$). The chiral centre is highlighted with an asterisk.

---

[a] *Deutsches Elektronen-Synchrotron DESY, Notkestr. 85, 22607 Hamburg, Germany. E-mail: pablo.pinacho@desy.de, melanie.schnell@desy.de*
[b] *Institute of Physical Chemistry, Christian-Albrechts-Universität zu Kiel, Max-Eyth-Str. 1, 24118 Kiel, Germany*
[c] *Institut fur Physikalische Chemie, Universität Göttingen, Tammannstr. 6, 37077 Göttingen, Germany*
[d] *Departamento de Química Inorgánica, Facultad de Ciencias, Universidad de Granada, Avda. Fuentenueva s/n, 18071 Granada, Spain*

† Electronic supplementary information (ESI) available: Additional figures on conversion and internal rotation scans. Experimentally determined structures and line lists for the observed conformers. See DOI: **https://doi.org/10.1039/d2cp03962a**

interactions allows benchmarking quantum-chemical calculations that help improve their performance.[8]

Alpha-methoxy phenylacetic acid (AMPA, $C_9H_{10}O_3$) is a derivative of mandelic acid (Fig. 1b) that serves as an NMR shift reagent and helps in the determination of enantiomeric purity.[9] It presents two strong electron-withdrawing groups, namely a methoxy group and a carboxylic acid group together with a phenyl ring, making it highly flexible and giving rise to different kinds of intramolecular interactions. The complexation of the carboxylic acid group of AMPA with sulfoxide functional groups gives rise to strongly bound adducts, resulting in its use in the stereochemical analysis of sulfoxides.[9] The phenylacetic acid group present in AMPA is an important moiety in many numerous pharmaceutical drugs such as atropine, camylofin, and phenacemide. Thus, the characterization of this group on the basis of AMPA can serve to model the internal dynamics of these kinds of drug molecules. Furthermore, studying AMPA helps in understanding the effect of solute–solvent interactions on the IR and VCD spectra in different solvents as reported by a recent study.[10] In that study, six conformations of the AMPA monomer were predicted from quantum-chemical calculations. Although the monomeric conformers of AMPA could not be observed directly in experiments, dimers arising from the complexation with the non-polar solvents were observed.[10] A detailed conformational analysis of AMPA is an important starting point to characterize its ability to interact with other molecules and predict the possible geometry changes. Here, we have investigated the monomer conformers of AMPA and unraveled its internal dynamics in the absence of further interactions in the gas phase using rotational spectroscopy.

Rotational spectroscopy is a powerful tool to obtain the structural information of molecules in the gas phase with high precision and resolution.[11,12] The development of chirped-pulse instruments revolutionized the field of rotational spectroscopy.[13] Using chirped-pulse Fourier-transform microwave (CP-FTMW) spectroscopy, it is possible to record the rotational spectra of complex, flexible molecular systems over a broad frequency range in a single experiment.[14] The experiments are complemented by high-level quantum-chemical calculations and supported by spectral assignment programs. From a broadband rotational spectrum, it is possible to extract information about the structure and internal dynamics of isolated molecules and clusters. Some recent studies on biologically relevant molecules by CP-FTMW spectroscopy demonstrate its capabilities to investigate terpenes,[3–7,15–18] monosaccharides,[19] amino acids,[20] drugs,[21,22] and micro-solvated complexes.[23–27] As a remarkable example, a study on citronellal[5] highlights the rich conformational landscape of a flexible molecule evaluated by broadband rotational spectroscopy.

The results presented in this work discuss the observed conformations, their structural similarities, the stabilization interactions, and the conversion pathways that are of interest to better understand and benchmark systems with rich conformational space arising from high flexibility, using AMPA as a model system. This study can also serve as an important basis for future work on solute–solvent interactions of carboxylic acids with different solvents.

Methods

Computational methods

The conformational landscape of AMPA was explored in two stages. First, a conformational search was performed by a semi-empirical method using the GFN-xTB code.[28] Several conformers were obtained, and their geometries were optimized using the B3LYP[29–31] (Becke, three-parameter, Lee–Yang–Parr) exchange–correlation functional along with Grimme's D3 dispersion corrections,[32] and Becke–Johnson (BJ) damping,[33] combined with the def2-TZVP basis set,[34] using the ORCA program.[35,36]

Second, a complementary stepwise manual search for the orientation of the functional groups was performed. The chiral centre of AMPA has three functional groups, a phenyl ring, a carboxylic acid group (COOH), and a methoxy group (OCH_3) (Fig. 1b). The individual orientations of these functional groups are responsible for the conformational flexibility of AMPA and characterize the naming scheme for different conformers as shown in Fig. 2.

In addition to the geometry optimizations at the B3LYP-D3(BJ)/def2-TZVP level of theory, single-point energy calculations at the DLPNO-CCSD/aug-cc-pVTZ level of theory were performed. Frequency calculations at the B3LYP-D3(BJ)/def2-TZVP level of theory were also performed to validate whether the equilibrium structures were real minima and to obtain the zero-point corrected relative energies. Systematic scans of some coordinates were carried out at the B3LYP-D3(BJ)/def2-TZVP level of theory to explore the relaxation pathways between the conformers, employing the ORCA[35,36] and Gaussian program packages.[37] Non-covalent interaction (NCI)[38,39] analysis was performed to help identify the weak intramolecular interactions involved in the stabilization of the conformers and to characterize and visualize the forces.

Experimental methods

The rotational spectrum of AMPA was recorded using a broadband compact-passage acquired coherence technique (COMPACT) spectrometer in the 2–8 GHz frequency range.[40] A sample of 99% purity purchased from Thermo Fischer Scientific was used for experiments without further purification. AMPA is a white crystalline solid at room temperature with a melting point of around 69–71 °C and a boiling point of around 165 °C according to the information of the supplier. The sample was heated in a reservoir at *ca.* 120 °C and mixed with neon as a carrier gas at a stagnation pressure of 2 bars. Additional experiments were performed under similar conditions using helium and argon as carrier gases to explore the conformational landscape of AMPA. The mixture was then supersonically expanded using a pulsed valve into a vacuum chamber at a repetition rate of 8 Hz. A microwave chirp pulse of 4 μs duration generated using an arbitrary waveform generator

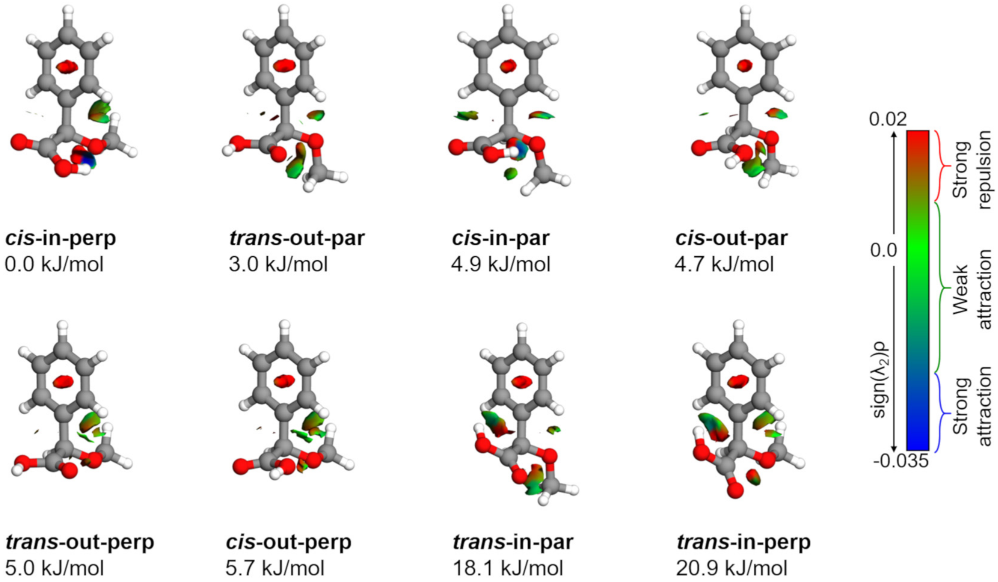

Fig. 2 Molecular structures of AMPA optimized at the B3LYP-D3(BJ)/def2-TZVP level of theory along with their relative zero-point corrected energies in kJ mol^{-1}. These structures were used as inputs for the non-covalent interaction (NCI) analysis; the sign of λ_2 obtained from this analysis distinguishes the different types of interactions.

and amplified using a 300 W traveling wave tube amplifier was broadcast into a vacuum chamber using a horn antenna to polarize the molecular ensemble. The molecular signal was collected in the time domain as a free-induction decay (FID) of the macroscopic dipole moment of the molecular ensemble. The application of the fast Fourier transformation results in the rotational spectrum in the frequency domain. A detailed description of the experimental setup can be found elsewhere.[40] A recent data acquisition scheme, the 'fast frame setup' option of a digital oscilloscope, was employed.[41] Eight back-to-back excitation chirps were performed on each gas pulse, and the subsequent eight FID acquisitions were then co-added and averaged. The use of the fast frame setup decreases the measurement time and the sample consumption rate, resulting in an effective repetition rate of 64 Hz. The final spectrum with Ne as a carrier gas was obtained by coadding 4.3 million FIDs. For spectra with He and Ar, 3.8 and 3.5 million FIDs, respectively, were coadded. All the spectra recorded using a COMPACT spectrometer had a resolution of around 25 kHz and an accuracy in the frequency measurement better than 15 kHz.

The initial assignment of experimental lines to rotational transitions was performed through a recurrent fit based on Watson's A-reduction Hamiltonian in the I^r representation as implemented in PGOPHER.[42,43] These initially fitted rotational constants (A, B, and C) and quartic centrifugal distortion constants (Δ_J, Δ_K, Δ_{JK}, δ_J, and δ_K) were then refined using the SPFIT/SPCAT programs developed by Pickett.[44] The observed line splittings in two of the conformers due to a large amplitude motion of AMPA were analysed using the XIAM program.[45] This applies the so-called ρ-axis method where ρ is a dimensionless vector that accounts for the interaction between the overall rotation and internal rotation.[46] For experimental structure determination, we used the KRA, EVAL, and STRFIT programs as available on the PROSPE website.[47]

Results and discussion

AMPA is a highly flexible molecule due to the possible configurations of the three functional groups and generates a rich conformational space (Fig. S1 and S2, ESI†). The spatial orientation of the methoxy group (dihedral angle τ, C_{13}–O_{12}–C_7–C_8) is observed to be either almost perpendicular or almost parallel with respect to the plane of the phenyl ring. The dihedral angle θ(O_{10}–C_8–C_7–O_{12}) can range from 0° to 360°, being either *cis* or *trans* with respect to the OCH_3 group. Finally, the hydroxyl (OH) group of carboxylic acid, defined by the dihedral angle ϕ(H_{11}–O_{10}–C_8–C_7), can rotate to be pointing either towards (in) the OCH_3 group or away from it (out). The combination of these possibilities produced eight minimum energy structures where the groups can be in perpendicular (perp) or parallel (par), *cis* or *trans*, and in or out configurations, respectively, as shown in Fig. 2. For example, the conformer *cis*-in-perp has the dihedral angle θ in *cis*, with the hydrogen of the OH group pointing towards the OCH_3 group (in), and OCH_3 is almost perpendicular to the phenyl ring. Table S1 of the ESI† lists the values of the three dihedral angles; τ, θ, and ϕ that characterize the different configurations for all eight conformers. The stepwise investigation revealed that one conformer, *trans*-in-perp, out of the eight possible structures was missed in the search by xTB. Six out of the eight conformations (Fig. 2) were found to be within a threshold of around 6 kJ mol^{-1} as listed in Table 1. Both the B3LYP and DLPNO-CCSD levels of theory predict a similar energy ordering of conformers, with the only exception of *cis*-in-par and *cis*-out-par. To obtain more accurate relative

Table 1 Quantum chemical rotational parameters (B3LYP-D3(BJ)/def2-TZVP) predicted for the eight conformers of AMPA

Parameters	*cis*-in-perp	*trans*-out-par	*cis*-in-par	*cis*-out-par	*trans*-out-perp	*cis*-out-perp	*trans*-in-par	*trans*-in-perp
A_e/MHz[a]	1436.0	1615.7	1612.9	1632.5	1365.0	1373.8	1660.7	1450.3
B_e/MHz	691.7	633.5	662.9	643.7	702.1	697.5	628.1	697.6
C_e/MHz	582.8	571.3	540.3	562.8	605.9	605.8	562.2	580.1
μ_a/D[b]	−1.6	0.1	−0.2	0.5	−1.8	1.4	−3.1	−5.1
μ_b/D	4.6	1.1	3.7	−0.8	0.0	1.4	−1.1	1.8
μ_c/D	−0.8	1.5	−0.8	−0.4	−2.0	0.4	−2.4	−2.0
ΔE_{rel}/kJ mol^{-1} [c]	0.0	3.9	4.5	5.4	5.8	6.3	19.5	22.2
ΔE_{ZPE}/kJ mol^{-1}	0.0	3.0	4.9	4.7	5.0	5.7	18.1	20.9
$\Delta E_{\mathrm{rel\text{-}CC}}$/kJ mol^{-1} [d]	0.0	1.5	3.9	2.5	3.9	4.0	18.9	22.4
$\Delta E_{\mathrm{ZPE\text{-}CC}}$/kJ mol^{-1} [e]	0.0	0.6	4.3	1.8	3.1	3.4	17.6	21.1

[a] A_e, B_e, and C_e are the equilibrium rotational constants in MHz. [b] μ_α values (α = a, b, and c) are the values of the electric dipole-moment components in Debye. [c] ΔE_{rel} and ΔE_{ZPE} are the calculated (B3LYP-D3(BJ)/def2-TZVP) relative energies without and with the zero-point energy (ZPE) correction, respectively. [d] $\Delta E_{\mathrm{rel\text{-}CC}}$ values are single point relative energies at the DLPNO-CCSD/aug-cc-pVTZ level of theory. [e] $\Delta E_{\mathrm{ZPE\text{-}CC}}$ values are the single point relative energies (DLPNO-CCSD/aug-cc-pVTZ) corrected with the zero-point energy term from the frequency calculations at the B3LYP-D3(BJ)/def2-TZVP level of theory.

energies, we added the zero-point correction term from the B3LYP-D3(BJ)/def2-TZVP calculations to the single point energies obtained at the DLPNO-CCSD/aug-cc-pVTZ level of theory (Table 1). The structures of the eight different conformers of AMPA with their NCI analysis and zero-point corrected relative energies obtained at the B3LYP-D3(BJ)/def2-TZVP level are shown in Fig. 2.

The upper black traces in Fig. 3 show two portions of the rotational spectrum (Ne-seeded) recorded using a COMPACT spectrometer. The experimental spectra are plotted against coloured traces, which represent the simulations of the observed conformers of AMPA using the experimentally fitted rotational constants. The typical energy threshold for observing conformers in our experiments is 6 kJ mol^{-1}. For example, the fifteen conformations of citronellal were observed within this energy window.[5] Each conformation has distinct rotational constants and dipole-moment components, giving rise to unique spectral signatures that allow differentiating them based on the rotational fingerprint and the type of spectrum observed. These distinct patterns of rotational transitions led to the identification of five conformers out of the six structures predicted in the above-mentioned energy window. All the experimentally determined sets of rotational constants can be assigned to a corresponding AMPA conformer as shown in Table 2.

The most intense transitions correspond to the low-energy conformers *cis*-in-perp and *trans*-out-par, due to their higher population. The rotational spectrum of the lowest energy conformer, *cis*-in-perp, shows all three a-, b- and c-type rotational transitions, while the second-lowest energy conformer, *trans*-out-par, presents only b- and c-type transitions, in good agreement with their predicted dipole-moment components as shown in Table 1. No transitions were observed for the third conformer, *cis*-in-par (*vide infra*). The rotational transitions of *cis*-out-par, the fourth most stable conformer, are in general weaker than those of the higher energy conformers, *trans*-out-perp and *cis*-out-perp. Based on the zero-point corrected relative energies, the fourth conformer should be more intense, so this effect could be explained by the relatively low values of the dipole-moment components for *cis*-out-par.

Conformational relaxation

As mentioned, one of the predicted isomers, *cis*-in-par, could not be identified in the experimental spectrum. The explanation for the non-observation of the *cis*-in-par conformer could be its

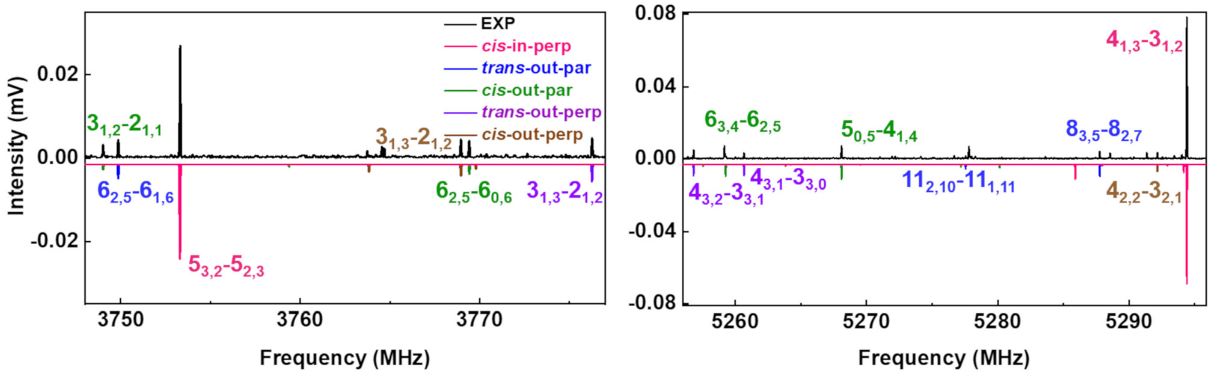

Fig. 3 Parts of the 2–8 GHz rotational spectrum of AMPA with the labelling scheme of the rotational transitions as $J'_{K'_aK'_c} \leftarrow J''_{K''_aK''_c}$. The top part shows the experimental spectrum and the bottom part represents the simulations using the fitted rotational parameters for AMPA conformers (Table 2). The relative intensities are based on the predicted dipole moment components (Table 1).

Table 2 Experimental rotational parameters for the five conformers of AMPA obtained using the fitting program SPFIT. For *cis*-in-perp and *trans*-out-par, only the A-state components were considered for this fit. The internal rotation barriers V_3 of the methyl top of *cis*-in-perp and *trans*-out-par conformers were obtained using the fitting program XIAM considering both A and E states

Parameters	*cis*-in-perp	*trans*-out-par	*cis*-out-par
A/MHz[a]	1436.68000(29)[d]	1619.14743(43)	1636.37884(58)
B/MHz	692.06967(12)	635.06285(26)	647.17771(31)
C/MHz	583.21822(12)	570.21890(26)	560.19412(28)
Δ_J/kHz	0.07892(78)	0.0723(20)	0.1470(25)
Δ_{JK}/kHz	0.3036(19)	0.1427(38)	—
Δ_K/kHz	−0.0684(64)	—	—
δ_J/kHz	0.00462(13)	0.00456(19)	—
δ_K/kHz	−0.4362(24)	0.867(10)	2.977(36)
a/b/c[b]	Y/Y/Y	N/Y/Y	Y/Y/Y
V_3/kJ mol^{-1}	8.263(9)	7.552(2)	—
N[c]	248	167	54
σ/kHz	7.8	9.8	8.6

Parameters	*trans*-out-perp	*cis*-out-perp
A/MHz	1368.69142(41)	1375.55303(71)
B/MHz	703.73277(28)	697.96749(45)
C/MHz	605.92022(23)	606.05148(44)
Δ_J/kHz	0.0458(25)	0.0468(79)
Δ_{JK}/kHz	0.4479(61)	0.333(10)
Δ_K/kHz	−0.323(16)	−0.0764()
δ_J/kHz	0.0059(11)	—
δ_K/kHz	−0.532(17)	—
a/b/c	Y/N/Y	Y/Y/Y
V_3/kJ mol^{-1}	—	—
N	87	59
σ/kHz	7.9	8.3

[a] A, B, and C are the rotational constants. Δ_J, Δ_{JK}, Δ_K, δ_J and δ_K are the quartic centrifugal distortion constants. [b] Y and N indicate whether a, b, or c type of rotational transitions were observed or not, respectively. [c] N is the number of fitted transitions. σ is the root-mean-square deviation of the fit. [d] Standard error in parentheses in units of the last digit.

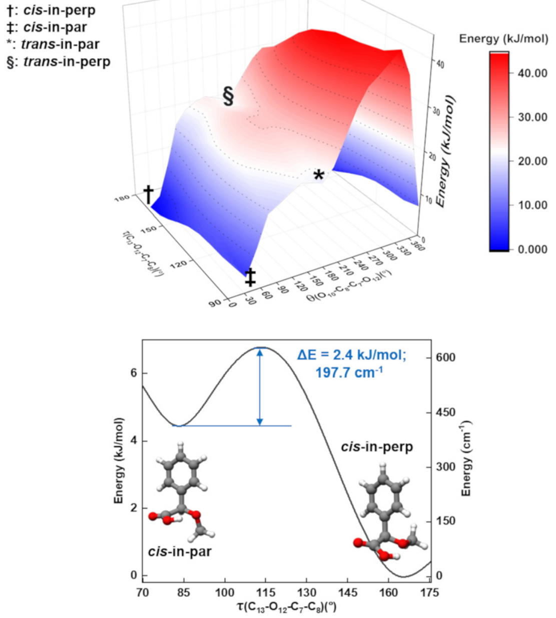

Fig. 4 Two-dimensional scan for the $\tau(C_{13}–O_{12}–C_7–C_8)$ and $\theta(O_{10}–C_8–C_7–O_{12})$ coordinates (top), showing the pathways between *cis*-in perp, *cis*-in-par, *trans*-in-perp, and *trans*-in-par. The surface was calculated at the B3LYP-D3(BJ)/def2-TZVP level of theory using steps of 10° for τ and 20° for θ. The lower graph shows a one-dimensional scan for the $\tau(C_{13}–O_{12}–C_7–C_8)$ coordinate, which connects *cis*-in-par and *cis*-in-perp. The curve was predicted at the B3LYP-D3(BJ)/def2-TZVP level of theory using steps of 10°. The barrier of around 2.4 kJ mol^{-1} explains the non-observation of *cis*-in-par.

conversion to a lower energy structure in the course of the supersonic expansion (Fig. 4).

Interestingly, each conformer of AMPA is connected to three other conformers by a change in the arrangement of one dihedral angle as shown in Fig. S3–S9 of the ESI.† These motions can be understood by performing systematic scans between the conformers, which give us the interconversion barriers for the conformer relaxation. In the case of the missing conformer (*cis*-in-par), the suggested relaxation pathway converts it into the lowest energy form by a change of the dihedral angle $\tau(C_{13}–O_{12}–C_7–C_8)$ (Fig. 4). This motion is predicted to be hindered by a barrier height of about 2.4 kJ mol^{-1} at the B3LYP-D3(BJ)/def2-TZVP level (3.6 kJ mol^{-1} at the DLPNO-CCSD/aug-cc-pVTZ level of theory), which is lower than the estimated barrier cut-off of 4.2 kJ mol^{-1} for conformer relaxation in a Ne-seeded supersonic expansion (Fig. 4).[48,49] Thus, the non-observation of this conformer is consistent with its conversion into the lowest energy form.

A two-dimensional scan (Fig. 4) for the $\tau(C_{13}–O_{12}–C_7–C_8)$ and $\theta(O_{10}–C_8–C_7–O_{12})$ coordinates shows the pathways and the relationships between several of the conformers. A second two-dimensional scan connecting the other four conformers is provided in Fig. S5 in the ESI.† The conformational relaxation pathways for the other detected conformers are hindered by potential barriers higher than 6 kJ mol^{-1} (Fig. S4–S9 of the ESI†), which prevent relaxation, in good agreement with the experimental observation of these conformers. Additional experiments were performed with He and Ar as carrier gases to explore their effect on the AMPA conformer relaxation pathways and are presented in Fig. S10 of the ESI.† In the experimental rotational spectra recorded using the three different carrier gases, the same five conformers were observed, and *cis*-in-par was always missing, even in the spectrum obtained with He as the carrier gas, where collisional relaxation processes are less efficient. The observation of the same five conformers regardless of the carrier gas demonstrates a selective relaxation of *cis*-in-par into *cis*-in-perp with all three different carrier gases and confirms the non-relaxation of the higher energy forms.

Internal rotation

A spectral fine structure due to a large amplitude motion was observed: some of the transitions for *cis*-in-perp and *trans*-out-par were split into doublets (Fig. 5), which were attributed to the methyl top internal rotation. Here, the methyl group internal rotation gives rise to three-equivalent minima represented by a periodic function that describes how it varies with the coordinate for the motion. The expansion term arising due to the three-fold symmetry of the methyl group depends on the barrier height parameters V_3 and V_6 with a major contribution from V_3,[11] while the term V_6 was not needed to obtain high-quality fits using XIAM, as presented in Table S3 of the ESI.† Each rotational energy level has two torsional sublevels denoted as the non-degenerate level A and a double degenerate level E, resulting in doublets in the rotational spectrum.

Quantum-chemical calculations were performed to obtain an approximation for the theoretical barrier for the methyl top internal rotation. The V_3 barrier depends on the position of the CH_3 group and its neighboring environment as well as the bond characters. The V_3 barriers for all observed AMPA conformers were calculated to be between 7 and 9 kJ mol^{-1} (B3LYP-D3(BJ)/def2-TZVP level of theory). The methyl internal rotation scans at the DLPNO-CCSD/aug-cc-pVTZ level of theory were also performed for the two lowest energy conformers *cis*-in-perp and *trans*-out-par, which predicted barrier heights of 8.1 and 7.7 kJ mol^{-1}, respectively. The predicted internal rotation barriers at the B3LYP-D3(BJ)/def2-TZVP level of theory for the two lowest energy conformers are shown in Fig. 6, while the others are presented in Fig. S11 of the ESI.† The moderately high V_3 barrier for the AMPA conformers makes most of the A and E state lines to appear blended in our spectrum. We could only resolve the splitting from transitions involving energy levels with K_a higher than 4, which are split into doublets spanning around 200–300 kHz. These components were analyzed and fitted using the XIAM program.[45]

The internal rotation barrier obtained from the experimental splittings for *cis*-in-perp (8.263(9) kJ mol^{-1})) is higher compared to that for *trans*-out-par (7.552(2) kJ mol^{-1}). This could be due to a CH···π interaction between the methyl group and the phenyl ring in *cis*-in-perp, which likely influences the rotation of the methyl top (*vide infra*). The computed barrier heights at the DLPNO-CCSD/aug-cc-pVTZ level for both conformers are in better agreement with the experimental values than those using B3LYP-D3(BJ)/def2-TZVP.

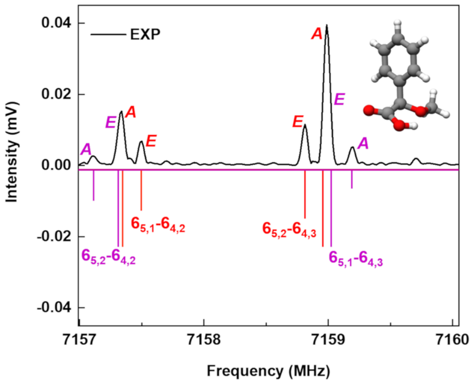

Fig. 5 Section of the rotational spectrum of AMPA to illustrate the fine structure of the spectrum for *cis*-in-perp due to the internal rotation of the methyl top. The lower traces represent the simulations using the fitted rotational parameters from XIAM. The labelling of the rotational transitions follows the $J'_{K'_a,K'_c} \leftarrow J''_{K''_a,K''_c}$ scheme, where b-type transitions are shown in red and c-type transitions are shown in violet.

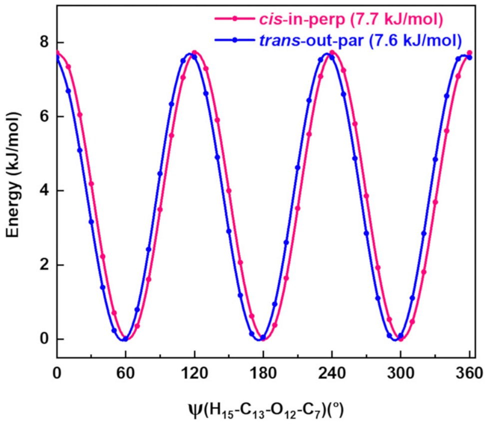

Fig. 6 Methyl internal rotation scan for *cis*-in-perp and *trans*-out-par performed at the B3LYP-D3(BJ)/def2-TZVP level of theory.

Experimental structure

In the rotational spectrum with Ne as the carrier gas, we observed a signal-to-noise ratio of 500 : 1 for the strongest transition, $6_{0,6}$–$5_{1,5}$ of the most stable conformer, *cis*-in-perp, with an intensity of 780 μV. This allowed us to observe the rotational spectra of all of its singly-substituted ^{13}C isotopologues in natural abundance (1.1%) and to derive its experimental structure. Table S2 in the ESI† summarizes the experimentally determined rotational parameters for the nine ^{13}C isotopologues and those of the parent species. The atom coordinates of these carbon atoms with respect to the center of mass of the molecule were derived using Kraitchman's equations,[50] allowing us to build the so-called substitution structure, r_s, atom by atom. This method provides only the absolute values for the atomic coordinates, so the signs were taken from the calculations. A comparison between the equilibrium structure r_e obtained from quantum-chemical calculations at B3LYP-D3(BJ)/def2-TZVP and the experimental structure r_s is displayed in Fig. 7, showing a remarkable agreement between them.

Alternative structural information was obtained by fitting the effective ground state structure, r_0. The r_0 structure was determined by performing a least-square fit of certain structural parameters using the rotational constants from all the observed species. The r_0 parameters are shown in blue in Fig. 7. Table S4 in the ESI† summarizes the experimental structural r_0 and r_s parameters, such as the bond lengths and angles, in comparison with the r_e parameters. The signal-to-noise ratio was not sufficient to observe the rotational spectra of the ^{18}O isotopologues in natural abundance (0.2%) or any rare isotopologue for the other isomers of AMPA.

Intramolecular interactions

The relative stability of the conformers can be further analyzed by investigating the intramolecular interactions present in AMPA. Fig. 2 shows the results of non-covalent interaction

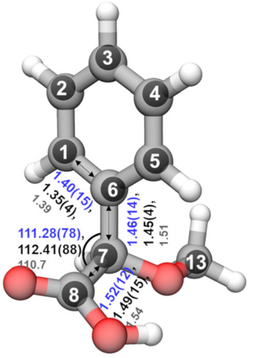

Fig. 7 Comparison of the calculated r_e (outer semi-transparent structure) and experimentally determined r_s substitution (black inner spheres) structures of *cis*-in-perp. The bond lengths and angles for the r_s structure are shown in black, for r_0 in blue, and for r_e in gray.

(NCI) plots, which help in visualizing and characterizing the different attractive and repulsive interactions present in the different AMPA conformers. The sign of the Laplacian of the density, $\nabla^2\rho$, is a widely used tool to distinguish between different types of interactions. This Laplacian has contributions from all the three principal axes of maximal variation, which have three eigenvalues λ_i of the electron density of the Hessian matrix. The second eigenvalue λ_2 then helps in discerning between different types of non-covalent interactions such as hydrogen bonding, dispersion, and steric interactions. When $\lambda_2 < 0$, it indicates the presence of strong attraction, while values around 0 reveal weak attraction. The positive values of λ_2 imply repulsive interactions.[38]

The *cis*-in-perp and *cis*-in-par conformers present the *cis* configuration together with the hydrogen atom from the carboxylic acid group pointing towards (in) the oxygen of the methoxy group. A moderately strong O–H···O intramolecular hydrogen bond is formed with bond lengths of 1.9 and 2.0 Å in *cis*-in-perp and *cis*-in-par, respectively. In the *trans*-in-par and *trans*-in-perp conformations, although the hydrogen atom from the carboxylic acid group is also pointing inwards, the intramolecular interaction is formed with the π-cloud of the benzene ring, O–H···π. In principle, that is also a stabilizing interaction based on the NCI plots, however, in order to form it, the carboxylic acid group is tilted from its preferred position, resulting in two high-energy conformations (Fig. 2).

Another stabilizing interaction is formed between one hydrogen atom of the phenyl ring and the lone pair of the oxygen atom of the OCH_3 group. This CH···O interaction is present in the eight isomers of AMPA and seems to be of similar strength regardless of the par–perp configuration of the OCH_3 group. There is another CH···O interaction, in this case between the hydrogen atom from the OCH_3 group and the lone pair of the oxygen atom from the carboxylic acid group. This interaction also seems to be stabilizing, but is only possible in conformers that are in par configuration since only for those conformers the methoxy group is in the correct orientation to establish the contact. However, the conformers with the OCH_3 group in the perp disposition have a possibility of an alternative interaction. This is a long-range CH···π interaction, bringing further stability to conformers in perp configuration. Finally, it is worth mentioning that a repulsive interaction is present in all the conformers of AMPA and occurs between two oxygen atoms opposed to each other. Regardless of the conformations, there is always a slight destabilization force between the oxygen from the methoxy group and one for the oxygen atoms from the carboxylic acid group.

As mentioned above, the interactions also influence the internal rotation barrier of the conformers. The experimental barrier height for *cis*-in-perp is slightly higher than that for *trans*-out-par due to the presence of the CH···π interaction between the methyl group and the phenyl ring. Fig. S11 in the ESI† shows the theoretical barrier heights for the *cis*-out-par, *trans*-out-perp, and *cis*-out-perp conformers. The theoretical calculations predict barriers to be slightly higher for the conformers in the perp configuration compared with those in par, in good agreement with the effect of the CH···π interaction. The presence of these interactions helps in explaining the energy ordering of the different conformers of AMPA and their internal dynamics.

Conclusions

We report new experimental and theoretical insights into the conformational landscape for the monomer of alpha-methoxy phenylacetic acid. We have successfully used broadband rotational spectroscopy and quantum-chemical calculations to probe its rich conformational space and internal dynamics. We experimentally identified and characterized five conformations out of six predicted low-energy structures, together with an accurate structure determination for the lowest energy conformer. The conformers are related to others *via* changes of the *cis*–*trans*, in-out, and perp-par configurations. The analysis of the interconversion pathways can explain why one conformer is not present in our experimental spectrum, regardless of the carrier gas used. The conformers are stabilized by non-covalent intramolecular interactions, and have been analysed to understand their energy order. Such intramolecular interactions govern the conformational landscape and influence the internal dynamics of AMPA, highlighting the importance of studying such interactions in detail. Both the DLPNO-CCSD/aug-cc-pVTZ and the B3LYP-D3(BJ)/def2-TZVP levels of theory seem to be good quantum-chemical methods to describe molecular systems such as AMPA, as is demonstrated by our detailed comparison with structural information from rotational spectroscopy. The present study forms the basis for future investigations about the micro-solvation of AMPA to understand solute–solvent interactions and to learn how solvation will affect the internal dynamics of similar molecules.

Author contributions

Himanshi Singh: investigation, formal analysis, writing – original draft, and writing – review and editing. Pablo Pinacho:

conceptualization, investigation, formal analysis, and writing – review and editing. Daniel A. Obenchain: formal analysis and writing – review and editing. María Mar Quesada-Moreno: investigation and writing – review and editing. Melanie Schnell: conceptualization, funding acquisition, project administration, and writing – review and editing.

Conflicts of interest

The authors declare no conflicts of interest.

Acknowledgements

We thank Prof. Dr. Christian Merten for bringing this molecule to our attention. This work was supported by the collaborative linkage grant "Extreme light for sensing and driving molecular chirality (ELCH)", SFB1319, of the Deutsche Forschungsgemeinschaft. Parts of the computations were performed by using the European XFEL and DESY funded Maxwell computational resources operated at Deutsches Elektronen-Synchrotron DESY, Hamburg, Germany. The benchmarking aspect of this work was profited from the environment provided by the local research training group BENCH (DFG -389479699/GRK2455). P. P. would like to thank the Alexander von Humboldt Foundation for a postdoctoral fellowship. M. M. Q. M. thanks Fundación Alfonso Martín Escudero for a postdoctoral grant and Junta de Andalucía for a postdoctoral contract (DOC_01282).

Notes and references

1 C. Min and D. Seidel, *Chem. Soc. Rev.*, 2017, **46**, 5889–5902.
2 S. Dayal, K. D. Kalra and P. Sahu, *J. Cosmet. Dermatol.*, 2020, **19**, 393–399.
3 H. V. L. Nguyen, H. Mouhib, S. Klahm, W. Stahl and I. Kleiner, *Phys. Chem. Chem. Phys.*, 2013, **15**, 10012–10018.
4 D. Schmitz, V. A. Shubert, T. Betz and M. Schnell, *Front. Chem.*, 2015, **3**, 15.
5 S. R. Domingos, C. Pérez, C. Medcraft, P. Pinacho and M. Schnell, *Phys. Chem. Chem. Phys.*, 2016, **18**, 16682–16689.
6 A. Krin, C. Pérez, P. Pinacho, M. M. Quesada-Moreno, J. J. López-González, J. R. Avilés-Moreno, S. Blanco, J. C. López and M. Schnell, *Chem. – Eur. J.*, 2018, **24**, 721–729.
7 M. M. Quesada-Moreno, A. Krin and M. Schnell, *Phys. Chem. Chem. Phys.*, 2019, **21**, 26569–26579.
8 R. A. Mata and M. A. Suhm, *Angew. Chem., Int. Ed.*, 2017, **56**, 11011–11018.
9 P. H. Buist and D. M. Marecak, *J. Am. Chem. Soc.*, 1992, **114**, 5073–5080.
10 K. Bünnemann and C. Merten, *Phys. Chem. Chem. Phys.*, 2017, **19**, 18948–18956.
11 W. Gordy and R. L. Cook, *Microwave Molecular Spectra*, Wiley, New York, 1984.
12 C. H. Townes and A. L. Schawlow, *Microwave Spectroscopy*, Dover, New York, 1975.
13 G. B. Park and R. W. Field, *J. Chem. Phys.*, 2016, **144**, 200901.
14 G. G. Brown, B. C. Dian, K. O. Douglass, S. M. Geyer, S. T. Shipman and B. H. Pate, *Rev. Sci. Instrum.*, 2008, **79**, 053103.
15 V. A. Shubert, D. Schmitz, C. Medcraft, A. Krin, D. Patterson, J. M. Doyle and M. Schnell, *J. Chem. Phys.*, 2015, **142**, 214201.
16 D. Schmitz, V. A. Shubert, B. M. Giuliano and M. Schnell, *J. Chem. Phys.*, 2014, **141**, 034304.
17 J. R. A. Moreno, T. R. Huet and J. J. L. González, *Struct. Chem.*, 2013, **24**, 1163–1170.
18 C. Medcraft and M. Schnell, *Z. Phys. Chem.*, 2016, **230**, 1–14.
19 E. J. Cocinero, A. Lesarri, P. Écija, Á. Cimas, B. G. Davis, F. J. Basterretxea, J. A. Fernández and F. Castaño, *J. Am. Chem. Soc.*, 2013, **135**, 2845–2852.
20 S. Blanco, A. Lesarri, J. C. López and J. L. Alonso, *J. Am. Chem. Soc.*, 2004, **126**, 11675–11683.
21 T. Betz, S. Zinn and M. Schnell, *Phys. Chem. Chem. Phys.*, 2015, **17**, 4538–4541.
22 M. Varela, C. Cabezas, J. C. López and J. L. Alonso, *J. Phys. Chem. A*, 2013, **117**, 13275–13278.
23 C. Pérez, A. Krin, A. L. Steber, J. C. López, Z. Kisiel and M. Schnell, *J. Phys. Chem. Lett.*, 2016, **7**, 154–160.
24 C. Pérez, J. L. Neill, M. T. Muckle, D. P. Zaleski, I. Peña, J. C. Lopez, J. L. Alonso and B. H. Pate, *Angew. Chem., Int. Ed.*, 2015, **54**, 979–982.
25 P. Pinacho, A. Krin, C. Pérez, S. Zinn, J. C. López, S. Blanco and M. Schnell, *Phys. Chem. Chem. Phys.*, 2018, **20**, 15635–15640.
26 S. Melandri, D. Consalvo, W. Caminati and P. G. Favero, *J. Chem. Phys.*, 1999, **111**, 3874–3879.
27 W. Li, M. M. Quesada-Moreno, P. Pinacho and M. Schnell, *Angew. Chem., Int. Ed.*, 2021, **60**, 5323–5330.
28 C. Bannwarth, S. Ehlert and S. Grimme, *J. Chem. Theory Comput.*, 2019, **15**, 1652–1671.
29 C. Lee, W. Yang and R. G. Parr, *Phys. Rev. B: Condens. Matter Mater. Phys.*, 1988, **37**, 785–789.
30 A. D. Becke, *J. Chem. Phys.*, 1993, **98**, 5648–5652.
31 S. H. Vosko, L. Wilk and M. Nusair, *Can. J. Phys.*, 1980, **58**, 1200–1211.
32 S. Grimme, J. Antony and S. Ehrlich, *J. Chem. Phys.*, 2010, **132**, 154104.
33 S. Grimme, S. Ehrlich and L. Goerigk, *J. Comput. Chem.*, 2011, **32**, 1456–1465.
34 F. Weigend and R. Ahlrichs, *Phys. Chem. Chem. Phys.*, 2005, **7**, 3297–3305.
35 F. Neese, *Wiley Interdiscip. Rev.: Comput. Mol. Sci.*, 2012, **2**, 73–78.
36 F. Neese, *Wiley Interdiscip. Rev.: Comput. Mol. Sci.*, 2018, **8**, e1327.
37 M. J. Frisch, *et al.*, *Gaussian 16, Revision B.01*, Gaussian, Inc., Wallingford CT, 2016.
38 E. R. Johnson, S. Keinan, P. Mori-Sánchez, J. Contreras-García, A. J. Cohen and W. Yang, *J. Am. Chem. Soc.*, 2010, **132**, 6498–6506.
39 J. Contreras-García, E. R. Johnson, S. Keinan, R. Chaudret, J. P. Piquemal, D. N. Beratan and W. Yang, *J. Chem. Theory Comput.*, 2011, **7**, 625–632.
40 D. Schmitz, V. A. Shubert, T. Betz and M. Schnell, *J. Mol. Spectrosc.*, 2012, **280**, 77–84.

41 C. Pérez, S. Lobsiger, N. A. Seifert, D. P. Zaleski, B. Temelso, G. C. Shields, Z. Kisiel and B. H. Pate, *Chem. Phys. Lett.*, 2013, **571**, 1–5.

42 C. M. Western, *J. Quant. Spectrosc. Radiat. Transfer*, 2017, **186**, 221–242.

43 J. K. Watson, *J. Mol. Spectrosc.*, 1977, **65**, 123–133.

44 H. M. Pickett, *J. Mol. Spectrosc.*, 1991, **148**, 371–377.

45 H. Hartwig and H. Dreizler, *Z. Naturforsch., A: Phys. Sci.*, 1996, **51**, 923–932.

46 R. C. Woods, *J. Mol. Spectrosc.*, 1967, **22**, 49–59.

47 PROSPE – Programs for ROtational SPEctroscopy, **https://www.ifpan.edu.pl/~kisiel/prospe.htm**, (accessed July, 2022).

48 R. S. Ruoff, T. D. Klots, T. Emilsson and H. S. Gutowsky, *J. Chem. Phys.*, 1990, **93**, 3142–3150.

49 P. Pinacho, J. C. López, Z. Kisiel and S. Blanco, *Phys. Chem. Chem. Phys.*, 2020, **22**, 18351–18360.

50 J. Kraitchman, *Am. J. Phys.*, 1953, **21**, 17–24.

5.1 Summary and outlook

The article presents a gas-phase investigation of the chiral molecule, AMPA, using broadband rotational spectroscopy. Five different conformers of AMPA were detected in the experiments, out of six low-energy structures predicted from quantum-chemical calculations. The conformational relaxation processes of the molecule were explored in three different carrier gases (He, Ne, and Ar) as different conformers are related to each other by distinct motions of the methoxy group and the carboxylic acid group. The analysis of the conversion pathways explained the non-observation of the third most stable conformer in the experimental conditions, as it relaxes into a lower energy structure. Line splittings attributed to the methyl group internal rotation were analysed and fitted for the two most stable conformers using the XIAM program. Furthermore, all singly substituted ^{13}C-isotopologues were identified and an accurate experimental structure for the lowest energy conformer was determined. The non-covalent intramolecular interactions play an important role in determining the energy ordering of the conformers of AMPA and influence their internal dynamics. This conformational analysis forms the foundation for further investigations into solute-solvent interactions, exploring how solvation affects the internal dynamics of AMPA.

Electron-withdrawing groups like the carboxylic acid, and the methoxy group offer favourable binding sites for solute-solvent interactions. As previously mentioned in Chapter 3, CP-FTMW spectroscopy coupled with supersonic expansion, provides a favourable environment to elucidate the accurate structures of weakly bound complexes isolated in the gas phase.

To model a broader range of solute-solvent interactions of AMPA, different solvent molecules were considered. As a first complex partner, water (H_2O) was chosen because of its small size and its double hydrogen bond donor-acceptor capability. Dimethyl sulfoxide (DMSO, C_2H_6OS) and phenol (Ph, C_6H_6O) were also selected to cover different interaction possibilities, such as $CH\cdots O$ and $\pi\cdots\pi$ interactions. To explore different conformations of the AMPA complexes, a similar workflow for conformational searches and optimisations of conformers was followed, as depicted in Fig. 2.6. Initial conformational searches of the complexes were performed with CREST; this was followed by refinement of structures through optimisation at the B3LYP-D3(BJ)/def2-TZVP level of theory. The optimised geometries of the most stable structures of complexes of AMPA with water, DMSO, and Ph obtained at the B3LYP-D3(BJ)/def2-TZVP level of theory are depicted in Fig. 5.1. All three solvent molecules prefer different conformations of AMPA during complexation detailed in the next paragraph.

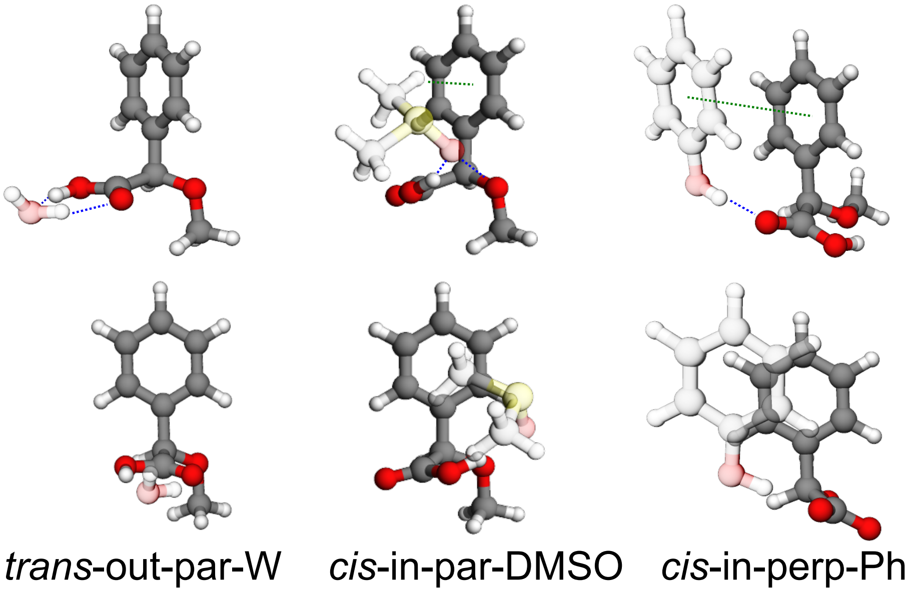

Figure 5.1: Most stable geometries of AMPA complexes with water (W), dimethyl sulfoxide (DMSO), and phenol (Ph). Water and DMSO prefer the *trans*-out-par, *cis*-in-par conformations of AMPA, respectively, while phenol complexes with the *cis*-in-perp conformation. These geometries were obtained at the B3LYP-D3(BJ)/def2-TZVP level of theory.

Initial investigations of optimised structures of AMPA complexes reveal that water prefers to bind to AMPA's second most stable structure, *trans*-out-par, while DMSO interacts with the *cis*-in-par conformation, previously unobserved in monomer experiments. In the *trans*-out-par-W complex, water positions itself between the hydroxyl and carbonyl groups, forming a six-membered hydrogen bond network. Meanwhile, in the *cis*-in-par-DMSO complex, the methyl group of DMSO engages in CH$\cdots\pi$ interactions atop the benzene ring. Additionally, the sulfoxide group of DMSO interacts with AMPA's hydroxyl group, forming an intermolecular OH$\cdots$O interactions and disrupting the intramolecular hydrogen bond of *cis*-in-par conformation of AMPA. The *cis*-in-perp-Ph complex has its two benzene rings in a parallel-displaced orientation similar to the parallel-displaced geometry of the benzene dimer.[206] These displaced phenyl rings engage in $\pi\cdots\pi$ interactions, along with intra- and intermolecular hydrogen bonds between the hydroxyl group of phenol and the carboxylic acid group of AMPA.

The preliminary conformational analysis of AMPA complexes from calculations shows distinct conformational preferences in the presence of solvent molecules. The rotational spectra for these complexes have already been obtained and will be examined in the future. The next step also involves analysing how these solvent molecules influence the line splittings observed in the rotational spectra of the two most stable conformers of AMPA, caused by methyl internal rotation. Additionally, it would be interesting to explore and identify the solvent interactions with alternate conformations of AMPA.

The quantum-chemical calculations of AMPA complexes indicate how intra- and intermolecular hydrogen bonding influences the conformational landscape of AMPA in diverse solvent environments. AMPA thus becomes a valuable model for exploring the interplay between different functional groups in solute-solvent interactions and serves as an ideal system for modeling the internal dynamics of drug molecules containing the phenylacetic acid moiety. This study and analysis of complexes with AMPA serve as a continuation of our research on the monomer, expanding our understanding of its interactions with solvents.

Chapter 6

Conformational flexibility in a bio-renewable chemical, 6-amyl-α-pyrone

Fossil fuels, including coal, oil, and natural gas, currently serve as the backbone of our global economy, supplying approximately 80% of the world's energy.[215] However, they are non-renewable resources diminishing rapidly, which has prompted the exploration of alternative and renewable fuel sources. In this respect, biomass, being renewable by nature, offers an ideal alternative to fossil fuels.

Starch, sugars, triglycerides, and lignocellulose are the general classes of raw materials derived from biomass used for producing biofuels and chemicals. Among these, plant-based lignocellulosic biomass, composed of lignin, cellulose, and hemicellulose, stands out as the most abundant and cost-effective alternative for biofuel. Significant efforts are in progress to develop novel processes that allow the conversion of lignocellulosic biomass and its derivatives into long-chain and branched hydrocarbon chemicals and fuels.

In one such strategy, Dumesic and coworkers proposed the synthesis of C_9 linear ketones from biomass-derived building blocks such as levulinic acid as feedstock using catalysts.[216, 217] Later, Alam and coworkers suggested another novel strategy of producing unsaturated or saturated linear ketones from biomass-derived precursors using an inexpensive catalyst with a simplified process compared to the previous methods requiring integration of several steps.[218] The proposed method is based on the ring-opening and decarboxylation of a flavouring agent, 6-amyl-α-pyrone (6PP), obtained from the fermentation of sugarcane bagasse.[218, 219] The reaction yields non-2-ene-4-one, a C_9 linear ketone, with a high yield (95% conversion) when performed in the aqueous phase in the absence of any catalyst. These unsaturated ketone products can then be hydrogenated and can react with other biomass materials such as furanics, to yield longer hydrocarbons like C_{14} or C_{15}, either via aldol condensation or hydroxy alkylation pathways.[220, 221] This makes 6PP a potential biomass-derived platform molecule for synthesising a myriad of interesting products to be used as fuels, chemicals, polymers, and pharmaceuticals (Fig. 6.1). In an alternative bio-based route, 6PP can undergo catalytic hydrogenation to produce another industrially important chemical, δ-decalactone, which is largely used in the perfume and food industries (Fig. 6.1). Furthermore, 6PP is used in the food and beverage industry as a flavour enhancer, due to its characteristic coconut aroma.

Given the wide range of potential applications for 6PP, understanding its stability, reactivity, and physicochemical properties becomes crucial. These aspects are closely linked to its structural characteristics, particularly the conformations it can adopt and their associated intramolecular forces. In this work, the conformational space of 6PP is explored. This exploration not only aids in understanding its structural properties but can also shed light on its interactions with other molecules.

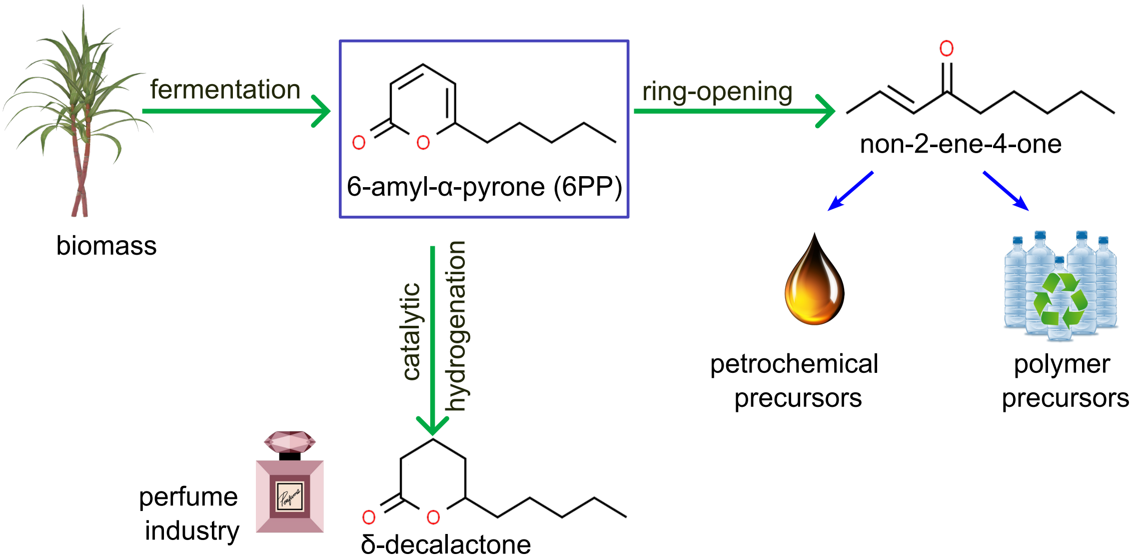

Figure 6.1: 6-amyl-α-pyrone (6PP) can be synthesised from the fermentation of the sugarcane bagasse. It acts as a precursor for the synthesis of other industrially relevant chemicals such as δ-decalactone and non-2-ene-4-one. These chemicals find their application in the food and perfume industries and as precursors for petrochemicals and polymers. The coconut aroma of 6PP makes it a good flavouring agent in the food and beverage industry.

Structurally, 6PP is an unsaturated lactone with two double bonds within the lactone ring and a pentyl linear chain attached at the carbon adjacent to the ring oxygen, as shown in Fig. 6.2. The pentyl substituent on the lactone ring contributes to its high flexibility and offers a rich conformational landscape. MW spectroscopy is a robust spectroscopic technique for gas phase structure determination and conformational analysis. The technique is well-suited for the study of multi-conformer systems due to its inherent high precision and resolution. Some of the recent MW spectroscopy investigations of flexible molecular systems include fruit esters,[222, 223] macrocycles,[224, 225] and monterpenes[226–228].

This study employs CP-FTMW spectroscopy to explore the conformational flexibility of 6-amyl-α-pyrone under the cold conditions of a molecular jet. The ensuing section provides a brief overview of the experimental and computational methodologies used in this study, followed by results section which elaborates on the identified conformations of 6PP, their structural similarities, and how they are energetically ordered.

6.1 Experimental and computational details

A sample of 6PP was purchased from TCI Chemicals (Europe) and used without purification. It is an orange-brown liquid with a boiling point of 286 °C. The rotational spectrum was obtained in the 2-8 GHz frequency range using the COMPACT spectrometer, described in Chapter 3. Only a concise overview of specific experimental parameters is provided here.

The molecules were introduced into a supersonic expansion using a pulsed nozzle operating at a repetition rate of 8 Hz. The sample was initially heated to 50 °C, gradually increasing to 160 °C to optimise the signal intensity for 6PP. The molecules were seeded into a constant flow of Ne carrier gas at a stagnation pressure of 2 bar to generate a cold molecular jet. The molecules in the expanded supersonic jet interact with a 4 µs long microwave chirp pulse spanning from 2 to 8 GHz. The latter chirp was generated using an AWG in interleave mode and amplified with a 300 W TWT amplifier. The amplified microwave pulse was broadcast using a dual-polarisation horn antenna. It then interacts with the molecules in the supersonic jet, oriented perpendicular to the microwave field. After the halt of the chirped pulse, the polarised molecular ensemble undergoes relaxation, which is measured in the form of a FID in the time domain using the oscilloscope. A 40 µs segment of the FID was Fourier transformed with a Kaiser-Bessel window resulting in a resolution of 25 kHz. A total of 3.7 million FID recordings were co-added and averaged to obtain the final spectrum.

The experimental analysis was supported by the quantum-chemical calculations performed using the program package ORCA.[119, 120] A rich conformational landscape arises due to the flexible pentyl chain attached to the pyrone ring resulting in several energy-stable structures. The conformational space of 6PP was explored in two stages, as shown in Fig. 2.6. Initially, a semi-empirical search was performed using the conformational sampling program xTB[229] and CREST.[121] The conformational ensemble was then refined by re-optimising structures using the B3LYP functional,[124, 202, 230] including Grimme's D3 dispersion correction[127] and Becke-Johnson(BJ) damping,[126] combined with the def2-TZVP basis set.[134] The optimised conformers were then tested for real minima structures and to obtain zero-point corrected energies through harmonic frequency calculations at the same level of theory. In addition to the geometry optimisations and harmonic frequency calculations at the B3LYP-D3(BJ)/def2-TZVP level of theory, single-point energy calculations at the DLPNO-CCSD/aug-cc-pVTZ[128, 136] level of theory were performed to obtain more accurate energies. Furthermore, dihedral scans were carried out to explore the possibility of relaxation in the conformers that can interconvert into each other.

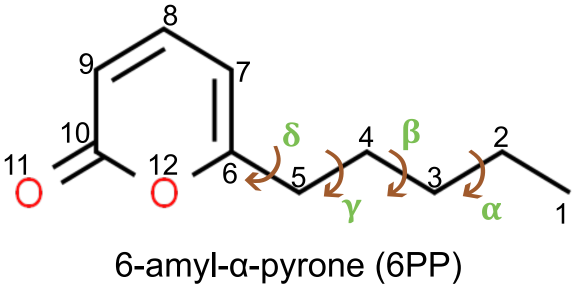

Figure 6.2: Schematic structure of 6PP ($C_{10}H_{14}O_2$). The carbon atoms that define the four dihedral angles-$\angle\alpha$ (C1-C2-C3-C4), $\angle\beta$ (C2-C3-C4-C5), $\angle\gamma$ (C3-C4-C5-C6), and $\angle\delta$ (C4-C5-C6-C7), which determine the conformational space of 6PP, are labelled. The same atom numbering is used for all conformers.

6.2 Results and discussions

The molecule exhibits conformational flexibility arising from the various possible configurations of four C-C single bonds in the linear pentyl chain attached to the pyrone ring as depicted in Fig. 6.2. The three torsional angles of this saturated pentyl side chain can be in *gauche* (60°(g), -60°(g')) or *trans*(t) orientations, resulting in approximately twenty-seven different conformations. These torsional angles are defined as $\angle\alpha$ (C1-C2-C3-C4; $g/g'/t$), $\angle\beta$ (C2-C3-C4-C5; $G/G'/T$), and $\angle\gamma$ (C3-C4-C5-C6; $g/g'/t$), as marked in Fig. 6.2. The conformers are named based on the conformational arrangements of these three dihedral angles. The most stable conformation of 6PP, as predicted by calculations, is *tTg'-A*, with α, β, and γ angles of 179°, 178°, and -62°, respectively. The orientation of the pentyl side chain with respect to the plane of the pyrone ring produces two more possibilities for each conformer. The pentyl chain can be either perpendicular or within the plane of the pyrone ring with C_1 and C_s symmetry, as observed for *tTt-A* and *tTt-B* conformations, respectively, and as shown in Fig. 6.3.

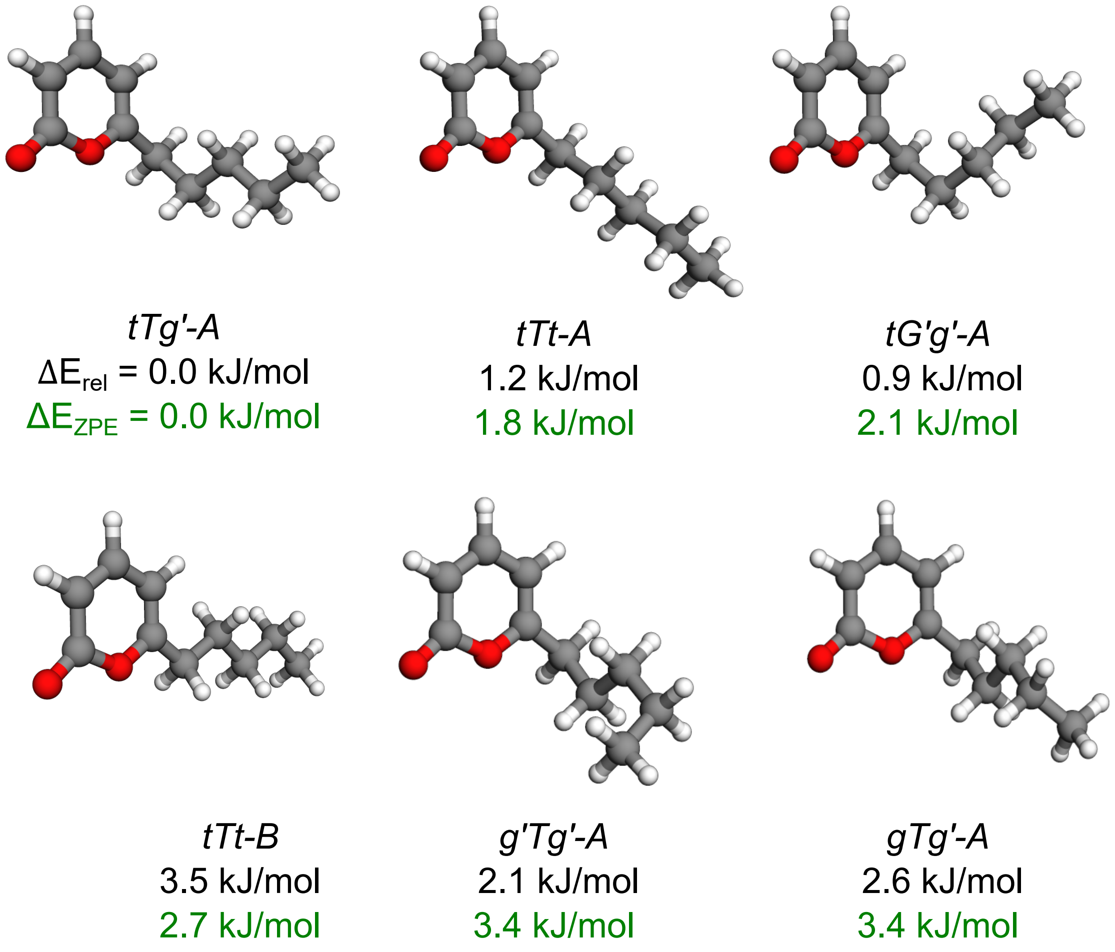

Figure 6.3: Optimised geometries of six conformations of 6PP obtained at the B3LYP-D3(BJ)/def2-TZVP level of theory. Relative energies and zero-point corrected energies are provided in black and green colour, respectively.

The dihedral angle ∠δ(C4-C5-C6-C7) in conformer *tTt-A* is 113.5°, while for its rotamer *tTt-B*, the same dihedral angle is 0.4°. The conformer *tTt-A* is predicted to be lower in energy than *tTt-B*, as depicted in Fig. 6.3.

Due to the different possibilities for these four dihedral angles, more than twenty-seven different structures are obtained from calculations. Out of these optimised geometries, nineteen conformations were found to be within a relative energy threshold of around 6 kJ/mol, as shown in Fig. 1 of the appendix and are listed in Table 6. Optimised structures of the six most stable conformers are provided in Fig. 6.3 along with their relative and zero-point corrected energies obtained at the B3LYP-D3(BJ)/def2-TZVP level of theory. It is observed that the four lowest energy structures have a preference for *trans* orientation for the first torsional ∠α, while the fifth and sixth stable conformers favour *trans* configuration for the dihedral ∠β. Table 6.1 presents the rotational parameters of the six low-energy conformations of 6PP, along with their relative zero-point corrected energies obtained from calculations at the B3LYP-D3(BJ)/def2-TZVP level of theory. Single-point relative energies obtained at the DLPNO-CCSD/aug-cc-pVTZ level of theory based on the DFT-optimised structures with and without the zero-point corrected energy terms obtained from the frequency calculations with the DFT method are also listed. Both methods predict the *tTg'-A* conformer as the global minimum and an energy gap of around 1.8 kJ/mol to the next conformer. The relative zero-point corrected energy ordering of conformers is slightly shuffled for the two levels of theories but with small differences in values starting from the second conformer *tTt-A*.

The predicted rotational parameters from quantum-chemical calculations were then used to identify different conformers of 6PP in the experimental spectrum. The positive trace in Fig. 6.4 represents a part of the experimental spectrum of 6PP. It exhibits a plethora of rotational transitions, which reflect the complex conformational landscape of 6PP. The calculated structures have sizeable μ_a and μ_b dipole-moment components and are expected to show predominantly *a*- and *b*-type spectra, which was used to guide the assignment. The spectral assignments were performed using two fitting programs. The initial fits were done using PGOPHER, followed by refinement with the SPFIT/SPCAT program, employing Watson's *A*-reduction Hamiltonian in I^r representation.[141, 142, 205]

Due to the strong *b*-type dipole-moment component of the most stable conformation of 6PP, *tTg'-A*, the *b*-type *R*-branch transition pattern could be easily identified and assigned to the *tTg'-A* conformer. The observed rotational transitions range from $J = 2$ to $J = 14$ with a maximum K_a of 6 in the experimental spectrum of the

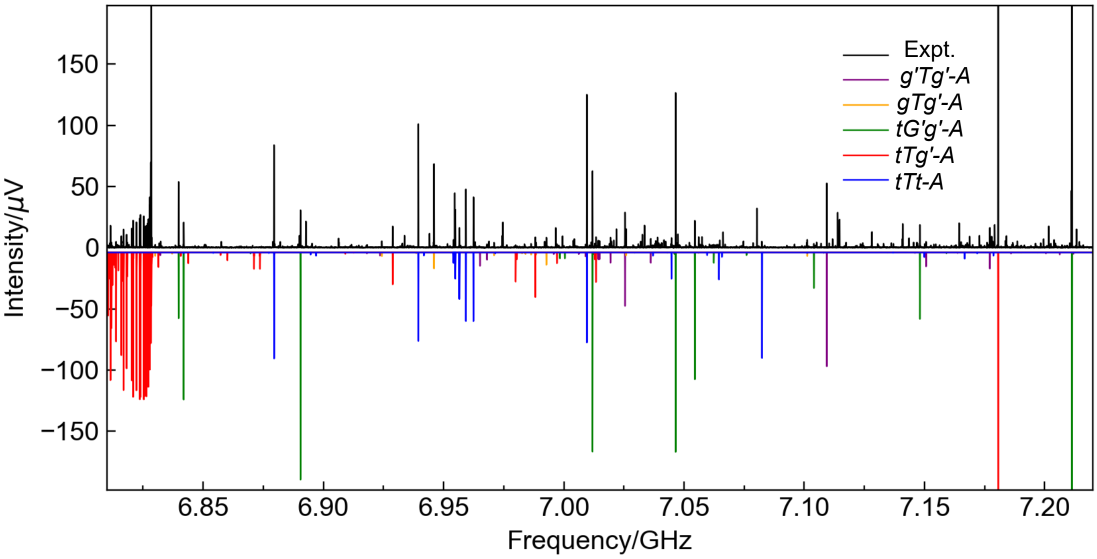

Figure 6.4: An excerpt of the experimental rotational spectrum of 6PP. The top black trace is the experimental spectrum while the bottom coloured traces are the simulated spectra obtained using experimentally fitted rotational parameters at a rotational temperature of 3 K for the six assigned species.

tTg'-A conformer. The most intense rotational transition in the experimental spectrum is observed at 7180.65 MHz for the $7_{17} - 6_{06}$ rotational transition of *tTg'-A* isomer with a SNR ratio of 1800:1. The singly substituted ^{13}C-isotopic species at the predicted frequency shifts with respect to the parent species were observed with a good SNR. All ten singly-substituted ^{13}C-isotopologues of the *tTg'-A* conformer were identified in their natural abundance (≈1.1%) and the determined rotational constants are collected in Table 7. The observation of the ^{13}C-monosubstituted isotopic species of the most stable conformer of 6PP allowed the derivation of the atomic coordinates of the carbon atoms with respect to the center of mass of the molecule using Kraitchman's equations, and the subsequent determination of the so-called substitution structure, r_s of the carbon framework.[118] Fig. 6.5 presents a comparison between the equilibrium structure (r_e) obtained from calculations at the B3LYP-D3(BJ)/def2-TZVP level of theory and the experimental structure (r_s) of 6PP, showing good agreement.

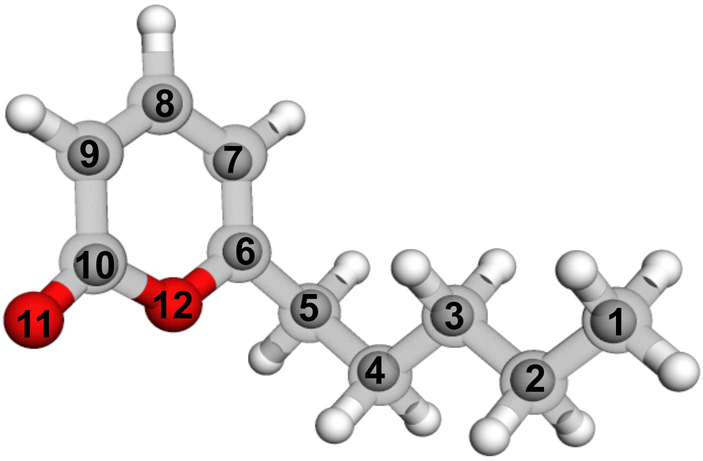

Figure 6.5: An overlay of the experimentally determined substitution structure, r_s (inner spheres), on the equilibrium structure, r_e (semi-transparent structure, obtained at the B3LYP-D3(BJ)/def2-TZVP level of theory), for the *tTg'-A* conformer of 6PP.

Four more conformers of 6PP, i.e., *tTt-A*, *tG'g'-A*, *g'Tg'-A*, and *gTg'-A* were assigned in the rotational spectrum. Conformers *tTt-A*, *g'Tg'-A*, and *gTg'-A* primarily showed *b*-type spectra, while the *tG'g'-A* conformation showed an *a*-type spectrum. Table 6.1 summarises the experimentally fitted rotational constants along with the centrifugal distortion constants obtained from fits using Pickett's SPFIT/SPCAT program suite.[142]

Rotational transitions corresponding to the rotamer of *tTt-A* of 6PP, i.e., *tTt-B* could not be identified in the spectrum analysis. The reason for its non-observation could be its conversion to a lower energy structure *tTt-A* during the supersonic expansion. As the two conformers differ by the orientation of the pentyl chain with respect to the pyrone, a torsional angle scan of $\angle\delta$(C4-C5-C6-C7) was performed to determine the interconversion barrier for this motion. This motion is predicted to be hindered by a barrier height of about 4.4 kJ/mol (depicted in Fig. 6.6) at the B3LYP-D3(BJ)/def2-TZVP level of theory. This computed interconversion barrier for the *tTt-B* conformation of 6PP is almost the estimated cut-off of 4.2 kJ/mol for conformer relaxation in a Ne-seeded supersonic expansion.[34, 184, 231] Thus, it could be expected that the *tTt-B* conformer relaxes into *tTt-A*, a lower energy structure of 6PP.

Table 6.1: Experimental rotational parameters of 6PP conformers along with the predicted parameters at the B3LYP-D3(BJ)/def2-TZVP level of theory are listed here. The experimental rotational parameters for the five conformers of 6PP are obtained by fitting using the SPFIT program.

Parameters	*tTg'-A*		*tTt*-A		*tG'g'-A*	
	calc.	exp.	calc.	exp.	calc.	exp.
A/MHz[1]	1449.3	1435.16333(20)	2239.8	2231.50861(43)	1563.2	1565.4626(15)
B/MHz	461.6	468.097845(68)	350.5	351.52361(13)	511.6	518.12835(62)
C/MHz	447.3	451.062169(66)	316.8	317.39684(13)	466.9	474.72230(70)
Δ_J/kHz	-	0.16036(22)	-	0.01213(58)	-	0.2161(36)
Δ_{JK}/kHz	-	-0.5549(12)	-	0.1271(34)	-	-1.453(13)
Δ_K/kHz	-	1.8830(65)	-	-	-	226.971(95)
δ_J/kHz	-	0.02928(10)	-	0.00152(29)	-	0.1515(34)
δ_K/kHz	-	1.347(10)	-	-	-	1.66(11)
μ_a/D	2.0	Y[2]	-1.7	Y	-3.3	Y
μ_b/D	3.9	Y	-4.4	Y	2.6	Y
μ_c/D	1.9	Y	0.4	Y	2.3	Y
N[3]	-	310	-	152	-	62
σ/kHz	-	5.7	-	6.5	-	7.4
ΔE_{rel} (kJ/mol)[4]	0.0	-	1.2	-	0.9	-
ΔE_{rel-CC} (kJ/mol)	0.0	-	2.1	-	0.8	-
ΔE_{ZPE} (kJ/mol)	0.0	-	1.8	-	2.1	-
ΔE_{ZPE-CC} (kJ/mol)	0.0	-	2.7	-	1.9	-

[1] A, B, and C are the rotational constants, and Δ_J, Δ_{JK}, Δ_K, δ_J, and δ_K are the quartic centrifugal constants in Watson's A-reduction scheme. [2] Y and N indicate whether the respective type of rotational transition was observed or not. [3] N denotes the number of fitted transitions, and σ is the root-mean-square deviation of the fit. [4]ΔE_{rel}, ΔE_{ZPE} are the relative energies without and with vibrational zero-point correction, respectively. ΔE_{rel-CC}, ΔE_{ZPE-CC} are single-point relative energies at the DLPNO-CCSD/aug-cc-pVTZ level of theory without and with the vibrational zero-point energy term from the B3LYP-D3(BJ)/def2-TZVP level of theory.

Parameters	*tTt-B*	*g'Tg'-A*		*gTg'-A*	
	calc.	calc.	exp.	calc.	exp.
A/MHz	3075.3	1429.3	1421.04688(40)	1731.3	1724.72306(74)
B/MHz	313.4	525.8	534.21685(18)	449.7	453.29754(18)
C/MHz	286.9	461.3	465.12518(20)	416.7	419.13003(18)
Δ_J/kHz	-	-	0.2099(12)	-	0.0822(11)
Δ_{JK}/kHz	-	-	-0.4858(52)	-	-0.1265(54)
Δ_K/kHz	-	-	1.265(22)	-	1.494(69)
δ_J/kHz	-	-	0.04625(72)	-	0.01210(52)
δ_K/kHz	-	-	0.595(25)	-	-
μ_a/D	-3.9	1.4	Y	1.8	Y
μ_b/D	-3.5	4.3	Y	-4.3	Y
μ_c/D	0.0	1.4	Y	-0.7	Y
N	-	-	125	-	114
σ/kHz	-	-	5.8	-	6.4
ΔE_{rel} (kJ/mol)	3.5	2.1	-	2.6	-
ΔE_{rel-CC} (kJ/mol)	3.7	2.2	-	2.7	-
ΔE_{ZPE} (kJ/mol)	2.7	3.4	-	3.4	-
ΔE_{ZPE-CC} (kJ/mol)	2.9	3.6	-	3.5	-

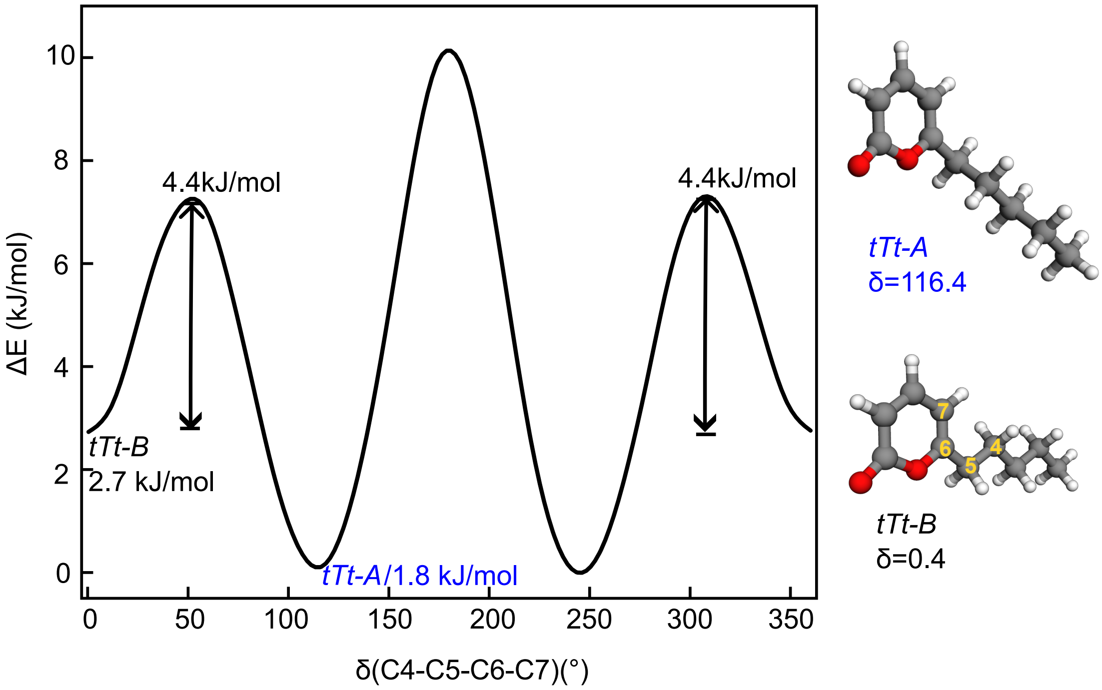

Figure 6.6: Potential energy profile calculated by scanning of the $\angle\delta$(C4-C5-C6-C7) dihedral angle at the B3LYP-D3(BJ)/def2-TZVP level of theory to explore the relaxation barrier of *tTt* rotamers of 6PP. The relative zero-point corrected energies of the two rotamers at the B3LYP-D3(BJ)/def2-TZVP level of theory are given and the arrows indicate the barrier between rotamers. Both conformers are depicted with their respective dihedral angles.

6-Amyl-α-pyrone is structurally similar to methyl hexanoate (MHO) in terms of the pentyl side chain attached to an ether carbon atom. 6PP is a pyrone with the alkyl pentyl chain attached to the carbon atom next to the oxygen inside the pyrone ring. In contrast, MHO is an aliphatic ester with a pentyl carbon chain attached to the methyl ester at the carbonyl carbon atom. MHO also exhibits significant conformational flexibility, featuring an ensemble of approximately 36 different conformers,[223] which is similar to what is observed in the case of 6PP. The most stable conformers of MHO and 6PP, observed experimentally, exhibit C_1 symmetry, as depicted in Fig. 6.7. These structures differ primarily in terms of two dihedral angles given as (O12-C6-C5-C4, as indicated in Fig. 6.5) and (C6-C5-C4-C3) which is -146° and 66.5° in MHO and -61° and 62° in 6PP, respectively. Of the five conformers of 6PP detected in experiments, none of the structurally identical MHO conformers were reported in the microwave investigation by Dang *et al.*[223] Furthermore, there is no consistent trend observed in the energy ordering of conformers in MHO and

6PP. Hence, it would be intriguing to compare an aliphatic form of 6PP in which the ketone group is attached next to the ether oxygen, and examine the energy ordering of its conformers. This comparison will provide valuable insights into the influence of the aliphatic and aromatic functional groups on the conformational flexibility of the alkyl chain.

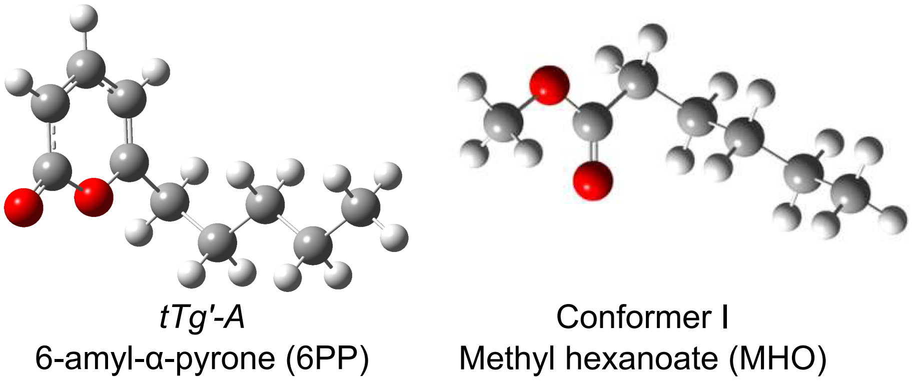

Figure 6.7: The most stable conformer of 6PP (6PP-*tTg'-A*) and methyl hexanoate (MHO-conformer I). The optimised geometry of MHO is taken from the reference [223].

6.3 Summary and outlook

The broadband rotational spectrum of 6-amyl-α-pyrone, a potential biomass molecule, revealed five out of nineteen predicted low-energy conformers of 6PP in the cold environment of a supersonic jet. The results from quantum-chemical calculations agree well with the experiments, confirming the same global minima. The most intense rotational spectrum for the dominant conformer *tTg'-A* led to its easier assignment and accurate structure determination of the carbon backbone of the molecule. The absence of the second rotamer of *tTt*, i.e., *tTt-B* in the rotational spectrum could be explained by its relaxation into a more stable structure, *tTt-A*. The differences in relative energy ordering of conformers obtained from optimisation at the B3LYP-D3(BJ)/def2-TZVP level of theory, and single-point energy calculations at the DLPNO-CCSD/aug-cc-pVTZ level of theory demand benchmarking methods for such structurally flexible molecules. Due to the richness of the experimental rotational spectrum, the presence of more conformers can be expected. Consequently, the search for these conformers will be continued. Furthermore, it is possible that certain high-energy conformers may undergo relaxation into their lower-energy structures, for which dihedral scans will be performed.

The strcutural and conformational insights into 6PP presented here lay the groundwork for further studies of 6PP, particularly in understanding its interactions with solvent molecules. This is especially significant considering its potential as a biorenewable platform precursor molecule. For example, 6PP offers a sustainable approach for the synthesis of another industrially important chemical, δ-decalactone (DDL), as illustrated in Fig. 6.1.[232] DDL is reported as an emerging monomer for producing high-quality polymers like polyurethanes and polyamides.[233, 234] Recently, Alam and co-workers demonstrated the production of DDL through catalytic transfer hydrogenation (CTH) of 6PP over a Pd/C catalyst, using formic acid as an in situ hydrogen source.[232] The CTH reaction, conducted in different solvents under similar conditions, resulted in significant variation in 6PP conversion and DDL yield, ranging from 6% to 79%.[232] These yield variations during CTH can be attributed to numerous reasons, such as the dielectric constants of the solvents or dispersive interactions during micro-solvation of 6PP. The dielectric constants and solvent-accessible surface area (SASA) of the reactant play a crucial role, where solvents with low dielectric constants and low SASA values are expected to yield better results, as seen in the case of cyclohexane.[232] In addition to electronic effects, dispersive interactions of solvent molecules with both the reactants and the catalyst surface may also influence the reaction yield.

The possible orientations of solvent molecules concerning the pyrone ring and amyl chain of 6PP are contingent upon the solvent type and the conformational arrangement of 6PP. The isolated gas-phase investigations of 6PP with solvent molecules offer insights into the preferred conformations of 6PP during complexation, which can significantly differ from the reaction conditions in liquid phase, largely influenced by the solvent effects. For the sake of clarity, the term ‘solvent effects’ primarily refers to changes induced by the solvent in chemical reactivity including reaction rate, reaction pathways, and yields.[235]

As mentioned in the Chapter 3, CP-FTMW spectroscopy is suitable for studying weakly bound complexes isolated in the gas phase. In this study, a polar protic solvent, ethanol, and a nonpolar solvent, cyclohexane, were selected, with one yielding the best results and the other producing moderate results in the CTH reaction. To explore different conformations of 6PP-complexes, a workflow similar to Fig. 2.6 was performed. Firstly, a conformational search of the complexes was conducted using CREST. Subsequently, structures were refined through optimisation at the B3LYP-D3(BJ)/def2-TZVP level of theory. Fig. 6.8 illustrates the most stable structures of 6PP with ethanol and cyclohexane solvents obtained from optimisation at the B3LYP-D3(BJ)/def2-TZVP level of theory. Both low-energy complexes of 6PP with ethanol and cyclohexane are formed with its most stable structure, *tTg'-A*. The acidic proton of ethanol forms a hydrogen bond with the carbonyl oxygen atom of 6PP, with methyl group interacting with the ether oxygen (as depicted in Fig. 6.8). Conversely, nonpolar cyclohexane lacks any acidic hydrogen like ethanol and does not establish hydrogen bonding with 6PP. Instead, cyclohexane assumes a parallel displaced position on top of the pyrone ring, interacting with the carbonyl oxygen and pyrone ring. The optimised structures of the most stable 6PP complexes suggest that a probable reason for the lower yield observed with the ethanol compared to the cyclohexane as solvent in the CTH reaction could be due to the presence of hydrogen bond interactions in 6PP-ethanol, which might be hindering the hydrogenation process. Preliminary analysis of 6PP-complexes from quantum-chemical calculations predicts the observation of the most stable conformations of these complexes in experiments.

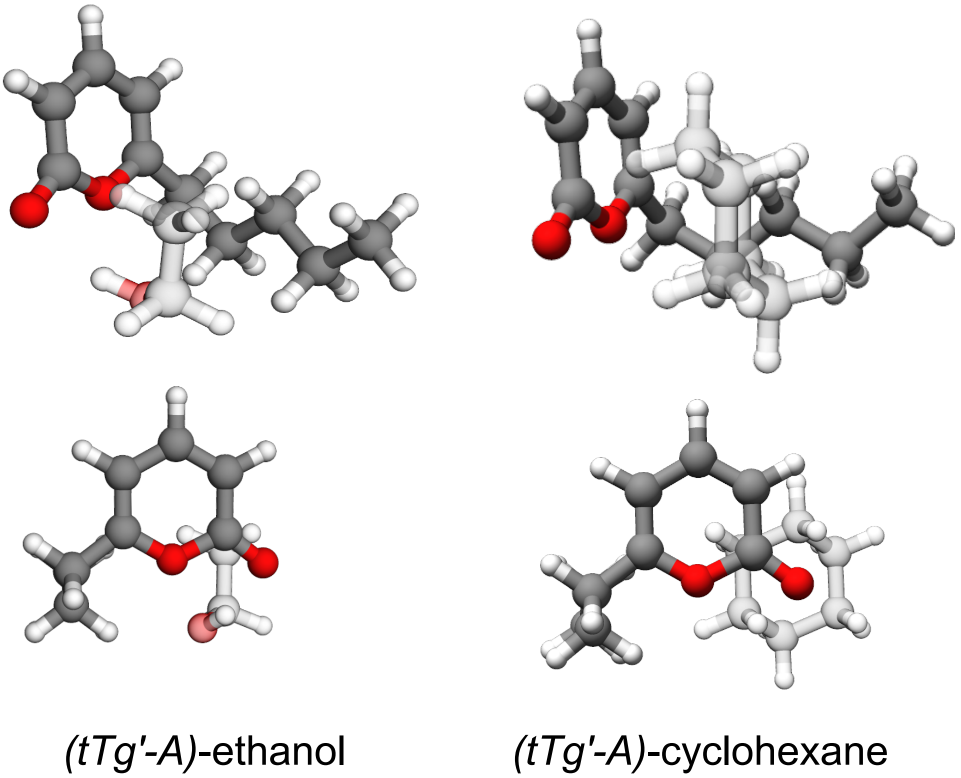

Figure 6.8: The optimised structures of the most stable 6PP-ethanol and cyclohexane complexes, formed with the lowest energy conformer of 6PP (*tTg'-A*), were obtained at the B3LYP-D3(BJ)/def2-TZVP level of theory. Side front view and back view are shown.

The rotational spectra for these complexes have already been acquired and will be analysed as the next step. Exploring whether other conformations of 6PP participate in complexation and whether this induces any structural changes in the 6PP monomer will be of further interest. Future work in this study could involve investigating the intermediate product of the CTH reaction, massoia lactone. Massoia lactone is structurally similar to 6PP but features one less double bond in the pyrone ring. Like 6PP, massoia lactone exhibits significant structural flexibility, resulting in a similarly complex conformational landscape. Analysing the solute-solvent interactions of massoia lactone with the chosen solvents for the 6PP-complexes will provide deeper insights into the role of solvent interactions in the CTH reaction of 6PP.

Further studies concentrating on longer hydrocarbon chain analogs of 6PP could offer insights into the impact on conformational space and structural alterations in 6PP. Suhm *et al.* characterised the critical chain length at which a stretched hydrocarbon nanorod prefers either the all-*trans* configuration or adopts a hairpin structure, aligning both ends of the carbon chain to maximise their interaction through conformational bending.[236] Similar characterisation involving varying lengths of alkyl chains in 6PP could determine the thresholds at which these hydrocarbon chains fold/curl to interact with the pyrone ring. This exploration will be crucial in understanding how the stability and reactivity of 6PP change with increasing hydrocarbon chain length and its implication for potential applications of 6PP as biomass-derived platform molecule.

Part II: Molecular chirality investigated with microwave spectroscopy

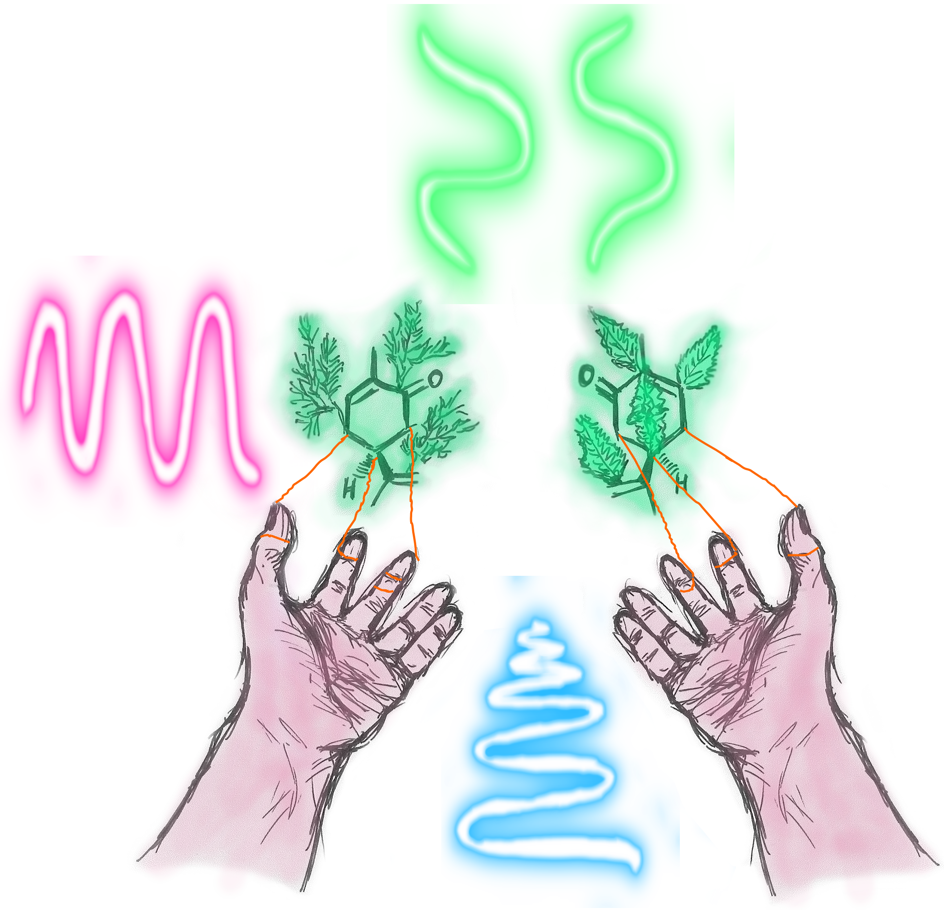

Chapter 7

Enhancing enantiomer-selective population enrichment by depleting the thermal population

Most biomolecules are inherently chiral, and their chirality significantly influences their stereochemistry in biochemical interactions. The distinct chemical and biological behaviors exhibited by enantiomers are a consequence of the subtle parity-violating energy difference between them. Hence, reliable methods are required that enable enantiomer differentiation, separation, and determination of the enantiomeric excess in chiral mixtures.

However, broadband rotational spectroscopy cannot differentiate enantiomers from their rotational spectrum because of their identical rotational constants. In the past decade, the development of M3WM[59, 60] has expanded the capabilities of MW spectroscopy to differentiate enantiomers. The M3WM approach has developed into a powerful tool for chiral analysis, allowing for the determination of the *ee* and the absolute configuration of chiral molecules,[60, 154, 237] even in complex chiral mixtures[49]. Further extended M3WM pulse sequences have been used to achieve enantiomer-selective population transfer in specific rotational states, i.e., the separation of the enantiomers in terms of energy. These experiments enable us to manipulate and control chiral molecules in the gas phase, representing an important step towards enantiomer separation, purification, and precision spectroscopy.

Enantiomer-selective population transfer was experimentally demonstrated for the first time with a buffer-gas cooled (T_{rot}=7-10 K) sample of 1,2-propanediol, where a 0.6% enantiomeric enrichment could be achieved.[153], which was enhanced by an order of magnitude in carvone with the use of a molecular jets (T_{rot}=1-2 K).[62]

However, the achieved enrichment is limited by the thermal population and spatial degeneracy (M_J-states) of the rotational levels involved in the scheme. These limitations can be circumvented by employing an energy level scheme involving low-lying rotational energy levels and by using controlled microwave or laser pulse schemes to maximise the population contrast between the initial states.

In this study, 2-trifluoromethyl oxirane ($C_3H_3F_3O$, TFO) was used as a model molecule to demonstrate the enhancement of the enantiomer-specific enrichment by depleting the initial thermal population at the relevant rotational energy level with a π-pulse or a fast chirp in the RAP regime. The effects of the tailored microwave pulses on the induced *ee* in particular rotational energy levels of TFO are discussed in section 2.3 of the article. The minireview highlights the development in the area of M3WM in the past decade and its extension to control and manipulate chiral molecules in sections 2.1 and 2.2, respectively.

Title	Chiral Control of Gas-Phase Molecules using Microwave Pulses
Authors	Himanshi Singh^{+}, Freya E. L. Berggötz^{+}, Wenhao Sun, and Melanie Schnell
Journal	*Angewandte Chemie*
Volume	62
Year	2023
Pages	e202219045
DOI	International edition: `https://doi.org/10.1002/anie.202219045` German edition: `https://doi.org/10.1002/ange.202219045`
Pages	11 pages of the article and 14 pages of supplementary information
My contributions	Experiment Analysis Manuscript preparation

How to cite: *Angew. Chem. Int. Ed.* **2023**, *62*, e202219045
doi.org/10.1002/anie.202219045

Rotational Spectroscopy

Chiral Control of Gas-Phase Molecules using Microwave Pulses

Himanshi Singh[+], *Freya E. L. Berggötz*[+], *Wenhao Sun*,* *and Melanie Schnell**

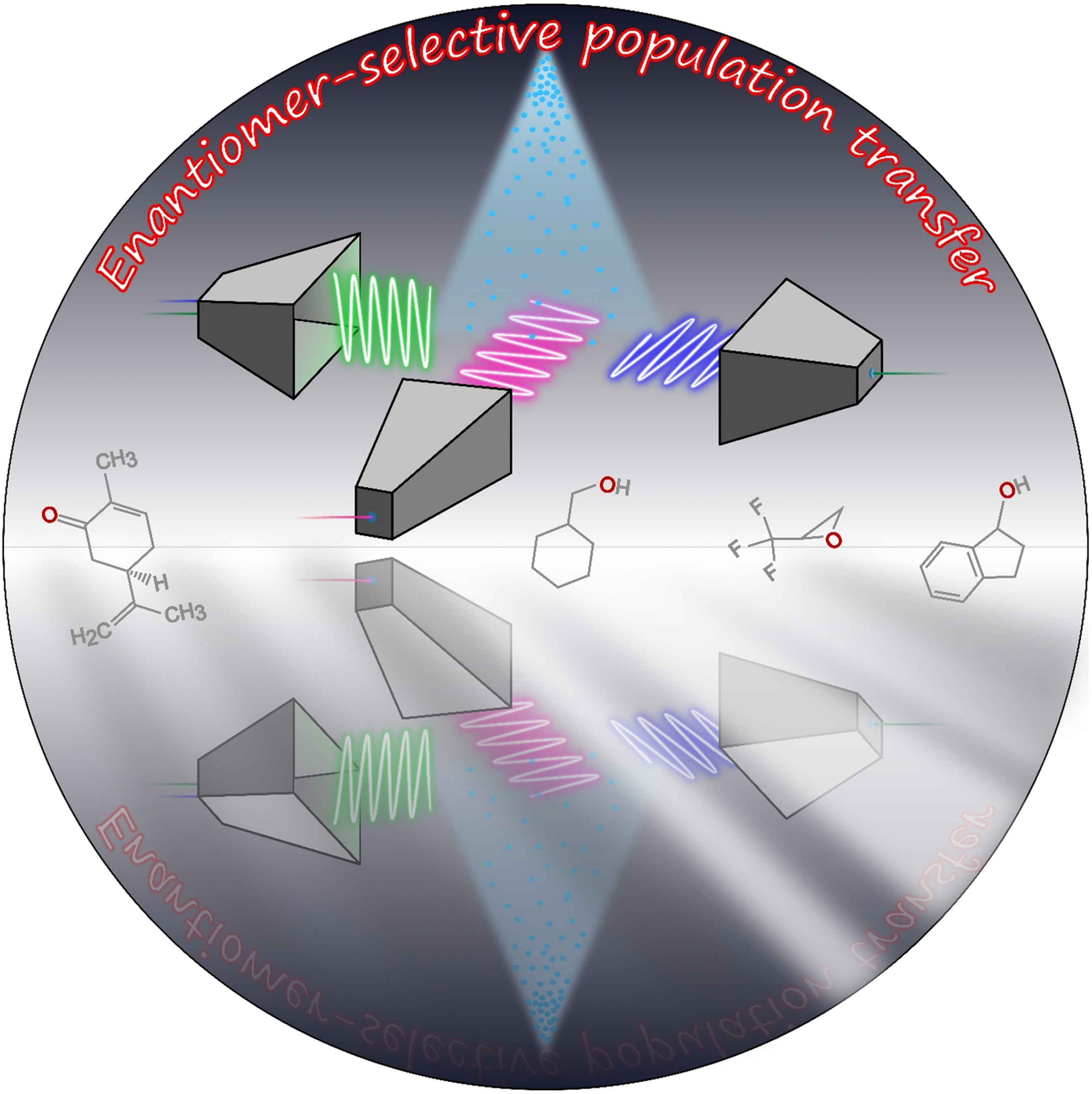

Abstract: Microwave three-wave mixing has emerged as a novel approach for studying chiral molecules in the gas phase. This technique employs resonant microwave pulses and is a non-linear and coherent approach. It serves as a robust method to differentiate between the enantiomers of chiral molecules and to determine the enantiomeric excess, even in complex chiral mixtures. Besides such analytical applications, the use of tailored microwave pulses allows us to control and manipulate chirality at the molecular level. Here, an overview of some recent developments in the area of microwave three-wave mixing and its extension to enantiomer-selective population transfer is provided. The latter is an important step towards enantiomer separation—in energy and finally in space. In the last section, we present new experimental results on how to improve enantiomer-selective population transfer to achieve an enantiomeric excess of about 40 % in the rotational level of interest using microwave pulses alone.

1. Introduction

Molecular chirality is an essential stereochemical property of molecular systems important in chemistry, biology, and medicine. Most biomolecules, such as amino acids, nucleic acids, and sugars, are chiral in nature and exist as a pair of non-superimposable mirror images called enantiomers. There is a stereoselective bias for biochemical interactions in different chemical or biological environments, which also expresses itself in the homochirality of life, whose origin is still highly debated to date.[1] Although the chemical and biological behaviors of the two enantiomers can vary dramatically in a chiral environment, their nearly identical physical properties, besides the extremely small energy difference arising from parity violation,[2,3] makes it intrinsically challenging to distinguish and separate them.

A powerful portfolio to differentiate between the enantiomers of chiral molecules has been developed, addressing chiral molecules in the solid state, the liquid or solution phase, and in the gas phase. Among those are X-ray diffraction, chirality-sensitive gas chromatography, polarimetry, and circular dichroism, to name a few.[4–7] In recent years, gas-phase spectroscopic techniques have emerged that allow for the analysis of chiral molecules with high resolution, free of solvent effects, bringing forward the ability to address the enantiomers of chiral molecules in an isomer- and conformer-selective way.[8,9] Furthermore, there is interesting progress to investigate chirality using ultrafast spectroscopy in the femtosecond to attosecond regime,[10–13] which gives access to ultrafast dynamics of chiral molecules, and in particular their electron dynamics.

These gas-phase techniques cover different ranges of the electromagnetic spectrum and thus address different molecular degrees of freedom. Photoelectron circular dichroism (PECD) has been shown to be able to differentiate between the enantiomers in simple chiral mixtures,[14–18] also in a conformer-selective way,[19,20] and it can be used to determine the enantiomeric excess (*ee*) with high precision.[21] This technique can be performed with synchrotron radiation[16,22–27] and nanosecond[28,29] up to femtosecond lasers so that also fast processes of the chiral molecules can be revealed.[30] It was also extended to photoelectron elliptical dichroism.[31] In another type of experiment, Coulomb explosion imaging of chiral molecules was performed, which allowed for the direct determination of the absolute configuration by calculating back the original structure.[32,33] Recently, the method could be applied to induce chiral fragmentation of a planar and thus achiral molecule upon interaction with helical light.[34,35] The outcome of the fragmentation, namely the observed fragment enantiomer, depends on the orientation of the molecule with respect to the light propagation direction and the helicity of the ionizing light. Moreover, enantioselective control of chiral molecular rotation using intense ultrashort laser fields has also been achieved experimentally,[36] following extensive theoretical demonstrations.[37–39] In addition to enantiomer differentiation, such gas-phase experiments also highlight their potential for separating, manipulating, and controlling chirality.

Another high-resolution gas-phase technique that will be central to this article is based on rotational spectroscopy and covers slower time scales and employs long-wavelength microwave radiation to excite molecules to quantized molecular rotational motions—microwave three-wave mixing (M3WM).[40,41] Since its first experimental implementation in 2013,[41,42] this M3WM technique, as a coherent, resonant, and non-linear approach, has showcased its capability and potential to control and manipulate chiral molecules. Microwave three-wave mixing has also inspired several theoretical studies and proposals on enantiomer differentiation and separation using optical fields.[43,44] In the following, we will discuss M3WM in more detail (Section 2) and then focus on its extension to generate enantiomer-selective population transfer. Using this extended transfer scheme, enantiomer excess in a rotational state of interest can be generated "on the fly" for a racemic starting sample

---

[*] H. Singh,[+] F. E. L. Berggötz,[+] Dr. W. Sun, Prof. Dr. M. Schnell
Deutsches Elektronen-Synchrotron DESY
Notkestr. 85, 22607 Hamburg (Germany)
E-mail: wenhao.sun@desy.de
melanie.schnell@desy.de

H. Singh,[+] Prof. Dr. M. Schnell
Institute of Physical Chemistry, Christian-Albrechts-Universität zu Kiel
Max-Eyth-Str. 1, 24118 Kiel (Germany)

F. E. L. Berggötz[+]
Institute for Experimental Physics, Universität Hamburg
Luruper Chausee 149, 22761 Hamburg (Germany)

[+] These authors contributed equally to this work.

of chiral molecules, which will be highly relevant for advanced experiments with chiral molecules, such as evaluating the frequency difference between the two enantiomers arising from parity violating weak interactions or enantiomer-selective collision studies.[45] The M3WM approach can be applied not only to permanently chiral molecules (e.g., carvone[46]) but also to transiently chiral species, such as benzyl alcohol,[47] where enantiomers can racemize due to quantum tunneling forming a racemic mixture, which is impossible to separate via conventional chemical methods. After reviewing some of the recent theoretical and experimental developments to improve enantiomer-selective population transfer, we report new experimental results to improve the efficiency of that scheme by the inclusion of a rapid adiabatic passage (RAP)- or a π-pulse.

2. Chiral analysis using high-resolution microwave spectroscopy

The analysis of chiral molecules with high-resolution microwave spectroscopy has developed into a powerful tool during the last years with different research applications and directions.[7,48–52] One particularly strong point is that the technique can be applied to the analysis of complex (chiral) mixtures due to its high resolution and fingerprint character for each molecule.[53,54] Once the rotational spectrum of a molecule is recorded, it can be unambiguously identified via its rotational transitions in later experiments. The narrow line widths on the order of 15–100 kHz (depending on the respective setup and frequency range applied) while covering several GHz of bandwidth in a single acquisition emphasize the potential of broadband rotational spectroscopy to record and identify several species at the same time. This was highlighted recently for the chiral analysis of essential oils, for example, which consist of numerous, structurally often very similar chiral compounds.[55]

Recently, two different approaches to analyse chiral samples using rotational spectroscopy have been developed: microwave chiral tagging[48] and microwave three-wave mixing.[7,41] In microwave chiral tagging, the sample of interest interacts with a well-characterized chiral tag molecule to form weakly bound complexes, resulting in diastereomers that can be differentiated via their structure.[7,48,52] By performing two different types of measurements, one with a racemic sample of the chiral tag molecule and one with an enantioenriched sample of known handedness for the tag, the excess enantiomer of the unknown sample as well as its corresponding enantiomeric excess can be determined with impressive statistics.[48,49,51,56,57]

While chiral tagging is experimentally more straightforward and thus promising as a routine application in chiral analysis, M3WM can additionally be applied to control and manipulate chiral molecules, which is the central part of this article.

2.1. Microwave three-wave mixing

M3WM is based on the mirror-image character of the two enantiomers of a chiral molecule, which results in opposite

Himanshi Singh obtained her BS-MS dual degree from the Indian Institute of Science Education and Research (IISER)-Mohali, India in 2019. She did her master's in the conformational study of alcohols using matrix isolation Fourier-transform infrared spectroscopy. Later, she joined the group of Prof. Melanie Schnell as a PhD student to explore high-resolution gas-phase spectroscopy. Her research interests are in studying molecular chirality and non-covalent interactions in flexible molecules using microwave spectroscopy.

Freya E. L. Berggötz obtained her Bachelor's degree in physics at the University of Hamburg, where she developed a setup to focus laser pulses in the extreme ultraviolet frequency range generated by a high harmonic source. Changing the field of research—and with it the frequency range—she later joined Prof. Melanie Schnell's group for her master's thesis to work on molecular chirality using microwave spectroscopy. After the successful completion of her thesis in 2021, she joined the group as a PhD student, continuing her work on molecular chirality.

Wenhao Sun obtained his PhD at the University of Manitoba in Canada, where he studied sulfur-containing molecular species of astrophysical interest through rotational spectroscopy and discharge techniques under the supervision of Prof. Jennifer van Wijngaarden. Later he joined Prof. Melanie Schnell's group as a postdoctoral researcher. His present research focuses on the understanding of molecular chirality and weakly bound molecular complexes using rotational spectroscopy.

Melanie Schnell is professor for Physical Chemistry at the CAU Kiel and a leading scientist at DESY in Hamburg. Her research activities concentrate on a better understanding of chemical processes on the molecular level. To reach these goals, her group develops novel spectroscopic methods, with a focus on rotational spectroscopy. She received her PhD in physical chemistry with Jens-Uwe Grabow at the Universität Hannover. Following a research stay with Jon Hougen at NIST (Gaithersburg, USA), she joined the Fritz Haber Institute in Berlin before she moved to Hamburg in 2010 to set up her independent research group.

signs of the triple product of their transition dipole moments ($\vec{\mu}_a \cdot (\vec{\mu}_b \times \vec{\mu}_c)$) within the molecular principal axis system.[40–42,58] Furthermore, according to the selection rules for pure rotational transitions, each rotational transition of a molecule only depends on one particular dipole-moment component within the molecular principal axis system, i.e., μ_a, μ_b, or μ_c. The corresponding transitions are then denoted as a-, b-, and c-type transitions, respectively.

It is thus possible to selectively address the two enantiomers of a chiral molecule by generating an excitation cycle consisting of three rotational transitions, where each rotational transition involves only one of the three dipole-moment components in one particular direction of the laboratory frame (Figure 1). The molecular ensemble is excited by two consecutive resonant microwave pulses, for example polarizing an a- and a b-type transition, respectively, which are linearly polarized in two perpendicular directions of the laboratory frame. The first resonant pulse is optimized to fulfill the Rabi flip angle of π/2, corresponding to maximum coherence between the rotational states involved. The Rabi flip angle (Θ_{Rabi}) is defined as the product of the Rabi frequency, Ω_{Rabi}, and the pulse duration of the microwave pulse, τ:

$$\Theta_{Rabi} = \Omega_{Rabi} \cdot \tau = \frac{\mu \cdot E}{\hbar} \cdot \tau$$

where μ denotes the transition dipole moment for the rotational transition, E is the electric field amplitude. This π/2 pulse transfers the population difference between the two states $|1\rangle$ and $|2\rangle$ into coherence, and the associated transition is denoted as drive transition in Figure 1. As discussed in more detail below, it is advantageous to start with a large population difference of the two rotational states $|1\rangle$ and $|2\rangle$ connected by the drive transition, which will result in large coherence and which is supported by the usage of a supersonically expanded pulsed jet. Using neon as a carrier gas, rotational temperatures (T_{rot}) around 1–2 K are routinely achieved.[59] However, even at these low temperatures the population difference between levels $|1\rangle$ and $|2\rangle$ is still rather small due to the inherently small energy difference between rotational levels, so that thermal population is one of the limiting factors for efficient M3WM (and its extension to enantiomer-selective population transfer, see below).

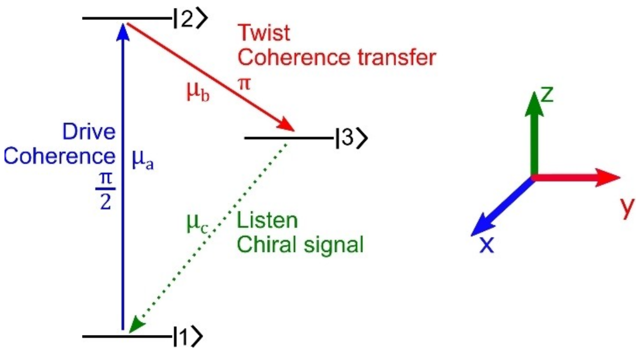

Figure 1. Generalized microwave three-wave mixing scheme consisting of drive transition (a-type, π/2-pulse, blue excitation), twist transition (b-type, π-pulse, red excitation), and listen signal (c-type, green detection). M_J degeneracies of the rotational energy levels are omitted here for clarity.

The second pulse, the so-called twist pulse (Figure 1), is linearly polarized orthogonally to the direction of the drive pulse and is optimized for π conditions to transfer the coherence between states $|1\rangle$ and $|2\rangle$ induced by the π/2 drive pulse to the pair of states $|3\rangle$ and $|1\rangle$. This results in a molecular signal for this third transition, denoted as listen transition, which is linearly polarized in the third, mutually orthogonal direction. Note that this listen transition connecting states $|3\rangle$ and $|1\rangle$ is not directly excited by a resonant transition but is induced via the three-wave mixing scheme. The molecular signal at the frequency of the listen transition is recorded in form of a free-induction decay (FID) in the time domain that can be recorded in a phase-sensitive manner. The corresponding FID exhibits an opposite phase of π radians (180) for the two enantiomers, which arises from the discussed opposite sign of the triple product of the three transition-dipole moments ($\vec{\mu}_a \cdot (\vec{\mu}_b \times \vec{\mu}_c)$), and it is the key to differentiating between the two enantiomers of chiral molecules via M3WM. The absolute phase provides information about the absolute configuration via the sign of ($\vec{\mu}_a \cdot (\vec{\mu}_b \times \vec{\mu}_c)$), while the calibrated intensity of the M3WM signal allows for the determination of the enantiomeric excess of the sample.[42,53,60,61] The former requires thorough knowledge of the timings of the excitation pulses and the listen signals traveling through the different electronic components of the instrument, which has been experimentally validated.[53,60] For a racemic sample, the two chiral signals destructively interfere so that no net signal is obtained at the frequency of the listen transition. As such, the technique is sensitive even to small *ee* values on the order of a few percent. Furthermore, M3WM is powerful to analyze also complex mixtures of chiral molecules because of its fingerprint character.[7,42,54,59] The handedness of the different chiral components can be analyzed simultaneously without any perturbations from the other chiral molecules in the sample, as shown in the case of essential oils.[54,55]

2.2. Enantiomer-selective population transfer using microwave three-wave mixing schemes

The phase difference of the two enantiomers generated for the FID of the listen transition can be used to enantiomer-selectively enhance the population of one enantiomer in a particular rotational state (and to deplete it in the connecting state of this transition), while the population of the second enantiomer will be depleted in this state but enhanced in the connecting state of the corresponding transition.[46,62–67] This enantiomer-selective population transfer is achieved by introducing a third pulse to the M3WM scheme, a so-called transfer pulse, which is resonant to the frequency of the listen transition, i.e., involving states $|1\rangle$ and $|3\rangle$, and which results in a direct excitation of this transition (Figure 2(a)). This direct excitation interferes with

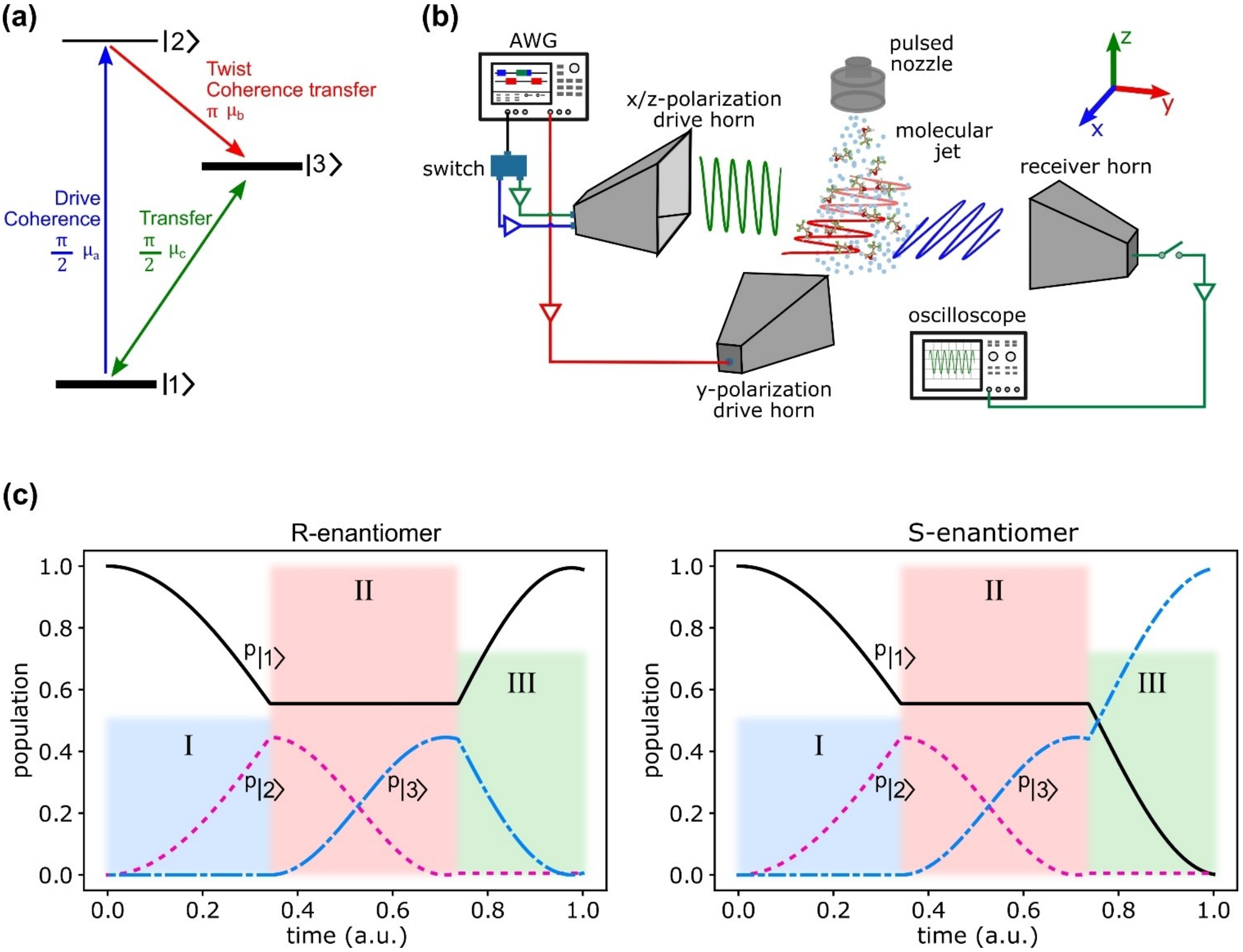

Figure 2. (a) Rotational energy level diagram for creating enantiomer-selective population transfer in the rotational levels $|1\rangle$ and $|3\rangle$ highlighted in bold. The created enantiomeric enrichment in the states $|1\rangle$ and $|3\rangle$ can be measured with any transitions connecting either state $|1\rangle$ or state $|3\rangle$. (b) Schematic of the Hamburg COMPACT spectrometer with relevant components and polarizations employed for performing M3WM or population transfer experiments. (c) Simulated enantiomer-selective population transfer for the R- and S-enantiomers in rotational states $|1\rangle$ and $|3\rangle$. Three pulses were applied subsequently (I: drive, II: twist, III: transfer), which enriched the R-enantiomer population in state $|1\rangle$ while the population of the S-enantiomer is enriched for state $|3\rangle$.

the phase-dependent listen signal induced by the M3WM scheme and converts the coherence into longer-lived population in states $|1\rangle$ and $|3\rangle$. Depending on the phase of the transfer pulse with respect to the M3WM scheme or the time delay in between, constructive or destructive interference between the two paths can be achieved, which is opposite for the two enantiomers as simulated in Figure 2(c) for the energy scheme shown in Figure 2(a). Thus, the populations of the two enantiomers are oppositely transferred to the rotational states $|1\rangle$ and $|3\rangle$, and chiral separation in energy is achieved.

This scheme has first been demonstrated using a buffer-gas cooled sample,[65] where 0.6 % enantiomeric enrichment was achieved (at $T_{rot} \approx 10$ K) and then, shortly after, it was realized for molecular jets with low rotational temperatures of 1–2 K, which allowed for an enhancement of the observed enantiomer-selective population transfer of one order of magnitude.[46] The effect was detected by determining the intensity change of an additional rotational transition as a probe involving either state $|1\rangle$ or state $|3\rangle$, respectively, as a function of the phase of the transfer pulse. The experiments for molecular jets were performed using the chirped-pulse Fourier transform microwave spectrometer COMPACT, modified for M3WM experiments (see Figure 2(b)), as reported elsewhere.[46,53,68]

Note that the handedness of the enantiomer enriched in a particular state (state $|1\rangle$ or state $|3\rangle$) only depends on the relative phase of the transfer pulse with respect to the pulses of the M3WM scheme. By changing one of the phases of the pulses involved by 180 (π radians), the type of enriched enantiomer for a respective energy level will be exchanged, while all other experimental conditions remain the same. Such experiments are thus not only of interest in their own rights, but they also deliver well-controlled starting samples for further advanced experiments on chiral molecules that depend on quickly changing the handedness of the enantiomer without changing the experimental conditions, such as precision experiments, because systematic effects can be minimized.

In the first experiments, enrichment of one selected enantiomer in a particular rotational state (and the corresponding depletion of the other enantiomer) has been demonstrated for enantioenriched or even enantiopure samples as starting points,[65] and state-selective enantiomer enrichment on the order of a few percent could be achieved using our molecular jet.[46] In a follow-up experiment, we used cyclohexyl methanol (CHM) to demonstrate that this method can also generate an *ee* starting from a racemic sample.[66] CHM consists of two chiral conformers of opposite handedness; its interconversion is hindered by a barrier of about 15 kJ mol^{-1} as computed at the MP2/6-311++G(d,p) level of theory. At room temperature, the two enantiomers can rapidly interconvert, while they are stabilized at the cold conditions of a supersonic expansion. As such, they present an ideally racemic molecular ensemble to start with. Using an optimized enantiomer-selective population transfer scheme, state-specific enantiomeric excess starting from this racemic sample could be generated in a controlled way. Again, the enriched enantiomer could be switched and controlled by a π phase change of one of the pulses involved.

For these experiments, another read-out scheme needed to be applied to demonstrate the enantiomer selectivity of the approach and the resulting *ee* generated from a racemic sample. Instead of determining the intensity of a transition connecting to one of the states involved in the transfer process, we added a M3WM cycle to the population transfer scheme, starting from state $|3\rangle$ as shown in Figure 3(a). Since M3WM shows zero signal for a racemic mixture, the achieved *ee* could be sensitively detected. As shown in Figure 3(b), two maxima at the transfer-pulse phases of 126 and 306 were obtained, which could be shown to be corresponding to different enantiomers. The absolute configuration of the two maxima can in principle be determined with careful phase calibration as mentioned previously in Section 2.1, however, this is not a straightforward procedure.

2.3. Enhancing enantiomer-selective population transfer

Recent studies, both of theoretical and experimental nature, are focusing on increasing the efficiency of this approach. It depends on the difference in the thermal population as well as the spatial degeneracy of the rotational states involved, which is described by the quantum number M_J.[69,70] Phase variations due to field inhomogeneities are also a challenge, which can be circumvented to a good extent by using low excitation frequencies with wavelengths of several centimeters, so that field inhomogeneities are reduced. For example, a frequency at 5 GHz corresponds to a wavelength of about 6 cm. In the following, a short summary of the proposed and demonstrated improvement schemes will be given.

Each rotational energy level of an asymmetric top is denoted by J_{KaKc} and is $(2J+1)$-fold degenerate; the values of the M_J quantum number range from $-J$, $-J+1$, …, J-1, $+J$. As a consequence, a simple pulse scheme as described above for M3WM (Figure 1) will result in several open cycles, reducing its efficiency. This effect is minimized for M3WM cycles involving $J=0$, for which only one M_J substate exists.[67,71] As theoretically derived in Ref. [71] using control theory applied to asymmetric tops, circularly polarized microwave radiation can increase the achieved enantiomer-

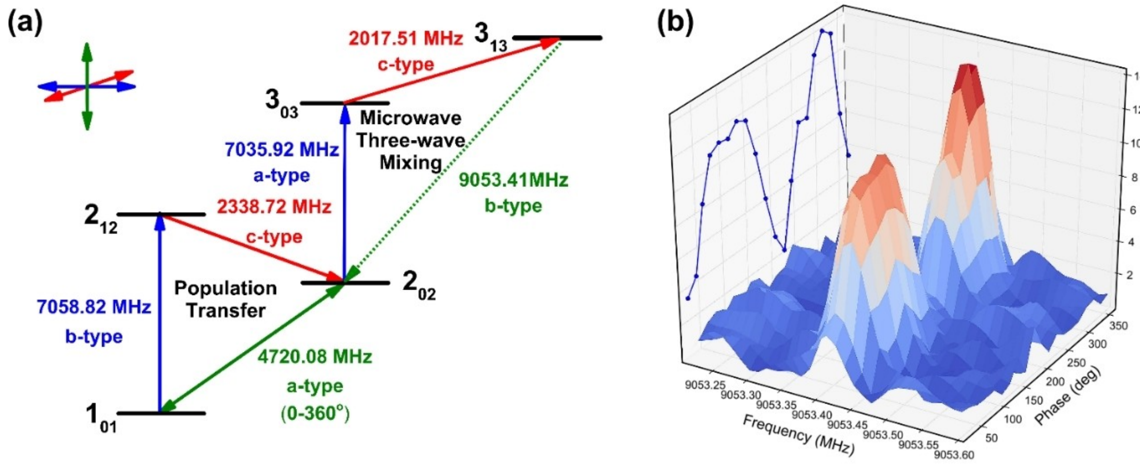

Figure 3. (a) Relevant rotational energy levels of cyclohexyl methanol (CHM) applied for state-specific enantiomeric enrichment. The rotational levels are denoted using the J_{KaKc} notation for an asymmetric top. The first set of triad creates an enantiomer-dependent population difference in the $|2_{02}\rangle$ and $|1_{01}\rangle$ rotational energy levels by varying the relative phase of the transfer pulse at 4720.08 MHz. This results in an opposite enantiomeric excess in both levels. The achieved enantiomeric excess in the rotational state $|2_{02}\rangle$ is then probed by the second cycle (M3WM) shown on the right. (b) The amplitude of the molecular signal of the listen signal at 9053.41 MHz was monitored as a function of the transfer pulse phase (0 –360 in 18 steps, 100,000 averages). Two maximal signals were observed, for the transfer pulse phases 126 and 306, respectively. These two maxima correspond to the two enantiomers selectively populating or depopulating the $|2_{02}\rangle$ rotational level, creating an enantiomeric excess (*ee*). Figure adapted from Ref. [66] with permission. Copyright 2018 American Chemical Society.

selective enrichment from 6 % to about 8 % by including the cycles involving all M_J substates.

Since the overall M3WM signal and thus also the achieved population transfer via destructive or constructive interference between the M3WM signal and a direct excitation pulse depend on the population difference between the states involved, this is an important factor to consider. Because of the small energy difference between rotational states, the population difference is often also rather small, even at the cold conditions of a supersonic jet with rotational temperatures on the order of $T_{rot} \approx 1$–2 K or in a buffer-gas cell with temperatures around 8–10 K.

A large population difference can be achieved by involving a vibrational transition to a vibrationally excited state, as proposed in Ref. [70]. Recently, the population depletion of a rotational level involved in the M3WM scheme via electronic excitation from the S_0 to the S_1 state was demonstrated as shown in Figure 4, resulting in a significant efficiency increase.[67] Furthermore, the read-out was achieved via state-selective laser-induced fluorescence (LIF). This approach is predominantly applicable to the subset of chiral molecules that contain a UV chromophore, and it is thus an interesting additional tool for controlling chiral molecules.

In the following, we describe and demonstrate a general approach to significantly increase the efficiency of enantiomer-selective population transfer solely via rotational excitations, so that the additional requirement of a UV chromophore is not needed.

3. A general approach for enhancing enantiomer-selective population transfer using rotational excitation

As mentioned, the efficiency of enantiomer-selective population transfer is mainly limited by the M_J-degeneracy and the thermal population.[69,70] These limitations can be circumvented respectively by employing an energy level scheme involving low-lying rotational levels, such as the $|0_{00}\rangle$ rotational state, and by using controlled microwave pulse schemes to maximize the population differences between the initial states. The latter can be realized by exchanging the unwanted thermal population to a connected higher state prior to the population transfer experiment via: i) a resonant rotational excitation in the π-pulse regime on the Bloch sphere; or ii) a microwave chirp in the rapid adiabatic passage (RAP) regime.[72]

Here, we have explored the effect of both pulses on the enantiomer-selective population transfer for the molecule 2-trifluoromethyl oxirane (TFO), as demonstrated in Figure 5. Figure 5(b) illustrates the energy level scheme for achieving enantiomer-selective population transfer with TFO, which is adapted from the above-mentioned experimental scheme to separate the chiral conformers of cyclohexyl methanol.[66] A fast chirp in the RAP regime or a π-pulse (#6) is applied to invert the undesired thermal population in state $|1_{10}\rangle$ with the $|2_{11}\rangle$ rotational level, which is less populated. In this manner, the efficiency of the population transfer cycle can be enhanced, as it is proportional to the population difference between the $|1_{10}\rangle$ and $|0_{00}\rangle$ states. The following excitations of all three microwave pulses in the population transfer cycle induce an enantiomer-specific enrichment in states $|1_{01}\rangle$ and $|0_{00}\rangle$, which are opposite for the R- and S-enantiomers. The enantioenrichment is controlled by varying the phase of the transfer pulse and read out with a probe cycle. The enhancement of the achieved enantioenrichment is quantitatively assessed by directly comparing the results obtained with and without the π-pulse or RAP pulse. The experimental details are provided in the Supporting Information and are briefly described as follows.

Prior to performing the population transfer experiments, the durations of each of the excitation pulses were optimized for π/2 or π conditions on the Bloch sphere by recording the corresponding nutation curves. The results are presented in

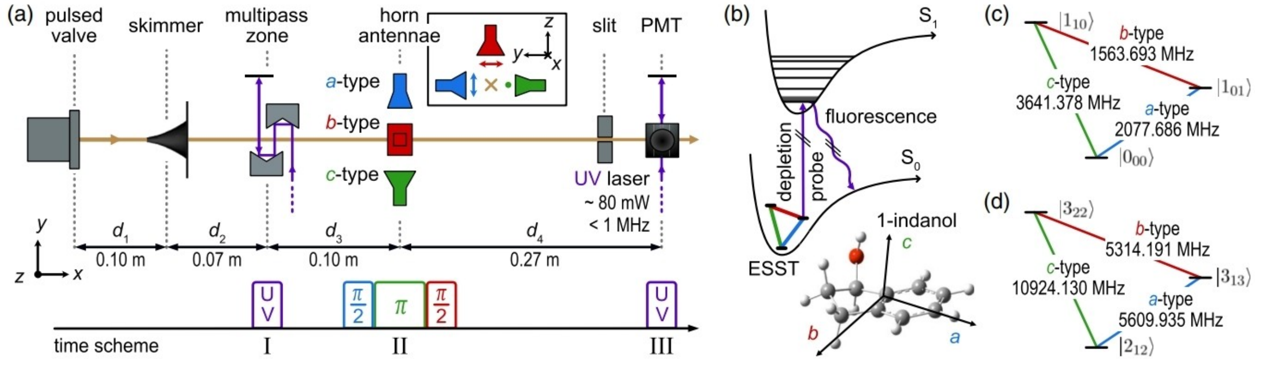

Figure 4. (a) Experimental setup, where jet-cooled 1-indanol is injected into the vacuum chamber through a pulsed valve. The molecules travel through a multi-pass zone where they interact with the UV depletion laser (step I). Further downstream, three microwave pulses with mutually orthogonal polarizations are applied for enantiomer-selective population transfer (step II). The molecules are interrogated by the same UV laser in the detection region, where the total laser-induced fluorescence intensity is measured with a photomultiplier tube (PMT) (step III). (b) Energy scheme consisting of electronic excitation and emission processes. The most stable conformer of 1-indanol is depicted together with the inertial axis system. (c+d) Energy-level schemes for two population-transfer cycles involved for 1-indanol. Figure is taken from Ref. [67] with Creative Commons Attribution 4.0 International license permission.

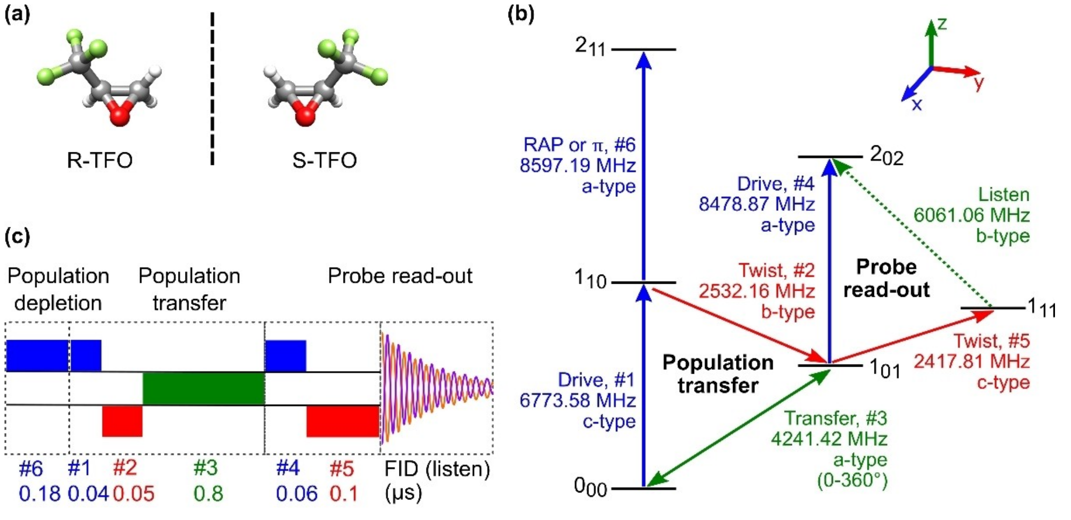

Figure 5. (a) Molecular structure of 2-trifluoromethyl oxirane (TFO) illustrating both enantiomers. (b) Rotational energy-level scheme for the coherent enantiomer-selective population transfer of TFO. The rotational levels are denoted using the J_{KaKc} notation. The color code indicates the polarization directions of the applied linearly polarized microwave fields (shown in Figure 2(b)). The population transfer cycle consisting of transitions #1, #2, and #3 creates an enantiomer-selective population difference between the $|0_{00}\rangle$ and $|1_{01}\rangle$ rotational levels. The selectivity can be controlled by varying the relative phase of the transfer pulse #3 at a frequency of 4241.42 MHz. This enantiomer enrichment is read out with a M3WM cycle (probe cycle) consisting of transitions #4, #5, and the listen transition (ν_L) at 6061.06 MHz. Pulse #6 is the preceding pulse applied to enhance the enantioenrichment, either as a rapid adiabatic passage (RAP) chirp or as a π-pulse. (c) Optimized pulse sequence in the time domain associated with the energy-level scheme in (b). Pulse #6 refers to either a π-pulse or a RAP-pulse of 4 MHz bandwidth.

Figures S2–S8 of the Supporting Information, and the optimal pulse conditions and durations are summarized in Table S2. The optimal five-pulse sequence for our experimental setup with a preceding pulse (pulse #6) is depicted in Figure 5(c). The pulses were fed in the respective mutually orthogonal polarizations using the dual-polarized horn antennas of the set-up shown in Figure 2(b). The color code in Figure 5 refers to the individual laboratory-fixed axes. The experiments were carried out with the racemic TFO sample, and the chiral signal of the probe cycle at the listen frequency ν_L (6061.06 MHz) yielded the created enantiomeric excess as a function of phase for the transfer pulse #3 (ϕ_3), at a frequency of 4241.42 MHz, varied from 0 to 360 in steps of 18, while keeping the phases of pulse #1 and #2 constant.

More than 15,000 FID acquisitions were collected and averaged for each transfer phase. To assess the reproducibility of the observations, each set of experiments was repeated three times, which are provided in Figures S9–S11 in the Supporting Information. The same experiments were also performed with the enantiopure R- and S-TFO samples, which are used as the references with 100 % *ee*.

By comparison with the results from the enantiopure samples, the induced enantiomeric excess in the rotational state $|1_{01}\rangle$ from the racemic TFO mixture can be quantitatively determined using the following equation:

$$ee_{1_{01}} = \frac{I_L \cdot \gamma}{\frac{1}{2} \cdot [\langle I_{R,L}\rangle \cdot \gamma_R + \langle I_{S,L}\rangle \cdot \gamma_S]} \times 100\,\%$$

where I_L is the molecular response at the listen frequency (ν_L) when performing the enantiomer-selective population transfer experiment with the racemic TFO sample, $\langle I_{R,L}\rangle$, and $\langle I_{S,L}\rangle$ are the mean signal intensities at ν_L averaged over all phase steps throughout the population transfer experiments using the enantiopure R- and S-TFO samples. As the gas mixtures of racemic, R-, and S-TFO are prepared separately for the experiments, the respective concentrations of TFO are different. In each experiment, the mean signal intensity of the transfer transition (ν_3), which has the same polarization as the listen transition, is proportional to the concentration of TFO in the gas mixture and independent of the enantiomeric excess, thus it is used to normalize the results. In this equation, γ, γ_R, and γ_S are the normalization factors, which are the inverse of the mean intensity of the transfer transition (ν_3) obtained with racemic, R- and S-TFO samples, respectively, as summarized in Table S3 in the Supporting Information.

The overall results describing the created enantiomeric excess in the $|1_{01}\rangle$ rotational state from the racemic TFO sample are summarized in Figure 6(a) as a function of ϕ_3. The red, blue, and black curves show the results with and without the preceding π- or RAP-pulse. Two maxima at $\phi_3 =$ 90 and 270 were consistently observed in all experiments, corresponding to the maximum enantioenrichment in the $|1_{01}\rangle$ state. They are assigned to S- and R-TFO, respectively, by comparing the signal phases at ν_L with that obtained from the enantiopure samples, as shown in Figure S12 in the Supporting Information. Benefiting from the population transfer cycle starting with the ground state $|0_{00}\rangle$, an enantiomeric excess of about 13 % is obtained in the $|1_{01}\rangle$ state, which is twice of that reported with carvone (about 6 % in the $|2_{02}\rangle$ state).[46] With the implementation of the preceding π- or RAP-pulse prior to the population transfer

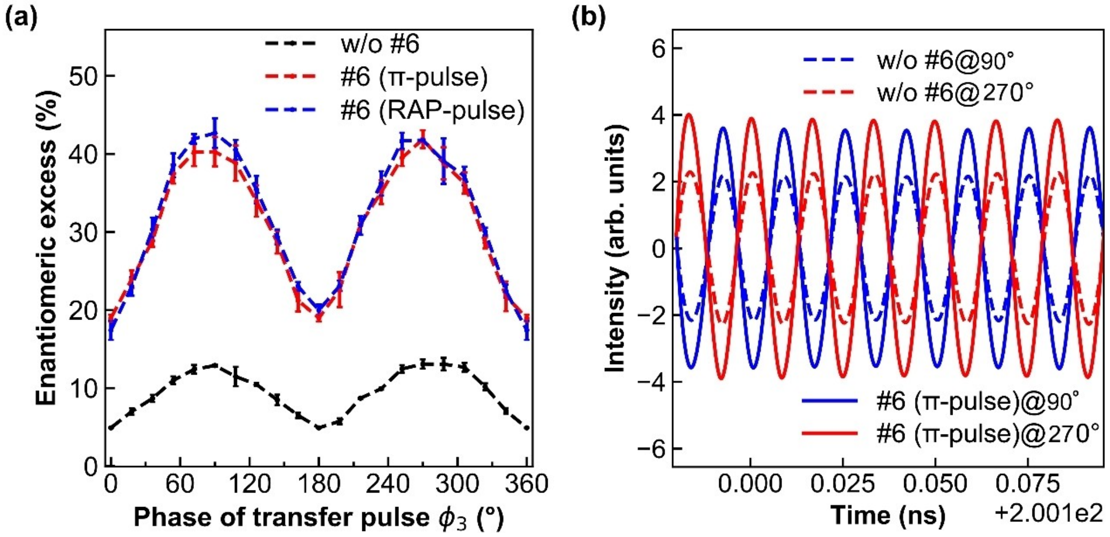

Figure 6. (a) The enantiomeric excess obtained for racemic TFO by applying the pulse sequence shown in Figure 5(c) is plotted as a function of the phase of the transfer pulse (ϕ_3), which was varied from 0 to 360 in steps of 18. For each phase step, 15,000 FIDs were averaged and repeated three times. The errors are calculated from the three repeated experiments. The two maxima at $\phi_3 = 90$ and 270 correspond to the maximum selective population transfer of the two enantiomers in the $|1_{01}\rangle$ rotational level. The black curve shows the enantiomer excess produced without any preceding pulse. The red and blue curves show the results with either a preceding π- or a RAP-pulse. (b) Portions of the free-induction decays (FIDs) at the listen frequency (ν_L) in the time domain with and without the preceding π-pulse when $\phi_3 = 90$ and 270. The phases of the obtained chiral signal at 90 and 270 show a shift of π radians, indicating the two different enantiomers in excess.

process, the induced *ee* is further improved to about 40%, increasing the enantiomeric excess by about a factor of three.

In addition to the experiments, we simulated the enantiomeric enrichment in TFO using the QDYN program package developed by the group of Prof. Christiane Koch at the Freie Universität Berlin.[73] For this, we implemented the energy scheme for the population transfer cycle including all M_J states and the thermal population of the rotational states at a rotational temperature of 2 K. While using the experimentally determined pulse durations, the electric field strengths of all the pulses were optimized as shown in Table S4 of the Supporting Information. For each enantiomer, the initial thermal population was then numerically propagated with the optimized pulses, employing the Chebyshev expansion.[74] The *ee* in the rotational state $|1_{01}\rangle$ can be then obtained by subtracting the final populations of both the enantiomers in this state.

The phase dependence of the *ee* is simulated by scanning the phase ϕ_3 from 0 to 360, as performed in the experiments. Figure 7 presents the simulated enantiomeric excess for the rotational state $|1_{01}\rangle$ with and without any preceding pulse. These simulated results agree qualitatively well with our experimental observations. The obtained quantitative differences between experiments and simulations can be accounted to differences in external factors such as different microwave field strengths used in the simulations than in our experiments.

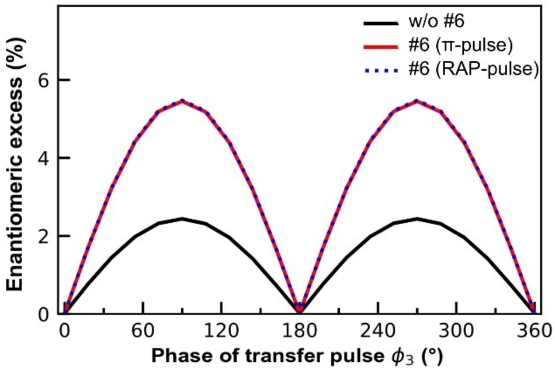

Figure 7. The simulated enantiomeric excess obtained for the rotational level $|1_{01}\rangle$ is plotted as a function of the phase of the transfer pulse #3, ϕ_3, using the program package QDYN.[73] The black curve represents the enantiomeric excess without a preceding pulse, while in red and blue the enantiomeric excess with either a preceding π- or RAP-pulse is shown.

4. Conclusions

The recent developments of chirality-sensitive techniques using gas-phase samples hold great promise for investigating and controlling chirality on different time scales and with different resolution. Approaches based on rotational spectroscopy can address chiral molecules even in complex chiral mixtures due to its fingerprint character.[7,42,54,59] With the recent development of the microwave three-wave mixing (M3WM) technique, which is a resonant, non-linear, and coherent approach, microwave spectroscopy can now be used to differentiate between enantiomers and to determine their respective enantiomeric excess in complex chiral mixtures. The resonant nature of the technique has established a robust method to detect individual chiral components in mixtures such as peppermint oil.[55]

Advanced developments of M3WM demonstrate its ability to manipulate and control chiral molecules at the molecular level in the gas phase. Quantum-state separation of enantiomers and chiral purification are some of the ongoing challenges of chiral research. The ability to generate samples for which the excess enantiomer can be controlled and switched "on the fly" will be highly useful for advanced experiments with state-selected chiral molecules, such as chiral collisions or precision spectroscopy. A first step in that direction is discussed in section 2.2., where we have discussed how tailored microwave pulses can be used not only to read out the handedness of chiral molecules but also to promote enantioseparation. With the concept of coherent enantiomer state-selective population transfer, a particular enantiomer can be enhanced in a chosen rotational state compared to the other handedness. Recent work focuses on how to overcome the obstacles towards enhancing this state-specific enantioselective population transfer, which we summarize in section 2.3. of this minireview.

The effect of thermal population as a major factor can be reduced prior to the enantiomer separation and leads to significant enhancement in enantiomer enrichment. A recent work shows the use of a UV laser for depleting the target rotational state prior to the population transfer process and measuring the enantiomer enrichment with laser-induced fluorescence.[67] Here, we provide new experimental results for an enhanced enantiomer-selective population transfer scheme, which is based solely on microwave pulses, which makes it a general approach. With the usage of tailored microwave pulses such as π- and RAP-pulses, the effect of thermal population could be reduced and the enantiomeric excess achieved for a set of chosen rotational states could be increased by a factor of three compared to experiments without a population-inversion pulse, resulting in samples with 40 % enantiomeric excess of a chosen enantiomer in a specific rotational state starting from a racemic sample. These latest experiments on controlling the composition of a chiral sample in certain rotational states impressively demonstrate the level of control that can be achieved with high-resolution rotational spectroscopy and gas-phase samples.

Acknowledgements

We thank Dr. Denis S. Tikhonov for fruitful scientific discussions. We would also like to thank Prof. Christiane Koch, Dr. Monika Leibscher, and Alexander Blech for providing us with the QDYN program for performing simulations and for helpful discussions. This work has been supported by the collaborative linkage grant "Extreme light for sensing and driving molecular chirality (ELCH)", SFB 1319, of the Deutsche Forschungsgemeinschaft. Open Access funding enabled and organized by Projekt DEAL.

Conflict of Interest

The authors declare no conflict of interest.

Keywords: Chirality · Chirality Control · Coherent Excitation · Microwave Spectroscopy · Population Transfer

---

[1] A. Brandenburg, in *Prebiotic Chemistry and the Origin of Life* (Eds.: A. Neubeck, S. McMahon), Springer, Cham, **2021**, pp. 87–115.

[2] M. Quack, *Angew. Chem. Int. Ed.* **2002**, *41*, 4618–4630.

[3] M. Quack, J. Stohner, M. Willeke, *Annu. Rev. Phys. Chem.* **2008**, *59*, 741–769.

[4] K. W. Busch, M. A. Busch, *Chiral Analysis*, Elsevier, Amsterdam, **2006**.

[5] L. A. Nafie, *Vibrational Optical Activity: Principles and Applications*, Wiley, Chichester, **2011**.

[6] P. L. Polavarapu, *Chiroptical Spectroscopy*, CRC Press, Boca Raton, **2016**.

[7] B. H. Pate, L. Evangelisti, W. Caminati, Y. Xu, J. Thomas, D. Patterson, C. Perez, M. Schnell, in *Chiral Analysis* (Eds.: P. L. Polavarapu), Elsevier, Amsterdam, **2018**, pp. 679–729.

[8] K. Le Barbu, V. Brenner, P. Millié, F. Lahmani, A. Zehnacker-Rentien, *J. Phys. Chem. A* **1998**, *102*, 128–137.

[9] A. Zehnacker, Eds., *Chiral Recognition in the Gas Phase*, CRC Press, Boca Raton, **2010**.

[10] O. Smirnova, Y. Mairesse, S. Patchkovskii, *J. Phys. B* **2015**, *48*, 234005.

[11] R. Cireasa, A. E. Boguslavskiy, B. Pons, M. C. H. Wong, D. Descamps, S. Petit, H. Ruf, N. Thiré, A. Ferré, J. Suarez, J. Higuet, B. E. Schmidt, A. F. Alharbi, F. Légaré, V. Blanchet, B. Fabre, S. Patchkovskii, O. Smirnova, Y. Mairesse, V. R. Bhardwaj, *Nat. Phys.* **2015**, *11*, 654–658.

[12] S. Beaulieu, A. Comby, A. Clergerie, J. Caillat, D. Descamps, N. Dudovich, B. Fabre, R. Géneaux, F. Légaré, S. Petit, B. Pons, G. Porat, T. Ruchon, R. Taïeb, V. Blanchet, Y. Mairesse, *Science* **2017**, *358*, 1288–1294.

[13] D. Ayuso, A. F. Ordonez, P. Decleva, M. Ivanov, O. Smirnova, *Opt. Express* **2022**, *30*, 4659–4667.

[14] H. G. Breunig, G. Urbasch, P. Horsch, J. Cordes, U. Koert, K. M. Weitzel, *ChemPhysChem* **2009**, *10*, 1199–1202.

[15] P. Horsch, G. Urbasch, K. M. Weitzel, *Chirality* **2012**, *24*, 684–690.

[16] C. Lux, M. Wollenhaupt, T. Bolze, Q. Liang, J. Köhler, C. Sarpe, T. Baumert, *Angew. Chem. Int. Ed.* **2012**, *51*, 5001–5005.

[17] U. Boesl, A. Bornschlegl, C. Logé, K. Titze, *Anal. Bioanal. Chem.* **2013**, *405*, 6913–6924.

[18] M. H. M. Janssen, I. Powis, *Phys. Chem. Chem. Phys.* **2014**, *16*, 856–871.

[19] G. A. Garcia, H. Soldi-Lose, L. Nahon, I. Powis, *J. Phys. Chem. A* **2010**, *114*, 847–853.

[20] G. A. Garcia, H. Dossmann, L. Nahon, S. Daly, I. Powis, *Phys. Chem. Chem. Phys.* **2014**, *16*, 16214–16224.

[21] A. Kastner, C. Lux, T. Ring, S. Züllighoven, C. Sarpe, A. Senftleben, T. Baumert, *ChemPhysChem* **2016**, *17*, 1119–1122.

[22] N. Böwering, T. Lischke, B. Schmidtke, N. Müller, T. Khalil, U. Heinzmann, *Phys. Rev. Lett.* **2001**, *86*, 1187–1190.

[23] G. A. Garcia, L. Nahon, M. Lebech, J. C. Houver, D. Dowek, I. Powis, *J. Chem. Phys.* **2003**, *119*, 8781–8784.

[24] U. Hergenhahn, E. E. Rennie, O. Kugeler, S. Marburger, T. Lischke, I. Powis, G. Garcia, *J. Chem. Phys.* **2004**, *120*, 4553–4556.

[25] I. Powis, C. J. Harding, G. A. Garcia, L. Nahon, *ChemPhysChem* **2008**, *9*, 475–483.

[26] G. A. Garcia, L. Nahon, S. Daly, I. Powis, *Nat. Commun.* **2013**, *4*, 2132.

[27] L. Nahon, L. Nag, G. A. Garcia, I. Myrgorodska, U. Meierhenrich, S. Beaulieu, V. Wanie, V. Blanchet, R. Géneaux, I. Powis, *Phys. Chem. Chem. Phys.* **2016**, *18*, 12696–12706.

[28] A. Kastner, T. Ring, H. Braun, A. Senftleben, T. Baumert, *ChemPhysChem* **2019**, *20*, 1416–1419.

[29] S. T. Ranecky, G. B. Park, P. C. Samartzis, I. C. Giannakidis, D. Schwarzer, A. Senftleben, T. Baumert, T. Schäfer, *Phys. Chem. Chem. Phys.* **2022**, *24*, 2758–2761.

[30] D. S. Tikhonov, A. Blech, M. Leibscher, L. Greenman, M. Schnell, C. P. Koch, *Sci. Adv.* **2022**, *8*, eade0311.

[31] A. Comby, E. Bloch, C. M. M. Bond, D. Descamps, J. Miles, S. Petit, S. Rozen, J. B. Greenwood, V. Blanchet, Y. Mairesse, *Nat. Commun.* **2018**, *9*, 5212.

[32] M. Pitzer, M. Kunitski, A. S. Johnson, T. Jahnke, H. Sann, F. Sturm, L. P. H. Schmidt, H. Schmidt-Böcking, R. Dörner, J. Stohner, J. Kiedrowski, M. Reggelin, S. Marquardt, A. Schießer, R. Berger, M. S. Schöffler, *Science* **2013**, *341*, 1096–1100.

[33] P. Herwig, K. Zawatzky, M. Grieser, O. Heber, B. Jordon-Thaden, C. Krantz, O. Novotný, R. Repnow, V. Schurig, D. Schwalm, Z. Vager, A. Wolf, O. Trapp, H. Kreckel, *Science* **2013**, *342*, 1084–1086.

[34] K. Fehre, S. Eckart, M. Kunitski, M. Pitzer, S. Zeller, C. Janke, D. Trabert, J. Rist, M. Weller, A. Hartung, L. P. H. Schmidt, T. Jahnke, R. Berger, R. Dörner, M. S. Schöffler, *Sci. Adv.* **2019**, *5*, eaau7923.

[35] K. Fehre, S. Eckart, M. Kunitski, C. Janke, D. Trabert, M. Hofmann, J. Rist, M. Weller, A. Hartung, L. P. H. Schmidt, T. Jahnke, H. Braun, T. Baumert, J. Stohner, P. V. Demekhin, M. S. Schöffler, R. Dörner, *Phys. Rev. Lett.* **2021**, *126*, 083201.

[36] A. A. Milner, J. A. M. Fordyce, I. MacPhail-Bartley, W. Wasserman, V. Milner, I. Tutunnikov, I. S. Averbukh, *Phys. Rev. Lett.* **2019**, *122*, 223201.

[37] A. Yachmenev, S. N. Yurchenko, *Phys. Rev. Lett.* **2016**, *117*, 033001.

[38] E. Gershnabel, I. S. Averbukh, *Phys. Rev. Lett.* **2018**, *120*, 083204.

[39] I. Tutunnikov, E. Gershnabel, S. Gold, I. S. Averbukh, *J. Phys. Chem. Lett.* **2018**, *9*, 1105–1111.

[40] E. Hirota, *Proc. Jpn. Acad. Ser. B* **2012**, *88*, 120–128.

[41] D. Patterson, M. Schnell, J. M. Doyle, *Nature* **2013**, *497*, 475–477.

[42] D. Patterson, J. M. Doyle, *Phys. Rev. Lett.* **2013**, *111*, 023008.

[43] J. L. Wu, Y. Wang, S. L. Su, Y. Xia, Y. Jiang, J. Song, *Opt. Express* **2020**, *28*, 33475–33489.

[44] F. Zou, Y. Y. Chen, B. Liu, Y. Li, *Opt. Express* **2022**, *30*, 31073–31085.

[45] A. Lombardi, F. Palazzetti, *J. Phys. Condens. Matter* **2018**, *30*, 063003.

[46] C. Pérez, A. L. Steber, S. R. Domingos, A. Krin, D. Schmitz, M. Schnell, *Angew. Chem. Int. Ed.* **2017**, *56*, 12512–12517.

[47] W. Sun, D. S. Tikhonov, H. Singh, A. L. Steber, C. Pérez, M. Schnell, *Nat. Commun.* **2023**, *14*, 934.

[48] L. Evangelisti, W. Caminati, D. Patterson, J. Thomas, Y. Xu, C. West, B. Pate, **2017**, Talk RG03, *The 72nd International Symposium on Molecular Spectroscopy*, Urbana-Champaign, https://dx.doi.org/10.15278/isms.2017.RG03.

[49] M. D. Marshall, H. O. Leung, K. Wang, M. D. Acha, *J. Phys. Chem. A* **2018**, *122*, 4670–4680.

[50] S. R. Domingos, C. Pérez, M. Schnell, *Annu. Rev. Phys. Chem.* **2018**, *69*, 499–519.

[51] S. R. Domingos, C. Pérez, M. D. Marshall, H. O. Leung, M. Schnell, *Chem. Sci.* **2020**, *11*, 10863–10870.

[52] M. D. Mills, R. E. Sonstrom, Z. P. Vang, J. L. Neill, H. N. Scolati, C. T. West, B. H. Pate, J. R. Clark, *Angew. Chem. Int. Ed.* **2022**, *61*, e202207275.

[53] V. A. Shubert, D. Schmitz, D. Patterson, J. M. Doyle, M. Schnell, *Angew. Chem. Int. Ed.* **2014**, *53*, 1152–1155.

[54] V. A. Shubert, D. Schmitz, M. Schnell, *J. Mol. Spectrosc.* **2014**, *300*, 31–36.

[55] A. Krin, M. M. Quesada Moreno, C. Pérez, M. Schnell, *Symmetry* **2022**, *14*, 1262.

[56] K. Mayer, C. West, F. E. Marshall, G. Sedo, G. S. Grubbs, L. Evangelisti, B. H. Pate, *Phys. Chem. Chem. Phys.* **2022**, *24*, 27705–27721.

[57] F. Xie, N. A. Seifert, A. S. Hazrah, W. Jäger, Y. Xu, *ChemPhysChem* **2021**, *22*, 455–460.

[58] J.-U. Grabow, *Angew. Chem. Int. Ed.* **2013**, *52*, 11698–11700.

[59] S. Lobsiger, C. Perez, L. Evangelisti, K. K. Lehmann, B. H. Pate, *J. Phys. Chem. Lett.* **2015**, *6*, 196–200.

[60] V. A. Shubert, D. Schmitz, C. Medcraft, A. Krin, D. Patterson, J. M. Doyle, M. Schnell, *J. Chem. Phys.* **2015**, *142*, 214201.

[61] D. Patterson, M. Schnell, *Phys. Chem. Chem. Phys.* **2014**, *16*, 11114–11123.

[62] M. Shapiro, P. Brumer, *Adv. At. Mol. Opt. Phys.* **2000**, *42*, 287–345.

[63] P. Král, M. Shapiro, *Phys. Rev. Lett.* **2001**, *87*, 183002.

[64] P. Král, I. Thanopulos, M. Shapiro, D. Cohen, *Phys. Rev. Lett.* **2003**, *90*, 033001.

[65] S. Eibenberger, J. Doyle, D. Patterson, *Phys. Rev. Lett.* **2017**, *118*, 123002.

[66] C. Pérez, A. L. Steber, A. Krin, M. Schnell, *J. Phys. Chem. Lett.* **2018**, *9*, 4539–4543.

[67] J. Lee, J. Bischoff, A. O. Hernandez-Castillo, B. Sartakov, G. Meijer, S. Eibenberger-Arias, *Phys. Rev. Lett.* **2022**, *128*, 173001.

[68] D. Schmitz, V. A. Shubert, T. Betz, M. Schnell, *J. Mol. Spectrosc.* **2012**, *280*, 77–84.

[69] K. K. Lehmann, *J. Chem. Phys.* **2018**, *149*, 094201.

[70] M. Leibscher, T. F. Giesen, C. P. Koch, *J. Chem. Phys.* **2019**, *151*, 014302.

[71] M. Leibscher, E. Pozzoli, C. Pérez, M. Schnell, M. Sigalotti, U. Boscain, C. P. Koch, *Commun. Phys.* **2022**, *5*, 110.

[72] V. S. Malinovsky, J. L. Krause, *Eur. Phys. J. D* **2001**, *14*, 147–155.

[73] C. Koch, A. Blech, D. Basilewitsch, M. Goerz, F. Krack, "QDYN - quantum dynamics and control," can be found under https://qdyn-library.net/, **2020** (accessed on 22 December 2022).

[74] A. Gil, J. Segura, N. M. Temme, in *Numerical Methods for Special Functions*, Society for Industrial and Applied Mathematics, Philadelphia, PA, **2007**, pp. 51–86.

Manuscript received: December 23, 2022
Accepted manuscript online: March 3, 2023
Version of record online: April 27, 2023

7.1 Summary and outlook

This minireview showcases the latest advancements in the field of M3WM and its application to enantiomer-selective population transfer. The most recent experiments aimed at enhancing the previously achieved enantiomeric enrichment are presented.

In particular, the effect of tailored microwave pulses on enantiomer-selective population enrichment is demonstrated for TFO. Using low-lying rotational states, i.e., starting with $|0_{00}\rangle$ in our scheme, an *ee* of approximately 13% for TFO could be achieved in a specific rotational state, which is twice the previously achieved *ee* of 6% for carvone.[62] This effect could be further enhanced by reducing the thermal population before the population transfer process using tailored microwave pulses. As demonstrated, the thermal population could be depleted by exchanging the unwanted thermal population to a connected higher state prior to the population transfer process, either with a fast chirp in the RAP regime or a π-pulse. Both of these microwave pulses have similar effects on the enantiomer-selective population transfer, resulting in an enantiomeric enrichment of about 40%. This is illustrated in Fig. 6(a) of the manuscript, where two maxima at 90° and 270° represent the maximum *ee* obtained in the experiments for S- and R-TFO, respectively. These results demonstrate the high level of control that can be achieved with high-resolution rotational spectroscopy and gas-phase samples.

In the future, the incoherent thermal population of rotational levels in the vibrational ground state can be overcome by addressing the thermally unoccupied rotational levels in the excited vibrational state by using IR pulses. Excitation schemes such as two IR and one microwave pulse (2IR + MW) instead of three microwave pulses in M3WM will provide an improved starting point for conducting enantiomer-selective population transfer experiments using microwave fields.[159] The combination of IR and microwave radiation will allow enantio-selective excitation for C_2 chiral molecules for which pure M3WM spectroscopy is not possible.

As outlined in section 2.5, the enantiomeric enrichment in the enantiomer-selective population transfer process is also restricted by the $(2J+1)$ degeneracy in the M_J quantum number. The theoretical demonstration by Leibscher *et al.* illustrates an enhancement in enantiomer-selective enrichment from 6% to 8% in carvone by addressing the M_J substates using M3WM schemes involving circularly polarised microwave pulses.[105] This effect could be further augmented by depleting the thermal population. Their findings suggest that through the depletion of thermal population and the utilisation of M3WM consisting of circularly polarised microwave pulses, nearly 100% enantio-selectivity can be achieved.[105]

These advanced pulse schemes presented to gain higher control over chiral molecules aim to generate samples of well-controlled quantum states and handedness. A sample prepared in this manner states an ideal starting point for further sophisticated molecular physics experiments, including precision measurements and chiral purification. Furthermore, it is important to extend the application of M3WM and its potential to create state- and enantiomer-controlled samples to various classes of molecules, including those with quadrupole hyperfine structure. Many chiral molecules, especially those relevant for investigating PV effects, contain quadrupolar nuclei, resulting in hyperfine structure. Therefore, exploring M3WM and enantiomer-selective population transfer experiments in such classes of chiral molecules, requiring specialised pulse sequences, holds substantial interest.

These experiments on attaining complete control through advanced pulse sequences and cooling techniques to achieve enantiomer- and quantum-state controlled species will help to enter the resolution regime of PV and unravel the parity-violating characteristics of weak interactions in mirror-image molecules.

Chapter 8

Manipulating chirality in a molecular quantum racemate with microwave fields

Many chiral molecules that have been studied using the M3WM approach possess a stereogenic center, making them permanently chiral during the timescales of our experiments. An example of such a chiral molecule is TFO, which was investigated in the previous chapter 7. On the other hand, flexible molecules without a stereogenic center can acquire chirality due to the spatial arrangement of their conformers, resulting in transient chirality. This category includes molecules that can be kinetically stabilised as two enantiomers through cooling in a supersonic expansion due to a sufficiently high interconversion barrier, such as cyclohexyl methanol,[65] as well as molecules with lower interconversion barriers enabling a change of their handedness upon tunneling, exemplified by benzyl alcohol (BA)[36]. Section 2.6 of chapter 2 outlines the different cases for permanently and transiently chiral molecules as the barrier height between the two enantiomers decreases (Fig. 2.13).

MW spectroscopy enables not only the detection of chirality but also the manipulation of population of the chiral molecules using tailored microwave pulses, as discussed in the preceding chapter. Pérez *et al.* demonstrated the state-specific enantiomeric enrichment of chiral conformers by applying an enantiomer-selective population transfer technique on kinetically trapped chiral conformers of cyclohexyl methanol.[65] In this work, flexible molecules with low barriers that can change their handedness via quantum tunneling through the barrier and can no longer be isolated in a cold supersonic jet are addressed. An approach based on M3WM can be devised to induce chirality in structurally flexible molecules, such as BA, as discussed in section 2.6 of chapter 2.

The two enantiomers of BA differ in the orientation of the CH_2OH group by rotation around a C-C single bond (Fig. 2.14), resulting in energy splittings that can be observed with our experiments. Each energy level is split into two tunneling states, where each state is a positive and negative linear combination of the two enantiomers, R and S. The transiently stabilised enantiomers of BA have opposite signs of the μ_b dipole moment component in the principal axis system. The b-type rotational transitions occur between the two tunneling states of opposite symmetry. These interstate transitions make both M3WM and related population transfer schemes inapplicable, as a set of three rotational transitions cannot form a closed cycle due to symmetry considerations.

Therefore, a more complex six-level energy scheme needs to be developed for BA instead. An experimental demonstration of a microwave six-wave mixing (M6WM) approach to induce and probe the enantiomeric enrichment in a chosen rotational state of BA in the gas phase is presented in this chapter. Fig. 1b of the manuscript depicts the rotational level scheme of BA used in the experiments. Fig. 2 illustrates the modified COMPACT spectrometer setup for the M6WM experiments. Each of the rotational transitions within the energy level scheme was optimised by measuring the nutation curves provided in the supplementary information. The optimised five microwave pulse sequence is presented in Fig. 3, along with the experimental results. The results section of the article elaborates on the principle of the M6WM approach and experimental findings.

Title	Inducing transient enantiomeric excess in a molecular quantum racemic mixture with microwave fields
Authors	Wenhao Sun$^+$, Denis S. Tikhonov$^+$, Himanshi Singh, Amand L. Steber, Cristóbal Pérez, and Melanie Schnell
Journal	*Nature communications*
Volume	14
Year	2023
Pages	934
DOI	https://doi.org/10.1038/s41467-023-36653-3
Pages	8 pages of the article and 62 pages of supplementary information
My contributions	Experiments

nature communications

Article

https://doi.org/10.1038/s41467-023-36653-3

Inducing transient enantiomeric excess in a molecular quantum racemic mixture with microwave fields

Received: 23 June 2022

Accepted: 10 February 2023

Wenhao Sun[1,2], **Denis S. Tikhonov**[1,2], **Himanshi Singh**[1,2], **Amanda L. Steber**[1,2,3], **Cristóbal Pérez**[1,2,3] & **Melanie Schnell**[1,2] ✉

Chiral molecules with low enantiomer interconversion barriers racemize even at cryogenic temperatures due to quantum tunneling, forming a racemic mixture that is impossible to separate using conventional chemical methods. Here we both experimentally and theoretically demonstrate a method to create and probe a state-specific enantiomeric enrichment for such molecular systems. The coherent, non-linear, and resonant approach is based on a microwave six-wave mixing scheme and consists of five phase-controlled microwave pulses. The first three pulses induce a chiral wavepacket in a chosen rotational state, while the consecutive two pulses induce a polarization for a particular rotational transition (listen transition) with a magnitude proportional to the enantiomeric excess created. The experiments are performed with the transiently chiral molecule benzyl alcohol, where a chiral molecular response was successfully obtained. This signal demonstrates that enantiomeric excess can be induced in a quantum racemic mixture of a transiently chiral molecule using the developed microwave six-wave mixing scheme, which is an important step towards controlling non-rigid chiral molecular systems.

Chirality is an ubiquitous and fundamental phenomenon in nature. A chiral molecule has a pair of enantiomers, which are non-superimposable mirror images of each other. They share almost all physical properties, but often possess distinct functionality in chemical reactions and biological activity with chiral environments. For instance, enantiomers of chiral drugs often exhibit different effectiveness and toxicity[1]. As molecular chirality plays an essential role in many fundamental aspects of physics, chemistry, and biology, great efforts have been made to characterize, differentiate, and manipulate chiral molecules. Besides the traditional methods in chemistry, such as chromatography[2] and capillary electrophoresis[3], various chiroptical techniques using circularly polarized radiation have been developed to determine the absolute configuration and enantiomeric excess (ee) of a chiral sample, such as vibrational circular dichroism (VCD)[4,5] and photoelectron circular dichroism (PECD)[6,7]. Recently, the microwave three-wave mixing (M3WM) approach, which is a resonant, coherent, and non-linear spectroscopic technique, became a new methodology for chiral differentiation and quantification[8,9]. The chiral sensitivity arises from the mirror symmetry of the electronic structures of enantiomers, making the triple products of their three electric dipole-moment components ($\boldsymbol{\mu}_a \cdot [\boldsymbol{\mu}_b \times \boldsymbol{\mu}_c]$) equal in magnitude but opposite in sign, which can be interrogated using a combination of selected rotational transitions.

In addition to chiral analysis, the M3WM technique showcased its capability to achieve chiral separation at the molecular level[10–13]. Through the interference between the chiral sensitive M3WM path and a direct excitation path, enantiomers can be selectively enriched in chosen rotational states. As the sample is studied in the gas phase with

---

[1]Deutsches Elektronen-Synchrotron DESY, Notkestr. 85, 22607 Hamburg, Germany. [2]Institute of Physical Chemistry, Christian-Albrechts-Universität zu Kiel, Max-Eyth-Str. 1, 24118 Kiel, Germany. [3]Present address: Departamento de Química Física y Química Inorgánica, Facultad de Ciencias-I.U. CINQUIMA, Universidad de Valladolid, E-47011 Valladolid, Spain. ✉e-mail: melanie.schnell@desy.de

cold molecular sources (e.g. buffer-gas cooling and supersonic jets), this technique can be applied not only to molecules with permanent chirality, such as 1,2-propanediol[10] and carvone[11] but also to molecules that exhibit transient chirality, such as cyclohexylmethanol (CHM)[12], which are impossible to separate via conventional separation techniques, such as chromatography. However, when it comes to molecules that can interconvert their handedness via quantum tunneling through a large-amplitude motion (LAM), the enantiomers can no longer be isolated in a cold supersonic jet, where the molecules are cooled to a rotational temperature (T_{rot}) of a few Kelvin[14]. The sample naturally appears as a racemic mixture during the jet expansion. These molecules have two (or more) minima on the potential energy surface. Each minimum corresponds to a certain enantiomer, separated by an achiral transition state (Fig. 1). The stationary states of such molecules are of a specific parity with respect to the inversion operation that we will denote as $|\pm\rangle$. They are the positive and negative combinations of the non-stationary localized wavepackets with a chosen parity ($|\pm\rangle = \frac{1}{\sqrt{2}}(|R\rangle \pm |S\rangle)$). A specific enantiomeric state of such a molecule thus can be achieved by generating a coherent superposition of the states $|\pm\rangle$ with opposite parity[15–18]. Such an approach has been proposed for rotational states of asymmetric rotors[19,20]; however, to date, no experimental demonstration has been reported.

Herein, we present both theoretical and experimental demonstration of inducing enantiomeric excess from a racemic mixture of a transiently chiral molecule, benzyl alcohol (BA), in the gas phase. This molecule undergoes a LAM, corresponding to a concerted rotation of the CH_2OH and OH groups in the plane above the phenyl ring. This tunneling motion with a barrier of about 280 cm^{-1} transfers one enantiomer into the other one (see Fig. 1)[21]. It changes the sign of the electric dipole-moment component along the b-axis in the inertial principal axis system (PAS). The corresponding b-type rotational transitions occur between the two tunneling states of opposite symmetry. Because of these interstate transitions, both microwave three-wave mixing[8,22–24] and the related microwave population transfer schemes become impossible[10,11,22], as three rotational transitions cannot form a closed cycle due to symmetry considerations. Instead, five resonant excitation pulses are needed to induce the chiral response in the form of a "listen" transition in a suitable system of six rotational levels (see Fig. 1). This chiral response is not directly excited, and its amplitude is dependent on the enantiomeric excess of the sample. By detecting a listen (L) signal with non-zero intensity, we demonstrate that this microwave six-wave mixing (M6WM) scheme is feasible to create a transiently chiral ensemble of BA molecules in the rotational state of interest, despite a fast interconversion of the two enantiomers via the tunneling motion. In the following, we first provide the theoretical derivation of the M6WM scheme, followed by the experimental implementation and demonstration.

Results

Principle of the M6WM approach

We will start with an introduction of the M6WM scheme, which consists of five sequential resonant pulses. They correspond to a closed loop of six transitions that connect six states ($J^{\pm}_{K_aK_c}$) in the following sequence: $|1^-_{01}\rangle \to |2^-_{11}\rangle \to |2^+_{02}\rangle \to |1^+_{01}\rangle \to |2^+_{11}\rangle \to |2^-_{02}\rangle$, as illustrated in Fig. 1. Here, $J_{K_aK_c}$ denote the asymmetric rotor rotational state with J being the total angular momentum quantum number, K_a/K_c being the projections of this momentum onto the a-/c- principal axes of the molecule, respectively, and ± indicating the parity of the torsional state of the molecule. For a theoretical description, the sequence of pulses is treated as a set of subsequent two-level Rabi oscillations (a detailed derivation is given in the Supplementary Information). After applying the five excitation pulses, a macroscopic polarization $\mathbf{P}$, which oscillates with amplitude A at the frequency of the $|2^-_{02}\rangle \to |1^-_{01}\rangle$ listen transition (ν_{L}), is coherently induced:

$$\mathbf{P}_{2^-_{02}\to 1^-_{01}} \propto \overbrace{-\boldsymbol{\mu}_{2^-_{02}\to 1^-_{01}} \cdot \sin(\Omega_1\tau_1) \cdot \left(\prod_{k=2}^{5} \sin\left(\frac{\Omega_k\tau_k}{2}\right)\right)}^{\propto A} \cdot \sin\left(2\pi\nu_{\mathrm{L}}t - \Phi + \sum_{k=1}^{5} s_k\varphi_k\right). \tag{1}$$

where $\boldsymbol{\mu}_{2^-_{02}\to 1^-_{01}}$ is the transition dipole moment for the induced listen transition $|2^-_{02}\rangle \to |1^-_{01}\rangle$, $\Omega_k = \frac{\boldsymbol{\mu}_k \mathbf{E}_k}{\hbar}$ is the Rabi frequency of the k-th pulse in the M6WM sequence, where the vector $\mathbf{E}_k$ describes its field strength and polarization direction, and $\boldsymbol{\mu}_k$ denotes the transition dipole moment of the transition induced with it[25,26], τ_k and φ_k are the pulse duration and phase, and Φ is the starting phase of the listen signal.

Equation (1) demonstrates the optimal conditions for the observation of the coherently induced polarization $\mathbf{P}_{2^-_{02}\to 1^-_{01}}$, the amplitude of which depends on the Rabi frequency. The first pulse is resonant to the $|1^-_{01}\rangle \leftrightarrow |2^-_{11}\rangle$ intrastate transition. This pulse should be a $\pi/2$-pulse ($\Omega_1\tau_1 = \pi/2$), which drives the population difference between the $|1^-_{01}\rangle$ and $|2^-_{11}\rangle$ rotational states into coherence. The other four pulses transfer this coherence to the final state $|2^-_{02}\rangle$ via the pathway $|2^-_{11}\rangle \to |2^+_{02}\rangle \to |1^+_{01}\rangle \to |2^+_{11}\rangle \to |2^-_{02}\rangle$, and they should be π-pulses ($\Omega_k\tau_k = \pi$ for $k = 2, \ldots, 5$). As a result, a final coherence at the listen

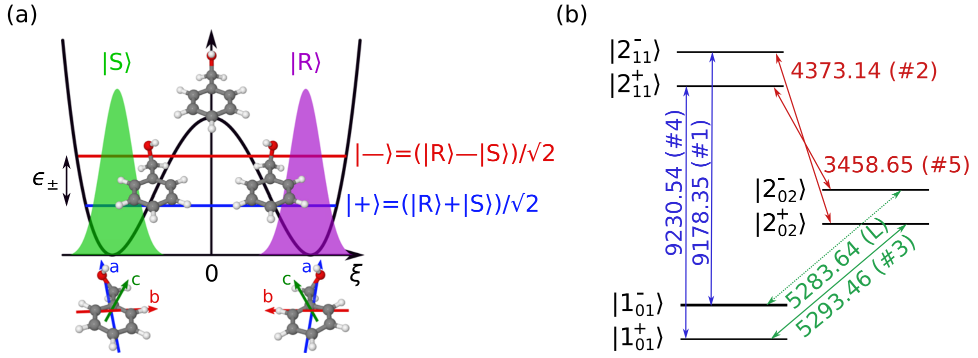

Fig. 1 | Double-well potential and rotational level scheme. a Schematic representation of the enantiomer interconversion mechanism in benzyl alcohol (BA). The $|\pm\rangle$ states denote the vibronic ground state with opposite parity. The $|R\rangle$ and $|S\rangle$ states represent the localized wavepackets of a particular chirality. ξ is the large amplitude motion coordinate. $\epsilon_{\pm}$ corresponds to the energy difference between the two tunneling states, which is experimentally determined to be 492.816(2) MHz for BA arising from a barrier with a height of about 280 cm^{-1}[21]. **b** Rotational level scheme of BA used in our experiment. Each rotational level is marked as $J^{\pm}_{K_aK_c}$, where J is the total angular momentum, K_a and K_c are the projections of the angular momentum onto the molecular axes a and c, and ± indicates the parity of the torsional state. M sublevels of the rotational states are omitted here for clarity[29]. The arrows indicate the transitions involved. Each transition is labeled with its frequency (in MHz) and its order in the sequence of the pulses (in parentheses). "L" indicates the "listen" transition, which is not directly excited by the pulse scheme but coherently induced.

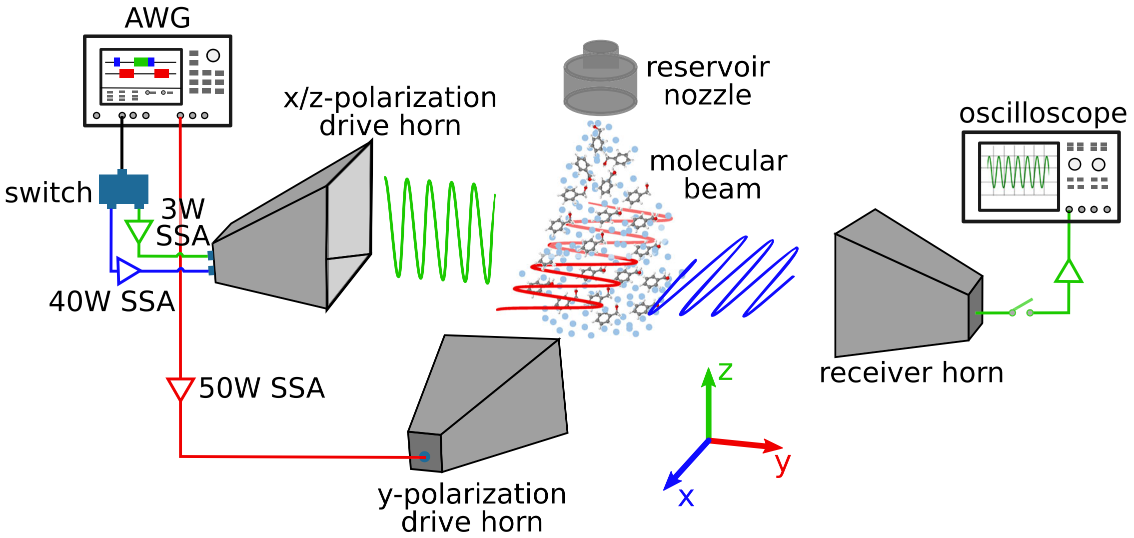

Fig. 2 | Schematic diagram of the state-specific enantiomeric enrichment experiment. The BA molecular sample seeded in neon with a stagnation pressure of about 3 bar is supersonically expanded into a vacuum chamber via a solenoid valve pulsing at 6 Hz. Five excitation pulses are generated from the two channels of the arbitrary waveform generator (AWG). The pulse sequence from channel 1 (CH1) is fed through the designated outputs of a single-pole-double-throw (SPDT) switch. Blue, red, and green colors represent the polarization directions of the microwave fields in the laboratory frame, which match the color code in the rotational level scheme as provided in Fig. 1. Each branch is equipped with a solid-state amplifier (SSA). The amplified microwave pulses are sequentially broadcast in the designated polarization directions to interact with the molecular jet using two dual-polarization horn antennae. The free induction decay (FID) of the resulting molecular response is collected in the z-polarization direction by a receiver horn and averaged by a fast digital oscilloscope.

transition is obtained with a maximum amplitude (A), when $\Omega_k\tau_k$ equals to $\pi/2$ for pulse #1, and π for pulse #2 – #5. The directions of the transition dipole moments (a-/b-/c-types are mutually orthogonal) also provide the required polarization directions of the pulses. There are three groups of pulses that need to be orthogonal to each other: pulses #1 and #4, pulses #2 and #5, and pulse #3, which is also indicated by the color scheme in Fig. 1b. The latter pulse (#3) should have the same polarization as the listen transition that is being collected.

The absolute phase of $\mathbf{P}_{2_{02}^{-}\rightarrow 1_{01}^{-}}$ depends on specific aspects of the experimental setup, such as the durations and phases of the five excitation pulses, delays between them, and cable lengths[27]. When the phase of pulse #k (φ_k) is varied, the phase of $\mathbf{P}_{2_{02}^{-}\rightarrow 1_{01}^{-}}$ changes accordingly, with a linear factor $s_k = \pm 1$. The factor s_k equals +1, when the transition goes up in energy ($k = 1, 4$), or equals −1, when the transition goes down in energy ($k = 2, 3, 5$), as described in more detail in the Supplementary Information.

M6WM spectroscopy

The experiment was carried out using a modified broadband Fourier transform microwave spectrometer, as shown schematically in Fig. 2. The molecular sample of BA was introduced into the vacuum chamber via supersonic jet expansions using neon as carrier gas. In the jet, the molecules were rapidly cooled to a T_{rot} of ~1–2 K via BA-neon collisions so that a substantial population difference was generated in the rotational states of interest. The ensemble of molecules was sequentially polarized with the five microwave pulses. In order to spatially broadcast the pulses in three mutually orthogonal planes, two dual-polarization horn antennae were installed at 90° in the vacuum chamber. After polarization, the decay of the induced macroscopic polarization at ν_{L} was received by a third horn on the detection side, digitized, and averaged on a fast digital oscilloscope.

Prior to the M6WM experiments, the pulse durations for the $\pi/2$ or π conditions were determined for each pulse by measuring the corresponding nutation curve. The collected nutation curves are provided in the Supplementary Section 2.2, and the optimized pulse sequence is presented in Fig. 3a. The determined pulse durations are approximate to the effective $\pi/2$ or π conditions averaged over M subsets of the rotational states[28–30]. Afterwards, we performed a series of M6WM experiments, in which the phase of one excitation pulse (φ_k) was systematically varied at a time in steps of 18° from 0° to 360° to evaluate the phase behavior of the M6WM signal at ν_{L}. The other remaining four pulses were kept unchanged in the scans. At each phase being scanned, 20,000 FIDs were collected and averaged at the frequency of the listen transition, $\nu_{\mathrm{L}} = 5283.64$ MHz. Each scan was carried out repeatedly five times, allowing us to assess the repeatability of the observations. The results are summarized in Fig. 3b.

Analysis of the M6WM signal

According to Eq. (1), the molecular response induced from the M6WM cycle, S_{M6WM}, at the frequency ν_{L} of the listen transition $2_{02}^{-} - 1_{01}^{-}$, should have a constant amplitude (A_{M6WM}) over the five sets of scans, and its phase (φ_{M6WM}) should be correlated with the phases of the five pulses. In each scan, the phase of one pulse (φ) was varied from 0° to 360°, whereas the phase of the other four pulses remained fixed. The induced polarizations can, thus, be expressed as $A_{\mathrm{M6WM}}\sin(2\pi\nu_{\mathrm{L}}t - \Phi' + s_k\varphi_k)$, where Φ' combines the starting phase Φ in Eq. (1) and the phases of the phase-invariant pulses in the pulse sequence. Hence, S_{M6WM} should have a linear phase dependence on φ_k with the coefficient s_k. In scans #1 and #4, $s_k = +1$; in scans #2, #3, and #5, $s_k = -1$. However, as shown in Fig. 3b, the observations in the experiments exhibit unanticipated phase dependence patterns. The signal intensities at ν_{L} are not constant, and the phases are not linearly correlated with φ_k.

With careful examinations that are described in the Supplementary Section 2.4, we analyzed that the observed signal at ν_{L} was a result of the interference between the expected S_{M6WM} signal and perturbation signals at ν_{L} (S_{c2} and S_{c3}) when applying pulses #2 and #3. The presence of S_{c2} and S_{c3} is presumably attributed to off-resonance excitations due to the power leakage in the electronic circuit. The two perturbation signals had constant amplitudes (A_{c2} and A_{c3}) throughout the experiments, and their phases (φ_{c2} and φ_{c3}) were positively and linearly dependent on the phase of pulses #2 and #3, respectively, as shown in Supplementary Figs. 18 and 19 in the Supplementary

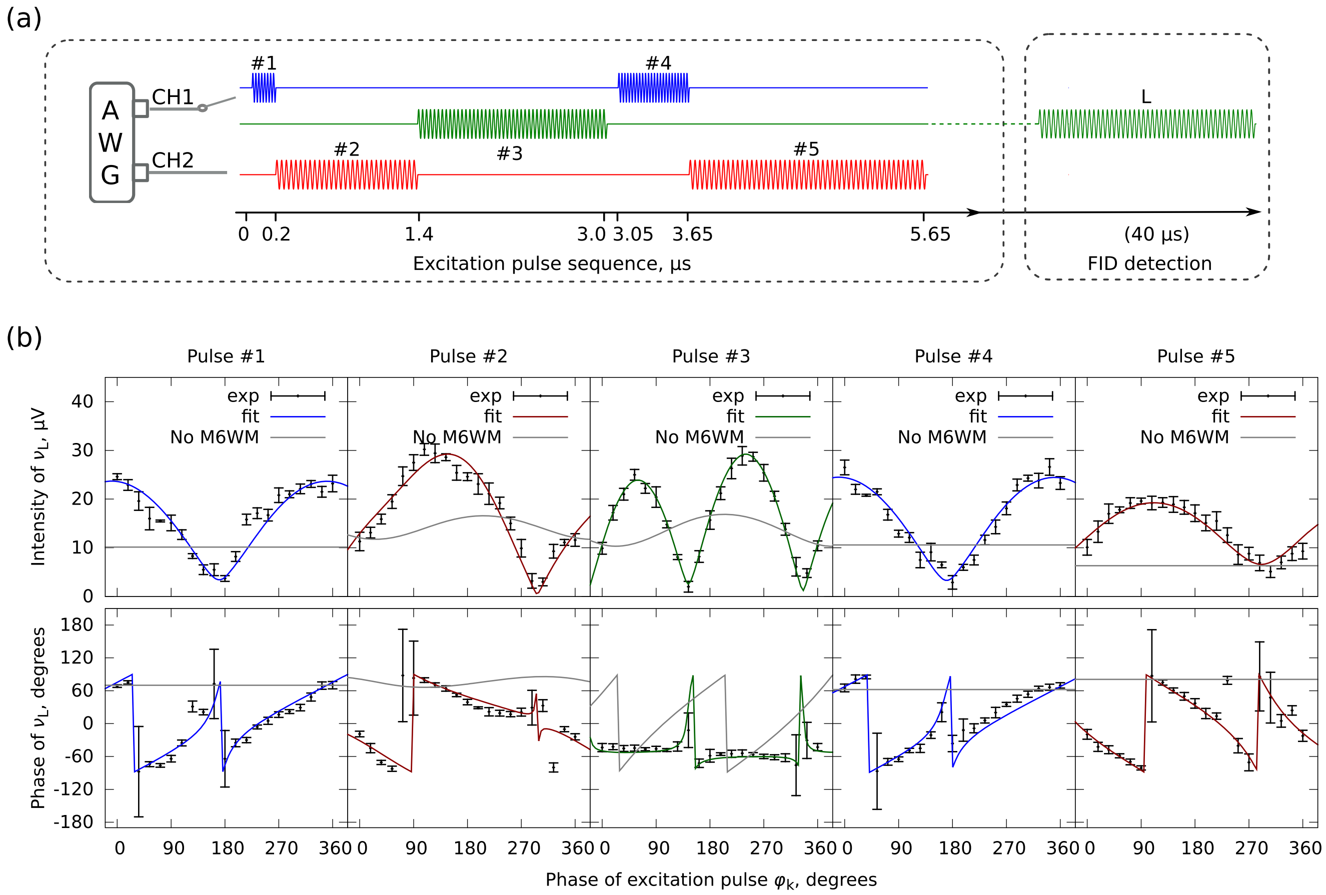

Fig. 3 | M6WM spectroscopy of BA. a The experimental M6WM pulse sequence, where the colors of the microwave pulses match the laboratory frame as in Fig. 2. The durations correspond to an optimized $\pi/2$-pulse for pulse #1 and π-pulses for pulses #2 – #5. 40 µs of FID for the frequency of the listen transition (ν_L) was recorded after the five excitation pulses, the duration of which is not to scale. **b** The resulting phase dependence patterns in amplitude (top) and phase (bottom) at the listen transition (ν_L). They were obtained by individually scanning the phases of the corresponding pulses (φ_k) and measuring the respective amplitude and phase of ν_L at 5283.64 MHz. Here, "phase of ν_L" denotes the arctangent of the tangent of the phase. The experimental results are represented in black with error bars. The errors are calculated from a set of five repeated measurements, in which each phase point was an average of 20,000 FIDs. In the least-squares fits, the amplitudes and the phases (in tangent) are fitted simultaneously. The overall fit for each set is represented in the color that matches the polarization of the corresponding microwave pulse whose phase was varied in the experiment. The gray line in each panel is the simulated amplitude or phase by excluding the M6WM component from the complete fit as discussed in the main text.

Information. The phase dependence coefficients of φ_{c2} and φ_{c3} are denoted as s_{c2} and s_{c3}. In scan #2, where the phase of pulse #2 (φ_2) was scanned, φ_{c2} positively and linearly varied with φ_2, while φ_{c3} was independent of φ_2. Therefore, $s_{c2} = +1$, and $s_{c3} = 0$. Likewise, φ_{c3} changed along with φ_3 in scan #3 and $s_{c3} = +1$, whereas φ_{c2} did not ($s_{c2} = 0$). In the other three scans, both φ_{c2} and φ_{c3} remained constant ($s_{c2} = 0$, and $s_{c3} = 0$), as φ_2 and φ_3 were not varied. With a clear understanding of the different phase dependencies of φ_{c2}, φ_{c3}, and φ_{M6WM}, we were able to perform a least-squares fit on each set of the scan to decompose the observed pattern and extract the S_{M6WM} signal. The molecular response from each scan is fitted independently as a sum of the individual interfering signals, where the total listen signal amplitude (A) and the total phase (Φ) are given by the following expressions:

$$\begin{cases} A^2 = \sum_{m=1}^{N}\sum_{n=1}^{N} A_m A_n \cos(s_m\varphi_k + \phi_m - s_n\varphi_k - \phi_n) \\ \tan(\Phi) = \frac{\sum_{m=1}^{N} A_m \sin(s_m\varphi_k + \phi_m)}{\sum_{m=1}^{N} A_m \cos(s_m\varphi_k + \phi_m)} \end{cases} . \quad (2)$$

Here, N is the number of interfering signals, φ_k is the scanned phase, A_m, A_n, ϕ_m, and ϕ_n are the amplitudes and the starting phases of the individual components, which are fitted to the observed experimental signals, s_m and s_n are the associated phase dependence coefficients. The square of the listen signal amplitude (A^2) and the tangent of the listen signal phase ($\tan(\Phi)$) are fitted simultaneously. The details on the procedure and the scripts used for the fitting are given in the Supplementary Information.

As in scans #2 and #3, the phases of all three interfering components have different phase dependencies on φ_k (i.e., in scan #2: $s_{c2} = +1$, $s_{c3} = 0$, and $s_2 = -1$; in scan #3: $s_{c2} = 0$, $s_{c3} = +1$, and $s_3 = -1$), they can be explicitly separated in the fit, as shown in Fig. 4. However, in the other three scans (#1, #4, and #5), as both S_{c2} and S_{c3} are phase-invariant, these two co-excited signals cannot be meaningfully separated. The sum of them is fitted as one phase-invariant signal instead. In each scan, the least-squares fit is obtained over the five repeats, and the experimental uncertainty is derived at each phase point as well. The fit results are summarized in Table 1 and are presented in Fig. 3b together with the experimental observations. The signal component with the anticipated phase dependence is assigned to S_{M6WM}, and it has a consistently constant amplitude of 13–14 µV throughout the five scans, clearly demonstrating the feasibility of the approach. In Fig. 3b, the curves based on the complete least-squares fits are represented using colored lines, while the simulations of the sum of S_{c2} and S_{c3} are plotted with gray lines, where the M6WM components are excluded. In this manner, the signal patterns with and without the presence of S_{M6WM} are revealed, and detailed demonstrations are further provided in Fig. 4.

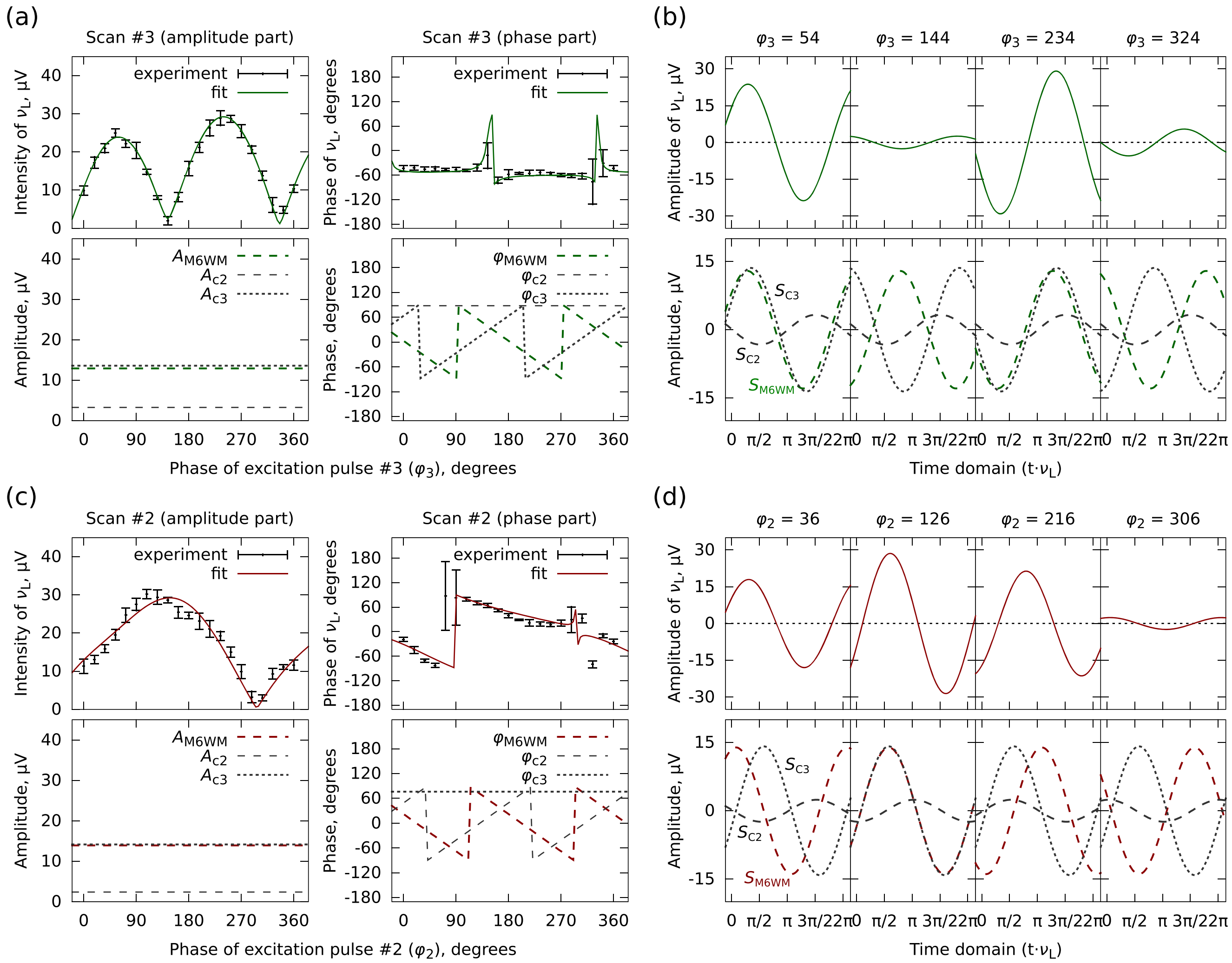

Fig. 4 | Illustration of the interference patterns. Left: experimentally observed interference patterns and the simulations based on the least-squares fits, when scanning the phase of pulse #3 (**a**) and pulse #2 (**c**). The upper traces show the experimental results together with the overall fit with regard to the intensity and phase at the frequency of the listen transition ν_L, respectively. The errors are calculated from a set of five repeated measurements, as mentioned for Fig. 3. The amplitudes and phases of the individual interfering wave components are presented in the lower traces. In each subplot of the phase part, the phase on the y-axis denotes the arctangent of the tangent of the phase. Right: interpretations of the interference in the time domain at four specific phases of φ_3 (**b**) and of φ_2 (**d**). The upper traces in panels **b** and **d** show the total listen signal in the time domain with the observed amplitude and phase, whereas the lower traces exhibit the three time-domain wave components on the basis of the least-squares fit and the experimental pattern. S_{M6WM} (colored dashed line) represents the signal induced from the M6WM scheme. S_{c2} (black dashed lines) and S_{c3} (black dotted lines) are the co-excited signals together with pulses #2 and #3, respectively.

Discussion

By analyzing the observed interference patterns, we have shown that a signal with a non-zero amplitude at the listen transition (ν_L) can be attributed to our phase-controlled M6WM excitation scheme. The amplitude of this signal (S_{M6WM}) is constant (13–14 μV) and the phase of it (φ_{M6WM}) is dependent on the phase φ_k of the k-th pulse with the linear factor s_k. For scans #2 and #3, all three interfering components (S_{M6WM}, S_{c2}, and S_{c3}) are explicitly disentangled, and the fitting results of the two scans show good agreement. As φ_3 or φ_2 is rotated through 360°, the amplitudes of these wave components stay constant, and their phases exhibit different dependencies on φ_3 or φ_2, which are presented in the lower traces of Fig. 4a, c. In scan #3, S_{M6WM} and S_{c3} have similar amplitudes, but their phases rotate with φ_3 in opposite directions. As a result, there are two in-phase and two out-of-phase interference coincidences, as demonstrated with the four time-domain snapshots in Fig. 4b, leading to two maxima/minima in the experimentally observed intensity profile (see Fig. 4a). The two unequal minima and maxima are attributed to the interference with the phase-fixed S_{c2} component. In contrast, in scan #2, the phase of S_{c3} is independent of φ_2, while the phase of S_{M6WM} varies with φ_2. This results in only one in-phase and out-of-phase interference for the S_{M6WM} and S_{c3} signals, one minimum and maximum in the experimental intensity profile, as shown in Fig. 4c and d, respectively. The presence of S_{c2} makes the intensity profile slightly asymmetric.

To understand why the signal S_{M6WM} observed in the experiment is a sign of induced chiral dynamics, we need to compute the *ee* obtained during the pulse sequence. The signed *ee* is an observable that can be expressed via the following operator[16–18]:

$$\hat{ee} = |R\rangle\langle R| - |S\rangle\langle S| = |+\rangle\langle -| + |-\rangle\langle +| . \tag{3}$$

The pulse sequence and the experiment itself resemble the population transfer experiment followed by a M3WM cycle as a probe of the induced enantiomeric excess as we performed earlier on cyclohexylmethanol (CHM)[12]. For a discussion of the results obtained in the current work, it is useful to compare it with the observations on CHM, where CHM is racemic at room temperature prior to the study, and transient chirality is

Table 1 | Pulse sequence parameters and the fit results of phase scans

Pulse parameters					S_{M6WM}		S_{c2}		S_{c3}	
#	v, MHz	τ, μs	$\Omega \cdot \tau$	Type	s_{M6WM}	A_{M6WM}, μV	s_{c2}	A_{c2}, μV	s_{c3}	A_{c3}, μV
1	9178	0.2	$\frac{\pi}{2}$	*c*	+1	14	–	–	0	10
2	4373	1.2	π	*b*	−1	14	+1	2	0	14
3	5293	1.6	π	*a*	−1	13	0	3	+1	14
4	9231	0.6	π	*c*	+1	14	–	–	0	11
5	3459	2.0	π	*b*	−1	13	–	–	0	7

"#" denotes the pulse number for which the phase is being scanned, v is the frequency of the pulse, τ is the pulse duration, and "type" shows the type of the rotational transition excited by the pulse, as well as the direction of the pulse polarization in the laboratory frame. The s are the dimensionless phase dependence coefficients, and the fitted signal amplitudes are denoted by A_{M6WM}, A_{c2}, and A_{c3}, where the subscripts indicate the source of the v_L signal. Details on the fitting procedures are in the Supplementary Information. Note that in scans #1, #4, and #5 the sum of S_{c2} and S_{c3} are fitted, and the corresponding results are shown in the S_{c3} columns.

stabilized in the supersonic jet expansion. The barrier between the enantiomers of CHM is high enough (~15 kJ/mol) to quench the tunneling interconversion of the enantiomers within the time scale of the experiment. Therefore, both the *R* and *S* forms of CHM are present in equal amounts in a gas jet and cannot be converted to each other, leading to $|ee| = 0$ as a starting condition. In the experiments on CHM, we first performed a population transfer for a set of rotational states, creating a non-zero $|ee|$ in two particular rotational states. This $|ee|$ was then probed by performing an additional M3WM experiment starting from these rotational states.

According to this analogy, in the present study with BA, the first three pulses of the M6WM sequence are analogous to the population transfer part of the experiment, which should induce a non-zero $|ee|$ in a specific rotational state. The last two pulses and the induced coherence for the listen transition act as a chiral probe of this enantiomeric enrichment. To elucidate this, one needs to calculate the $|ee|$ in the system in the rotational state $|1_{01}\rangle$ after three pulses starting, naturally, with a racemic sample. This quantity is given by the operator $\hat{ee}_{1_{01}} = |1^+_{01}\rangle\langle 1^-_{01}| + |1^-_{01}\rangle\langle 1^+_{01}|$. The explicit calculation (see Supplementary Information for details) shows that after the first three pulses, the resulting state $|\psi\rangle$ will be an oscillating chiral wavepacket, with an amplitude proportional to $|ee|$:

$$\langle\psi|\hat{ee}_{1_{01}}|\psi\rangle \propto \overbrace{\sin(\Omega_1\tau_1)\left(\prod_{k=2}^{3}\sin\left(\frac{\Omega_k\tau_k}{2}\right)\right)}^{\propto\,|ee|} \cdot \sin\left(2\pi\nu_{\pm}t + \sum_{k=1}^{3}s_k\varphi_k - \Phi'\right). \tag{4}$$

The frequency of the $R \leftrightarrow S$ interconversion is simply a tunneling frequency $\nu_{\pm} = (E_{1^-_{01}} - E_{1^+_{01}})/h = \epsilon_{\pm}/h$ (see Fig. 1). Due to the quantum tunneling, the created chiral wavepacket does not have a persistent chirality. However, the polarization induced by the M6WM experiment (Eq. (1)) is proportional to the total magnitude of the $|ee|$ induced by the first three pulses. The probed S_{M6WM} with an amplitude of 13–14 μV indicates that a non-zero $|ee|$ was created in the rotational state $|1_{01}\rangle$, and the M6WM approach allows us to measure the magnitude of the induced enantiomeric enrichment.

In conclusion, our experiment successfully steered a quantum racemic mixture of two interconvertible enantiomers off-equilibrium in the rotational state of interest by exploiting five microwave radiation pulses from three mutually orthogonal polarizations. This result demonstrates that transient enantiomeric excess can be induced in a quantum tunneling system with a suitable pulse sequence of resonant microwave fields. This provides an approach for manipulating molecular chirality in flexible molecules like BA.

Methods

Sample preparation

The commercial sample of benzyl alcohol (BA) was purchased from Sigma-Aldrich and used without further purification. Experiments were performed using a modified Fourier transform microwave (FTMW) spectrometer in Hamburg, as reported elsewhere[12], and a sketch is provided in Fig. 2. The commercially available sample of BA was placed in an internal sample reservoir close to the solenoid nozzle valve (Parker General Valve, Series 9) and maintained at 70 °C. The sample vapor was seeded by a neon buffer gas with a stagnation pressure of ~3 bar and supersonically expanded into the vacuum chamber via the pulsed valve operating at 6 Hz. The adiabatic expansion efficiently cooled the gas-phase sample to a T_{rot} of ~1–2 K. For each gas pulse, the molecular ensemble was polarized with a series of eight pulse sequences, and 40 μs of FID were recorded following each excitation and averaged on an oscilloscope. After Fourier transformation, the typical frequency resolution of the spectrum is about 25 kHz, giving a full-width at half maximum (FWHM) linewidth of about 60 kHz.

Optimal pulse conditions

To achieve the optimal condition of the proposed M6WM scheme for the population transfer, pulse #1 should be a $\pi/2$-pulse, while the other four pulses (#2 – #5) should be π-pulses. Therefore, nutation curves were performed for each excitation pulse to investigate the evolution of the signal amplitude over the pulse duration in a single-photon excitation experiment. Of them, the power of pulses #1 and #4, #2 and #5, and #3 was amplified to 40 W, 50 W and 3 W, respectively, using solid-state amplifiers (SSA), matching the setup in the subsequent M6WM experiment. The resulting nutation curves are shown in Supplementary Fig. 8, and the obtained optimal durations are summarized in Table 1.

M6WM experiments

To achieve a state-specific enantiomer enrichment, the proposed M6WM experiment was carried out. Using the results of the nutation curves, the five pulses with optimal durations were generated with a two-channel arbitrary waveform generator (AWG), where pulses #1, #3, and #4 are from channel 1 (CH1), and pulses #2 and #5 are from channel 2 (CH2), as illustrated in Fig. 3a. As the polarization direction of pulse #3 needs to be orthogonal to pulses #1 and #4, a single pole double throw (SPDT) pin-diode switch was utilized to feed the signals into the dedicated SSAs. After amplification, the microwave pulses were broadcast into the vacuum chamber to interact with the molecules from three orthogonal polarization directions via two dual-polarization horn antennae. In order to explore the phase dependence of the signal induced from the M6WM scheme, the phase of each signal in the pulse sequence was systematically changed in steps of 18°. The free induction decays (FIDs) of the molecular response were recorded and averaged in the time domain and Fourier transformed into the frequency domain after applying a Gaussian window function. Each phase scan was repeated five times, in which 20,000 FIDs were averaged for each phase point. More details can be found in the Supplementary Information.

Data availability

All the data that support the findings of this study are available within the main text and the Supplementary Information file, and also available from the corresponding author on request.

Code availability

The Python scripts used in this study are provided in the Supplementary Information.

References

1. Nguyen, L. A., He, H. & Pham-Huy, C. Chiral drugs: an overview. *Int. J. Biomed. Sci.* **2**, 85–100 (2006).
2. Beesley, T. E. & Scott, R. P. *Chiral chromatography* (John Wiley & Sons, 1999).
3. Gübitz, G. & Schmid, M. G. Recent progress in chiral separation principles in capillary electrophoresis. *Electrophoresis* **21**, 4112–4135 (2000).
4. Stephens, P. J., Devlin, F. J. & Pan, J. J. The determination of the absolute configurations of chiral molecules using vibrational circular dichroism (VCD) spectroscopy. *Chirality* **20**, 643–663 (2008).
5. Nafie, L. A. *Vibrational optical activity: principles and applications* (John Wiley & Sons, 2011).
6. Lux, C. et al. Circular dichroism in the photoelectron angular distributions of camphor and fenchone from multiphoton ionization with femtosecond laser pulses. *Angew. Chem. Int. Ed.* **51**, 5001–5005 (2012).
7. Garcia, G. A., Nahon, L., Daly, S. & Powis, I. Vibrationally induced inversion of photoelectron forward-backward asymmetry in chiral molecule photoionization by circularly polarized light. *Nat. Commun.* **4**, 2132 (2013).
8. Patterson, D., Schnell, M. & Doyle, J. M. Enantiomer-specific detection of chiral molecules via microwave spectroscopy. *Nature* **497**, 475–477 (2013).
9. Shubert, V. A., Schmitz, D., Patterson, D., Doyle, J. M. & Schnell, M. Identifying enantiomers in mixtures of chiral molecules with broadband microwave spectroscopy. *Angew. Chem. Int. Ed.* **53**, 1152–1155 (2014).
10. Eibenberger, S., Doyle, J. & Patterson, D. Enantiomer-specific state transfer of chiral molecules. *Phys. Rev. Lett.* **118**, 123002 (2017).
11. Pérez, C. et al. Coherent enantiomer-selective population enrichment using tailored microwave fields. *Angew. Chem. Int. Ed.* **56**, 12512–12517 (2017).
12. Pérez, C., Steber, A. L., Krin, A. & Schnell, M. State-specific enrichment of chiral conformers with microwave spectroscopy. *J. Phys. Chem. Lett.* **9**, 4539–4543 (2018).
13. Lee, J. et al. Quantitative study of enantiomer-specific state transfer. *Phys. Rev. Lett.* **128**, 173001 (2022).
14. Quack, M. & Seyfang, G. Chapter 7 - Atomic and molecular tunneling processes in chemistry. In Marquardt, R. & Quack, M. (eds.) *Molecular spectroscopy and quantum dynamics*, 231–282, https://doi.org/10.1016/B978-0-12-817234-6.00012-X (Elsevier, 2021).
15. Ordonez, A. F. & Smirnova, O. Propensity rules in photoelectron circular dichroism in chiral molecules. I. Chiral hydrogen. *Phys. Rev. A* **99**, 043416 (2019).
16. Bychkov, S. S., Grishanin, B. A. & Zadkov, V. N. Laser synthesis of chiral molecules in isotropic racemic media. *J. Exp. Theoretical Phys.* **93**, 24–32 (2001).
17. Bychkov, S. S., Grishanin, B. A., Zadkov, V. N. & Takahashi, H. Laser coherent control of molecular chiral states via entanglement of the rotational and torsional degrees of freedom. *J. Raman Spectrosc.* **33**, 962–973 (2002).
18. Zhdanov, D. V. & Zadkov, V. N. Absolute asymmetric synthesis from an isotropic racemic mixture of chiral molecules with the help of their laser orientation-dependent selection. *J. Chem. Phys.* **127**, 244312 (2007).
19. Hirota, E. Triple resonance for a three-level system of a chiral molecule. *Proc. Jpn Acad. Ser. B* **88**, 120–128 (2012).
20. Hirota, E. Molecular chirality: a new approach from a dynamical point of view. *Proc. Jpn Acad. Ser. B* **93**, 841–849 (2017).
21. Utzat, K. A., Bohn, R. K., Montgomery, J. A., Michels, H. H. & Caminati, W. Rotational spectrum, tunneling motions, and potential barriers of benzyl alcohol. *J. Phys. Chem. A* **114**, 6913–6916 (2010).
22. Domingos, S. R., Pérez, C. & Schnell, M. Sensing chirality with rotational spectroscopy. *Ann. Rev. Phys. Chem.* **69**, 499–519 (2018).
23. Grabow, J.-U. Fourier transform microwave spectroscopy: Handedness caught by rotational coherence. *Angew. Chem. Int. Ed.* **52**, 11698–11700 (2013).
24. Koumarianou, G., Wang, I., Satterthwaite, L. & Patterson, D. Assignment-free chirality detection in unknown samples via microwave three-wave mixing. *Comm. Chem.* **5**, 31 (2022).
25. Rabi, I. I. Space quantization in a gyrating magnetic field. *Phys. Rev.* **51**, 652–654 (1937).
26. Landau, L. D. & Lifshitz, E. M. *Quantum mechanics: non-relativistic theory*, vol. 3 (Elsevier, 2013).
27. Shubert, V. A. et al. Rotational spectroscopy and three-wave mixing of 4-carvomenthenol: a technical guide to measuring chirality in the microwave regime. *J. Chem. Phys.* **142**, 214201 (2015).
28. Leibscher, M., Giesen, T. F. & Koch, C. P. Principles of enantio-selective excitation in three-wave mixing spectroscopy of chiral molecules. *J. Chem. Phys.* **151**, 014302 (2019).
29. Leibscher, M. et al. Full quantum control of enantiomer-selective state transfer in chiral molecules despite degeneracy. *Comm. Phys.* **5**, 110 (2022).
30. Leibscher, M., Kalveram, J. & Koch, C. P. Rational pulse design for enantiomer-selective microwave three-wave mixing. *Symmetry* **14**, https://doi.org/10.3390/sym14050871 (2022).

Acknowledgements

This work has been funded by the Deutsche Forschungsgemeinschaft (DFG, German Research Foundation) - Projektnummer 328961117 - SFB 1319 ELCH. We acknowledge scientific discussions with J.-U. Grabow, T. Giesen, C. Koch, and M. Leibscher. C.P. acknowledges funding from the PID2021-125015NB-I00 grant.

Author contributions

W.S. and D.S.T. contributed equally to this work. C.P. and M.S conceived the project. W.S, H.S, A.L.S, and C.P. performed the experiment. W.S and D.S.T analyzed the data and wrote the paper. All authors contributed to the discussions of the results, and reviewed the manuscript.

Funding

Open Access funding enabled and organized by Projekt DEAL.

Competing interests

The authors declare no competing interests.

Additional information

Supplementary information The online version contains supplementary material available at https://doi.org/10.1038/s41467-023-36653-3.

Correspondence and requests for materials should be addressed to Melanie Schnell.

Peer review information *Nature Communications* thanks the anonymous reviewer(s) for their contribution to the peer review of this work.

8.1 Summary and outlook

The article provides a demonstration of the M6WM approach for inducing transient chirality in a molecular quantum racemic mixture. M6WM is a non-linear, coherent, and resonant technique used for performing enantio-selective population transfer in a set of selected rotational states. The process entails five phase-controlled microwave pulses, with the initial three pulses creating a chiral wavepacket in a specific rotational state and the following two pulses inducing a polarisation at the listen transition, the magnitude of which is proportional to the created *ee*.

During the experiment, the phase of each microwave pulse in the scheme was scanned to monitor the signal intensity of the listen transition. In each phase scan, the signal intensity at the listen transition displayed a pulse-phase dependence, which is the result of signal interference. The observed interference pattern was fitted independently as the sum of three individual interference signals: one from the M6WM cycle and two from direct excitation from two amplifiers used in the experiment. The fitting procedures provided information about the amplitude and phase of the listen transition, which is summarised in Table 1 and presented in Fig. 3b of the manuscript. The M6WM signal at the listen transition exhibited an amplitude of 13-14 µV in the five scans.

The excitation of the first three pulses generates an *ee* in the rotational state $|1_{01}^{-}\rangle$. Due to quantum tunneling, the chiral wavepacket with *ee* oscillates and does not have persistent handedness. However, the polarisation induced by the M6WM experiment is proportional to the *ee* induced by the excitation of the first three pulses, as expressed in eq. 2.95 of Chapter 2. Thus, the last two microwave pulses of the M6WM scheme and the induced coherence for the listen transition act as a chiral probe for the enantiomeric enrichment. The probed M6WM signal with an amplitude of 13-14 µV indicated that a non-zero *ee* was created in the rotational state $|1_{01}^{-}\rangle$ of BA. This outcome illustrates that a transient *ee* can be induced in a quantum tunneling system with a suitable pulse sequence of resonant microwave fields. This study successfully demonstrated how molecular flexibility can be exploited to steer the handedness of chiral molecules.

The approach can be extended to other molecules, such as benzyl mercaptan,[168] to explore different tunneling dynamics and timescales. This involves accounting for various systematic effects, such as reducing the interference with the direct excitation pulses in this level scheme. Future experiments could involve real-time measurements of tunneling rates in transiently chiral molecules with slower tunneling rates. By introducing a time delay between the first (pulses #1-#3) and second (pulses #4-#5) set of microwave pulses of the M6WM approach used with BA, tunneling rates can be determined in experiments and thus dynamical information for chiral molecules can be accessed. This information will contribute to a better characterisation of chiral molecules and prove useful for high-precision experiments aiming at determining the energy difference between enantiomers due to PV.

Chapter 9

Summary and outlook

The stability, reactivity, and physicochemical properties of a molecule are closely intertwined with its structural characteristics, particularly the conformations it can adopt. The functionality of biomolecules is governed not only by conformational flexibility but also by intra- and intermolecular interactions. Hence, knowledge of molecular structure, their intramolecular dynamics, and chirality becomes essential for developing an understanding of their reactivity and functionalities. MW spectroscopy is a highly sensitive technique for chemical and chiral analysis, allowing the study of the structure, internal dynamics and chirality of molecules (Fig. 1.1).

The primary focus of this thesis was to study flexible chiral molecules using the high-resolution CP-FTMW spectroscopy. The measurement principle was presented and implemented on various types of molecular systems, showcasing its inherent potential in determining molecular structures, as well as in enantiomer differentiation and separation. In the first part of this thesis, the conformational analysis of various molecules with increasing structural flexibility was explored using broadband rotational spectroscopy. Different derivatives of [2,2]-paracyclophane were characterised in Chapter 4, followed by an examination of the conformational panorama of a chiral carboxylic acid, α-methoxy-phenylacetic acid (Chapter 5), and 6-amyl-α-pyrone (Chapter 6), a potential biomass candidate.

Even though there is very limited conformational flexibility in monosubstituted [2,2]-paracyclophanes, they remain an intriguing class of molecules due to their unique transannular interactions arising from the co-facial stacking of benzene rings bridged by an ethylene chain. [2,2]-Paracyclophane could not be characterised, due to its lack of a permanent electric dipole-moment component. Therefore, monosubstituted derivatives were investigated, including aldehyde-, ketone-, hydroxy-, and carboxylic acid-substituted [2,2]-paracyclophanes. Rotational spectra were obtained for all four of them, with some experimental challenges in the case of carboxylic acid-substituted [2,2]-paracyclophane. The analysed experimental rotational spectra, along with their experimentally fitted rotational parameters, are provided in the section 4.2 of Chapter 4.

Two conformers in the case of aldehyde-substituted and only the most stable conformations of ketone-, hydroxy-, and carboxylic acid-substituted [2,2]-paracyclophanes were observed in the experimental spectra. The hydroxy-substituted [2,2]-paracyclophane exhibited more flexibility than the other derivatives due to the presence of the hydroxy group at the stereogenic center (Fig. 4.7). Quantum-chemical calculations predicted the three rotamers (gp, gm, and a) of hydroxy-substituted [2,2]-paracyclophane below 5 kJ/mol (as indicated in Table 4.3), but only the most stable conformation, pcp-(tBu)-CHOH-gm, was detected in the spectrum (Fig. 4.8). This observation could be attributed to the cooling behaviour in the supersonic expansion and the low interconversion barriers for the pcp-(tBu)-CHOH-a and pcp-(tBu)-CHOH-gp rotamers to the observed gm conformation of hydroxy-substituted [2,2]-paracyclophane (Fig. 4.9). The accurate experimental structure of the aldehyde-substituted [2,2]-paracyclophane was determined, as depicted in Fig. 4.5, due to the observation of all singly substituted ^{13}C isotopologues of the most stable conformation (pcp-CHO-1) in the rotational spectrum. The determined gas-phase structure of the [2,2]-paracyclophane moiety from aldehyde-substituted [2,2]-paracyclophane was in good agreement with the solid-state structure obtained from X-ray crystallography studies on [2,2]-paracyclophane (comparison is presented in Table 4.5).[209]

The NCI analysis of the four derivatives revealed the presence of doughnut-shaped transannular interactions between the stacked benzene rings of attractive nature near the aromatic carbons and the repulsive nature close to the bridging ethylene carbons. Additionally, CH$\cdots$O interactions were observed between the oxygen atom of the substituted functional group and the ethylene hydrogen atoms, as illustrated in Fig. 4.11.

In the next chapter, a chiral carboxylic acid, AMPA, was explored with CP-FTMW spectroscopy. Compared to the singly substituted [2,2]-paracylophanes, AMPA exhibits higher flexibility. The rich conformational space of AMPA arises from the possible configurations of the methoxy and carboxylic acid groups present at the chiral center highlighted in Fig. 1b of the manuscript presented in Chapter 5. The conformers are related to each other via the parallel-perpendicular orientation of the methoxy group to the plane of the phenyl ring, and *cis-trans* configurations of the hydroxyl group with respect to the methoxy group. Furthermore, the rotation of the hydroxyl group either towards the methoxy group or away from it gives rise to in-out configurations and extends the conformational space leading to eight different structures of AMPA. Among the six predicted low-energy structures, five stable structures were identified and characterised in the experiments. The third-lowest energy conformer (*cis*-in-par) was not observed in the experiments. The reason for its absence could be its conversion to a lower-energy structure (*cis*-in-perp) in the course of the supersonic expansion using Ne as carrier gas (Fig. 4 of the manuscript). For the two most stable conformers, line splittings due to methyl internal rotation were observed. The experimental barrier heights for the *cis*-in-perp and *trans*-out-par were determined to be 8.263(9) kJ/mol and 7.552(2) kJ/mol, respectively. The higher barrier for the *cis*-in-perp conformer, compared to the *trans*-out-par conformer, is due to the $\mathrm{CH}\cdots\pi$ interactions between the methyl group and the phenyl ring in the *cis*-in-perp conformation. These intramolecular interactions do not only influence the internal dynamics of the molecule but also govern the conformational landscape of AMPA. The higher stability of the *cis*-in-perp and *cis*-in-par conformers, in comparison to the other structures, can be attributed to the presence of a moderate intramolecular hydrogen bond between the hydroxyl group and the oxygen atom of the methoxy group, as illustrated in Fig. 2 of the manuscript attached in Chapter 5.

In Chapter 6, 6PP was examined, which has a higher degree of flexibility in contrast to the [2,2]-paracyclophane derivatives and AMPA. The amyl chain attached to the pyrone ring increases the flexibility and results in a more complex conformational space. Quantum-chemical calculations predicted nineteen conformers below 6 kJ/mol (Fig. 6.3, Fig. 1 of appendix), only five conformers have been identified in the experimental rotational spectrum so far, as shown in Fig 6.4. The rotational spectrum and the experimentally obtained rotational constants of the five observed conformers of 6PP are reported in Fig. 6.4 and Table 6.1. Out of the six low-energy conformers predicted by calculations (Fig. 6.3), the fourth lowest-energy conformer, *tTt-B* could not be identified in the experiments. The absence of *tTt-B* conformer could be attributed to relaxation in the supersonic expansion with a Ne carrier gas and a low interconversion barrier of *tTt-B* conformer to the observed rotamer, *tTt-A*, as depicted in Fig. 6.6. A comparison of the calculated and experimental rotational constants showed a good match (Table 6.1). Furthermore, the calculations predict that for the four lowest energy conformers of 6PP, the *trans* configurations for the $\angle\alpha$, $\angle\beta$ dihedral angles of the amyl chain are preferred.

Future work related to the conformational flexibility of molecules studied in this thesis will focus on analysing solute-solvent interactions. Understanding these interactions holds crucial importance in both biology and physical organic chemistry, as solute-solvent interactions play a central role in controlling solubility, molecular structure, and functioning of the molecules in solvent environments. As discussed in the last sections of Chapter 5 and 6, the rotational spectra for the complexes of AMPA and 6PP have been recorded. Preliminary analysis of AMPA complexes from quantum-chemical calculations predicts the different conformational preference during complexation with various solvent molecules. In the case of 6PP, distinct types of interactions arise upon complexation with both protic and nonpolar solvent molecules, suggesting their potential role in the CTH reaction of 6PP to produce DDL. These gas phase investigations of complexes of AMPA and 6PP will aid in understanding the influence of solvent molecules on the conformational space, intramolecular interactions and internal dynamics of this and similar kinds of molecules.

The second part of this thesis focused on controlling and manipulating chiral molecules using MW spectroscopy. While broadband MW spectroscopy is effective at identifying the conformers and isotopologues, it cannot differentiate between enantiomers as they share identical moments of inertia and thus have identical rotational spectral features with only small differences arising from PV effects. In order to identify enantiomers and perform chiral analysis using MW spectroscopy, a M3WM approach was proposed by Hirota[59] and experimentally demonstrated with the buffer-gas Fourier transform microwave spectrometer by Patterson *et al.*[60]. M3WM is an electric dipole allowed method, where two rotational transitions of a triad are excited, which results in a chiral molecular response at the listen transition closing the triad. M3WM has been extended to achieve coherent enantiomer-selective population transfer by applying a transfer pulse in the direction of the listen transition and resonant to its frequency. Depending on the phase of the transfer pulse, one enantiomer is selectively promoted to a particular rotational state while the population of the opposite enantiomer is depleted in this state but enhanced in the connecting state of the corresponding transition. In this thesis framework, the objective was to enhance the efficiency of enantiomer-selective population transfer from previously reported results.

The two factors hampering the efficiency of enantiomer-selective population transfer are the thermal population and the spatial degeneracy characterized by M_J quantum number. Tailored microwave pulses (RAP-pulse and a π-pulse) were used to reduce the thermal population in energetically higher states. Initiating the population transfer from the ground-state enabled an enantiomeric excess of 13% in the $|1_{01}\rangle$ rotational state of TFO (Fig. 6(a) of the article provided in Chapter 7), which was twice of that reported for carvone (about 6% in $|2_{02}\rangle$ rotational state). Applying a preceding π or a RAP-pulse before the population transfer process further improved the induced enantiomeric excess to about 40%, a threefold enhancement compared to without any preceeding pulse. Both tailored microwave pulses exhibited similar effects on the efficiency of the enantiomer-selective population transfer. The experiments demonstrated a higher level of control that could be achieved over chiral molecules using high-resolution MW spectroscopy and gas-phase samples.

M3WM and its extended approach, as employed in the previous chapter, are applicable for sensing and controlling chirality in permanently and transiently chiral molecules separable under the cold conditions of the supersonic jet. However, for flexible chiral molecules such as BA with low enantiomer interconversion barriers, even at cryogenic temperatures, racemisation occurs due to quantum tunneling, forming a quantum racemate that cannot be separated via conventional chemical methods. In such class of chiral molecules, M3WM and related population transfer schemes are inapplicable, as a closed three-cycle loop cannot be formed due to interstate rotational transitions that do not satisfy symmetry conditions. Therefore, a more complex M6WM scheme is developed, which is detailed in the subsequent Chapter 8.

M6WM is a non-linear, coherent, and resonant approach to generate a transiently chiral ensemble of molecules at a specific rotational level of interest. The M6WM technique involves the excitation of five resonant microwave pulses to induce a chiral response in the form of a listen transition in a suitable system of six rotational levels. Experimental demonstration of the M6WM scheme on BA showcased a probed M6WM signal of 13-14 µV, indicating a non-zero enantiomeric excess created in the $|1_{01}\rangle$ rotational level of BA. These experimental results showcase how molecular flexibility can be exploited to steer the handedness of chiral molecules. The future extension of the M6WM approach could involve real-time measurement of the tunneling rates in transiently chiral molecules with slow tunneling motions, providing access to dynamical information about chiral molecules.

The demonstrated quantum-controlled chiral separation through the extended M3WM and M6WM approaches highlights the potential of MW spectroscopy in gaining control over molecular degrees of freedom through cooling techniques and advanced pulse sequences. The high resolution and precision obtained with these pulse schemes bring us a step closer for performing precision spectroscopy experiments aimed at determining the frequency difference between enantiomers, and addressing fundamental questions about the origin of homochirality of life.

Appendix

A [2,2]-Paracyclophane derivatives

Table 1: Experimentally determined rotational parameters for the ^{13}C isototpologues of pcp-CHO-1 conformer, according to the labelling of the Fig. 4.5.

Parameters	pcp-CHO-1	^{13}C$_1$	^{13}C$_2$	^{13}C$_3$	^{13}C$_4$
A/MHz[1]	703.45372(19)	703.1271(53)	702.2460(28)	700.4559(13)	698.4479(13)
B/MHz	466.28972(11)	461.89412(26)	464.37789(14)	464.94900(24)	466.03695(19)
C/MHz	407.45446(12)	404.18926(24)	405.87085(12)	405.56269(17)	405.86017(11)
Δ_J/kHz	0.0119(10)	[0.011857288]	[0.011857288]	[0.011857288]	[0.011857288]
δ_{JK}/kHz	0.0215(31)	[0.021476957]	[0.021476957]	[0.021476957]	[0.021476957]
Δ_K/kHz	-	-	-	-	-
δ_J/kHz	-	-	-	-	-
δ_K/kHz	[0.0762(48)]	[0.07618327]	0.07618327]	[0.07618327]	[0.07618327]
N [2]	196	28	34	34	30
σ/kHz	6.8	6.2	3.7	6.6	6.2

[1] A, B, and C are the rotational constants and Δ_J, Δ_{JK}, Δ_K, δ_J, and δ_K are the quartic centrifugal constants. The errors given here for the measured values are the standard errors. [2] N is the number of lines included in the fit and σ is the standard deviation of the fit.

Parameters	^{13}C$_5$	^{13}C$_6$	^{13}C$_7$	^{13}C$_8$	^{13}C$_9$	^{13}C$_{10}$
A/MHz	700.1148(43)	699.6705(39)	699.99434(26)	700.40566(37)	701.7581(35)	702.04362(63)
B/MHz	466.11190(22)	465.35456(20)	464.60305(18)	464.44535(23)	463.39006(17)	465.12890(26)
C/MHz	406.22206(19)	406.86541(17)	406.84227(12)	405.06452(14)	405.61640(16)	406.86457(18)
Δ_J/kHz	[0.011857288]	[0.011857288]	[0.011857288]	[0.011857288]	[0.011857288]	[0.011857288]
Δ_{JK}/kHz	[0.021476957]	[0.021476957]	[0.021476957]	[0.021476957]	[0.021476957]	[0.021476957]
Δ_K/kHz	-	-	-	-	-	-
δ_J/kHz	-	-	-	-	-	-
δ_K/kHz	[0.07618327]	[0.07618327]	[0.07618327]	[0.07618327]	[0.07618327]	[0.07618327]
N	39	35	38	33	32	28
σ/kHz	6.0	5.0	5.6	5.6	6.8	7.2

Parameters	13C$_{11}$	^{13}C$_{12}$	^{13}C$_{13}$	^{13}C$_{14}$	^{13}C$_{15}$	^{13}C$_{16}$	^{13}C$_{17}$
A/MHz	699.1699(51)	699.5359(18)	700.8990(41)	700.0418(49)	701.7784(44)	700.10905(78)	701.1578(49)
B/MHz	464.52792(25)	464.59228(18)	465.48488(21)	466.21893(24)	465.80423(22)	463.86548(24)	463.15694(25)
C/MHz	407.33321(22)	406.70234(11)	406.09491(18)	406.35921(21)	406.52375(19)	405.24796(16)	404.29526(21)
Δ_J/kHz	[0.011857288]	[0.011857288]	[0.011857288]	[0.011857288]	[0.011857288]	[0.011857288]	[0.011857288]
Δ_{JK}/kHz	[0.021476957]	[0.021476957]	[0.021476957]	[0.021476957]	[0.021476957]	[0.021476957]	[0.021476957]
Δ_K/kHz	-	-	-	-	-	-	-
δ_J/kHz	-	-	-	-	-	-	-
δ_K/kHz	[0.07618327]	[0.07618327]	[0.07618327]	[0.07618327]	[0.07618327]	[0.07618327]	[0.07618327]
N	34	31	37	33	30	33	29
σ/kHz	6.4	5.9	5.6	5.9	5.3	6.8	6.0

Table 2: Experimentally determined bond distances of conformer pcp-CHO-1 determined using effective structure r_0-, and substitution structure r_s-method in comparison with the equilibrium r_e-values obtained from quantum-chemical calculations at B3LYP-D3(BJ)/def2-TZVP level of theory.

Bond distance	r_0(Å)	r_s(Å)	r_e(Å)
r(O1-C2)	1.214(92)	-	1.2
r(C3-C2)	1.482(54)	1.568(28)	1.5
r(C3-C4)	1.38(14)	1.219(33)	1.4
r(C3-C8)	1.418(58)	1.317(30)	1.4
r(C4-C5)	1.40(13)	1.607(30)	1.4
r(C5-C6)	1.418(66)	1.3924(43)	1.4
r(C7-C6)	1.41(14)	1.3876(94)	1.4
r(C7-C8)	1.39(12)	1.3980(77)	1.4
r(C8-C9)	1.511(45)	1.5081(33)	1.5
r(C10-C9)	1.584(47)	1.5837(48)	1.6
r(C11-C10)	1.516(69)	1.5112(68)	1.5
r(C12-C11)	1.400(85)	1.365(11)	1.4
r(C13-C12)	1.391(76)	1.4073(38)	1.4
r(C14-C13)	1.406(61)	1.4085(36)	1.4
r(C15-C14)	1.395(53)	1.3961(23)	1.4
r(C16-C15)	1.38(14)	1.3653(82)	1.4
r(C16-C11)	1.406(72)	1.432(14)	1.4
r(C14-C17)	1.518(42)	1.5611(98)	1.5
r(C18-C17)	1.615(56)	1.587(17)	1.6
r(C18-C5)	1.493(49)	1.4603(88)	1.5
r(C7-C12)	3.118(58)	3.1100(39)	3.1
r(C3-C16)	3.099(58)	3.151(18)	3.1
r(C6-C13)	3.111(36)	3.1085(21)	3.1
r(C4-C15)	3.105(59)	3.172(13)	3.1

Table 3: Experimentally determined bond angles of conformer pcp-CHO-1 determined using effective structure r_0-, and substitution structure r_s-method in comparison with the equilibrium r_e-values obtained from quantum-chemical calculations at B3LYP-D3(BJ)/def2-TZVP level of theory.

Bond angles	r_0(°)	r_s(°)	r_e(°)
∠(O1-C2-C3)	126.37(4)	-	126.9
∠(C2-C3-C4)	115.20(47)	103.07(24)	116.0
∠(C2-C3-C8	123.58(32)	124.11(15)	123.8
∠(C3-C4-C5)	121.69(47)	115.82(14)	121.9
∠(C4 –C5-C6)	116.05(49)	112.08(71)	116.2
∠(C5-C6-C7)	120.08(33)	120.41(18)	120.7
∠(C6 –C7-C8)	121.42(30)	121.69(18)	121.5
∠(C8-C3-C4)	120.70(47)	131.34(19)	119.7
∠(C3-C8-C7)	116.28(45)	113.87(68)	116.2
∠(C4-C5-C18)	123.58(66)	131.65(13)	120.9
∠(C5-C18-C17)	112.60(19)	113.01(26)	112.9
∠(C9-C8-C3)	123.19(31)	125.55(77)	123.6
∠(C7-C8-C9)	119.30(38)	119.84(26)	118.9
∠(C8-C9-C10)	112.42(21)	112.15(13)	112.4
∠(C9-C10-C11)	112.57(21)	111.82(35)	112.5
∠(C10-C11-C12)	120.59(48)	121.92(11)	121.4
∠(C10-C11-C16)	121.37(70)	120.33(76)	120.2
∠(C11-C12-C13)	120.45(35)	120.62(42)	120.5
∠(C11-C16-C15)	121.44(35)	121.43(50)	120.9
∠(C12-C13-C14)	120.86(31)	120.48(19)	120.9
∠(C12-C11-C16)	116.55(76)	116.58(56)	117.0
∠(C13-C14-C15)	117.26(25)	117.09(12)	117.0
∠(C13-C14-C17)	120.36(76)	119.41(25)	120.4
∠(C14-C15-C16)	120.34(30)	120.34(15)	120.5

Bond angles	r_0(°)	r_s(°)	r_e(°)
∠(C14-C17-C18)	112.75(18)	113.56(23)	113.1
∠(C6-C5-C18)	119.28(41)	115.44(11)	121.7
∠(C15-C14-C17)	120.99(36)	121.65(31)	121.2

Table 4: Experimentally determined dihedral angles of conformer pcp-CHO-1 determined using effective structure r_0-, and substitution structure r_s-method in comparison with the equilibrium r_e-values obtained from quantum-chemical calculations at B3LYP-D3(BJ)/def2-TZVP level of theory.

Dihedral angles	r_0(°)	r_s(°)	r_e(°)
∠(O1 -C2 -C3 -C4)	165.71(53)	-	126.9
∠(O1 -C2 -C3 -C8)	-5.99(67)	-	-5.9
∠(C2 -C3 -C4 -C5)	-171.42(35)	-169.42(43)	-171.4
∠(C2 -C3 -C8 -C7)	-173.33(44)	-176.23(11)	173.5
∠(C2 -C3 -C8 -C9)	19.43(52)	13.74 (19)	19.4
∠(C3 -C4 -C5 -C6)	-15.68(54)	-15.18(12)	-15.7
∠(C3 -C4 -C5 -C18)	152.22(41)	153.67(12)	151.7
∠(C3 -C8 -C7 -C6)	-16.00(70)	-18.25(99)	-16.0
∠(C3 -C8 -C9 -C10)	67.57(41)	70.10(89)	68.0
∠(C4 -C5 -C6 -C7)	14.95(47)	15.50(30)	15.0
∠(C4 -C5 -C18-C17)	-91.45(43)	-85.52(14)	92.2
∠(C5 -C6 -C7 -C8)	0.88(68)	0.47(48)	0.9
∠(C5 -C18-C17-C14)	11.17(65)	4.22(21)	12.6
∠(C6 -C7 -C8 -C9)	151.76(37)	152.40(25)	151.8
∠(C7 -C8 -C3 -C4)	15.41(62)	20.10(26)	15.2
∠(C7 -C8 -C9 -C10)	-99.30(52)	-99.38(37)	-98.8
∠(C8 -C9 -C10-C11)	19.38(42)	20.45(63)	19.4
∠(C9 -C10-C11-C12)	68.73(29)	68.96(30)	69.1
∠(C9 -C10-C11-C16)	-96.83(44)	-98.30(73)	-96.7
∠(C10-C11-C12-C13)	-151.81(27)	-152.04(20)	-151.8
∠(C10-C11-C16-C15)	151.72(47)	152.17(44)	152.3
∠(C11-C12-C13-C14)	-0.54(46)	-1.18(49)	-0.5
∠(C11-C16-C15-C14)	0.24(58)	0.69(40)	-0.2
∠(C12-C13-C14-C17)	152.94(29)	150.82(45)	152.9

Dihedral angles	r_0(°)	r_s(°)	r_e(°)
∠(C12-C11-C16-C15)	-14.39(48)	-15.75(57)	-14.1
∠(C13-C14-C17-C18)	-92.09(42)	-87.12(12)	-92.1
∠(C15-C14-C17-C18)	74.09(51)	76.95(11)	74.0
∠(C16-C15-C14-C17)	-152.75(37)	-150.42(42)	-152.5
∠(C13-C12-C11-C16)	14.42(39)	15.67(63)	14.4
∠(C9-C8-C3-C4)	-151.83(37)	-149.93(18)	-152.0
∠(C5-C4-C3-C8)	0.53(62)	-3.26(28)	0.6

Table 5: Dihedral angles obtained from r_0 structure that were used to calculate the deviation of four edge carbon atoms (C5, C8, C11, and C14) from the benzene ring.

Dihedral angle	$r_0(^\circ)$	Deviation ($r_0{}^\circ$)	$r_e(^\circ)$	Deviation($r_e{}^\circ$)
∠(C3-C4-C6-C8)	4.43(21)	4.04	4.41	4.9
∠(C3-C4-C6-C7)	-0.39(35)	-	0.46	-
∠(C7-C6-C3-C5)	-172.52(35)	7.48	-172.63	7.4
∠(C3-C4-C7-C5)	171.83(34)	8.17	171.84	8.2
∠(C7-C6-C4-C8)	-4.83(26)	-4.44	-4.87	-5.3
∠(C16-C15-C13-C11)	-4.19(21)	-4.04	-4.05	-3.7
∠(C16-C15-C13-C12)	0.15(2.7)	-	0.32	-
∠(C12-C13-C16-C14)	173.14(31)	6.86	173.22	6.8
∠(C16-C15-C12-C14)	-172.86(35)	7.14	-172.66	7.3
∠(C12-C13-C15-C11)	4.35(1.6)	4.2	4.37	4.1

B 6-amyl-α-pyrone

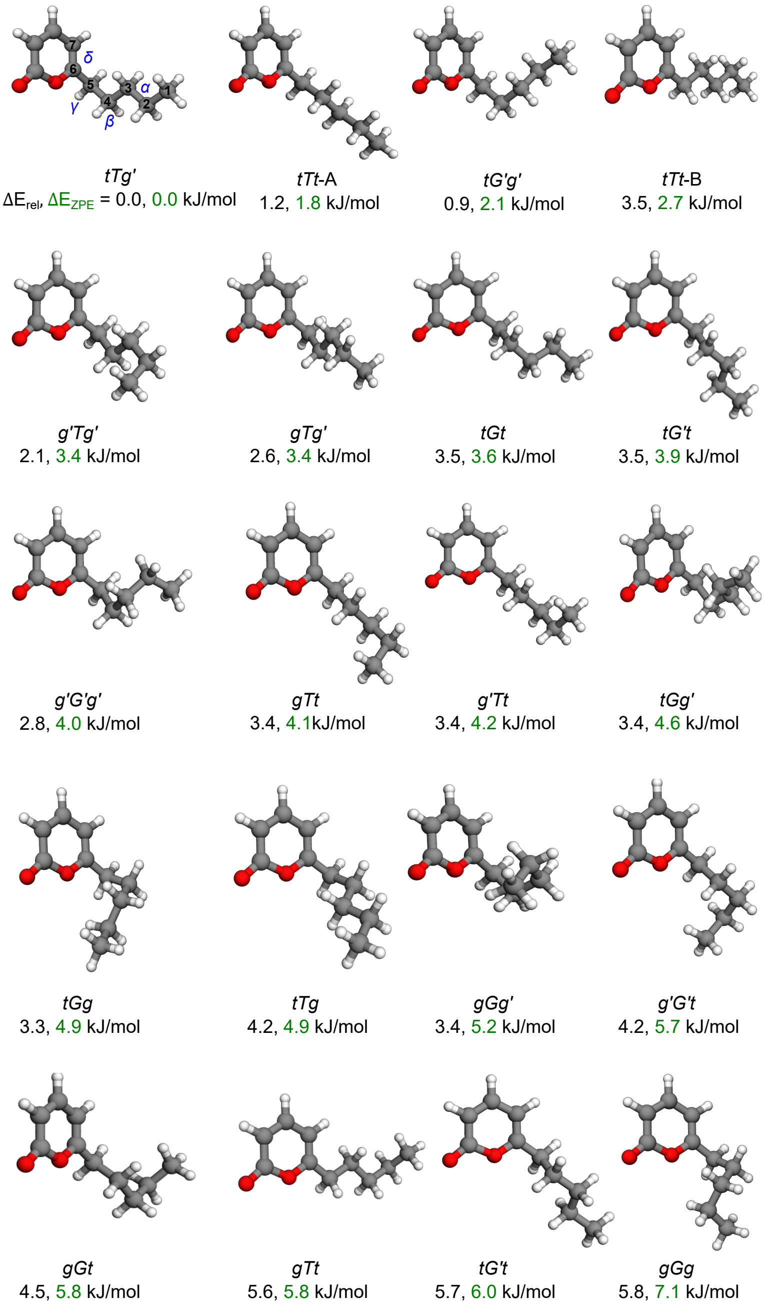

Figure 1: Optimised geometries of nineteen conformers within threshold energy of 6 kJ/mol obtained at the B3LYP-D3(BJ) /def2-TZVP level of theory.

Table 6: Relative energies and computed rotational parameters of twelve low energy conformers of 6-amyl-α-pyrone (6PP) obtained at the B3LYP-D3(BJ)/def2-TZVP level of theory. ΔE_{rel}, ΔE_{ZPE} are the relative energies without and with vibrational zero-point correction, respectively. ΔE_{rel-CC}, ΔE_{ZPE-CC} are single-point relative energies at the DLPNO-CCSD/aug-cc-pVTZ level of theory without and with the vibrational zero-point energy term from the B3LYP-D3(BJ)/def2-TZVP level of theory

Rotational parameters	*tTg'*	*tTt*-A	*tG'g'*	*tTt*-B	*g'Tg'*	*gTg'*	*tGt*	*tG't*	*g'G'g'*	*gTt*	*g'Tt*	*tGg'*
A/MHz	1449.3	2239.8	1563.2	3075.3	1429.3	1731.3	2488.1	2197.2	1905.6	1827.7	1898.8	1245.8
B/MHz	461.6	350.5	511.6	313.4	525.8	449.7	360.6	377.7	491.1	408.6	385.7	618.0
C/MHz	447.3	316.8	466.9	286.9	461.3	416.7	324.3	337.0	445.3	353.5	356.6	575.2
μ_a/D	2.0	-1.7	-3.3	-3.9	1.4	1.8	-2.6	1.6	3.2	-1.3	1.9	-2.0
μ_b /D	3.9	-4.4	2.6	-3.5	4.3	-4.3	-4.1	-4.5	3.5	4.5	-4.3	-1.7
μ_c/D	1.9	0.4	2.3	0.0	1.4	-0.7	-0.2	-0.1	-0.9	-0.7	0.2	3.8
ΔE_{rel}/kJmol^{-1}	0.0	1.2	0.9	3.5	2.1	2.6	3.5	3.5	2.8	3.4	3.4	3.4
ΔE_{rel-CC} /kJmol^{-1}	0.0	2.1	0.8	3.7	2.2	2.7	4.0	4.3	2.5	4.1	4.2	3.6
ΔE_{ZPE}(kJ/mol)	0.0	1.8	2.1	2.7	3.4	3.4	3.6	3.9	4.0	4.1	4.2	4.6
ΔE_{ZPE-CC}(kJ/mol)	0.0	2.7	1.9	2.9	3.6	3.5	4.1	4.7	3.7	4.8	5.0	4.8

Table 7: Experimentally determined rotational parameters for the ^{13}C isotopologues of most stable conformer of 6PP, *tTg'*, according to the labelling provided in Fig. 6.2

Rotational parameters	Parent	$^{13}C_1$	$^{13}C_2$	$^{13}C_3$
A/MHz[a]	1435.16335(23)	1424.85365(71)	1433.27175(31)	1434.88818(33)
B/MHz	468.097834(76)	460.10119(18)	462.882008(88)	465.86064(12)
C/MHz	451.062150(74)	443.84722(24)	446.03454(12)	448.96008(13)
Δ_J/kHz	0.16025(25)	[0.160279105]	[0.160279105]	[0.160279105]
Δ_{JK}/kHz	-0.5548(14)	[-0.554822339]	[-0.554822339]	[-0.554822339]
Δ_K/kHz	1.8845(74)	[1.866904945]	[1.866904945]	[1.866904945]
δ_J/kHz	0.02928(11)	[-0.029264238]	[0.029264238]	[0.029264238]
δ_k/kHz	1.348(12)	[1.344064074]	[1.344064074]	[1.344064074]
N[b]	314	30	39	46
σ/kHz	6.5	6.2	5.2	5.9

[a] A, B, and C are the rotational constants and Δ_J, Δ_{JK}, Δ_K, δ_J, and δ_K are the quartic centrifugal constants. The errors given here for the measured values are the standard errors.

[b] N is the number of lines included in the fit and σ is the standard deviation of the fit.

$^{13}C_4$	$^{13}C_5$	$^{13}C_6$	$^{1}3C_7$	$^{13}C_8$	$^{1}3C_9$	$^{13}C_{10}$
1427.8164(19)	1420.70002(99)	1431.08963(73)	1423.3132(28)	1423.0907(22)	1430.52291(33	1431.55261(74)
466.33780(90)	467.49001(20)	467.88650(15)	467.3362(20)	465.11104(79)	464.48853(10)	466.03563(10)
449.91511(92)	450.02884(23)	450.53664(18)	449.5160(17)	448.88189(63)	448.05798(14)	448.82507(15)
0.1962(51)	[0.160279105]	[0.160279105]	0.094(11)	0.1738(56)	[0.160279105]	[0.160279105]
-0.547(16)	[-0.554822339]	[-0.554822339]	-0.455(63)	-0.604(25)	[-0.554822339]	[-0.554822339]
1.80(11)	[1.866904945]	[1.866904945]	2.98(26)	1.81(11)	[1.866904945]	[1.866904945]
0.0343(36)	[0.029264238]	[0.029264238]	[0.029264238]	[0.029264238]	[0.029264238]	[0.029264238]
1.83(31)	[1.344064074]	[1.344064074]	-4.92(85)	[1.344064074]	[1.344064074]	[1.344064074]
30	31	31	23	20	26	26
9.7	8.2	6.9	8.8	9.0	4.7	5.6

Bibliography

[1] N. Mousseau and M. F. Thorpe, “Flexibility in biomolecules”, Physical Biology **2**, E01 (2005).

[2] N. R. Council, *Opportunities in biology* (National Academies Press, 1989).

[3] P. A. Rejto and S. T. Freer, “Protein conformational substates from X-ray crystallography”, Progress in Biophysics and Molecular Biology **66**, 167–196 (1996).

[4] J. P. Allen, C. Seng, and C. Larson, “Structures of proteins and cofactors: X-ray crystallography”, Photosynthesis Research **102**, 231–240 (2009).

[5] T. Ekeberg, M. Svenda, C. Abergel, F. R. N. C. Maia, V. Seltzer, J.-M. Claverie, M. Hantke, O. Jönsson, C. Nettelblad, G. van der Schot, M. Liang, D. P. DePonte, A. Barty, M. M. Seibert, B. Iwan, I. Andersson, N. D. Loh, A. V. Martin, H. Chapman, C. Bostedt, J. D. Bozek, K. R. Ferguson, J. Krzywinski, S. W. Epp, D. Rolles, A. Rudenko, R. Hartmann, N. Kimmel, and J. Hajdu, “Three-Dimensional Reconstruction of the Giant Mimivirus Particle with an X-Ray Free-Electron Laser”, Physical Review Letters **114**, 098102 (2015).

[6] T. R. M. Barends, L. Foucar, S. Botha, R. B. Doak, R. L. Shoeman, K. Nass, J. E. Koglin, G. J. Williams, S. Boutet, M. Messerschmidt, and I. Schlichting, “*De novo* protein crystal structure determination from X-ray free-electron laser data”, Nature **505**, 244–247 (2014).

[7] C. F. Tormena, “Conformational analysis of small molecules: NMR and quantum mechanics calculations”, Progress in Nuclear Magnetic Resonance Spectroscopy **96**, 73–88 (2016).

[8] J. S. Fraser, H. van den Bedem, A. J. Samelson, P. T. Lang, J. M. Holton, N. Echols, and T. Alber, “Accessing protein conformational ensembles using room-temperature X-ray crystallography”, Proceedings of the National Academy of Sciences **108**, 16247–16252 (2011).

[9] M. S. de Vries and P. Hobza, “Gas-Phase Spectroscopy of Biomolecular Building Blocks”, Annual Review of Physical Chemistry **58**, 585–612 (2007).

[10] R. D. Brown, P. D. Godfrey, J. W. V. Storey, and M.-P. Bassez, "Microwave spectrum and conformation of glycine", Journal of the Chemical Society, Chemical Communications, 547–548 (1978).

[11] R. D. Suenram and F. J. Lovas, "Millimeter wave spectrum of glycine", Journal of Molecular Spectroscopy **72**, 372–382 (1978).

[12] S. Blanco, A. Lesarri, J. C. López, and J. L. Alonso, "The Gas-Phase Structure of Alanine", Journal of the American Chemical Society **126**, 11675–11683 (2004).

[13] A. Lesarri, R. Sánchez, E. J. Cocinero, J. C. López, and J. L. Alonso, "Coded Amino Acids in Gas Phase: The Shape of Isoleucine", Journal of the American Chemical Society **127**, 12952–12956 (2005).

[14] G. Maccaferri, W. Caminati, and P. G. Favero, "Free jet investigation of the rotational spectrum of glycerol", Journal of the Chemical Society, Faraday Transactions **93**, 4115–4117 (1997).

[15] V. V. Ilyushin, R. A. Motiyenko, F. J. Lovas, and D. Plusquellic, "Microwave spectrum of glycerol: Observation of a tunneling chiral isomer", Journal of Molecular Spectroscopy **251**, 129–137 (2008).

[16] B. M. Giuliano, S. Blanco, S. Melandri, and W. Caminati, "Laboratory Observation of the Rotational Spectrum of a C4 Sugar, 1, 4-Anhydroerythritol", The Astrophysical Journal Supplement Series **179**, 355 (2008).

[17] P. D. Godfrey, L. D. Hatherley, and R. D. Brown, "The Shapes of Neurotransmitters by Millimeter-wave Spectroscopy: 2-Phenylethylamine", Journal of the American Chemical Society **117**, 8204–8210 (1995).

[18] P. D. Godfrey, S. J. McGlone, and R. D. Brown, "The shapes of neurotransmitters by millimetrewave spectroscopy: amphetamine", Journal of Molecular Structure **599**, 139–152 (2001).

[19] B. Vogelsanger, P. D. Godfrey, and R. D. Brown, "Rotational spectra of biomolecules: histamine", Journal of the American Chemical Society **113**, 7864–7869 (1991).

[20] S. Lobsiger, C. Perez, L. Evangelisti, K. K. Lehmann, and B. H. Pate, "Molecular Structure and Chirality Detection by Fourier Transform Microwave Spectroscopy", The Journal of Physical Chemistry Letters **6**, 196–200 (2015).

[21] S. T. Shipman, J. L. Neill, R. D. Suenram, M. T. Muckle, and B. H. Pate, "Structure Determination of Strawberry Aldehyde by Broadband Microwave Spectroscopy: Conformational Stabilization by Dispersive Interactions", The Journal of Physical Chemistry Letters **2**, 443–448 (2011).

[22]M. M. Quesada Moreno, P. Pinacho, C. Pérez, M. Šekutor, P. R. Schreiner, and M. Schnell, “London Dispersion and Hydrogen-Bonding Interactions in Bulky Molecules: The Case of Diadamantyl Ether Complexes”, Chemistry-A European Journal **26**, 10817–10825 (2020).

[23]P. Pinacho, D. Loru, T. Šumanovac, M. Šekutor, and M. Schnell, “Increasing Complexity in Adamantyl Thioethers Characterized by Rotational Spectroscopy”, ChemPhysChem **24**, e202300561 (2023).

[24]S. Zinn and M. Schnell, “Flexibility at the Fringes: Conformations of the Steroid Hormone β-Estradiol”, ChemPhysChem **19**, 2915–2920 (2018).

[25]E. Hirota, “Rotational Isomerism and Microwave Spectroscopy. I. The Microwave Spectrum of Normal Propyl Fluoride”, The Journal of Chemical Physics **37**, 283–291 (1962).

[26]W. Caminati, “Evidence of the weakness of the OH$\cdots$F hydrogen bond from a conformational study of 3-fluoro-1-propanol by microwave spectroscopy”, Journal of Molecular Spectroscopy **92**, 101–116 (1982).

[27]G. T. Fraser, R. Suenram, and C. Lugez, “Rotational Spectra of Seven Conformational Isomers of 1-Hexene”, The Journal of Physical Chemistry A **104**, 1141–1146 (2000).

[28]C. Burevschi, “The rich conformational landscape of musks and their precursors revealed by broadband rotational spectroscopy”, PhD thesis (King’s College London, 2021).

[29]C. Cabezas, M. Varela, I. Pena, J. C. Lopez, and J. L. Alonso, “The microwave spectrum of neurotransmitter serotonin”, Physical Chemistry Chemical Physics **14**, 13618–13623 (2012).

[30]C. Pérez, A. Krin, A. L. Steber, J. C. López, Z. Kisiel, and M. Schnell, “Wetting Camphor: Multi-Isotopic Substitution Identifies the Complementary Roles of Hydrogen Bonding and Dispersive Forces”, The Journal of Physical Chemistry Letters **7**, 154–160 (2016).

[31]A. L. Steber, B. Temelso, Z. Kisiel, M. Schnell, and C. Pérez, “Rotational dive into the water clusters on a simple sugar substrate”, Proceedings of the National Academy of Sciences **120**, e2214970120 (2023).

[32]S. Blanco, P. Pinacho, and J. C. López, “Hydrogen-Bond Cooperativity in Form--amide$_2$-Water: A Model for Water-Mediated Interactions”, Angewandte Chemie International Edition **55**, 9331–9335 (2016).

[33]C. Pérez, J. C. Lopez, S. Blanco, and M. Schnell, “Water-Induced Structural Changes in Crown Ethers from Broadband Rotational Spectroscopy”, The Journal of Physical Chemistry Letters **7**, 4053–4058 (2016).

[34] H. Singh, P. Pinacho, D. A. Obenchain, M. M. Quesada-Moreno, and M. Schnell, "The many forms of alpha-methoxy phenylacetic acid in the gas phase: flexibility, internal dynamics, and their intramolecular interactions", Physical Chemistry Chemical Physics **24**, 27312–27320 (2022).

[35] H. V. L. Nguyen, W. Caminati, and J.-U. Grabow, "The LAM of the rings: Large Amplitude Motions in Aromatic Molecules Studied by Microwave Spectroscopy", Molecules **27**, 3948 (2022).

[36] K. A. Utzat, R. K. Bohn, J. A. Montgomery, H. H. Michels, and W. Caminati, "Rotational Spectrum, Tunneling Motions, and Potential Barriers of Benzyl Alcohol", The Journal of Physical Chemistry A **114**, 6913–6916 (2010).

[37] J. C. Pearson, K. V. L. N. Sastry, E. Herbst, and F. C. De Lucia, "The millimeter- and Submillimeter-Wave Spectrum of Gauche-Ethyl Alcohol", Journal of Molecular Spectroscopy **175**, 246–261 (1996).

[38] H. V. L. Nguyen, I. Gulaczyk, M. Kręglewski, and I. Kleiner, "Large amplitude inversion tunneling motion in ammonia, methylamine, hydrazine, and secondary amines: From structure determination to coordination chemistry", Coordination Chemistry Reviews **436**, 213797 (2021).

[39] J. C. López, J. L. Alonso, M. E. Charro, G. Wlodarczak, and J. Demaison, "The millimeter-wave spectrum of cyclopentene", Journal of Molecular Spectroscopy **155**, 143–157 (1992).

[40] J. Laane, *Frontiers of Molecular Spectroscopy* (Elsevier, 2011).

[41] W. Caminati, "Microwave spectroscopy of large molecules and molecular complexes", in *Handbook of High-resolution Spectroscopy* (John Wiley & Sons, 2011).

[42] *CDMS-The Cologne Database for Molecular Spectroscopy*, `https://cdms.astro.uni-koeln.de/classic/doku.php?id=molecules&rev=1695821928`, Accessed: 2023-10-11.

[43] *ALMA- Atacama Large Millimeter/submillimeter Array*, `https://www.eso.org/public/teles-instr/alma/`, Accessed: 2023-10-11.

[44] *Herschel*, `https://sci.esa.int/web/herschel`, Accessed: 2023-10-11.

[45] E. Herbst and J. T. Yates Jr, "Introduction: astrochemistry", Chemical Reviews **113**, 8707–8709 (2013).

[46] E. F. Van Dishoeck, "Astrochemistry: overview and challenges", Proceedings of the International Astronomical Union **13**, 3–22 (2017).

[47] S. V. M. Caliebe, P. Pinacho, and M. Schnell, "Steroid Hormone Androsterone Observed in the Gas Phase by Rotational Spectroscopy", The Journal of Physical Chemistry Letters **13**, 11913–11917 (2022).

[48] *McGuire Group Molecules*, `https://mcguirelab.mit.edu/molecules.html`, Accessed: 2023-10-11.

[49] M. M. Quesada-Moreno, A. Krin, and M. Schnell, “Analysis of thyme essential oils using gas-phase broadband rotational spectroscopy”, Physical Chemistry Chemical Physics **21**, 26569–26579 (2019).

[50] H. Singh, F. E. L. Berggötz, W. Sun, and M. Schnell, “Chiral Control of Gas-Phase Molecules using Microwave Pulses”, Angewandte Chemie International Edition **62**, e202219045 (2023).

[51] K. Mayer, C. West, F. E. Marshall, G. Sedo, G. S. Grubbs, L. Evangelisti, and B. H. Pate, “Accuracy of quantum chemistry structures of chiral tag complexes and the assignment of absolute configuration”, Physical Chemistry Chemical Physics **24**, 27705–27721 (2022).

[52] J.-B. Biot, *Mémoire sur un nouveau genre d’oscillation que les molécules de la lumiere éprouvent en traversant certains cristaux* (Chez Firmin Didot, 1814).

[53] L. Pasteur, “Sur les relations qui peuvent exister entre la forme crystalline, la composition chimique et le sens de la polarization rotatoire”, Annales Chimie Phys. **24**, 442–459 (1848).

[54] G. Vantomme and J. Crassous, “Pasteur and chirality: A story of how serendipity favors the prepared minds”, Chirality **33**, 597–601 (2021).

[55] D. W. Deamer and J. W. Szostak, *The origins of life: a subject collection from cold spring harbor perspectives in biology*, First edition (Cold Spring Harbor Laboratory Press, 2010).

[56] M. Quack, “On Biomolecular Homochirality as a Quasi-Fossil of the Evolution of Life”, in *Proceedings of the 240 Conference: Science’s Great Challenges* (John Wiley & Sons, 2014).

[57] B. H. Pate, L. Evangelisti, W. Caminati, Y. Xu, J. Thomas, D. Patterson, C. Perez, and M. Schnell, “Quantitative Chiral Analysis by Molecular Rotational Spectroscopy”, in *Chiral Analysis*, Second Edition (Elsevier, 2018).

[58] S. R. Domingos, C. Pérez, M. D. Marshall, H. O. Leung, and M. Schnell, “Assessing the performance of rotational spectroscopy in chiral analysis”, Chemical Science **11**, 10863–10870 (2020).

[59] E. Hirota, “Triple resonance for a three-level system of a chiral molecule”, Proceedings of the Japan Academy, Series B **88**, 120–128 (2012).

[60] D. Patterson, M. Schnell, and J. M. Doyle, “Enantiomer-specific detection of chiral molecules via microwave spectroscopy”, Nature **497**, 475–477 (2013).

[61] S. Eibenberger, J. Doyle, and D. Patterson, “Enantiomer-Specific State Transfer of Chiral Molecules”, Physical Review Letters **118**, 123002 (2017).

[62] C. Pérez, A. L. Steber, S. R. Domingos, A. Krin, D. Schmitz, and M. Schnell, "Coherent Enantiomer-Selective Population Enrichment Using Tailored Microwave Fields", Angewandte Chemie International Edition **56**, 12512–12517 (2017).

[63] D. W. Pratt and B. H. Pate, "Chiral Imprinting in the Gas Phase", Angewandte Chemie International Edition **56**, 16122–16124 (2017).

[64] W. Sun, D. S. Tikhonov, H. Singh, A. L. Steber, C. Pérez, and M. Schnell, "Inducing transient enantiomeric excess in a molecular quantum racemic mixture with microwave fields", Nature Communications **14**, 934 (2023).

[65] C. Pérez, A. L. Steber, A. Krin, and M. Schnell, "State-Specific Enrichment of Chiral Conformers with Microwave Spectroscopy", The Journal of Physical Chemistry Letters **9**, 4539–4543 (2018).

[66] M. Quack, J. Stohner, and M. Willeke, "High-Resolution Spectroscopic Studies and Theory of Parity Violation in Chiral Molecules", Annual Review of Physical Chemistry **59**, 741–769 (2008).

[67] C. H. Townes, "The Ammonia Spectrum and Line Shapes Near 1.25-cm Wave-Length", Physical Review **70**, 665–671 (1946).

[68] W. E. Good, "The Inversion Spectrum of Ammonia", Physical Review **69**, 539–539 (1946).

[69] B. P. Dailey, R. L. Kyhl, M. W. P. Strandberg, J. H. Van Vleck, and E. B. Wilson, "The Hyperfine Structure of the Microwave Spectrum of Ammonia and the Existence of a Quadrupole Moment in N^{14}", Physical Review **70**, 984–984 (1946).

[70] J. P. Gordon, H. J. Zeiger, and C. H. Townes, "Molecular Microwave Oscillator and New Hyperfine Structure in the Microwave Spectrum of NH_3", Physical Review **95**, 282–284 (1954).

[71] J. P. Gordon, H. J. Zeiger, and C. H. Townes, "The Maser—New Type of Microwave Amplifier, Frequency Standard, and Spectrometer", Physical Review **99**, 1264–1274 (1955).

[72] K. B. McAfee, R. H. Hughes, and E. B. Wilson Jr, "A Stark-Effect Microwave Spectrograph of High Sensitivity", Review of Scientific Instruments **20**, 821–826 (1949).

[73] H. Abe, K. Ohtani, D. Suzuki, Y. Chida, Y. Shimada, S. Matsumoto, and M. Inouye, "Alternating 2,6-/3,5-Substituted Pyridine-Acetylene Macrocycles: π-Stacking Self-Assemblies Enhanced by Intermolecular Dipole–Dipole Interaction", Organic Letters **16**, 828–831 (2014).

[74] R. H. Dicke and R. H. Romer, "Pulse Techniques in Microwave Spectroscopy", Review of Scientific Instruments **26**, 915–928 (1955).

[75] D. G. Scroggin, J. M. Riveros, and E. B. Wilson, “Microwave spectrum and rotational isomerism of ethyl nitrate”, The Journal of Chemical Physics **60**, 1376–1385 (1974).

[76] R. G. Ford and R. A. Beaudet, “Microwave Spectrum, Barrier to Internal Rotation, and Dipole Moment of *cis*-3-Pentene-1-yne”, The Journal of Chemical Physics **55**, 3110–3113 (1971).

[77] T. J. Balle and W. H. Flygare, “Fabry–Perot cavity pulsed Fourier transform microwave spectrometer with a pulsed nozzle particle source”, Review of Scientific Instruments **52**, 33–45 (1981).

[78] H. Günther, *NMR Spectroscopy: Basic Principles, Concepts, and Applications in Chemistry*, Third edition (John Wiley & Sons, 1994).

[79] P. D. Soper, A. C. Legon, and W. H. Flygare, “Microwave rotational spectrum, molecular geometry, and intermolecular interaction potential of the hydrogen-bonded dimer OC–HCl”, The Journal of Chemical Physics **74**, 2138–2142 (1981).

[80] M. R. Keenan, L. W. Buxton, E. J. Campbell, A. C. Legon, and W. H. Flygare, “Molecular structure of ArDF: An analysis of the bending mode in the rare gas–hydrogen halides”, The Journal of Chemical Physics **74**, 2133–2137 (1981).

[81] J.-U. Grabow, W. Stahl, and H. Dreizler, “A multioctave coaxially oriented beam-resonator arrangement Fourier-transform microwave spectrometer”, Review of Scientific Instruments **67**, 4072–4084 (1996).

[82] B. Vogelsanger, M. Andrist, and A. Bauder, “Two-dimensional correlation experiments in microwave Fourier transform spectroscopy”, Chemical Physics Letters **144**, 180–186 (1988).

[83] B. Vogelsanger, A. Bauder, and H. Mäder, “Two-dimensional experiments with collision-induced transfer of populations in microwave Fourier transform spectroscopy”, The Journal of Chemical Physics **91**, 2059–2068 (1989).

[84] B. Vogelsanger and A. Bauder, “Two-dimensional microwave Fourier transform spectroscopy”, The Journal of Chemical Physics **92**, 4101–4114 (1990).

[85] W. Stahl, E. Fliege, and H. Dreizler, “Two-Dimensional Microwave Fourier Transform Spectroscopy”, Zeitschrift für Naturforschung A **39**, 858–864 (1984).

[86] G. G. Brown, B. C. Dian, K. O. Douglass, S. M. Geyer, S. T. Shipman, and B. H. Pate, “A broadband Fourier transform microwave spectrometer based on chirped pulse excitation”, Review of Scientific Instruments **79**, 053103 (2008).

[87] C. Pérez, D. P. Zaleski, N. A. Seifert, B. Temelso, G. C. Shields, Z. Kisiel, and B. H. Pate, “Hydrogen Bond Cooperativity and the three-Dimensional Structures of Water Nonamers and Decamers”, Angewandte Chemie International Edition **53**, 14368–14372 (2014).

[88] C. Cabezas, M. A. Robben, A. M. Rijs, I. Peña, and J. L. Alonso, “Fourier transform microwave spectroscopy of Ac-Ser-NH_2: the role of side chain interactions in peptide folding”, Physical Chemistry Chemical Physics **17**, 20274–20280 (2015).

[89] M. Fatima, C. Pérez, B. E. Arenas, M. Schnell, and A. L. Steber, “Benchmarking a new segmented K-band chirped-pulse microwave spectrometer and its application to the conformationally rich amino alcohol isoleucinol”, Physical Chemistry Chemical Physics **22**, 17042–17051 (2020).

[90] D. P. Zaleski, J. L. Neill, M. T. Muckle, N. A. Seifert, P. B. Carroll, S. L. Widicus Weaver, and B. H. Pate, “A K_a-band chirped-pulse Fourier transform microwave spectrometer”, Journal of Molecular Spectroscopy **280**, 68–76 (2012).

[91] B. Reinhold, I. Finneran, and S. T. Shipman, “Room temperature chirped-pulse Fourier transform microwave spectroscopy of anisole”, Journal of Molecular Spectroscopy **270**, 89–97 (2011).

[92] G. B. Park, A. H. Steeves, K. Kuyanov-Prozument, J. L. Neill, and R. W. Field, “Design and evaluation of a pulsed-jet chirped-pulse millimeter-wave spectrometer for the 70–102 GHz region”, The Journal of Chemical Physics **135**, 024202 (2011).

[93] K. Prozument, A. P. Colombo, Y. Zhou, G. B. Park, V. S. Petrović, S. L. Coy, and R. W. Field, “Chirped-pulse Millimeter-Wave Spectroscopy of Rydberg-Rydberg transitions”, Physical Review Letters **107**, 143001 (2011).

[94] D. Schmitz, V. Alvin Shubert, T. Betz, and M. Schnell, “Multi-resonance effects within a single chirp in broadband rotational spectroscopy: The rapid adiabatic passage regime for benzonitrile”, Journal of Molecular Spectroscopy **280**, 77–84 (2012).

[95] S. Mata, I. Peña, C. Cabezas, J. C. López, and J. L. Alonso, “A broadband Fourier-transform microwave spectrometer with laser ablation source: The rotational spectrum of nicotinic acid”, Journal of Molecular Spectroscopy **280**, 91–96 (2012).

[96] K. Prozument, G. Barratt Park, R. G. Shaver, A. K. Vasiliou, J. M. Oldham, D. E. David, J. S. Muenter, J. F. Stanton, A. G. Suits, G. Barney Ellison, and R. W. Field, “Chirped-pulse millimeter-wave spectroscopy for dynamics and kinetics studies of pyrolysis reactions”, Physical Chemistry Chemical Physics **16**, 15739–15751 (2014).

[97] G. B. Park and R. W. Field, “Perspective: The first ten years of broadband chirped pulse Fourier transform microwave spectroscopy”, The Journal of Chemical Physics **144**, 200901 (2016).

[98] P. F. Bernath, *Spectra of Atoms and Molecules*, Fourth edition (Oxford University Press, 2020).

[99] F. Merkt and M. Quack, “Molecular Quantum Mechanics and Molecular Spectra, Molecular Symmetry, and Interaction of Matter with Radiation”, in *Handbook of High-resolution Spectroscopy* (John Wiley & Sons, 2011).

[100] M. Born and R. Oppenheimer, “Zur Quantentheorie der Molekeln”, Annalen der Physik **389**, 457–484 (1927).

[101] W. Gordy and R. I. Cook, *Microwave Molecular Spectra* (John Wiley & Sons, 1984).

[102] A. Bauder, “Fundamentals of Rotational Spectroscopy”, in *Handbook of High-resolution Spectroscopy* (John Wiley & Sons, 2011).

[103] G. W. King, R. M. Hainer, and P. C. Cross, “The Asymmetric Rotor I. Calculation and Symmetry Classification of Energy Levels”, The Journal of Chemical Physics **11**, 27–42 (2004).

[104] D. Schmitz, “Structural flexibility and chirality of polar molecules elucidated with broadband rotational spectroscopy”, PhD thesis (Universität Hamburg, 2015).

[105] M. Leibscher, E. Pozzoli, C. Pérez, M. Schnell, M. Sigalotti, U. Boscain, and C. P. Koch, “Full quantum control of enantiomer-selective state transfer in chiral molecules despite degeneracy”, Communications Physics **5**, 110 (2022).

[106] J. K. G. Watson, “Indeterminacies of Fitting Parameters in Molecular Spectroscopy”, in *Handbook of High-resolution Spectroscopy* (John Wiley & Sons, 2011).

[107] H. H. Nielsen, “The Vibration-Rotation Energies of Molecules”, Reviews of Modern Physics **23**, 90–136 (1951).

[108] J. K. G. Watson, “Determination of centrifugal distortion coefficients of asymmetric-top molecules”, The Journal of Chemical Physics **46**, 1935–1949 (1967).

[109] S. A. Cooke and P. Ohring, “Decoding Pure Rotational Molecular Spectra for Asymmetric Molecules”, Journal of Spectroscopy **2013**, 1–10 (2013).

[110] Q. Gou, G. Feng, L. Evangelisti, A. Maris, M. Marchini, B. Velino, and W. Caminati, “Rotational Spectrum and Internal Dynamics of Tetrahydrofuran–Krypton”, ChemPhysChem **13**, 221–225 (2012).

[111] D. J. Millen, “Determination of stretching force constants of weakly bound dimers from centrifugal distortion constants”, Canadian Journal of Chemistry **63**, 1477–1479 (1985).

[112] S. L. Baughcum, Z. Smith, E. B. Wilson, and R. W. Duerst, “Microwave spectroscopic study of malonaldehyde. 3. vibration-rotation interaction and one-dimensional model for proton tunneling”, Journal of the American Chemical Society **106**, 2260–2265 (1984).

[113] D. R. Herschbach, "Calculation of Energy Levels for Internal Torsion and Over-All Rotation. III", The Journal of Chemical Physics **31**, 91–108 (1959).

[114] J. D. Dunitz, "*Accurate molecular structures, their determination and importance. (IUCr Monograph on Crystallography* No. 1) edited by A. Domenicano and I. Hargittai", Acta Crystallographica Section B **49**, 145–146 (1993).

[115] J. Demaison, "Accurate structures of non-rigid molecules by microwave spectroscopy", in *Structures and Conformations of Non-Rigid Molecules* (Springer, 1993).

[116] Z. Kisiel, "Least-squares mass-dependence molecular structures for selected weakly bound intermolecular clusters", Journal of Molecular Spectroscopy **218**, 58–67 (2003).

[117] *PROSPE - Programs for ROtational SPEctroscopy*, `http://info.ifpan.edu.pl/~kisiel/prospe.htm`, Accessed: 2023-08-07.

[118] J. Kraitchman, "Determination of Molecular Structure from Microwave Spectroscopic Data", American Journal of Physics **21**, 17–24 (1953).

[119] F. Neese, "The ORCA program system", Wiley Interdisciplinary Reviews: Computational Molecular Science **2**, 73–78 (2012).

[120] F. Neese, "Software update: the ORCA program system, version 4.0", Wiley Interdisciplinary Reviews: Computational Molecular Science **8**, e1327 (2018).

[121] P. Pracht, F. Bohle, and S. Grimme, "Automated exploration of the low-energy chemical space with fast quantum chemical methods", Physical Chemistry Chemical Physics **22**, 7169–7192 (2020).

[122] S. Grimme, C. Bannwarth, and P. Shushkov, "A Robust and Accurate Tight-Binding Quantum Chemical Method for Structures, Vibrational Frequencies, and Noncovalent Interactions of Large Molecular Systems Parametrized for All spd-Block Elements (Z = 1-86)", Journal of Chemical Theory and Computation **13**, 1989–2009 (2017).

[123] D. I. Sharapa, A. Genaev, L. Cavallo, and Y. Minenkov, "A Robust and Cost-Efficient Scheme for Accurate Conformational Energies of Organic Molecules", ChemPhysChem **20**, 92–102 (2019).

[124] C. Lee, W. Yang, and R. G. Parr, "Development of the Colle-Salvetti correlation-energy formula into a functional of the electron density", Physical Review B **37**, 785–789 (1988).

[125] A. D. Becke, "Density-functional thermochemistry. III. The role of exact exchange", The Journal of Chemical Physics **98**, 5648–5652 (1993).

[126] S. Grimme, S. Ehrlich, and L. Goerigk, “Effect of the damping function in dispersion corrected density functional theory”, Journal of Computational Chemistry **32**, 1456–1465 (2011).

[127] S. Grimme, J. Antony, S. Ehrlich, and H. Krieg, “A consistent and accurate *ab initio* parametrization of density functional dispersion correction (DFT-D) for the 94 elements H-Pu”, The Journal of Chemical Physics **132**, 154104 (2010).

[128] C. Riplinger and F. Neese, “An efficient and near linear scaling pair natural orbital based local coupled cluster method”, The Journal of Chemical Physics **138**, 034106 (2013).

[129] C. Riplinger, B. Sandhoefer, A. Hansen, and F. Neese, “Natural triple excitations in local coupled cluster calculations with pair natural orbitals”, The Journal of Chemical Physics **139**, 134101 (2013).

[130] C. Riplinger, P. Pinski, U. Becker, E. F. Valeev, and F. Neese, “Sparse maps–A systematic infrastructure for reduced-scaling electronic structure methods. II. Linear scaling domain based pair natural orbital coupled cluster theory”, The Journal of Chemical Physics **144**, 024109 (2016).

[131] M. Saitow, U. Becker, C. Riplinger, E. F. Valeev, and F. Neese, “A new near-linear scaling, efficient and accurate, open-shell domain-based local pair natural orbital coupled cluster singles and doubles theory”, The Journal of Chemical Physics **146** (2017).

[132] Y. Guo, C. Riplinger, U. Becker, D. G. Liakos, Y. Minenkov, L. Cavallo, and F. Neese, “Communication: An improved linear scaling perturbative triples correction for the domain based local pair-natural orbital based singles and doubles coupled cluster method [DLPNO-CCSD(T)]”, The Journal of Chemical Physics **148**, 011101 (2018).

[133] I. Sandler, J. Chen, M. Taylor, S. Sharma, and J. Ho, “Accuracy of DLPNO-CCSD(T): Effect of Basis Set and System size”, The Journal of Physical Chemistry A **125**, 1553–1563 (2021).

[134] F. Weigend and R. Ahlrichs, “Balanced basis sets of split valence, triple zeta valence and quadruple zeta valence quality for H to Rn: Design and assessment of accuracy”, Physical Chemistry Chemical Physics **7**, 3297–3305 (2005).

[135] *Turbomole*, `https://www.turbomole.org/company/`.

[136] T. H. Dunning, “Gaussian basis sets for use in correlated molecular calculations. I. The atoms boron through neon and hydrogen”, The Journal of Chemical Physics **90**, 1007–1023 (1989).

[137] R. F. W. Bader, “Atoms in molecules”, Accounts of Chemical Research **18**, 9–15 (1985).

[138] J. Contreras-García, E. R. Johnson, S. Keinan, R. Chaudret, J.-P. Piquemal, D. N. Beratan, and W. Yang, "NCIPLOT: A Program for Plotting Noncovalent Interaction Regions", Journal of Chemical Theory and Computation **7**, 625–632 (2011).

[139] E. F. Pettersen, T. D. Goddard, C. C. Huang, G. S. Couch, D. M. Greenblatt, E. C. Meng, and T. E. Ferrin, "UCSF Chimera–A visualization system for exploratory research and analysis", Journal of Computational Chemistry **25**, 1605–1612 (2004).

[140] G. Schaftenaar and J. H. Noordik, "Molden: a pre- and post-processing program for molecular and electronic structures*", Journal of Computer-Aided Molecular Design **14**, 123–134 (2000).

[141] C. M. Western, "PGOPHER: A program for simulating rotational, vibrational and electronic spectra", Journal of Quantitative Spectroscopy and Radiative Transfer **186**, 221–242 (2017).

[142] H. M. Pickett, "The fitting and prediction of vibration-rotation spectra with spin interactions", Journal of Molecular Spectroscopy **148**, 371–377 (1991).

[143] H. Hartwig and H. Dreizler, "The Microwave Spectrum of trans-2,3-Dimethyloxirane in Torsional Excited States", Zeitschrift für Naturforschung A **51**, 923–932 (1996).

[144] R. C. Woods, "A general program for the calculation of internal rotation splittings in microwave spectroscopy: Part II. The n-top problem", Journal of Molecular Spectroscopy **22**, 49–59 (1967).

[145] M. D. Mills, R. E. Sonstrom, Z. P. Vang, J. L. Neill, H. N. Scolati, C. T. West, B. H. Pate, and J. R. Clark, "Enantioselective Synthesis of Enantioisotopomers with Quantitative Chiral Analysis by Chiral Tag Rotational Spectroscopy", Angewandte Chemie International Edition **61**, e202207275 (2022).

[146] F. Xie, N. A. Seifert, A. S. Hazrah, W. Jäger, and Y. Xu, "Conformational Landscape, Chirality Recognition and Chiral Analyses: Rotational Spectroscopy of Tetrahydro-2-Furoic Acid $\cdots$ Propylene Oxide Conformers", ChemPhysChem **22**, 455–460 (2021).

[147] A. Jacob and K. Hornberger, "Effect of molecular rotation on enantioseparation", The Journal of Chemical Physics **137**, 044313 (2012).

[148] P. W. Atkins and R. S. Friedman, *Molecular Quantum Mechanics*, Fifth edition (Oxford University Press, 2010).

[149] K. Blum, *Density matrix theory and applications* (Springer, 2012).

[150] J.-U. Grabow, "Fourier Transform Microwave Spectroscopy Measurement and Instrumentation", in *Handbook of High-resolution Spectroscopy* (John Wiley & Sons, 2011).

[151] J.-U. Grabow, “Fourier Transform Microwave Spectroscopy: Handedness Caught by Rotational Coherence”, Angewandte Chemie International Edition **52**, 11698–11700 (2013).

[152] V. A. Shubert, D. Schmitz, C. Medcraft, A. Krin, D. Patterson, J. M. Doyle, and M. Schnell, “Rotational spectroscopy and three-wave mixing of 4-carvomenthenol: A technical guide to measuring chirality in the microwave regime”, The Journal of Chemical Physics **142**, 214201 (2015).

[153] D. Patterson and J. M. Doyle, “Sensitive Chiral Analysis via Microwave Three-Wave Mixing”, Physical Review Letters **111**, 023008 (2013).

[154] V. A. Shubert, D. Schmitz, D. Patterson, J. M. Doyle, and M. Schnell, “Identifying Enantiomers in Mixtures of Chiral Molecules with Broadband Microwave Spectroscopy”, Angewandte Chemie International Edition **53**, 1152–1155 (2014).

[155] P. Král and M. Shapiro, “Cyclic Population Transfer in Quantum Systems with Broken Symmetry”, Physical Review Letters **87**, 183002 (2001).

[156] M. Shapiro, E. Frishman, and P. Brumer, “Coherently Controlled Asymmetric Synthesis with Achiral Light”, Physical Review Letters **84**, 1669–1672 (2000).

[157] J. Lee, J. Bischoff, A. O. Hernandez-Castillo, B. Sartakov, G. Meijer, and S. Eibenberger-Arias, “Quantitative Study of Enantiomer-Specific State Transfer”, Physical Review Letters **128**, 173001 (2022).

[158] K. K. Lehmann, “Influence of spatial degeneracy on rotational spectroscopy: Three-wave mixing and enantiomeric state separation of chiral molecules”, The Journal of Chemical Physics **149**, 094201 (2018).

[159] M. Leibscher, T. F. Giesen, and C. P. Koch, “Principles of enantio-selective excitation in three-wave mixing spectroscopy of chiral molecules”, The Journal of Chemical Physics **151**, 014302 (2019).

[160] I. Thanopulos, E. Paspalakis, and Z. Kis, “Laser-driven coherent manipulation of molecular chirality”, Chemical Physics Letters **390**, 228–235 (2004).

[161] P. Král, I. Thanopulos, M. Shapiro, and D. Cohen, “Two-Step Enantio-Selective Optical Switch”, Physical Review Letters **90**, 033001 (2003).

[162] I. Thanopulos, P. Král, and M. Shapiro, “Theory of a two-step enantiomeric purification of racemic mixtures by optical means: The D_2S_2 molecule”, The Journal of Chemical Physics **119**, 5105–5116 (2003).

[163] V. S. Malinovsky and J. L. Krause, “General theory of population transfer by adiabatic rapid passage with intense, chirped laser pulses”, The European Physical Journal D - Atomic, Molecular, Optical and Plasma Physics **14**, 147–155 (2001).

[164] A. Zehnacker and M. A. Suhm, “Chirality Recognition between Neutral Molecules in the Gas Phase”, Angewandte Chemie International Edition **47**, 6970–6992 (2008).

[165] Y. Shen and C.-F. Chen, “Helicenes: Synthesis and Applications”, Chemical Reviews **112**, 1463–1535 (2012).

[166] A. Lesarri, S. T. Shipman, J. L. Neill, G. G. Brown, R. D. Suenram, L. Kang, W. Caminati, and B. H. Pate, “Interplay of Phenol and Isopropyl Isomerism in Propofol from Broadband Chirped-Pulse Microwave Spectroscopy”, Journal of the American Chemical Society **132**, 13417–13424 (2010).

[167] S. R. Domingos, C. Pérez, and M. Schnell, “Sensing Chirality with Rotational Spectroscopy”, Annual Review of Physical Chemistry **69**, 499–519 (2018).

[168] R. T. Saragi, M. Juanes, W. Caminati, A. Lesarri, L. Enríquez, and M. Jaraíz, “Rotational Spectrum, Tunneling Motions, and Intramolecular Potential Barriers in Benzyl Mercaptan”, The Journal of Physical Chemistry A **123**, 8435–8440 (2019).

[169] A. F. Ordonez and O. Smirnova, “Propensity rules in photoelectron circular dichroism in chiral molecules. II. General picture”, Physical Review A **99**, 043417 (2019).

[170] D. V. Zhdanov and V. N. Zadkov, “Absolute asymmetric synthesis from an isotropic racemic mixture of chiral molecules with the help of their laser orientation-dependent selection”, The Journal of Chemical Physics **127**, 244312 (2007).

[171] E. Hirota, “Molecular chirality: A new approach from a dynamical point of view”, Proceedings of the Japan Academy, Series B **93**, 841–849 (2017).

[172] D. S. Tikhonov, A. Blech, M. Leibscher, L. Greenman, M. Schnell, and C. P. Koch, “Pump-probe spectroscopy of chiral vibrational dynamics”, Science Advances **8**, eade0311 (2022).

[173] S. S. Bychkov, B. A. Grishanin, V. N. Zadkov, and H. Takahashi, “Laser coherent control of molecular chiral states via entanglement of the rotational and torsional degrees of freedom”, Journal of Raman Spectroscopy **33**, 962–973 (2002).

[174] S. S. Bychkov, B. A. Grishanin, and V. N. Zadkov, “Laser synthesis of chiral molecules in isotropic racemic media”, Journal of Experimental and Theoretical Physics **93**, 24–32 (2001).

[175] Z. Zhu, A. C. Fahrenbach, H. Li, J. C. Barnes, Z. Liu, S. M. Dyar, H. Zhang, J. Lei, R. Carmieli, A. A. Sarjeant, C. L. Stern, M. R. Wasielewski, and J. F. Stoddart, “Controlling Switching in Bistable [2]Catenanes by Combining Donor–Acceptor and Radical–Radical Interactions”, Journal of the American Chemical Society **134**, 11709–11720 (2012).

[176] D. H. Levy, “Laser Spectroscopy of Cold Gas-Phase Molecules”, Annual Review of Physical Chemistry **31**, 197–225 (1980).

[177] T. A. LeGreve, E. E. Baquero, and T. S. Zwier, “Infrared and Ultraviolet Spectral Signatures and Conformational Preferences of Jet-Cooled Serotonin”, Journal of the American Chemical Society **129**, 4028–4038 (2007).

[178] J. I. Seeman, H. V. Secor, P. J. Breen, V. H. Grassian, and E. R. Bernstein, “A study of nonrigid aromatic molecules. Observation and spectroscopic analysis of the stable conformations of various alkylbenzenes by supersonic molecular jet laser spectroscopy”, Journal of the American Chemical Society **111**, 3140–3150 (1989).

[179] R. Weinkauf, J.-P. Schermann, M. S. de Vries, and K. Kleinermanns, “Molecular physics of building blocks of life under isolated or defined conditions”, The European Physical Journal D-Atomic, Molecular, Optical and Plasma Physics **20**, 309–316 (2002).

[180] M. V. Johnston, “Supersonic jet expansions in analytical spectroscopy”, TrAC Trends in Analytical Chemistry **3**, 58–61 (1984).

[181] M. D. Morse, “Supersonic Beam Sources”, in *Atomic, molecular, and optical physics: atoms and molecules* (Academic Press, 1996).

[182] *Monte Carlo Maxwell Boltzmann Distribution*, `https://github.com/tpogden/quantum-python-lectures/blob/master/11_Monte-Carlo-Maxwell-Boltzmann-Distributions.ipynb`, Accessed: 2023-11-22.

[183] K. H. Lau and D. L. Hildenbrand, “Thermochemical studies of the gaseous uranium chlorides”, The Journal of Chemical Physics **80**, 1312–1317 (1984).

[184] R. S. Ruoff, T. D. Klots, T. Emilsson, and H. S. Gutowsky, “Relaxation of conformers and isomers in seeded supersonic jets of inert gases”, The Journal of Chemical Physics **93**, 3142 (1998).

[185] J. C. McGurk, T. G. Schmalz, and W. H. Flygare, “Fast passage in rotational spectroscopy: Theory and experiment”, The Journal of Chemical Physics **60**, 4181–4188 (1974).

[186] A. Krin, M. M. Quesada Moreno, C. Pérez, and M. Schnell, “A Scent of Peppermint–A Microwave Spectroscopy Analysis on the Composition of Peppermint Oil”, Symmetry **14**, 1262 (2022).

[187] S. Kotha, M. E. Shirbhate, and G. T. Waghule, “Selected synthetic strategies to cyclophanes”, Beilstein Journal of Organic Chemistry **11**, 1274–1331 (2015).

[188] A. Schmitt, O. Perraud, E. Payet, B. Chatelet, B. Bousquet, M. Valls, D. Padula, L. D. Bari, J.-P. Dutasta, and A. Martinez, “Improved hemicryptophane hosts for the stereoselective recognition of glucopyranosides”, Organic & Biomolecular Chemistry **12**, 4211–4217 (2014).

[189] J. C. Barnes, M. Juríček, N. L. Strutt, M. Frasconi, S. Sampath, M. A. Giesener, P. L. McGrier, C. J. Bruns, C. L. Stern, A. A. Sarjeant, and J. F. Stoddart, “ExBox: A Polycyclic Aromatic Hydrocarbon Scavenger”, Journal of the American Chemical Society **135**, 183–192 (2013).

[190] M. Juríček, J. C. Barnes, E. J. Dale, W.-G. Liu, N. L. Strutt, C. J. Bruns, N. A. Vermeulen, K. C. Ghooray, A. A. Sarjeant, C. L. Stern, Y. Y. Botros, W. A. Goddard, and J. F. Stoddart, “Ex^2Box: Interdependent Modes of Binding in a Two-Nanometer-Long Synthetic Receptor”, Journal of the American Chemical Society **135**, 12736–12746 (2013).

[191] E. Elacqua, T. Friščić, and L. R. MacGillivray, “[2.2]Paracyclophane as a Target of the Organic Solid State: Emergent Properties via Supramolecular Construction”, Israel Journal of Chemistry **52**, 53–59 (2012).

[192] C. J. Bruns, M. Frasconi, J. Iehl, K. J. Hartlieb, S. T. Schneebeli, C. Cheng, S. I. Stupp, and J. F. Stoddart, “Redox Switchable Daisy Chain Rotaxanes Driven by Radical–Radical Interactions”, Journal of the American Chemical Society **136**, 4714–4723 (2014).

[193] I. Roy, A. H. G. David, P. J. Das, D. J. Pe, and J. F. Stoddart, “Fluorescent cyclophanes and their applications”, Chemical Society Reviews **51**, 5557–5605 (2022).

[194] H. Hopf, “[2.2]Paracyclophanes in Polymer Chemistry and Materials Science”, Angewandte Chemie International Edition **47**, 9808–9812 (2008).

[195] C. J. Brown and A. C. Farthing, “Preparation and Structure of Di-*p*-Xylylene”, Nature **164**, 915–916 (1949).

[196] D. J. Cram and H. Steinberg, “Macro Rings. I. Preparation and Spectra of the Paracyclophanes”, Journal of the American Chemical Society **73**, 5691–5704 (1951).

[197] Z. Hassan, E. Spuling, D. M. Knoll, J. Lahann, and S. Bräse, “Planar chiral [2.2]paracyclophanes: from synthetic curiosity to applications in asymmetric synthesis and materials”, Chemical Society Reviews **47**, 6947–6963 (2018).

[198] H. Hopf, “Intramolecular Reactions in Cyclophanes”, in *Modern Cyclophane Chemistry* (John Wiley & Sons, 2004).

[199] S. Grimme and C. Mück-Lichtenfeld, "Accurate Computation of Structures and Strain Energies of Cyclophanes with Modern DFT Methods", Israel Journal of Chemistry **52**, 180–192 (2012).

[200] Y. Morisaki and Y. Chujo, "Planar Chiral [2.2]Paracyclophanes: Optical Resolution and Transformation to Optically Active π-Stacked Molecules", Bulletin of the Chemical Society of Japan **92**, 265–274 (2019).

[201] Z. Hassan, E. Spuling, D. M. Knoll, and S. Bräse, "Regioselective Functionalization of [2.2]Paracyclophanes: Recent Synthetic Progress and Perspectives", Angewandte Chemie International Edition **59**, 2156–2170 (2020).

[202] S. H. Vosko, L. Wilk, and M. Nusair, "Accurate spin-dependent electron liquid correlation energies for local spin density calculations: a critical analysis", Canadian Journal of Physics **58**, 1200–1211 (1980).

[203] E. R. Johnson, S. Keinan, P. Mori-Sánchez, J. Contreras-García, A. J. Cohen, and W. Yang, "Revealing Noncovalent Interactions", Journal of the American Chemical Society **132**, 6498–6506 (2010).

[204] A. L. Steber, W. Li, B. H. Pate, A. Lesarri, and C. Pérez, "The First Stages of Nanomicelle Formation Captured in the Sevoflurane Trimer", The Journal of Physical Chemistry Letters **13**, 3770–3775 (2022).

[205] J. K. G. Watson, "A planarity relation for sextic centrifugal distortion constants", Journal of Molecular Spectroscopy **65**, 123–133 (1977).

[206] M. Schnell, U. Erlekam, P. R. Bunker, G. von Helden, J.-U. Grabow, G. Meijer, and A. van der Avoird, "Structure of the Benzene Dimer—Governed by Dynamics", Angewandte Chemie International Edition **52**, 5180–5183 (2013).

[207] R. Podeszwa, R. Bukowski, and K. Szalewicz, "Potential Energy Surface for the Benzene Dimer and Perturbational Analysis of $\pi - \pi$ Interactions", The Journal of Physical Chemistry A **110**, 10345–10354 (2006).

[208] E. Arunan and H. S. Gutowsky, "The rotational spectrum, structure and dynamics of a benzene dimer", The Journal of Chemical Physics **98**, 4294–4296 (1993).

[209] K. A. Lyssenko, M. Y. Antipin, and D. Y. Antonov, "The Transannular Interaction in [2.2]Paracyclophane: Repulsive or Attractive?", ChemPhysChem **4**, 817–823 (2003).

[210] A. Przybylska-Balcerek and K. Stuper-Szablewska, "Phenolic acids used in the cosmetics industry as natural antioxidants", European Journal of Medical Technologies **4**, 24–32 (2019).

[211] L. Kolesniková, "The conformational panorama of mandelic acid", in International Symposium on Molecular Spectroscopy (2019).

[212] C. Min and D. Seidel, “Asymmetric Brønsted acid catalysis with chiral carboxylic acids”, Chemical Society Reviews **46**, 5889–5902 (2017).

[213] H. Alhendawi, E. Brunet, E. R. Payán, and H. Alkahlout, “Novel optically active 2D materials based on λ-zirconium phosphate and chiral monocarboxylic acids: Synthesis and characterization”, Journal of Inclusion Phenomena and Macrocyclic Chemistry **99**, 217–226 (2021).

[214] D. E. Brenneman, G. R. Smith, Y. Zhang, Y. Du, S. K. Kondaveeti, M. J. Zdilla, and A. B. Reitz, “Small Molecule Anticonvulsant Agents with Potent In Vitro Neuroprotection”, Journal of Molecular Neuroscience **47**, 368–379 (2012).

[215] *EESI- Environmental and Energy Study Institute*, `https://www.eesi.org/topics/fossil-fuels/description`, Accessed: 2023-10-11.

[216] J. C. Serrano-Ruiz, D. Wang, and J. A. Dumesic, “Catalytic upgrading of levulinic acid to 5-nonanone”, Green Chemistry **12**, 574–577 (2010).

[217] D. M. Alonso, J. Q. Bond, J. C. Serrano-Ruiz, and J. A. Dumesic, “Production of liquid hydrocarbon transportation fuels by oligomerization of biomass-derived C_9 alkenes”, Green Chemistry **12**, 992–999 (2010).

[218] M. I. Alam, S. Gupta, A. Bohre, E. Ahmad, T. S. Khan, B. Saha, and M. A. Haider, “Development of 6-amyl-α-pyrone as a potential biomass-derived platform molecule”, Green Chemistry **18**, 6431–6435 (2016).

[219] A. S. Ramos, S. B. Fiaux, and S. G. F. Leite, “Production of 6-pentyl-α-pyrone by trichoderma harzianum in solid-state fermentation”, Brazilian Journal of Microbiology **39**, 712–717 (2008).

[220] J. N. Chheda, G. W. Huber, and J. A. Dumesic, “Liquid-Phase Catalytic Processing of Biomass-Derived Oxygenated Hydrocarbons to Fuels and Chemicals”, Angewandte Chemie International Edition **46**, 7164–7183 (2007).

[221] M. Balakrishnan, G. E. Arab, O. B. Kunbargi, A. A. Gokhale, A. M. Grippo, F. Dean Toste, and A. T. Bell, “Production of renewable lubricants via self-condensation of methyl ketones”, Green Chemistry **18**, 3577–3581 (2016).

[222] H. V. L. Nguyen, M. Andresen, and W. Stahl, “Conformational sampling and large amplitude motion of methyl valerate”, Physical Chemistry Chemical Physics **23**, 2930–2937 (2021).

[223] N.-N. Dang, H.-N. Pham, I. Kleiner, M. Schwell, J.-U. Grabow, and H. V. L. Nguyen, “Methyl Internal Rotation in Fruit Esters: Chain-Length Effect Observed in the Microwave Spectrum of Methyl Hexanoate”, Molecules **27**, 2639 (2022).

[224] E. Burevschi, I. Peña, and M. E. Sanz, “Medium-sized rings: conformational preferences in cyclooctanone driven by transannular repulsive interactions”, Physical Chemistry Chemical Physics **21**, 4331–4338 (2019).

[225] E. Burevschi and M. E. Sanz, “Seven Conformations of the Macrocycle Cyclododecanone Unveiled by Microwave Spectroscopy”, Molecules **26**, 5162 (2021).

[226] S. R. Domingos, C. Pérez, C. Medcraft, P. Pinacho, and M. Schnell, “Flexibility unleashed in acyclic monoterpenes: conformational space of citronellal revealed by broadband rotational spectroscopy”, Physical Chemistry Chemical Physics **18**, 16682–16689 (2016).

[227] J. R. A. Moreno, T. R. Huet, and J. J. L. González, “Conformational relaxation of S-(+)-carvone and R-(+)-limonene studied by microwave Fourier transform spectroscopy and quantum chemical calculations”, Structural Chemistry **24**, 1163–1170 (2013).

[228] J. R. A. Moreno, F. P. Ureña, J. J. L. González, and T. R. Huet, “Terpenes in the gas phase: The structural conformation of S-(−)-perillaldehyde investigated by microwave spectroscopy and quantum chemical calculations”, Chemical Physics Letters **473**, 17–20 (2009).

[229] S. Grimme, “Exploration of Chemical Compound, Conformer, and Reaction Space with Meta-Dynamics Simulations Based on Tight-Binding Quantum Chemical Calculations”, Journal of Chemical Theory and Computation **15**, 2847–2862 (2019).

[230] A. D. Becke, “A new mixing of Hartree–Fock and local density-functional theories”, The Journal of Chemical Physics **98**, 1372–1377 (1993).

[231] P. Pinacho, J. C. López, Z. Kisiel, and S. Blanco, “Microsolvation of ethyl carbamate conformers: effect of carrier gas on the formation of complexes”, Physical Chemistry Chemical Physics **22**, 18351–18360 (2020).

[232] M. I. Alam, T. S. Khan, and M. A. Haider, “Alternate Biobased Route to Produce δ-Decalactone: Elucidating the Role of Solvent and Hydrogen Evolution in Catalytic Transfer Hydrogenation”, American Chemical Society Sustainable Chemistry and Engineering **7**, 2894–2898 (2019).

[233] D. K. Schneiderman, C. Gilmer, M. T. Wentzel, M. T. Martello, T. Kubo, and J. E. Wissinger, “Sustainable Polymers in the Organic Chemistry Laboratory: Synthesis and Characterization of a Renewable Polymer from δ-Decalactone and L-lactide”, Journal of Chemical Education **91**, 131–135 (2014).

[234] M. T. Martello, A. Burns, and M. Hillmyer, “Bulk Ring-Opening Transesterification Polymerization of the Renewable δ-decalactone Using an Organocatalyst”, American Chemical Society Macro Letters **1**, 131–135 (2012).

[235] L. Shuai and J. Luterbacher, “Organic solvent effects in biomass conversion reactions”, ChemSusChem **9**, 133–155 (2016).

[236] N. O. B. Lüttschwager and M. A. Suhm, “Stretching and folding of 2-nanometer hydrocarbon rods”, Soft Matter **10**, 4885–4901 (2014).

[237]V. Alvin Shubert, D. Schmitz, and M. Schnell, “Enantiomer-sensitive spectroscopy and mixture analysis of chiral molecules containing two stereogenic centers – Microwave three-wave mixing of menthone”, Journal of Molecular Spectroscopy **300**, 31–36 (2014).

Acknowledgement

I am deeply grateful to my supervisor, Prof. Dr. Melanie Schnell, for her guidance, support, and continuous encouragement throughout the research process. Most importantly, thank you for inspiring me every day.

I would like to thank my co-supervisor, Prof. Dr. Friedrich Temps. I am also grateful to Jun.-Prof. Dr. Daniel Obenchain and Dr. Pablo Pinacho for teaching me and helping me during my doctoral research.

I am very happy that I pursued my doctoral research at DESY. I am thankful to SFB-ELCH for financing my doctoral research. The biannual ELCH workshops, summer and winter schools have been great platforms for scientific exchange and enjoyment. To my fellow IMPRS-UFAST and PIER Ph.D. students, thank you for the scientific exchanges and the social interactions.

A big shoutout to all the past and present FS-SMP group members, past members: Cristóbal Pérez, Amanda L. Steber, Sérgio R. Domingos, Weixing Li, Mariyam Fatima, Pragya Chopra, Benjamin Arenas; and present members: Wenhao Sun, Denis Tikhonov, Donatella Loru, Eva Gougoula, Diksha Garg, Gayatri Batra, Fan Xie, Swantje Caliebe, Maureen Ayon Alfaro, Christina Tonauer, and Jiayi Li. The insightful discussions with you all make me learn something new every day, from science to food to different cultures. Thank you, Cristobal, for introducing me to chirality experiments. I am glad to have shared my initial time in the group with you to learn about the experiments. Special thanks to Wenhao Sun and Denis Tikhonov for the tunneling experiments. It has been a great learning experience from both of you, and there is still a lot to learn from you guys. Denis, thank you for such a pretty picture of microwave three-wave mixing. Pablo, thank you for listening to my ideas and helping me get them into shape. I miss you. I extend my thanks to all the people who have helped me during my thesis writing. Pablo, Mariyam, Wenhao, Denis, Freya, Swantje, Donatella, and Eva for proofreading my thesis. Freya, thanks for translating my thesis abstract into German.

Special thanks to my parents, Mrs. Meena Kumari and Mr. Madan Lal Kureel, for their love, encouragement, and understanding during this academic pursuit. The unwavering support and encouragement from my siblings Satyam Singh (bhaiya) and Shivam Singh was the cornerstone of my perseverance. Shubham Bhatt, thank you for being there and always motivating me to aim for the best. And thank you for proofreading my thesis.

This thesis is dedicated to my late nana, Ram Sanehi. I miss you, Nana. I would also like to thank Dr. Bhim Rao Ambedkar, who has been an inspiration to me and many others.

A shoutout to all my friends I made coming to Europe: Diksha Garg, Surbhi Sharma, Srashtasrita Das, Alisha Sharma, Dipali Singh, Perveer Singh, Sravya Mounika Kantamneni, Mukhtar Singh, and Sonu Kumar. Diksha thank you understanding me and having my back. Surbhi and Srashta thank you for all those conversations at midnight during COVID lockdown. Thanks for all the good times we shared cooking, dancing and shopping. You all have been a great family away from home. Sonu and Diksha thank you for feeding me with home cook food when I missed it the most. A special acknowledgment to my university friends, Vehlas (Ajeet, Noor, and Jorawar) and Ritika.

Lastly, I extend my gratitude to my master supervisor, Prof. K. S. Viswanathan. Thank you for introducing me to the realm of spectroscopy that made me uncover this exciting Ph.D. journey.

Sworn declaration

I, Himanshi Singh, hereby declare under oath that apart from the advice of Prof. Dr. Melanie Schnell, the content and design of the thesis is all my own work. I have duly acknowledged all the sources of information used in this thesis. This work has not been previously submitted, either partially or in its entirety, for consideration for a doctoral degree by any other examining body. Portions of this work have been published in academic journals as detailed below.

- Chapter: The many forms of α-methoxy phenylacetic acid in the gas phase: flexibility, internal dynamics, and their intramolecular interactions.: H. Singh, P. Pinacho, D. A. Obenchain, M. M. Quesada-Moreno, and M. Schnell "The many forms of alpha-methoxy phenylacetic acid in the gas phase: flexibility, internal dynamics, and their intramolecular interactions", Physical Chemistry Chemical Physics **24**, 27312-27320 (2022).

- Chapter: Enhancing enantiomer-selective population enrichment by depleting the thermal population.: H. Singh$^+$, F. E. L. Berggötz$^+$, W. Sun, and M. Schnell, "Chiral control of gas-phase molecules using microwave pulses", Angewandte Chemie International Edition **62**, e202219045 (2023).

- Chapter: Manipulating chirality in a molecular quantum racemate with microwave fields.: W. Sun, D. S. Tikhonov, H. Singh, A. L. Steber, C. Pérez, and M. Schnell, "Inducing transient enantiomeric excess in a molecular quantum racemic mixture with microwave fields", Nature Communications **14**, 934 (2023).

This work is in compliance with the Rules of Good Scientific Practice of the German Research Foundation. No academic degree of mine has ever been withdrawn.

Himanshi Singh

07.12.2023

Hamburg, Germany